Engineering Receptor-Based Decoys for the Treatment of Cancer Using a Yeast Surface Display Platform

Yizhou Wang

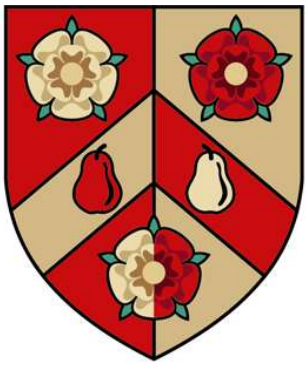
Thesis submitted to University of Oxford in partial fulfilment of the requirements for the degree of Doctor of Philosophy in Oncology

University of Oxford

Wolfson college

Trinity Term 2023





Supervisor

Prof Amato J. Giaccia

Dr Ejung Moon

Prof Nicola Sibson

Assessment Committee

Prof Ester Hammond

Prof Edward Graves

Engineering Receptor-Based Decoys for the Treatment of Cancer Using a Yeast Surface Display Platform

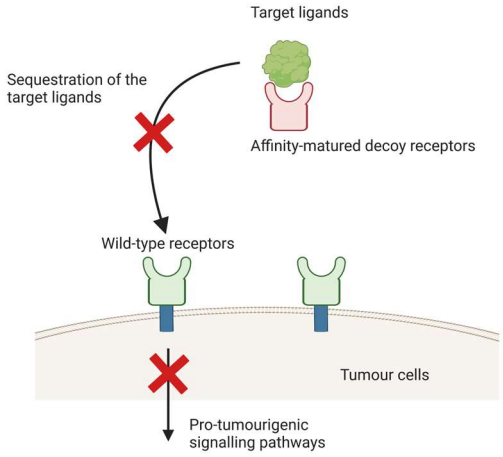
Yizhou Wang

Wolfson College, University of Oxford

Thesis submitted for the degree of Doctor of Philosophy in Oncology

Abstract

Decoy receptors form a distinct class of targeted therapeutics that offer unique advantages compared to traditional antibody therapy. Since they are derived from pre-existing signaling processes, they possess inherent ligand specificity and immune tolerance, which can significantly reduce off-target effects and enhance clinical efficacy. The use of receptor-based biologics to target aberrant signalling pathways that promote cancer cell proliferation and metastasis has emerged as a new frontier in cancer therapy. The major drawback of using "wild-type" receptor-based biologics is their limited competitive advantage over cellular receptors. Therefore, in this thesis, I employed directed evolution approaches to engineer high affinity TACI and RAGE receptor-based therapeutics that target tumour-promoting components in diffused large B cell lymphoma (DLBCL) and triple-negative breast cancer (TNBC), respectively.



DLBCL is characterised by the expansion of malignant B cells in the lymphocytes and the overexpression of autoantibodies. APRIL and BAFF are essential ligands for B cell development, which have been shown to promote DLBCL growth. In this study, I used yeast surface display-based affinity maturation processes to develop TACI variants with enhanced APRIL and BAFF binding affinity. Structural and biochemical analyses were carried out to investigate the basis of the enhanced ligand binding affinity. The TACI variants were reformatted into Fc fusion proteins to examine their *in vitro* and *in vivo* anti-tumour activity. The affinity-enhanced TACI variant, namely BS7-10, was shown to have an 8-fold increase in binding affinity to both APRIL and BAFF compared to atacicept, a commercially available WT-TACI decoy receptor. Also, BS7-10-Fc showed higher efficacy in B cell proliferation assay but demonstrated modest anti-tumour activity in a DLBCL mouse model. Collectively, our findings indicated that BS7-10 is an affinity-

enhanced decoy receptor that binds APRIL and BAFF with higher affinity that should perform better than atacicept in clinical indications for both malignant diseases as well as not malignant indications such as lupus erythematosus.

TNBC is an aggressive type of breast cancer that fails to express three hormonal regulatory receptors at targetable levels: estrogen, progesterone and HER2. Due to the lack of these three receptors, there is limited approaches for the treatment of TNBC. Receptor for advanced glycation end productions (RAGE) is a multi-ligand receptor that has been associated with TNBC metastasis. RAGE ligands pleiotropically interact with a range of receptors that can trigger TNBC progression and inflammation. In this study, I used yeast surface display and directed evolution approaches to engineer a high affinity RAGE V domain, the ligand binding domain of the RAGE receptor, that has an enhanced binding capacity to multiple RAGE ligands. Structural analysis was performed to investigate the basis of the improved binding ability. IgG1 Fc fusion proteins of RAGE V decoy receptors were produced to evaluate their anti-tumour activity in both *in vitro* and *in vivo* studies. IP-MS and RNA sequencing were used to investigate the underlying tumour-suppressive mechanism of the RAGE V variants. Overall, RAGE V13 was the most robust variant which had elevated binding capacity to multiple RAGE ligands compared to WT-RAGE V and demonstrated superior anti-proliferative and anti-migratory activity in both *in vitro and in vivo* studies. I found through IP-MS analysis that GRP78 was a novel interactor with both WT-RAGE V-Fc and RAGE V13-Fc. In addition, RNA-seq data revealed that RAGV13-Fc treatment resulted in CXCL3 downregulation in MDA-MB-231. I hypothesize that RAGE V13-Fc suppresses TLR4 signalling by sequestering GRP78, which in turn downregulates CXCL3 expression by reducing phosphor-IRF3 level. Given the complexity of RAGE-ligands interactions, further studies are needed to fully understand the underlying anti-tumour mechanism of RAGE V13-Fc.

Acknowledgements

This dissertation and my 4-year Dphil study would not have been possible without generous and unfaltering support from my friends, colleagues, supervisors and family. Hereby, I want to express my deepest gratitude to all of you.

I would first like to thank my Dphil supervisor Prof Amato J. Giacca who has always supported me since the beginning of my Dphil study. He gave me the freedom to think and to explore while guiding me whenever I was lost. His expertise in translational research sparked my interest in the biotech industry. He also went above and beyond by sending heart-warming messages on special occasions.

I am thankful for the mentorship and guidance from Dr Ejung Moon, Dr Su Myat Phyu, Dr Yanyan Jiang, Dr Hala Estephan, Dr Nuria Vilaplana Lopera, Dr Wei Song, Dr Hongbin Yang, Dr Yu Rebecca Miao, Dr Kaushik Thakkar, Dr Caiyun Grace Li, Dr Saravanan Andalur Nandagopal and Dr Quaovi Hemeka Sodji. I would also like to thank my secondary supervisor, Dr Ejung Moon, who provided full support on my projects. Also, as a dear friend of mine, Ejung often treated me to lunch and bubble tea on busy days. Su, my “older sister”, offered a lot of assistance and training on my projects who can also easily get irritated by me just like my dear sister. Yanyan spent months in the lab teaching and helping me with animal experiments effortlessly. Hala selflessly helped me with many experiments and provided countless solutions for issues I encountered. Nuria provided me with many cell culture samples, saving me a lot of time. Wei provided plenty of structural biology knowledge to assist my project and taught me about the protein purification pipeline. Hongbin, the most knowledgeable friend in immunoprecipitation, taught me how IP should be performed for mass spectrometry. Despite being located at Stanford University, Rebecca, Grace, Kaushik, Saravanan and Quaovi provided me with generous assistance on my project. There were countless phone calls and emails helping me with technical issues and career plans.

I have been fortunate to have had the opportunity to work alongside Bruno Beernaert Dominguez, Dr Kay Shigemori, Jiyoung Kim, Jimmy Xu, Haonan Xu, Fariha Mahfooz, Eric Zhang, Pauline Lascaux and Cristiano Peron, Jamie Kwon and Matthew Jackson. Bruno Beernaert. Bruno helped me create the best figures with his excellent coding skills. Kay, my bench mate and impromptu Japanese teacher, helped me with animal experiments and taught me both spoken and written Japanese (先生のご指導のおかげです from Google translation). Haonan helped me with studying and tracking cell movement. Jiyoung provided technical support for adhesion and migration assays. Many thanks also go to Jamie, Fariha, Eric, Pauline and Cristiano who have provided assistance on my projects.

I would also like to thank Dr Chen-chun Pai , Dr Carol Walker and Dr Sovan Sarkar from Tim Humphrey lab for their support of my yeast works. My gratitude also goes to our collaborators Structural Genomics Consortium (SGC), Chempartner (Chenjun Jia), Jenner Institute (Andrew Worth), Sir William Dunn School of Pathology (Mikhail Kutuzov) and Target Discovery Institute (Iolanda Vendrell).

Lastly, I want to thank my family and Yakun Tang my fiancée for their unconditional support which kept me moving forward on many difficult days.

Table of Contents

Abstract 3
Acknowledgements 5
Table of Contents 6
Abbreviations 11
List of figures 14
List of tables 17
Chapter 1. Introduction 18
1.1 Hallmarks of cancer 19
1.2 Molecular targeted therapy with a special focus on receptor-based drugs 20
1.3 FDA-approved receptor-based drugs 22
1.4 Affinity-enhanced decoy receptors 24
1.5 Therapeutic potential of engineered Transmembrane activator calcium modulator and cyclophilin ligand interactor (TACI) for the treatment of B cell lymphoma 25
1.5.1 Diffuse Large B Cell Lymphoma 25
1.5.2 The APRIL and BAFF Ligands and their Receptors 26
1.5.3 BAFF and APRIL in DLBCL 28
1.5.4 Structural characteristics of the TACI receptor 29
1.5.5 Previous attempts to target APRIL and BAFF 29
1.5.6 Engineering TACI decoy receptor 30
1.6 Therapeutic potential of engineered “Receptor for Advanced Glycation End products” (RAGE) for treatment of Triple Negative Breast Cancer 30
1.6.1 Triple Negative breast cancer (TNBC) 30
1.6.2 Hetergenicity of TNBC 32
1.6.3 TNBC therapy 33
1.6.4 RAGE receptor 37
1.6.5 RAGE structural characteristics 37
1.6.6 Targeting the RAGE Receptor and its ligands in TNBC 38
1.6.7 Assessing the safety profile of targeting RAGE. 40
1.6.8 Engineering RAGE decoy receptor 41
1.7 Aims of this thesis 41
1.8 Dissertation overview 41
Chapter 2. Methods 43
2.1 Cell Lines and their Maintenance 44
2.1.1 Bacteria and yeast strains, plasmids, and media 44

2.1.2 Mammalian cell strains, plasmids and media 44
2.1.3 Cryopreservation of cell lines 45
2.2 Yeast library-based screening 46
2.2.1 Cloning 46
2.2.2 Generation of yeast-displayed TACI and RAGE V mutant libraries 46
2.2.3 Screening for high affinity TACI and RAGE V variants 48
2.2.4 On-yeast characterisation of wild-type and mutant decoy receptors using flow cytometry 50
2.3 Recombinant protein production 51
2.3.1 Recombinant protein production (WT-RAGE V-Fc, RAGE V13-Fc, WT-TACI-Fc, BS7-10-Fc (68-110 a.a.) and BS7-10-Fc) 51
2.3.2 Recombinant protein production (GRP78) 52
2.4 Molecular biology methods and technologies 52
2.4.1 RT-PCR 52
2.4.2 SDS-PAGE (Sodium dodecyl sulfate-polyacrylamide gel electrophoresis) 53
2.4.3 Western blot 54
2.4.4 Enzyme-Linked Immunosorbent Assays (ELISA) to measure CXCL3 level in the cell culture supernatant. 55
2.4.5 RNA interference 55
2.5 Cancer cell growth and mobility assays 56
2.5.1 Proliferation assay 56
2.5.2 Clonogenic assay 56
2.5.3 Annexin V assay with PI 57
2.5.4 Adhesion assay 57
2.5.5 Migration assay 57
2.5.6 Invasion assay 58
2.5.7 Wound healing assay 58
2.6 Primary cell growth and mobility 58
2.6.1 B cell proliferation assay 58
2.6.2 NK cells and CD8+ T cell migration assay 59
2.6.3 Assessing the purity of B, NK and T cells using flow cytometry 59
2.7 Animal study 60
2.7.1 Animal welfare 60
2.7.2 Tumour induction, treatment and measurement 60
2.7.3 Hematoxylin and eosin staining 61
2.7.4 Conjugation of BS7-10-Fc with Alexa Fluor® 488 61
2.7.5 ELISA to measure mouse serum BAFF level 61

2.8 Immunoprecipitation-Mass Spectrometry (IP-MS) 62
2.8.1 Immunoprecipitation 62
2.8.2 Mass spectrometry identification of potential interactors in MDA-MB-231 cell lysate and human serum 62
2.9 RNA sequencing and functional analysis 63
2.9.1 RNA sequencing 63
2.9.2 Bioinformatic analysis for RNA sequencing results 64
2.10 *In silico* structural analysis 65
2.10.1 Alpha-fold 2 structural prediction 65
2.10.2 Computational structural simulation 65
2.11 Immunofluorescence 66
2.12 Reciprocal immunoprecipitation 66
2.14 Flow cytometry 67
2.15 Statistics 67
Chapter 3: Engineering a high affinity TACI decoy receptor for DLBCL and evaluating its therapeutic potential 68
3.1 Introduction 69
3.2 Results 70
3.2.1 Principle of yeast surface display technology 70
3.2.2 Interaction between yeast-displayed TACI and two TACI ligands, APRIL and BAFF 73
3.2.3 Mutant library generation (Yeast-displayed TACI) 74
3.2.4 Sort progression (APRIL- and BAFF-directed sorting) 75
3.2.5 Sequence analysis of variants identified in AS5 and BS7 78
3.2.6 Determining binding affinity of yeast-displayed TACI variants 81
3.2.7 Artificial TACI mutants have no major improvement in APRIL or BAFF binding. 82
3.2.8 Exploring the high affinity basis of BS7-10 through mutagenesis (reverse mutations and truncations) 84
3.2.9 Computational structural simulation of TACI-derived sequences in complex with their ligands 89
3.2.10 Reformatting TACI-10 into Fc fusions 91
3.2.11 SPR analysis of APRIL and BAFF concentration-dependent binding of BS7-10, WT-TACI, Atacicept 93
3.2.12 Effects of BS7-10 on Human Su-DHL-6 cell growth. 95
3.2.13 Mouse and Human B cell proliferation assay. 97
3.2.14 Evaluating the therapeutic potential of BS7-10 in DLBCL lymphoma mouse models. 99

3.3 Discussion 102
Chapter 4. Engineering and characterising high affinity variants of the RAGE receptor. 109
4.1 From TACI to RAGE 110
4.2 Introduction 110
4.3 Results 111
4.3.1 Interaction between yeast-displayed RAGE V and C3a 111
4.3.2 Mutant library generation (Yeast-displayed RAGE V) 112
4.3.3 Sort progression (C3a-directed sorting) 113
4.3.4 Sequence analysis of RAGE V variants identified in the CS5 library 114
4.3.5 Reformatting WT-RAGE V and RAGE V13 into Fc fusions 119
4.3.6 Assessing binding of WT-RAGE V-Fc and RAGE V13-Fc to MDA-MB-231 cellular components. 121
4.4 Discussion 123
Chapter 5: Evaluating the therapeutic potential of RAGE V13-Fc. 125
5.1 Introduction 126
5.2 Results 126
5.2.1 Inhibitory effects of RAGE V13-Fc on MDA-MB-231 in vitro cell growth 126
5.2.2 Inhibitory effects of RAGE V13-Fc on MDA-MB-231 migration and invasion 131
5.2.3 Inhibitory effects of WT-RAGE V-Fc and RAGE V13-Fc on human NK and T cell mobility 136
5.2.4 Investigating the impact of WT-RAGE V-Fc and RAGE V13-Fc on MDA-MB-231 xenograft growth and its lung metastasis in NSG mice 138
5.2.5 Investigating the impact of WT-RAGE V-Fc and RAGE V13-Fc on EO771 xenograft growth in C57/BL6 mice. 140
5.3 Discussion 141
Chapter 6. Understanding the mechanistic basis of WT-RAGE V-Fc and RAGE-V13-Fc using Mass spectrometry and RNA sequencing 145
6.1 Introduction 146
6.2 Results 147
6.2.1 Immunoprecipitation and mass spectrometry (IP-MS) revealed potential interactors of WT-RAGE V-Fc and RAGE V13-Fc in MDA-MB-231 cell lysate 147
6.2.2 Immunoprecipitation and mass spectrometry revealed potential interactors of WT-RAGE V-Fc and RAGE V13-Fc in MDA-MB-231 human serum 151
6.2.3 RNA Sequencing 157
6.3 Discussion 165
Chapter 7. General discussion and conclusion 172

7.1 Summary of BS7-10-Fc and its prospects 173
7.2 Summary of RAGE V13-Fc and its prospects 175
7.3 What factors determine the success of affinity maturation? 178
7.4 Yeast surface display is a better approach than phage display for engineering high affinity decoy receptors 180
7.5 Limitations of yeast-surface display-based affinity maturation process 181
7.6 Golden Gate cloning coupled with error-prone PCR to create DNA sequence with regional mutations. 182
References 185
Appendix 202

Abbreviations

Abbreviation	Full term
APRIL	A proliferation-inducing ligand
ASCT	Autologous stem cell transplantation
ADCs	Antibody-drug conjugates
AR	Androgen receptor
ALS	Amyotrophic lateral sclerosis
AGEs	Advanced glycation end products
A.U.	Arbitrary units
Aga1	A-agglutinin anchorage subunit 1
Aga2	A-agglutinin anchorage subunit 2
AKT	Protein kinase B
BCR	B cell receptor
BCMA	B-cell maturation antigen
BSA	Bovine Serum Albumin
BAFF	B-cell activating factor
BAFF-R	B-cell activating factor receptor
BRCA1/2	Breast cancer type 1/2 susceptibility protein
BMSCs	Bone marrow-derived mesenchymal stem cells
B_{max}	Maximum binding capacity
BP	Binding potential
CAR	Chimeric Antigen Receptor
cGAS	cyclic GMP–AMP
CTLA-4	Cytotoxic T-lymphocyte–associated antigen 4
CRD	Cysteine-rich domain
CXCR-4	C-X-C chemokine receptor type 4
C3a	Complement fragment 3a
CYP3A5	Cytochrome P450 3A5
C3aR	Complement fragment 3a receptor
CXCL1	C-X-C Motif Chemokine Ligand 1
CXCL3	C-X-C Motif Chemokine Ligand 3
CXCL8	C-X-C Motif Chemokine Ligand 8
CD3	Cluster of Differentiation 3
CD19	Cluster of Differentiation 19
CD45	Cluster of Differentiation 45
CD56	Cluster of Differentiation 56
CYP3A5	Cytochrome P450 Family 3 Subfamily A Member 5
CBX3	Chromobox protein homolog 3
DNA	Deoxyribonucleic acid
DLBCL	Diffused large B cell lymphoma
DAMPs	Damage-associated molecular patterns
dPTP	2'-Deoxy-P-nucleoside-5'-Triphosphate
ELISA	Enzyme-Linked Immunosorbent Assays
ER	Estrogen receptor
EEF1D	Elongation factor 1-delta
FDA	Food and drug administration
FACS	Fluorescence-activated cell sorting
FBS	Fetal Bovine Serum

GRP78	78-kDa glucose-regulated protein
GAL1	Galactokinase
GPRC5A	G Protein-Coupled Receptor Class C Group 5 Member A
GSEA	Gene Set Enrichment Analysis
HER2	Human epidermal growth factor receptor 2
HLA-G	Human leukocyte antigen G
HRP	horseradish peroxidase
H2AX	H2A histone family member X
HRR	Homologous recombination DNA repair
H3K9	histone H3 lysine 9
HIF1AN	Hypoxia Inducible Factor 1 Subunit Alpha Inhibitor
HSPG	Heparan sulphate proteoglycans
HMGB1	High mobility group box 1
HMMR	Hyaluronan Mediated Motility Receptor
Hsp72	Heat shock protein 72
Hsc70	Heat shock cognate 70
H & E	Hematoxylin and eosin
KD	Binding affinity
LDDT	Local Distance Difference Test
IP-MS	Immunoprecipitation-Mass Spectrometry
IL-1R	Interleukin-1 receptor
IGSF9B	Immunoglobulin Superfamily Member 9B
IRF3	Interferon regulatory factor 3
IgG	Immunoglobulin G
JAK	Janus kinase
LAG3	Lymphocyte-activation gene 3
LCN2	Lipocalin 2
LB	Luria-Bertani
LPA	Lysophosphatidic acid
LY6E	Lymphocyte Antigen 6 Family Member E
MHC I	major histocompatibility complex I
MAPK	Mitogen-activated protein kinase
MS	Mass Spectrometry
Mac-1	Macrophage integrin
MDSCs	Myeloid-derived suppressor cells
NMR	Nuclear magnetic resonance
NHL	Non-Hodgkin's lymphoma
NF-κB	Nuclear factor kappa B
OD	Optical density
PD-1	Programmed cell death protein 1 (PD-1)
PD-L1	Programmed cell death ligand 1
PARPs	Poly (adenosine diphosphate-ribose) polymerases
PDB	Protein data bank
PCR	Polymerase chain reaction
PR	Progesterone receptor
PTM	Post-translational modifications
PEG10	Paternally Expressed Gene 10
PDCD2L	Programmed Cell Death 2 Like
PSMB8	Proteasome subunit beta type-8
RR-DLBCL	Relapsed-Refractory Diffuse Large B Cell Lymphoma
pI	Isoelectric points

RNA	Ribonucleic acid
RAGE	Receptor for advanced glycation end products
STING	Stimulator of interferon genes
SLE	Systemic lupus erythematosus
STAT	Signal transducer and activator of transcription
SAA2	Serum Amyloid A2
SDS-PAGE	Sodium dodecyl sulfate polyacrylamide gel electrophoresis
SPR	Surface Plasmon Resonance
TACI	Transmembrane activator and CAML interactor
TLR2	Toll-like receptor 2
TLR4	Toll-like receptor 4
TNFRII	Tumour necrosis factor receptor II
TNBC	Triple negative breast cancer
TME	Tumour microenvironment
TBK1	TANK-binding kinase 1
TILs	Tumour infiltrating lymphocytes
TROP2	Trophoblast cell-surface antigen 2
TWEAK	TNF-related weak inducer of apoptosis
VEGFs	Vascular endothelial growth factors
VEGF A	Vascular endothelial growth factor A
VEGF B	Vascular endothelial growth factor B
VEGFR1	Vascular endothelial growth factor receptor 1
VEGFR2	Vascular endothelial growth factor receptor 2
TACI	Transmembrane activator calcium modulator and cyclophilin ligand interactor
YPD	Yeast Extract–Peptone–Dextrose
8-oxo-dGTP	8-oxo-2'-deoxyguanosine-5'-Triphosphate

List of figures

Figure 1.1. Diagrammatic representation of the hallmarks of cancer. 20
Figure 1.2. Diagrammatic representation of different types of FDA-approved decoy receptors fused with human IgG1 Fc.. 23
Figure 1.3. Diagrammatic representation of the interplay between three TNF receptors and their ligands APRIL and BAFF. 27
Figure 1.4. Crystal structure of RAGE extracellular domains..... 38
Figure 1.5. Diagrammatic representation of how RAGE decoy receptor (Bait) suppresses activation of multiple receptors. 39

Figure 3.1. Diagrammatic representation of direct evolution of receptor ectodomain using yeast display. 72
Figure 3.2. Interaction between yeast-displayed WT-TACI and its ligands, APRIL and BAFF. 74
Figure 3.3. Flow cytometry dot plots representing the sorting strategies used for screening high affinity APRIL and BAFF binders from yeast-displayed TACI mutant library. 77
Figure 3.4. Determination of binding affinity of yeast-displayed variants to APRIL or BAFF.. 82
Figure 3.5. Determination of binding affinity of yeast-displayed artificial TACI mutants to APRIL and BAFF.. 83
Figure 3.6. Binding of yeast-displayed BS7-10 reverse mutations to APRIL and BAFF.. 85
Figure 3.7. Determination of binding affinity of yeast-displayed truncated WT-TACI and BS7-10 to APRIL or BAFF. 88
Figure 3.8. Analytical size exclusion chromatography (Superose 6 Increase 10/300 GL) and SDS-PAGE results of recombinant IgG1 Fc fusion proteins. 93
Figure 3.9. Biacore surface plasmon resonance (SPR) analysis of BS7-10-Fc, WT-TACI-Fc and atacicept.. 94
Figure 3.10. CCK-8 proliferation assay showing no inhibitory effects of RAGE V13-Fc on MDA-MB-231 and Su-DHL-6 proliferation in *in vitro*.. 96
Figure 3.11 CCK-8 proliferation assay showing the inhibitory effects of RAGE V13-Fc on mouse B cell and Human B cell proliferation.. 98
Figure 3.12 Pharmacokinetic study of BS7-10-Fc in NSG mice.. 99
Figure 3.13 Evaluating the anti-tumour activity of WT-TACI-Fc, BS7-10-Fc (68-110 a.a.) and BS7-10-Fc in Su-DHL-6 bearing NSG mice. 101
Figure 3.14 Mutation I92V in BS7-10 could potentially enhance mouse APRIL binding by promoting hydrophobic interactions. 104

Figure 4.1 Interaction between yeast-displayed WT-RAGE V and C3a.. 112
Figure 4.2 Flow cytometry dot plots representing the sorting strategies used for screening high affinity C3a binders from yeast-displayed RAGE V mutant library. 114
Figure 4.3. Sequence and Structural characteristics of RAGE V13, an artificial mutant designed based on CS5 library sequencing results. (A) 116
Figure 4.4. Four-parameter sigmoidal curves showing the interaction between four different RAGE ligands and yeast-displayed WT-RAGE V and RAGE V13. 118

Figure 4.5 Alpha-fold 2 predicted ribbon structures of RAGE V13, WT-RAGE V-Fc and RAGE V13-Fc. 120
Figure 4.6 Analytical size exclusion chromatography and SDS-PAGE results. 121
Figure 4.7 Binding of WT-RAGE V-Fc and RAGE V13-Fc to MDA-MB-231 cellular components. 122

Figure 5.1 CCK-8 proliferation assay showing the inhibitory effects of RAGE V13-Fc on MDA-MB-231 proliferation..... 128
Figure 5.2 CCK-8 proliferation assay demonstrating that WT-RAGE V-Fc and RAGE V13-Fc have limited or no growth inhibition on six breast cancer cell lines, including SUM-159-PT, HCC1866, MDA-MB-468, CAL-51, MCF7 and BT-549. 129
Figure 5.3 Clonogenic assay indicating that RAGE V13-Fc treatment did not suppress clonogenicity but instead delay colony growth..... 130
Figure 5.4 Annexin V assay with PI showing no apparent cell apoptosis after WT-RAGE V-Fc and RAGE V13-Fc treatment. 131
Figure 5.5 Trans-well migration assay showing that RAGE V13-Fc treatment suppresses MDA-MB-231 cell migration and invasion. 133
Figure 5.6 Trans-well migration assay demonstrating the WT-RAGE V-induced and RAGE V13-Fc-induced suppressive effects on cell migration in multiple TNBC cell lines including MDA-MB-231, MDA-MB-468 and HCC1886.. 135
Figure 5.7 Wound healing assay suggesting an inhibitory effect of RAGE V13-Fc on cell migration.. 136
Figure 5.8 RAGE V13-Fc treatment suppresses NK cell and CD8+ T cell migration.. 137
Figure 5.9 Evaluating the anti-tumour activity of WT-RAGE-Fc and RAGE V13-Fc in MDA-MB-231 bearing NSG mice. 140
Figure 5.10 Evaluating the anti-tumour activity of WT-RAGE-Fc and RAGE V13-Fc in EO771 bearing C57BL/6 mice. 141

Figure 6.1. Immunoprecipitation and mass spectrometry revealed potential interactors of WT-RAGE V-Fc and RAGE V13-Fc in MDA-MB-231 cell lysate..... 150
Figure 6.2 Reciprocal Immunoprecipitation indicates that HMMR is not likely to be a direct interactor of WT-RAGE V-Fc and RAGE V13-Fc. (A) Western blot results showing detection of HMMR. Protein A beads coated with WT-RAGE V-Fc and RAGE V13-Fc were incubated with recombinant HMMR-HIS. Red rectangles highlight the HMMR-HIS protein band. (B) Western blot results showing the detection of IgG1 Fc, WT-RAGE V-Fc or RAGE V13-Fc. Anti-His beads coated with HMMR-HIS were incubated with WT-RAGE V-Fc and RAGE V13-Fc. Short exposure (Top) and long (bottom) exposure images were shown to highlight differences. 151
Figure 6.3 Immunoprecipitation and mass spectrometry revealed potential interactors of WT-RAGE V-Fc and RAGE V13-Fc in 1/100 diluted human serum..... 152
Figure 6.4 Ni-NTA agarose affinity chromatography, SEC and SDS-PAGE analysis of recombinant HSPA5-His/GRP78-His.. 154
Figure 6.5. Reciprocal Immunoprecipitation showing that GRP78 could be a direct interactor of WT-RAGE V-Fc and RAGE V13-Fc.. 155
Figure 6.6. RAGE V13 exhibits higher B_{max} than WT-RAGE V to GRP78. 156
Figure 6.7. CCK8 proliferation assay showing that GRP78 might be able to rescue RAGE V13-Fc-induced growth inhibition on MDA-MB-231..... 157

Figure 6.8. RNA sequencing results showing that RAGE V13-Fc treatment suppressed multiple pro-tumorigenic pathways in MDA-MB-231. 160
Figure 6.9. RT-PCR showing the relative mRNA fold-change of WT-RAGE V-Fc-treated and RAGE V13-Fc-treated MDA-MB-231 cells compared to IgG1 Fc-treated samples.. 161
Figure 6.10 The effects of WT-RAGE V-Fc and RAGE V13-Fc on CXCL3 expression in MDA-MB-231. 162
Figure 6.11. Knock-down of CXCL3 by siRNA inhibits MDA-MB-231 cell growth.. 164
Figure 6.12. Western blot results showing the effects of WT-RAGE V-Fc and RAGE V13-Fc on protein expression in MDA-MB-231. MDA-MB-231 cells were treated with 40 μg/ml of IgG1, WT-RAGE V-Fc or RAGE V13-Fc for 24 hours before cell lysate preparation for western blot analysis..... 165

Figure 7.1 Diagrammatic summary of the TACI project from engineering high affinity TACI variants to in vitro and in vivo efficacy testing. 174
Figure 7.2. Diagrammatic summary of RAGE project from engineering the high affinity RAGE V variants, to in vitro and in vivo testing and investigating underlying anti-tumor mechanism.. 176
Figure 7.3 Diagrammatic representation of partial coding sequence mutagenesis by combining Golden Gate cloning with error-prone PCR.. 183

Figure A1. CCK-8 proliferation assay showing the inhibitory effects of WT-RAGE V-Fc on B cell lymphoma cell (Su-DHL-6) growth. 202
Figure A2. Clustering of RNA sequencing results.. 203

List of tables

Table 1.1. FDA-approved decoy receptor fused with human IgG1 Fc. 22
Table 1.2. Classification of TNBC subtypes and their corresponding genetic abnormalities, cell lines. 31

Table 2.1 RT-PCR primer sequences 53

Table 3.1 Sequencing results of randomly isolated clones from AS5 and BS7. 78
Table 3.2. Comparison of intermolecular interactions between WT-TACI and BS7-10. 90
Table 3.3 Computionally estimated variations of affinity and stability (in kcal/mol) for individual mutations in BS7-10. 91

Table 4.1 Sequencing results of 20 clones from the CS5 library.. 115

Table A1. List of significantly differentially expressed genes (padj < 0.05) between IgG1 Fc and WT-RAGE V-Fc groups (n=23 genes).. 204
Table A2. List of significantly differentially expressed genes between IgG1 Fc and RAGE V13-Fc-treated groups (n=31 genes).. 205
Table A3. List of significantly differentially expressed genes between WT-RAGE V-Fc-treated and RAGE V13-Fc-treated groups (n=12 genes). 206
Table A4. Amino acid sequences of all decoy receptors and recombinant proteins used in this study. 207
Table A5. Amino acid sequences used for the computational structural simulation of TACI-derived sequences in complex with their ligands.. 209

Chapter 1. Introduction

1.1 Hallmarks of cancer

Cancer is caused by the uncontrolled cell growth of a single cell from a specific tissue that possesses the ability to spread into neighbouring tissues or distant organs in the body through the blood or lymphatic systems when a certain cell density is reached (Hanahan & Weinberg, 2011). Over the last two decades, Hanahan and Weinberg have proposed ten hallmarks of cancer and four enabling characteristics which established a solid basis for understanding cancer biology (**Figure 1.1**) (Hanahan, 2022; Hanahan & Weinberg, 2000, 2011). These concepts about the critical changes in oncogenic pathways that result as a part of cell transformation can potentially be translated into targets for cancer therapy.

Targeting hallmarks of cancer has facilitated and contributed to cancer therapy development. Ten classes of anti-cancer drugs have therefore been proposed, with each class targeting one of the cancer hallmarks or enabling characteristics (**Figure 1.1**). The majority of these drugs are designed to directly target a specific molecule or pathway that is responsible for a particular phenotype (Hanahan & Weinberg, 2011). Theoretically, such specificity would allow the target to be strongly suppressed, usually resulting in limited off-target effects. Unfortunately, in practice, therapeutics that have targeted these pathways have had significant side effects but have shown efficacy as well. However, drug resistance and ultimate relapses are almost inevitable for these single-target therapies. It was also proposed that inhibition of a particular cancer hallmark could promote cancer cells to reduce their reliance on the targeted hallmark and compensate for the “loss” of other hallmarks (Hanahan & Weinberg, 2011). For instance, resistance to antiangiogenic therapy is usually caused by augmenting other hallmarks such as upregulating proangiogenic molecules and promoting an immune-suppressive environment (Ebos et al., 2009). In this thesis, I have focused on developing new specific therapeutics that target sustained tumour growth. At the same time, to circumvent drug

resistance, another exploratory study was carried out to develop a promiscuous multi-target therapeutic that simultaneously inhibits tumour-promoting inflammation and tumour metastasis.

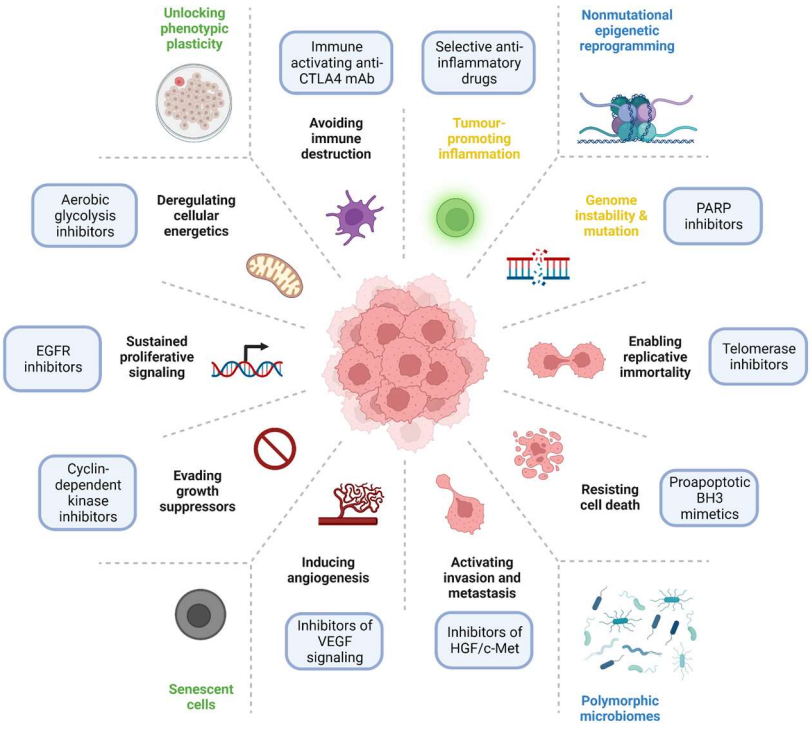


Figure 1.1. Diagrammatic representation of the hallmarks of cancer. (Adapted from (Hanahan, 2022; Hanahan & Weinberg, 2011) and "Hallmarks of cancer", by BioRender.com (2011). Retrieved from https://app.biorender.com/biorender-templates). By 2011, eight hallmarks of cancer (Black) and two enabling characteristics (Yellow) were considered as the core drivers of oncogenesis. Until recently, two additional hallmarks including senescent cells and unblocking phenotypic plasticity (Green), and two enabling characteristics (Blue) including non-mutational epigenetic reprogramming and polymorphic microbiomes were added to the chart. Ten classes of anti-cancer therapies that target the different hallmarks or enabling characteristics are highlighted in blue boxes.

1.2 Molecular targeted therapy with a special focus on receptor-based drugs

In the context of cancer, molecular targeted therapy is a type of treatment that applies biological proteins or small molecules to directly or indirectly suppress cancer growth and metastasis by targeting specific molecules (Y. T. Lee et al., 2018). These targets include cancer cell structural or functional components (e.g. cell receptors and signal

transduction pathways) as well as proteins and cells found in the tumour microenvironment that promote cancer growth or regulate immune system (e.g. growth factors, immune cells) (Saijo, 2010). Molecular targeted therapeutics are broadly classified into four categories; small molecules, monoclonal antibodies/fusion proteins, vaccines, and gene therapy (Guedan et al., 2019). Monoclonal antibodies are one of the fast-growing targeted therapies, accounting for around 20% of pharmaceutical companies' new drug approval each year since 2000s (Mullard, 2021). By 2021, one hundred monoclonal antibodies have been approved by the FDA for clinical use, and forty-one of those approved were developed for cancer therapy such as the PD1 inhibitor dostarlimab, the human epidermal growth factor receptor 2 (HER-2) inhibitor Trastuzumab and the VEGF inhibitor Bevacizumab (Mullard, 2021).

Although these monoclonal antibodies have been extensively used for cancer treatment, they have not always been able to achieve a satisfactory clinical outcome due to unexpected on-target effects, failure to inhibit receptors with multiple ligands and low target binding affinity (Castelli et al., 2019). To solve these limitations, receptor-based drugs (e.g. ligand traps) have come into the spotlight. Efforts have been made to harness the inherent immunotolerance, ligand binding affinity and specificity of natural human cellular receptors. The homeostatic shedding of receptor ectodomains to regulate receptor activity grants a high level of immunotolerance to receptor-based drugs, which could improve the pharmacokinetic properties and reduce the risk of side-effects. Moreover, receptor-based therapeutics have an identical ligand binding affinity to the wild-type receptor found at the cell surface which allows for competitive inhibition of the target ligand. Additionally, receptors usually have multiple stimulating ligands, with each ligand often potentially capable of interacting with more than one receptor. The design and development of a multi-target monoclonal antibody is more challenging compared to receptor-based drugs which already have inherent specificity to their ligands.

1.3 FDA-approved receptor-based drugs

Several receptor-based human IgG Fc fusion proteins have been approved by the FDA over the last three decades (**Table 1.1**). Etanercept was the first approved receptor-based drug by FDA in 1998 (Hassett et al., 2018). Etanercept is a fusion protein composed of a tumour necrosis factor receptor II (TNFRII) extracellular domain with human IgG1 Fc, and is used to target tumour necrosis factor for the treatment of rheumatoid arthritis (Hassett et al., 2018). In the subsequent years, FDA has additionally approved alefacept (lymphocyte-function antigen 3 decoy receptor) for psoriasis and transplant rejection, and rilonacept (IL-1R decoy) for cryopyrin-associated periodic syndromes (Czajkowsky et al., 2012).

Table 1.1. FDA-approved decoy receptor fused with human IgG1 Fc. Adapted from (Czajkowsky et al., 2012; Mansour et al., 2019; Markham, 2020).

Trade name (generic name)	Description	Indication of first FDA approval	Stage	Company
Reblozyl (luspatercept)	A modified extracellular domain of the human activin receptor type IIB fused to the Fc of human IgG1 which binds to certain TGF-β ligands	Anaemia	FDA Approved (2019)	Acceleron Pharma and Celgene Corporation
Zaltrap (ziv-aflibercept)	A naturally occurring vascular endothelial growth factor binding (VEGF) sequences	Metastatic colorectal cancer (mCRC) that is resistant to or has progressed following an oxaliplatin containing regimen	FDA Approved (2012)	Regeneron
Nulojix (belatacept)	Mutated CTLA-4 fused to the Fc of human IgG1	Organ rejection	FDA Approved (2011)	Bristol-Meyers Squibb
Eylea (aflibercept)	VEGFR1/VEGFR2 fused to the Fc of human IgG1	Age related macular degeneration	FDA Approved (2011)	Regeneron Pharmaceuticals
Arcalyst (rilonacept)	IL-1R fused to the Fc of human IgG1	Cryopyrin-associated periodic syndromes	FDA Approved (2008)	Regeneron Pharmaceuticals
NPlate (romiplostim)	Thrombopoietin-binding peptide fused to the Fc of human IgG1	Thrombocytopenia in chronic immune thrombocytopenic purpura patients	FDA Approved (2008)	Amgen/Pfizer
Orencia (abatacept)	Mutated CTLA-4 fused to the Fc of human IgG1	Rheumatoid arthritis	FDA Approved (2005)	Bristol-Meyers Squib
Amevive (alefacept)	LFA-3 fused to the Fc of human IgG1	Psoriasis and transplant rejection	FDA Approved (2003)	Astellas Pharma
Enbrel (etanercept)	TNFR fused to the Fc of human IgG1	Rheumatoid arthritis	FDA Approved (1998)	Amgen/Pfizer

The major limitation of using wild-type receptor ectodomains as ligand traps is that their inherent ligand binding affinity does not always confer a strong competitive advantage over membrane-bound receptors. In addition, many native receptors with low ligand binding affinity are not suitable to be converted into decoy receptors since the weak binding affinity yields low target clearance. For example, the binding affinity of PD-1 to PD-L1 is within lower micromolar range (Magnez et al., 2017).

To improve receptor-based ligand traps as therapeutics, genetic engineering of receptors solves a number of these problems (**Figure 1.2**). For example, Abatacept is a CTLA-4-Fc fusion protein with mutations in both CTLA-4 and Fc which change disulphide bond positions to achieve the optimal therapeutic effects for RA patients (Lynaugh et al., 2013).

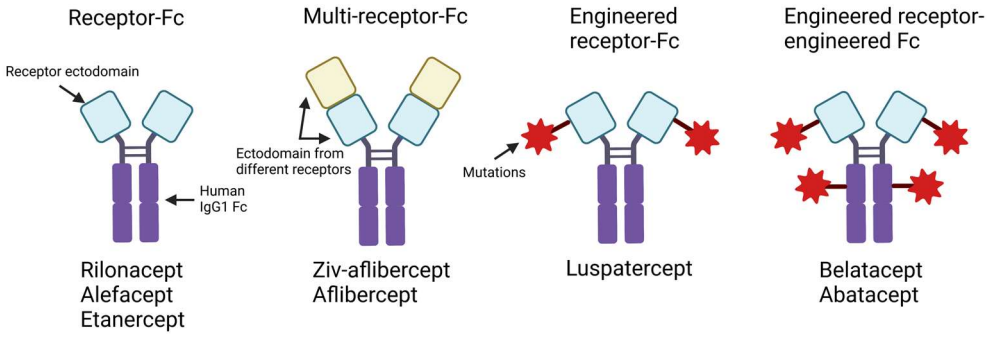


Figure 1.2. Diagrammatic representation of different types of FDA-approved decoy receptors fused with human IgG1 Fc. Decoy receptors fused with human IgG1 Fc that have been approved by FDA are indicated below each model. Muti-receptor-Fc has a binding domain comprised of different receptor ectodomains. Engineered receptor-Fc has a modified receptor ectodomain. Engineered receptor-engineered Fc has a modified receptor ectodomains fused with a modified Fc domain. Examples are shown at the bottom of each model.

To enhance the clinical efficacy of the soluble CTLA-4 ligand trap abatacept, two additional point mutations were later introduced to generate a new biologic belatacept that is 10 times more potent than abatacept in suppressing T-cell activation (Larsen et al., 2005; Wekerle & Grinyo, 2012). Moreover, multiple receptor binding domains can be fused together to broaden target coverage. Both ziv-aflibercept and aflibercept are IgG1

Fc fusion proteins that harbour both vascular endothelial growth factor receptor 1 and 2 (VEGFR1/VEGFR2) ligand binding domains which enable the simultaneous neutralisation of VEGF-A, VEGF-B, and placenta growth factor (PlGF) (Clarke & Hurwitz, 2013). In addition, an engineered angiotensin-converting enzyme 2 (ACE2) obtained through deep mutagenesis was recently shown to have an enhanced binding affinity to Spike proteins from multiple variants of SARS-CoV-2 (Zhang et al., 2022). In summary, manipulating decoy receptor architecture has the potential to not only enhance the binding affinity to target ligands but also change the ligand diversity for better clinical outcomes.

1.4 Affinity-enhanced decoy receptors

As receptor-based therapeutics, decoy receptors have a pre-established high immunotolerance and a high target-specificity profile which provides significant advantages over traditional antibodies. Creating tailored decoy receptors that are engineered for different disease settings could further provide substantial benefits for patients. Even with the recent successes of therapeutic decoy receptors, the full potential of soluble receptor-based cancer therapy is still yet to be harnessed.

A yeast surface display technique was used by our group as a unique platform to carry out high throughput screening for high affinity decoy receptor variants. Our group has reported on the engineering of decoy receptors using yeast surface display and have shown them to be superior than their wild-type counterparts. For example, the Giaccia lab engineered an Axl receptor that has 80 times higher affinity to its ligand Gas6 than wild-type Axl which is currently in a Phase 3 trial for platinum-resistant ovarian cancer (Kariolis et al., 2014). The binding affinity of an engineered PD1 ectodomain to PD-L1 and PD-L2 increased by approximately 10,000-fold and 100-fold respectively relative to wild-type PD-1 (Miao et al., 2021). An affinity-enhanced BCMA variant was shown to have 4-fold and 500-fold increase in affinity to its ligands including APRIL and BAFF,

respectively (Miao et al., 2022). Another study developed a CD4 variant that bears two mutations which results in a 40-fold increase in binding affinity to its ligand HLA-DR1 (Wang et al., 2011). In this case, both HLA-DR1 tetramers and monomers were used in screening to ensure the resulting variants with high ligand binding affinity and avidity. These successful attempts to engineer high affinity decoy receptors with yeast surface display provided a solid foundation for my studies.

1.5 Therapeutic potential of engineered Transmembrane activator calcium modulator and cyclophilin ligand interactor (TACI) for the treatment of B cell lymphoma

1.5.1 Diffuse Large B Cell Lymphoma

Diffused large B cell lymphoma (DLBCL) is a type of non-Hodgkin's lymphoma characterised by uncontrolled proliferation of mature B lymphocytes within the lymph nodes (He & Kridel, 2021). As the most common type of non-Hodgkin's lymphoma, DLBCL represents around 25% of all non-Hodgkin's lymphoma cases (Teras et al., 2016). Currently, R-CHOP, a multi-drug cocktail comprising of an anti-CD20 monoclonal antibody, cyclophosphamide, doxorubicin, vincristine, and prednisone, is the standard treatment for DLBCL (Coiffier et al., 2010). 60% of patients who receive R-CHOP treatment experience long-term disease-free survival. In contrast, relapsed or refractory tumours were found in 40% of all patients who had a complete remission (He & Kridel, 2021). Unfortunately, 80% of these patients will succumb to DLBCL despite being treated with additional chemotherapies and autologous stem cell transplantation (ASCT) (Crump et al., 2017). R-CHOP resistance is thought to arise from tumour heterogeneity and an immunosuppressive tumour microenvironment (TME) (He & Kridel, 2021).

Chimeric Antigen Receptor (CAR)-T therapy is a type of cellular treatment where autologous T cells are engineered to recognise specific tumour antigens that results in cytotoxicity independent of interactions between T-cell receptor and the major

histocompatibility complex (MHC). Several CAR-T cell therapies have been approved by FDA for patients with Relapsed-Refractory Diffuse Large B Cell Lymphoma, resulting in a significant improvement in patient outcomes (Abramson et al., 2020; Neelapu et al., 2017; Schuster et al., 2019). For example, 45% of RR-DLBCL patients had complete remission after receiving CD-19 targeted CAR-T cell treatment (Abramson et al., 2020; Neelapu et al., 2017; Schuster et al., 2019). Nonetheless, drug resistance in DLBCL is still a problem that needs to be overcome since some studies have reported that CD-19 negative RR-DLBCL could be found in patients treated with CD-19 targeted CAR-T cell treatment (Schuster et al., 2017; Shalabi et al., 2018). Furthermore, CD-19 targeted CAR-T cell treatment has been associated with multiple adverse effects such as cytokine release syndrome and immune effector cell–associated neurotoxicity syndrome (Zhang et al., 2022). Therefore, more effective and safer treatments for RR-DLBCL are needed.

1.5.2 The APRIL and BAFF Ligands and their Receptors

The interplay between B-cell activating factor (BAFF; BLys; TNFSF13B) and a proliferation-inducing ligand (APRIL; TNFSF13) and their receptors BAFF receptor (BAFF-R, TNFRSF13C; BR3), B-cell maturation antigen (BCMA; TNFRSF17) and transmembrane activator and CAML interactor (TACI; TNFRSF13B) is critical for B cell development (**Figure 1.3**) (Vincent et al., 2014). Both APRIL and BAFF can bind TACI equally well with a binding affinity in the nanomolar range (Hengeveld & Kersten, 2015). Wild-type BCMA has a nanomolar binding affinity to APRIL but a micromolar binding affinity to BAFF. Interestingly, BAFF is the only ligand for BAFF-R and has a nanomolar binding affinity (Day et al., 2005).

The TACI receptor has been associated with antibody class switching, responses of B cell to thymus-independent antigen 1 and 2 and B cell regulation (Vincent et al., 2013). BAFF-R and BCMA are critical for immature B cell survival and plasma cell survival respectively. The BAFF-R has an additional role in B cell maturation. The ectodomains

of TACI are constitutively shed as decoy receptors through ADAM-10-mediated proteolytical cleavages (Hoffmann et al., 2015). Unlike TACI, shedding of BAFF-R ectodomains by ADAM-10 requires direct BAFF binding (Smulski & Eibel, 2018). The release of BCMA ectodomains is a constitutive process catalysed by another enzyme γ-secretase (Smulski & Eibel, 2018).

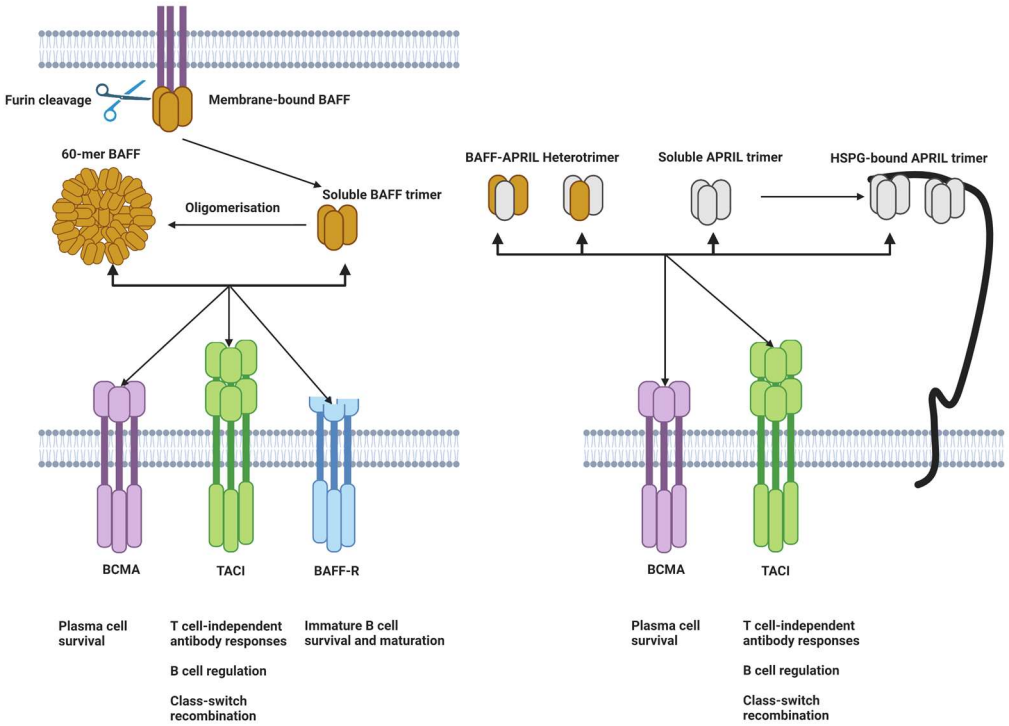


Figure 1.3. Diagrammatic representation of the interplay between three TNF receptors and their ligands APRIL and BAFF. Figure adapted from (Hengeveld & Kersten, 2015; Vincent et al., 2014). Membrane-bound BAFF trimers can be released by a furin protease. APRIL primarily exists in its soluble form. Binding affinity of the three receptors to BAFF is ordered from strongest to weakest as TACI, BCMA and BAFF-R. APRIL does not interact with BAFF-R and binds TACI and BCMA with a nanomolar range affinity. Oligomerization of 3-mer BAFF produces 60-mer BAFF which interacts with all the three receptors. HSPG-bound APRIL trimers can interact with both TACI and BCMA receptor. Heterotrimers formed by APRIL and BAFF monomers are also biologically active. Structurally, TACI, BCMA and BAFF-R contain two, single and partial cysteine-rich domains respectively.

APRIL and BAFF can also exist in soluble and membrane-bound forms. As type II transmembrane proteins, BAFF can be proteolytically cleaved into a soluble form by furin proteases while APRIL is predominantly secreted as a soluble protein (Hahne et al., 1998;

Lopez-Fraga et al., 2001; Moore et al., 1999). Membrane-bound APRIL was only found when APRIL appears as a APRIL-δ isoform or as a fusion protein of APRIL and TNF-related weak inducer of apoptosis (TWEAK) (Maia et al., 2011; Pradet-Balade et al., 2002). Stochiometrically, twenty soluble BAFF trimers can oligomerise into a 60-mer BAFF multimer (Cachero et al., 2006). Heterotrimers of BAFF-APRIL have been reported in rheumatoid arthritis patients and are biologically active (Dillon et al., 2010; Roschke et al., 2002).

1.5.3 BAFF and APRIL in DLBCL

B cell survival and development requires BAFF (Schneider et al., 1999). In contrast to BAFF, APRIL plays a critical role in plasma cell survival in the bone marrow (Belnoue et al., 2008). In addition to their functions in normal B cell development, APRIL and BAFF are also implicated in the survival and growth of DLBCL. Both BAFF and APRIL levels are increased in DLBCL patients and contribute to disease progression (Kuo et al., 2008). BAFF and APRIL have been shown to protect non-Hodgkin's lymphoma (NHL) B cells from undergoing apoptosis by inducing BCL-2 (He et al., 2004). BAFF is constitutively expressed in DLBCL and plays an important role in promoting DLBCL cell growth (Fu et al., 2006). APRIL produced by neutrophils tends to be trapped in the TME of DLBCL through interactions with proteoglycans (Schwaller et al., 2007). The trapping of APRIL in the TME may facilitate tumour growth, resulting in poor patient survival (Schwaller et al., 2007). In comparison, BAFF most probably has a more important role than APRIL in DLBCL survival because DLBCL originates from BAFF-driven B lymphocytes instead of APRIL-driven plasmablasts. Studies have shown that sequestration of APRIL has little effect on DLBCL growth, while neutralisation of both APRIL and BAFF dramatically reduces tumour volume in DLBCL mouse models (Miao et al., 2022).

1.5.4 Structural characteristics of the TACI receptor

Structurally, TACI is comprised of two cysteine-rich domains (CRDs) in comparison to BCMA and BAFF which contain a single and partial CRD, respectively. The DXL motif is a highly conserved short amino acid sequence (Phe/Tyr/Trp)-Asp-Xaa-Leu-(Val/Thr)-(Arg/Gly) shared by all the CRDs from the three receptors (Hymowitz et al., 2005). This motif is important for both APRIL and BAFF binding (Patel et al., 2004). TACI CRD2 is primarily responsible for APRIL and BAFF binding compared to TACI CRD1, which in comparison has a weaker binding affinity to APRIL and BAFF (Vincent et al., 2014). In fact, CRD2 alone is sufficient to trigger ligand-dependent signaling (Hymowitz et al., 2005). TACI CRD1 is not functionally required and might be a result of a gene duplication event (Hymowitz et al., 2005).

TACI CRD2 binding interface shares a similar conserved beta-hairpin structure with BCMA and BAFF-R, which is known to be the binding pocket for APRIL and BAFF (Bossen & Schneider, 2006). The C-terminal helix-loop-helix varies significantly across the three receptors (TACI, BCMA and BAFF-R) and has been proposed to determine ligand specificity (Bossen & Schneider, 2006). For both BCMA and BAFF-R, it was reported that several amino acid residues are detrimental for APRIL or BAFF binding (Bossen & Schneider, 2006). However, all amino acid residues within the TACI CRD2 binding interface have little or no negative impact on both APRIL and BAFF binding, thereby explaining its dual specificity.

1.5.5 Previous attempts to target APRIL and BAFF

The high affinity interactions between APRIL and BAFF and their receptors make the suppression of their signalling extremely diffcult with traditional antibodies and wild-type decoy receptors. Belimumab is an anti-BAFF monoclonal antibody which has been approved for the treatment of systemic lupus erythematosus (SLE) (Tong et al., 2019). Belimumab targets BAFF alone leaving serum APRIL levels unchanged, resulting in

insufficient suppression of TACI and BCMA activation (Tong et al., 2019). Atacicept is a recombinant fusion protein composed of a human IgG1 Fc with part of the ectodomain of TACI (Kaegi et al., 2020). Atacicept sequesters APRIL and BAFF, and has been used to suppress autoreactive B cell activities in autoimmune diseases such as multiple sclerosis in clinical trials (Kaegi et al., 2020). However, no clinical indications have been approved to date and Atacicept may not have a competitive advantage over the wild-type TACI receptor (Rossi et al., 2009). Recently, an engineered BCMA decoy receptor with enhanced APRIL and BAFF binding was shown to effectively suppress tumour growth in BAFF-driven DLBCL mouse models (Miao et al., 2022). Currently, this molecule is in clinical development. In summary, insufficient blokade of APRIL and BAFF hinders the progress of anti-APRIL and anti-BAFF therapy.

1.5.6 Engineering TACI decoy receptor

Unlike BCMA and BAFF-R that have one CRD which binds only one ligand with high affinity, TACI has two CRDs that exhibit high affinity binding to both APRIL and BAFF. TACI is therefore a promosing candidate for developing high affinity APRIL and BAFF antagonists. My first project in this thesis describes the development and efficacy of an engineered TACI decoy receptor in treating DLBCL. This study also highlights the need for further understanding of TACI structure and optimisation to reveal its full potential.

1.6 Therapeutic potential of engineered “Receptor for Advanced Glycation End products” (RAGE) for treatment of Triple Negative Breast Cancer

1.6.1 Triple Negative breast cancer (TNBC)

Triple negative breast cancer is an aggressive form of breast cancer that does not express the estrogen receptor (ER), the progesterone receptor (PR), or the HER2 (Yin et al., 2020). TNBC represents around 15-20% of all breast cancer cases and has a

higher prevalence in females from African and Hispanic descent and individuals carrying mutations in breast cancer susceptibility genes (Foulkes et al., 2010).

Table 1.2. Classification of TNBC subtypes and their corresponding genetic abnormalities, cell lines. Table adapted from (Yin et al., 2020).

TNBC subtype	Genetic abnormalities	Cell line
Basal-like 1	Cell cycle gene expression DNA repair gene (ATR-BRCA pathway) Proliferation genes	HCC2157 HCC1599 HCC1937 HCC1143 HCC3153 MDA-MB-468 HCC38
Basal-like 2	Growth factor-signaling pathways (EGFR, MET, NGF, Wnt/β-catenin, IGF-1R) Glycolysis, gluconeogenesis Expression of myoepithelial markers	SUM149PT CAL-851 HCC70 HCC1806 HDQ-P1
Immunomodulatory	Immune cell processes (CTLA4, IL2, IL7 pathways, antigen processing/presentation) Gene signature for medullary BC (rare TNBC with a favorable prognosis)	HCC1187 DU4475
Mesenchymal-like	Cell motility Cell differentiation Growth factor signaling EMT	BT-549 CAL-51 CAL-120
Mesenchymal stem-like	Similar to M+ Low proliferation Angiogenesis genes	HS578T MDA-MB-157 SUM159PT MDA-MB-436 MDA-MB-231
Luminal androgen receptor	Androgen receptor gene Luminal gene expression pattern Molecular apocrine subtype	MDA-MB-453 SUM185PE HCC2185 CAL-148 MFM-223

Based on bulk mRNA sequencing results, TNBC is classified into six subtypes: basal-like 1, basal-like 2, immunomodulatory, mesenchymal (M), mesenchymal stem-like, and luminal androgen receptor type (**Table 1.2**) (Lehmann et al., 2011). The basal-like 1 subtype has high genomic instability and is enriched in proteins for DNA damage response and cell cycle progression (Toft & Cryns, 2011). Basal-like 2 is characterised by overexpression of growth factors and myoepithelial markers (Lehmann et al., 2016). The immunomodulatory subtype is enriched in immune signaling molecules like chemokines and cytokines which are thought to be produced by tumour cells and tumour-infiltrating lymphocytes (Yin et al., 2020). The mesenchymal and mesenchymal stem-like subtypes result from elevated levels of growth factors that promote epithelial-to-

mesenchymal-transitions. The luminal androgen receptor subtype is enriched in androgens, estrogens and porphyrins (Vtorushin et al., 2022). These classifications highlight the importance of both cancer-cell intrinsic and tumour-microenvironment extrinsic characteristics in TNBC development.

1.6.2 Hetergenicity of TNBC

Intrinsic heterogeneity of TNBC is associated with genomic alterations which have been identified and well-documented through the use of genomics, epigenomics, transcriptomics and proteomics (Bianchini et al., 2016). For example, TP53 mutation is frequently found in TNBC and may contribute to immune evasion by suppressing the cGAS (GMP–AMP synthase)–STING (stimulation of interferon genes) pathway-mediated type I interferon response (Ghosh et al., 2021). In another example, DNA damage response deficiency due to BRCA1/2 mutations, homologous recombination deficiency (HRD) or high microsatellite instability are commonly found in TNBC cancer and differentially affect the immune response in the tumour microenvironment (TME) (Samstein et al., 2021).

Heterogeneity of TNBC is reflected in the immune composition of the TME. The TNBC TME has been classified into four subtypes based on the spatial distribution and immune cell population. Immune desert and fully inflamed subtypes represent tumours with little and high numbers of CD8+ T cells, respectively (Gruosso et al., 2019). Tumours with a majority of CD8+ T cell that accumulate in the margin of stromal areas are considered to be margin restricted or stroma restricted subtypes (Gruosso et al., 2019). A small number of PD-L1+ tumour-associated macrophages and exhausted T cells are the major component of immune cell population in immune desert tumours (Wagner et al., 2019). Margin restricted and stroma restricted tumours usually have neutrophil accumulation at the border area with B cells at a distance (Keren et al., 2018).

Co-evolution of TNBC cells with the TME is found in metastasis where increased mutation burden leads to more suppressive anti-cancer immunity (Bianchini et al., 2022). Intrinsically, an enhanced tumour mutational burden in metastatic TNBC is usually associated with deficient homologous recombination DNA repair (HRR) and a reduced expression of antigen presenting components such as major histocompatibility complex (MHC) class 1 (Bertucci et al., 2019; Szekely et al., 2018). Extrinsically, metastatic tumours have a more immune-evasive TME with fewer tumour infiltrating lymphocytes (TILs) and lower levels of anti-tumour immune modulators such as interferon-induced proteins (Hutchinson et al., 2020; Zhu et al., 2019). In contrast, macrophages with immunosuppressive phenotypes like Lymphocyte-activation gene 3 (LAG3) and Human leukocyte antigen G (HLA-G) are more prevalent (Zhu et al., 2019). In addition, the co-evolution of TNBC with the TME is also affected by tissue-specific factors at the metastatic sites (Rozenblit et al., 2020). For example, liver metastasis is commonly depleted of TILs and enriched in PD-L1 negative immune cells (Y. Li et al., 2021).

The intrinsic and extrinsic heterogeneity of TNBC contributes to the dynamically changing cell features in this cancer. The pathological differences between the primary and metastatic tumour increase the aggressiveness of the TNBC phenotype. Targeting a single molecule is hard to achieve with sufficient clinical efficacy and is likely to result in drug resistance in the short term. Therefore, more intense and multi-targeted therapy is required to control the growth and expansion of TNBC.

1.6.3 TNBC therapy

Given the absence of the three targetable surface receptors, conventional breast cancer therapy, such as hormone therapy (e.g. tamoxifen) and HER2-targeted therapy (e.g trastuzumab), are of limited effectiveness (Mahtani et al., 2021). Currently, systematic chemotherapy remains the standard of care treatment for TNBC patients. Anthracycline and taxanes are the chemotherapies that are used to treat TNBC, and are administered

in a sequential manner (Zaheed et al., 2019). Anthracyclines are a class of antibiotics that include agents such as doxorubicin which intercalate into DNA as well as alkylating agents (Taymaz-Nikerel et al., 2018). In contrast to cytotoxic anthracyclines, taxanes suppress TNBC growth by triggering the spindle assembly checkpoint (SAC) and inhibiting mitosis (Russell et al., 2012). To improve treatment outcomes, additional chemotherapies, such as platinum agents, have been tested in combination with anthracycline and taxanes in neoadjuvant treatment. However, while platinum agents were able to increase pathological complete response rates by 12.5%, they also exacerbated haematological toxicities (Poggio et al., 2018).

1.6.3.1 PARP inhibitors

Homologous recombination deficiency is frequently detected in TNBC as a result of breast cancer type 1/2 susceptibility protein (BRCA1/2) mutation, PALB2 mutation or epigenetic suppression of *BRAC1* and RAD51 (Polak et al., 2017; Staaf et al., 2019). Approximately 10% of TNBC patients have BRCA1/2 mutations which makes them eligible for treatment with poly(ADP-ribose) polymerase (PARP) inhibitors (den Brok et al., 2017). PARP plays an essential role in recognising single-strand breaks in DNA and promoting DNA repair (Jackson & Bartek, 2009). In fact, TNBC cells with BRCA1/2 mutations rely heavily on PARP to maintain genomic stability and are therefore more sensitive to PARP inhibitors such as olaparib and talazoparib (Bryant et al., 2005; Farmer et al., 2005).

1.6.3.2 Antibody-drug conjugates (ADCs)

Antibody-drug conjugates (ADCs) are a novel class of therapies with a focus on treating metastatic TNBCs (Drago et al., 2021). ADCs are comprised of recombinant monoclonal antibodies covalently conjugated with cytotoxic chemicals through a flexible linker (Drago et al., 2021). This approach allows specific delivery of cytotoxic agents to antigen-expressing TNBC cells with reduced toxicity to normal tissues. Sacituzumab govitecan

is a FDA approved ADC for TNBC which contains a pH-sensitive linker which connects an antibody targeting trophoblast cell-surface antigen 2 (TROP2) and the DNA topoisomerase I inhibitor SN-38 (Bardia et al., 2017). TROP2 is a transmembrane glycoprotein involved in cell proliferation, survival and invasion and is highly expressed in many cancers including TNBC (Bardia et al., 2017; Shvartsur & Bonavida, 2015). SN-38 is a cytotoxic topoisomerase inhibitor that impedes DNA unwinding (Voigt et al., 1998).

1.6.3.3 Androgen Receptor inhibitors

The luminal androgen receptor subtype represents 30% of TNBC cases and upregulates the expression of the androgen receptor (AR) (Lehmann et al., 2011; Michmerhuizen et al., 2020). Despite AR being a drugable target, there is currently no evidence of AR inhibitors or AR biosynthesis inhibitors exhibiting any meaningful anti-tumour activity in individuals with luminal androgen receptor TNBC (Bianchini et al., 2022). Bicalutamide, a AR inhibitor, is in an ongoing clinical Phase III trial where its efficacy is compared with chemotherapy in metastatic TNBC patients. This study will provide insights into the importance of AR suppression in TNBC treatment.

1.6.3.4 Immunotherapy

Immune checkpoint inhibitors represent significant advancement for cancer therapy in recent years. T cell activation in an immune-suppressive TME can be increased in some patients by targeting lymphocyte associated antigen-4 (CTLA-4), programmed death 1 (PD-1) or programmed death ligand-1 (PD-L1) (Lee et al., 2021). CTLA-4 is a T cell receptor that competes with a T cell-stimulating receptor CD28 for interaction with CD80/CD86, thereby limiting T cell responses to weak antigens on tumours (Seidel et al., 2018). PD-1 acts as a checkpoint receptor that inhibits T cell activation, proliferation, cytokine secretion and survival by interacting with PD-L1 or PD-L2 on tumour cells (Han et al., 2020). Ipilimumab, an anti-CTLA-4 monoclonal antibody, was the first immune checkpoint inhibitor approved by FDA for metastatic melanoma in 2011. Later, multiple

anti-PD-1 (e.g. pembrolizumab) and anti-PD-L1 (atezolizumab) monoclonal antibodies were approved for treating patients with metastatic cancers (Lee et al., 2021).

Unlike most tumours that are responsive to anti-PD-1 treatment, TNBC is highly inflammatory due to higher levels of tumour infiltrating lymphocytes present in the TME and a lower somatic mutational rate (Liu et al., 2018). In addition, TNBC still has the highest tumour mutational burden and a higher PD-L1 expression level compared to other breast cancer subtypes, suggesting a potential benefit of anti-PD-L1 or PD-1 treatement (Tung et al., 2016; Zhou et al., 2018). To determine the potential benefit of T cell checkpoint therapy, a phase III (KEYNOTE-119) compared pembrolizumab to single-agent chemotherapy in TNBC. Unfortunately, pembrolizumab was not able to increase overall survival greater than chemotherapy, although a higher tolerance and lower toxicity were observed for pembrolizumab over chemotherapy (Winer et al., 2021).

Following the disappointing trial results of pembrolizumab monotherapy, investigators tested the combination of immunotherapy with chemotherapy. The advantages of combination therapy include a lower risk of early progression in TNBC patients and a chemotherapy-induced immunogenic environment (Galluzzi et al., 2020). In two clinical trials, the combination of either atezolizumab (anti-PD-L1; IMpassion130) or pembrolizumab (anti-PD-1; KEYNOTE-355), with chemotherapy elevated the overall response rate by around 15% and reduced progression by approximately 36%, and have been approved for first-line treatment for PD-L1+ metastatic TNBC (Cortes et al., 2020; Schmid et al., 2018). The success of these two combination therapies demonstrates the advantages of combination therapy over monotherapy for TNBC. Additionally, the combination of PD-1 and PD-L1 blockade with other novel immunotherapies, such as cancer vaccines, oncolytic viruses and immunomodulators are currently being investigated for the treatment of TNBC patients (Bianchini et al., 2022).

1.6.4 RAGE receptor

RAGE is an immunoglobulin-like (Ig) receptor that recognises multiple ligands such as advanced glycation end products (AGEs), high mobility group box 1 (HMGB1), S100 proteins, Lysophosphatidic Acid (LPA), nucleic acids, C3a, amyloid β-peptide (Fritz, 2011; Ruan et al., 2010). Interactions between RAGE and its ligand usually result in activation of multiple downstream signalling pathways such as mitogen-activated protein kinase (MAPK) pathway, Janus kinase (JAK)-signal transducer and activator of transcription (STAT) pathway and nuclear factor kappa B (NF-κB) pathway (El-Far et al., 2020). The RAGE receptor is expressed on a wide range of cells such as macrophages, neutrophils, mast cells natural killer cells, CD8+ T cells, endothelial cells, nerve cells and cancer cells (Akirav et al., 2012; Narumi et al., 2015; Palanissami & Paul, 2018). Constant activation of the RAGE receptor has been associated with many diseases such as diabetes, neurodegeneration, Alzheimer's, and especially cancer (Cai et al., 2016; Kay et al., 2016; Logsdon et al., 2007; Ray et al., 2016).

1.6.5 RAGE structural characteristics

As a type I transmembrane protein, RAGE consists of a single transmembrane domain that bridges three Ig-like surface domains (V domain: residues 23-119. C1 domain: residues 120-233. C2: residues 234-325) and a cytoplasmic tail (**Figure 1.4**). The V domain is primarily responsible for ligand binding and forms a rigid structural entity with the C1 domain (Fritz, 2011). C2 is connected with V-C1 unit by a flexible linker. The structural arrangement of these domains was confirmed by nuclear magnetic resonance (NMR), suggesting that V-C1 domain acts as an individual unit independent of C2 domain (Dattilo et al., 2007).

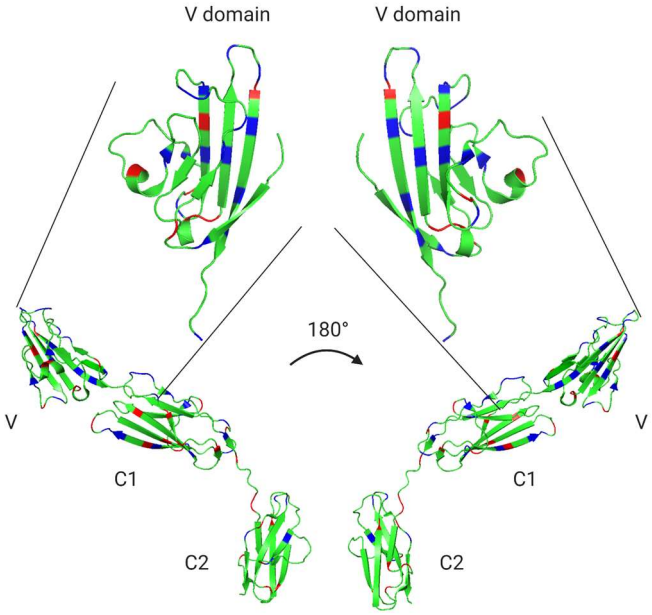


Figure 1.4. Crystal structure of RAGE extracellular domains. Figure adapted from (Yatime and Andersen, 2013) and PDB ID 4LP5. RAGE is comprised of three immunoglobulin-like extracellular domains including V, C1 and C2. RAGE V domain as the major ligand binding domain is highlighted in the figure. Positively charged amino acid residues are highlighted in blue. Negatively charged amino acid residues are highlighted in red.

One characteristic of RAGE surface domains is their difference in charge. Overall, the VC1 domain displays a positive charge while C2 domain possesses a negative charge under pH-neutral conditions. There is an exceptionally high content of Lys and Arg in the RAGE V domain, which exceeds 95% of immunoglobulin V domains found in the Pfam database (http://pfam.sanger.ac.uk/) (Fritz, 2011). The Lys and Arg residues in VC1 domains are mainly distributed on the protein surface with few basic residues located on one side. As a receptor that recognises common patterns, RAGE tends to interact with molecules that are negatively charged at neutral pH and are usually able to form oligomers (Fritz, 2011).

1.6.6 Targeting the RAGE Receptor and its ligands in TNBC

Both the RAGE receptor and its ligands are implicated in TNBC tumour progression. RAGE receptor overexpression has been experimentally demonstrated to promote TNBC tumour growth and metastasis (Kwak et al., 2017). In a RAGE knock-out TNBC

mouse model, despite a lower level of tumour infiltrating lymphocytes, reduced tumour growth and lung metastasis were observed (Kwak et al., 2017). Taken together, RAGE blockade suppresses tumour cell growth and metastasis but suppresses infiltrating lymphocytes, intriguingly leading to tumour inhibition. The pro-tumorigenic activity of the RAGE receptor has also been documented in a study where soluble RAGE administration in TNBC-bearing mice suppresses tumour growth and metastasis by sequestering S100A7 (Nasser et al., 2015).

Many of the RAGE ligands (e.g. AGE, HMGB1, C3a, LPA) pleiotropically interact with multiple receptors involved in tumourigenesis (**Figure 1.5**). For instance, both AGE-TLR4 and AGE-RAGE axis could result in an increased breast cancer cell migration and invasion through MyD88-dependent signalling pathways (Pan et al., 2022).

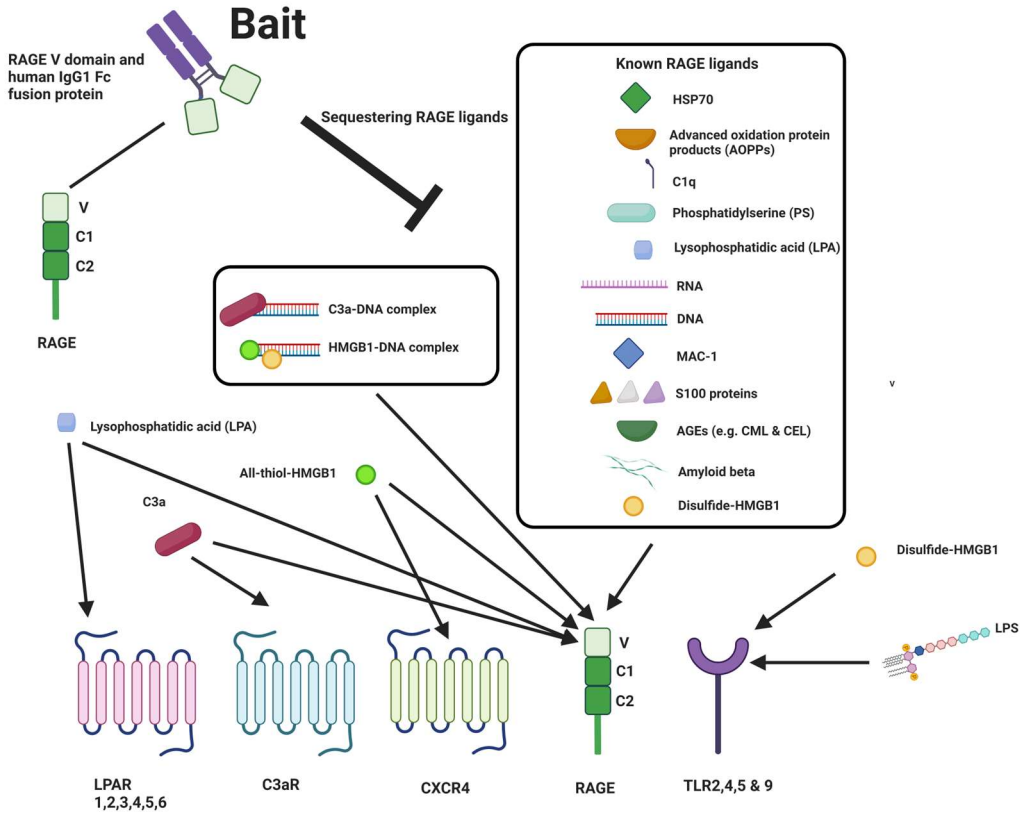


Figure 1.5. Diagrammatic representation of how RAGE decoy receptor (Bait) suppresses activation of multiple receptors. Given that RAGE V domain interacts with the majority of RAGE ligands, RAGE V-Fc fusion protein could be used as a bait to

sequester multiple RAGE ligands and thereby suppresses multiple receptor signalling pathways.

The HMGB1-TLR2 signalling pathway was shown to promote lung metastasis by triggering CD62Ldim neutrophil polarisation (Wang et al., 2020). Furthermore, acetylated HMGB1-CXCR4 is involved in converting mesenchymal stem cells to cancer-associated fibroblasts in TNBC (Ryan et al., 2019). In contrast, the complement C3a-C3aR axis not only directly promotes TNBC cell metastasis through regulating cancer-associated fibroblasts but also suppresses the infiltration of cytotoxic NK cells in the TME (Nandagopal et al., 2022; Shu et al., 2020). Interactions between LPA and the LPA receptor 3 in TNBC facilitate cancer stem cell proliferation (Hirata et al., 2022). Overall, RAGE ligands are able to promote cancer cell metastasis and modify tumour microenvironment.

1.6.7 Assessing the safety profile of targeting RAGE.

Before exploring the potential therapeutic use of a genetically engineered RAGE receptor, the safety profile of such a RAGE decoy needs to be carefully assessed. A vast majority of RAGE receptors in humans are dysfunctional and expressed as different isoforms including soluble RAGE (sRAGE), N-truncated RAGE and C-terminal truncated RAGE (Fishman et al., 2018). This finding suggests that RAGE signalling is regulated by different feedback mechanisms. However, there are no documented severe side effects in RAGE knock-out mice other than elevated sensitivity to auditory stimuli (Sakatani et al., 2009). A wild-type soluble RAGE receptor has been successfully used in a mouse model for the treatment of amyotrophic lateral sclerosis (ALS) (Juranek et al., 2016). In addition, Azeliragon (TTP488), a RAGE inhibitor that blocks the binding of multiple RAGE ligands to RAGE is currently in a Phase III clinical trial for the treatment of Alzheimer's disease (Hudson & Lippman, 2018). Therefore, general inhibition of RAGE ligands is likely to have a high safety profile.

1.6.8 Engineering RAGE decoy receptor

Overall, RAGE receptor and RAGE ligands are promising targets for TNBC. Due to the pleiotropic effects of RAGE ligands, RAGE receptor inhibitors are unlikely to achieve the best clinical efficacy. To this end, using a soluble RAGE receptor as a decoy to sequester RAGE ligands in the tumour microenvironment could maximise the therapeutic potential by inhibiting RAGE receptor activation as well as sequestering RAGE ligands. A major issue associated with wild-type RAGE decoy is that the binding affinity between the majority of RAGE ligands and RAGE receptor is relatively low compared to typical decoy receptor-based drugs (Teissier & Boulanger, 2019). To tackle this issue, I hypothesised that engineering a high affinity RAGE decoy receptor with yeast surface display would be a plausible solution (**Figure 5**).

1.7 Aims of this thesis

The aims of this thesis are to

1. Engineer a high affinity TACI decoy to sequester APRIL and BAFF in the TME for the treatment of DLBCL.
2. Engineer a high affinity RAGE V decoy to sequester RAGE ligands in the TME for the treatment of triple negative breast cancer.

1.8 Dissertation overview

In this dissertation, I engineered two receptor-based therapeutics able to competitively antagonise TACI ligands and RAGE ligands, and assessed their anti-tumour activity in DLBCL and TNBC models, respectively. The TACI ligands, APRIL and BAFF, provide essential survival signals for B cells and have been implicated in promoting DLBCL tumour growth. RAGE ligands such as S100 proteins, AGEs and HMGB1 have been implicated in TNBC tumour progression and metastasis and have thus become promising therapeutic targets for TNBC treatment. In Chapter 2, I describe the use of yeast surface display technology to screen for high affinity soluble TACI variants.

Although the engineered TACI variants demonstrate a higher ligand binding affinity than wild-type TACI in *in vitro* studies, the improvement in tumour inhibition over wild-type soluble TACI was modest. In Chapter 3, my focus moves to engineering a soluble RAGE V decoy receptor. The identified RAGE V variant has a higher binding capacity to multiple RAGE ligands. In Chapter 4, I describe the structural characteristics of the engineered RAGE receptor and reformate it as a Fc fusion protein. In Chapter 5, I present data on the effect of the RAGE variant on TNBC cell growth and invasion under both *in vitro* and *in vivo* settings. In Chapter 6, I performed mass spectrometry and RNA sequencing to understand the underlying anti-tumour mechanism of the RAGE variant. In Chapter 7, I summarise the findings of this thesis and provide other promising applications of engineered soluble TACI and RAGE decoy receptors.

Chapter 2. Methods

2.1 Cell Lines and their Maintenance

2.1.1 Bacteria and yeast strains, plasmids, and media

Escherichia coli DH5α was used for molecular cloning. *E. coli* BL21 was used for recombinant protein production, which is further discussed in section 2.3.2. During the cloning process, *E. coli* strains were grown in Luria-Bertani (LB) medium supplemented with Ampicillin at a final concentration of 35 μg/ml at 37°C. *Saccharomyces cerevisiae* EBY100 (ATCC® MYA-4941™) were normally grown in the complete medium, Yeast Extract–Peptone–Dextrose (YPD) media at 30°C with shaking (220 rpm). pctCon2 as a shuttle vector was used in both *E. coli* and *S. cerevisiae*. For selectively growing pctCon2 plasmid transformants, *S. cerevisiae* EBY100 were grown in SD-CAA minimal media at 30°C with shaking (220 rpm). SG-CAA media was used to induce protein expression encoded by pctCon2 in yeast.

Yeast Extract–Peptone–Dextrose (YPD) Medium was comprised of 20 g/L dextrose, 20 g/L peptone, and 10 g/L yeast extract. SD-CAA media included 20 g/L dextrose, 6.7 g/L yeast nitrogen base without amino acids, 5.4 g/L Na_2HPO_4, 7.4 g/L NaH_2PO_4 and 5 g/L Bacto casamino acid. SG-CAA media has the same components as SD-CAA except for replacing 20 g/L dextrose with 20 g/L galactose. The pH was titrated to pH4.5 for SD-CAA and pH6.0 for SG-CAA. The pH was unadjusted for SD-CAA and SG-CAA agar plates.

2.1.2 Mammalian cell strains, plasmids and media

Su-DHL-6 was cultured in RPMI 1640 supplemented with 10% FBS and penicillin-streptomycin. MDA-MB-231, MDA-MB-468, CAL-51, MCF7, BT-549 and HCC1886 were cultured in DMEM supplemented by 10% FBS and penicillin-streptomycin. SUM159PT was cultured in Ham's F-12 supplemented by 5% FBS, 10 mM HEPES, 1 μg/ml hydrocortisone, 5 μg/ml insulin and penicillin-streptomycin. MycoStrip™ - Mycoplasma

detection kit was routinely used to ensure the mammalian cell lines free of mycoplasma contamination.

Human NK cells were cultured in RPMI 1640 supplemented by 10% FBS and 200 ng/ml IL-2 (130-097-744; Miltenyi). Human CD8+ T cells were cultured in RPMI 1640 supplemented by 10% FBS, 2 mM L-glutamine, 200 ng/ml IL-2 (130-097-744; Miltenyi), 3 µg/mL of anti-human CD3 (16-0037-81; Thermo Scientific) and 5 µg/mL of anti-CD28 (16-0289-81; Thermo Scientific). Human B cells were grown in RPMI supplemented with 10% FBS, 0.5 µg/ml of Goat anti-Human IgG, IgM (H+L) antibody (16-5099-025; Thermo Scientific). Mouse B cell was grown in RPMI supplemented with 10% FBS, 0.1% 2-Mercaptoethanol, 0.5 µg/ml of Goat anti-Mouse IgM (Mu chain) antibody (16-5092-85; Thermo Scientific).

2.1.3 Cryopreservation of cell lines

Bacteria and yeast cell culture were prepared and mixed with 50% glycerol at a ratio of 1:1 in cryogenic tubes. The labelled samples were then stored at -80 ℃. When recovering cells, the bacteria or yeast were first streaked onto an agar plate and incubated for cell growth. Single colonies were then transferred into liquid culture for downstream applications.

For yeast library stock preparation, around 1 x 10^8 cells were pelleted with a centrifuge at 500 x g for 5 minutes at room temperature. The supernatant was removed carefully. The remaining cells were resuspended in 500 µl of the freezing medium comprised of 50% glycerol stock supplemented with 6.7 g/L yeast nitrogen base without amino acids. The resuspended yeast library was then placed into a cryogenic tube and stored at -80 ℃. For recovering yeast library, the thawed vials were directly transferred into 1 L SD-CAA media and grown at 30°C with shaking (220 rpm) for 24 hours.

Mammalian cells were trypsinised and resuspended in a fresh medium after reaching 70% confluency. Non-adherent cell line Su-DHL-6 was resuspended in a fresh medium without trypsinisation. The cells were then pelleted with a centrifuge at 300 x g for 3 minutes at room temperature. Subsequently, the cell pellets were resuspended in freezing media consisting of 90% FBS and 10% DMSO. Alternatively, cells with relatively lower recovering viability were resuspended in another freezing medium containing 10% FBS, 80% medium and 10% DMSO. All mammalian cells in cryogenic vials were placed in a Mr Frosty containing isopropanol and stored at -80 ℃. For long-term storage, the frozen vials were then transferred from a -80 ℃ freezer to a liquid nitrogen tank. When recovering mammalian cells, the frozen vials were quickly thawed in a 37 ℃ water bath. Thawed cells were resuspended in 10 ml medium and centrifuged at 300 x g for 3 minutes at room temperature. After removing the supernatant, the pelleted cells were grown in the fresh medium.

2.2 Yeast library-based screening

2.2.1 Cloning

The coding sequence of wild-type RAGE V and wild-type TACI ectodomain was purchased from Integrated DNA Technologies (IDT) as double-stranded DNA fragments. The fragments were then assembled into pctCon2 plasmids by using NEBuilder HiFi DNA assembly cloning kit. The ratio of inserts to vectors was 3/1, in which NEBioCalulator was used for the calculation. The assembled plasmids were then transformed into *E. coli* DH5alpha for plasmid amplification. The correctly assembled plasmids were verified by DNA sequencing performed by Source Biosciences.

2.2.2 Generation of yeast-displayed TACI and RAGE V mutant libraries

The TACI and RAGE V mutant libraries were generated using an error-prone PCR-based approach. The coding sequence of human TACI ectodomain (Ensembl: TNFRSF13B ENSG00000240505; amino acid Met1-Ser165) and human RAGE V domain (Ensembl:

AGER ENSG00000204305; amino acids Ala23-Lys123K) were cloned in between NheI and BamHI restriction sites of the yeast display plasmid pCTcon2. Error-prone PCR was performed to randomly introduce mutations into the decoy receptor coding sequence by using low-fidelity Taq polymerase (Invitrogen) and the nucleotide analogues, 8-oxo-dGTP (TriLink Biotech) & dPTP (TriLink Biotech). The primers used for PCR-based mutagenesis have 50 bp homology to the pctCon2 plasmids. Primer sequences are shown below.

Fwd mutagenesis primer

TGGAGGAGGCTCTGGTGGAGGCGGTAGCGGAGGCGGAGGGTCGGCTAGC

Rev mutagenesis primer

ATCTCGAGCTATTACAAGTCCTCTTCAGAAATAAGCTTTTGTTCGGATCC

Five individual PCR reactions were conducted with different concentrations of analogues and a varying number of amplification cycles in a bid to acquire a spectrum of mutation rates: 10 cycles (200 μM or 100 μM of nucleotide analogue mixture) and 20 cycles (50 μM, 40 μM or 20 μM of nucleotide analogue mixture). To amplify the mutagenised sequences, additional PCR reactions were carried out with high-fidelity Q5 polymerase (New England Biolab).

The mutagenised PCR products and linearised pCTcon2 plasmids were co-transformed into the EBY100 via ultra-high efficiency electroporation at 2.5 kV and 25 μF with a typical time constant ranging from 3.0 to 4.5 milliseconds (Gene Pulser Xcell Electroporation Systems, BIO-RAD). The electroporation reaction mixture contained 100 μl of 1 M sorbitol, $3.2x10^9$ competent EBY100 cells, 4μg of linearised pCTcon2 vectors and 12 μg of RAGE V mutant DNA. Sequence homology shared by the mutagenised PCR products and the linearised pCTcon2 enabled *in vivo* plasmid assembly via yeast-driven

homologous recombination. A collection of the resulting yeast transformants was considered an unsorted yeast library.

2.2.3 Screening for high affinity TACI and RAGE V variants

After the library generation, screening high affinity yeast-displayed TACI variants was performed. The first sorting approach was equilibrium binding sorts where yeasts were treated with an increasingly lower concentration of recombinant human APRIL (HA tag; 5860-AP) or recombinant human BAFF (His tag; BAF-H5248) to enrich high affinity mutants through sorting progression. PBSA, comprised of phosphate-buffered saline with the addition of 0.1% bovine serum albumin, was used as a buffer for all binding assays. All equilibrium binding assays were subject to a maximum of 10% ligand depletion and a minimum reaction time that allows a 99% binding event to reach equilibrium. All formulas used for determining binding assay conditions are shown below (Hunter & Cochran, 2016).

Ligand depletion functions

Number of ligands = (ligand nM * 10^-9) * (6.022 x 10^23)/1 * 10^6 * reaction volume µl

Number of displayed receptors = Number of cells * 10^5 receptors/cell

Maximum percentage of ligand depletion = 100 – ((Number of ligands – Number of display receptors ligands)/ Number of ligands)) * 100

Equilibrium time constant calculations

KD = Koff/Kon (KD was an estimated value according to literature)

Tau (hour) = ((((ligand nM * 10^-9) * Kon) + Koff)^-1) / 60 / 60

Time to reach 95% equilibrium = 3 * Tau

Time to reach 99% equilibrium = 4.6 * Tau

Competitor calculations for 1* 10^8 cells in a 15 ml reaction mixture

Number of competitors = 1 * 10^8 cells * 10^5 ligands/cell * desired ratio of competitors to the bound ligands * (Competitor nM)

Number of competitors / 6.022 * 10^23 molecules/mol = competitor M

Competitor M / 0.015 L = Concentration of competitor in 1 mL

After washing off unbound ARRIL or BAFF after each binding assay, yeasts were incubated with 1:200 diluted anti-myc tag antibody (ab1393, Abcam) and 1:200 diluted anti-ligand antibody at 4℃ for 1 hour. In this case, anti-6X His tag antibody DyLight® 650 (ab117504) was used for His-tagged BAFF-directed screening, and HA Tag monoclonal antibody Alexa Fluor™ 647 (26183-A647) was used for HA-tagged APRIL-directed screening. The yeasts with high binding signals were collected using a BD FACSAria™ Fusion Cell Sorter (The Jenner Institute).

0.2 nM was the lowest concentration used for APRIL and BAFF equilibrium binding assay due to the ligand depletion issues. Therefore, a second sorting approach, namely kinetic off-rate sort, was used where the yeasts were first incubated with APRIL or BAFF until the binding reactions reach equilibrium followed by off-rate washing with a competitor to enrich variants with a slow off-rate. In this case, the TACI yeast library was incubated with certain concentrations of APRIL or BAFF followed by a wash with competitor sBCMA-V3, an engineered soluble BCMA with high affinity binding to both APRIL and BAFF (Miao et al., 2022). The time of incubation, time of competitor washing, concentration of ligands and concentration of competitors were adjusted for each round of sorting to gradually increase selective stringency. The downstream staining procedures were the same as the equilibrium binding assay. After several rounds of cell sorting, the plasmids were extracted from yeasts that displayed high affinity TACI mutants using a Zymoprep Yeast Plasmid Miniprep Kit (Zymo Research) and

transformed into DH5alpha *E. coli* for plasmid expansion. Sequencing was performed by Source Bioscience to identify enriched mutations in the TACI variants.

Similar to TACI library sorting, the high affinity RAGE V mutants were isolated from the RAGE V mutant library using several progressive rounds of FACS sorting. Briefly, equilibrium binding sorts were conducted where yeasts displaying various RAGE V mutants were treated with different concentrations of C3a overnight to reach binding equilibrium. After washing off the unbound C3a with PBSA buffer, yeasts were incubated with 1:200 diluted anti-myc tag antibody (ab1393, Abcam) and anti-C3a antibody Alexa Fluor® 647 (NBP1-05122AF647, Novus Biologicals) at 4℃ for 1 hour. Stained yeasts were sorted by using a BD FACSAria™ Fusion Cell Sorter (The Jenner Institute). After the last sort, the plasmids were extracted from the yeasts that displayed RAGE V varaints using a Zymoprep Yeast Plasmid Miniprep Kit (Zymo Research) and transformed into DH5alpha *E. coli* for plasmid expansion. DNA Sequencing was performed by Source Bioscience.

2.2.4 On-yeast characterisation of wild-type and mutant decoy receptors using flow cytometry

Flow cytometry was conducted to determine the binding affinity and maximum binding capacity of yeast-displayed receptors to their ligands. The binding assay was conducted by incubating yeast cells that displayed decoy receptors with various concentrations of corresponding ligands. The binding reaction volumes and time to reach equilibrium were calculated using the formula shown in section 2.2.3. After the binding assay, yeast cells were washed and resuspended in PBSA and stained with anti-ligand antibodies and anti-myc antibodies. The binding signal was quantified using Attune NxT Flow Cytometer. All flow cytometry data were analysed by using FlowJo 10.4 software. The binding titrations were fit as a four-parameter logistic curve using Prism 8.4.3 (GraphPad Software Inc., La Jolla, California) to determine KD and B_{max}.

2.3 Recombinant protein production

2.3.1 Recombinant protein production (WT-RAGE V-Fc, RAGE V13-Fc, WT-TACI-Fc, BS7-10-Fc (68-110 a.a.) and BS7-10-Fc)

The recombinant IgG1 Fc fusion production and purification were performed by our collaborators ChemPartner and Structural Genomics Consortium. The genes encoding WT-RAGE V-Fc, RAGE V13-Fc, WT-TACI-Fc, BS7-10-Fc (68-110 a.a.) and BS7-10-Fc were incorporated into a pHL-sec plasmid. The amino sequences of all recombinant proteins are summarised in **Table A4.** 5-6 mg of the correctly assembled plasmid weres obtained from 2 L culture of DH5alpha *E.Coli* cells using a GigaPrep kit. 2 mg/L plasmids were then transfected into Expi293F cells using polyethyleneimine (PEI; Sigma, 408727). The cells were then incubated in Freestyle293 medium at 37°C, 8% CO_2, 75% humidity with shaking at 150 rpm for 7 days after transfection. Next, cell culture supernatant containing the secreted protein of interest was harvested after centrifugation at 500 g in 1 L centrifuge bottles using a JLA8.1 rotor at 6°C for 30 minutes. The supernatant was then filtered through a 0.22 µm membrane filter into a new container. rProteinA resin (Cytiva, 17127903) was used to purify IgG1 Fc tagged proteins. 5 mL of rProteinA resin was added to a 100 mL Econo-column, washed with water, and equilibrated with PBS. Culture supernatant was passed through the column by gravity flow twice for binding. The rProteinA resin coated with target proteins was washed with 100 ml (x20 column volume) of PBS. 250ml (50 column volume) of 0.1% TritonX-114 (Sigma-Aldrich) was used to remove endotoxin, which is followed by washing with 100ml (x20 column volume) of PBS. Target proteins were eluted by applying 9 mL of elution buffer (0.1 M Glycine pH 2.5) into the column and quickly collected into 15 ml falcon tubes containing 1 M Tris pH 8.0. All elution fractions were pooled together and concentrated down to 1 ml using a 30 kDa Amicon concentrator unit. The concentrated samples were then spun at maximum speed for 5 min on a benchtop centrifuge. Subsequently, the supernatant was then injected into a Superdex 200 Increase 10/300 GL (endo-toxin free column) pre-

equilibrated with 1xPBS. The sample was run at a low rate of 0.5 ml/min. Eluted fractions were analysed by SDS-PAGE. Endotoxin level was measured using Pierce™ Chromogenic Endotoxin Quant Kit following the manufacturer's protocol. An endotoxin level standard curve (linear regression) was generated to determine the endotoxin concentration of each sample. Finally, protein samples are concentrated to 1-2 mg/mL using a 30 kDa Amicon concentrator unit. The final samples were aliquoted and stored in liquid nitrogen.

2.3.2 Recombinant protein production (GRP78)

The gene encoding HSPA5/GRP78 was cloned into pCold I plasmid. DH5alpha was used to amplify plasmid DNA. Plasmid isolation was carried out using a Monarch® plasmid miniprep kit (T1010L). After validating the correct insertion of GRP78 into the plasmid by DNA sequencing (Source biosciences), the plasmids were transformed into *E.coli* BL21 for producing HSPA5-his. The *E.coli* BL21 cells were grown to OD1-1.6 at 37°C with shaking at 220 rpm. Subsequently, the *E.coli* BL21 cells were treated with 500 µmol/L IPTG and incubated at 4°C with shaking at 220 rpm for 24 hours. After preparing the cell lysate with sonication, two HisTrap FF (5 ml) columns were used to capture His-tagged GRP-78 from the cell lysate supernatant. After elution with 300 mM of imidazole, GRP-78-His was then subjected to size exclusion chromatography (HiLoad® 16/600 Superdex® 200 pg (28-9893-35; Merck)). All purification steps were performed by using ÄKTA Pure Protein Purification System (Cytiva). Amicon® Ultra-15 Centrifugal Filter Unit (UFC905096; Sigmal Aldrich) was used to concentrate the purified GRP78-HIS.

2.4 Molecular biology methods and technologies

2.4.1 RT-PCR

Total RNA was isolated from MDA-MB-231 treated with IgG1 Fc, WT-RAGE V-Fc or RAGE V13-Fc using RNeasy Kits (74104, Invitrogen). cDNA preparation was performed

using SuperScript™ III First-Strand Synthesis SuperMix for qRT-PCR (11752-050; Invitrogen) where 1 µg of RNA was used as a template for creating each cDNA library. The RT-PCR was carried out using the tepOne™ Real-Time PCR System (4376357; Thermo Scientific). 3 µl of 1 in 4 diluted cDNA library was used as the templates for RT-PCR. PowerTrack™ SYBR Green Master Mix (A46109; Thermo Scientific) was used as a quantitative indicator of cDNA amplification. The RT-PCR primer sequences are shown in **Table 2.1**

Table 2.1. RT-PCR primer sequences

Target	**Forward primer (5' – 3')**	**Reverse primer (5' – 3')**
18S rRNA	GCCCGAAGCGTTTACTTTGA	TCCATTATTCCTAGCTGCGGTATC
LCN2	TCACCTCCGTCCTGTTTAGG	CGAAGTCAGCTCCTTGGTTC
EEF1D	ACAGACCCAGCACGTATCTC	CCAGCAGGATGGAGGACTTG
CXCL1	GCTCCTGCGAGTGGCACTGC	GGGCCTCCTTCAGGAACAGCC
CXCL8 (IL-8)	GACTTCCAAGCTGGCCGT	GAATTCTCAGCCCTCTTCA
HIF1AN	TGAGAATGAGGAGCCTGTGGT	TGTTGGACCTCGGCTTAAAGT
PEG10	GCTAAGCTTCGATGACCGAAC GAAGAAGGGACGAG	ATATAGTCGACCTACAGCGGGGC CGGGGAGTTT
LY6E	CTCCAGGCAGGACGGCCATC	CGAGATTCCCAATGCCGGCACT
SAA2	GCTTCTTTTCGTTCCTTGGCG	GCCGATGTAATTGGCTTCTCTCA
CYP3A5	AAGGAAGACTCACAGAACACA GTTGA	GGTTTCCACCGCCAAATTT

The reaction was triplicated and executed under the following conditions: Holding stage: 95℃ for 20 seconds, followed by 40 cycles (Cycling stage): 95℃ for 30 seconds, 60℃ for 30 seconds. Melt curve stage: 95℃ for 15 seconds, 60℃ for 1 minute, 95℃ for 30 seconds, 60℃ for 10 seconds. The relative mRNA expression was calculated as $2^{\wedge}\Delta\Delta Ct$ value with 18S rRNA as a control for normalising gene expression.

2.4.2 SDS-PAGE (Sodium dodecyl sulfate-polyacrylamide gel electrophoresis)

All the recombinant proteins were resuspended in Bolt™ LDS Sample Buffer (B0007; Invitrogen) supplemented with Bolt™ sample reducing agent (B0009; Invitrogen) for SDS-PAGE gel analysis. For reducing conditions, the mixture was incubated at 95℃ for 5 minutes before running the gel. For non-reducing conditions, the samples were loaded

directly without boiling. PageRuler Plus prestained protein ladder (26619; Thermo Scientific) were used for SDS-PAGE gel electrophoresis. After electrophoresis, the protein gels were stained with Quickblue protein stain (LU001000; Stratech) for 1 h followed by 30 min wash with tap water. The protein bands were visualised using iBright™1500 Imaging System.

2.4.3 Western blot

Cell lysates were prepared by sonicating cells resuspended in the RIPA Buffer (89900; Abcam) supplemented with Complete™ protease inhibitor cocktail (04693116001; Merck) and PhosSTOP (4906845001; Merck). Protein quantification was carried out by using BCA assay (23228; Thermo Scientific). Protein lysates were then incubated in Bolt™ LDS Sample Buffer (B0007; Invitrogen) supplemented with Bolt™ sample reducing agent (B0009; Invitrogen) at 95℃ for 5 minutes. Subsequently, the protein samples (30 µg per sample) were separated on 4-12% Bis-Tris Plus (NW04120BOX; Invitrogen) SDS-PAGE gel, transferred to 0.2 µm polyvinylidene difluoride (PVDF) membrane (1704156; Bio-Rad) and blocked with 3% Bovine Serum Albumin (BSA; Sigma Aldrich). The blocked membranes were then incubated with different primary antibodies overnight at 4℃, which includes Phospho-IRF-3 (Ser396) (4947; Cell Signaling); IRF-3 (4302; Cell Signaling), phospho-Histone H2A.X (Ser139) (05-636-I; Merck), Phospho-NF-κB p65 (Ser536) (3033; Cell Signaling); Phospho-Akt (Ser473) Antibody (9271; Cell Signaling), Phospho-p44/42 MAPK (Erk1/2) (Thr202/Tyr204) Antibody (9101; Cell Signaling), Phospho-TBK1/NAK (Ser172) Antibody (5483; Cell Signaling), Phospho-p38 MAPK (Thr180/Tyr182) Antibody (4511; Cell Signaling), GRP78 (610978; BD biosciences), CXCL3 (PA5-103136; Thermo Scientific), p-JNK Antibody (G-7) (sc-6254; Santa Cruz), Phospho-Stat3 (Tyr705) Antibody (9131; Cell Signaling), Phospho-c-Myc (Ser62) Antibody (13748; Cell Signaling) and Stat3 Antibody (D1B2J; Cell signaling) Rabbit mAb #30835. After washing off unbound primary antibodies, the membranes were incubated

with horseradish peroxidase (HRP)-conjugated secondary antibodies for 1 hour at room temperature. Forte western HRP substrate (WBLUF0500) was used for visualising targeted proteins. The images were taken using iBright™1500 Imaging System.

2.4.4 Enzyme-Linked Immunosorbent Assays (ELISA) to measure CXCL3 level in the cell culture supernatant.

To measure the secreted CXCL3 level in the MDA-MB-231 cell culture supernatant after IgG1 Fc, WT-RAGE V-Fc and RAGE V13-Fc treatment, CXCL3 ELISA kit (ab234574; Abcam) was used. The MDA-MB-231 cell culture supernatant used for CXCL3 ELISA was 1 in 20 diluted. All steps were carried out according to the manufacturer's protocol. OD 450 nm was measured by using a plate reader BMG Labtech POLARstar Omega. A standard curve was created and used for estimating the CXCL3 concentration in the samples.

2.4.5 RNA interference

ON-TARGETplus non-targeting control pool (Dharmacon) or ON-TARGETplus human CXCL3 (2921) siRNA – Smartpool (Dharmacon) were transfected into MDA-MB-231 cells using Lipofectamine™ RNAiMAX transfection reagent (Invitrogen, 13778075). The target sequences of the siCXCL3 pool includes CCAACUGACAGGAGAGAAG, UCCAAAGUGUGAAUGUAAG, GGGAGACCAUAAUGUGUCA and UACGAGGGUUCUACUUAUU. One thousand cells and 2 x 10^5 cells were seeded in 96-well plates and 6-well plates, respectively. The following day, transfection was performed. The siRNA pools were diluted to 20 µM in nuclease-free water. Two tubes of reagents were prepared. For one, 10 µl of the siRNA stock (20uM) were mixed with 190 µl serum free media (Optimem) and incubated for 5 minutes at room temperature. For another, 7.5 µl of RNAiMAX was mixed with 193.5 µl serum free media (Optimem) and incubated for 5 minutes at room temperature. The two tubes were then mixed and incubated for 20 minutes at room temperature. Subsequently, 1.6ml of antibiotic-free media

supplemented with 10% FBS were mixed with 400ul of siRNA + RNAiMAX solutions to create the transfection media. The pre-washed cells were then grown in the transfection media for 24 hours at 37℃ and 5% CO_2. The media were then changed to DMEM supplemented with 10% FBS and penicillin-streptomycin and incubated for 96 hours at 37℃ and 5% CO_2 before performing the CCK8 proliferation assay. For the transwell assay, the transfected cells were trpsinised and transferred to transwell inserts.

2.5 Cancer cell growth and mobility assays

2.5.1 Proliferation assay

$1x10^3$ MDA-MB-231 or $1x10^4$ Su-DHL-6 cells were seeded in 96-well plates and incubated at 37℃ and 5% CO_2. Different treatments were conducted 24 hours after the cell seeding procedure. Cell Counting Kit 8 (WST-8 / CCK8) (ab228554; Abcam) was used for measuring the relative cell growth 24, 48, 72 and 96 hours post-treatment. Each sample was treated with 10 µl of CCK8 reagent for 4 hours at 37℃ before measuring OD460 by using a plate reader (BMG Labtech POLARstar Omega).

2.5.2 Clonogenic assay

One hundred MDA-MB-231 cells were seeded in six-well plates and incubated at 37℃ and 5% CO_2 overnight. Different concentrations of IgG1 Fc, WT-RAGE V-Fc and RAGE V13-Fc were replenished every 96 hours. Crystal violet solution was used to fix and visualise colonies 12 days after the first treatment. One litre of crystal violet solution consists of 0.5 g/L crystal violet, 27 ml of 37% formaldehyde violet, 100 ml of 10 x PBS, 10 ml of methanol and 863 ml of distilled water. The images of stained colonies were taken by using GEL COUNT (Oxford Optronix). The colony number and colony area average were calculated by Gel Count (Oxford Optronix).

2.5.3 Annexin V assay with PI

The apoptotic effect of WT-RAGE V-Fc and RAGE V13-Fc on MDA-MB-231 was evaluated by using BioLegend's FITC Annexin V Apoptosis Detection Kit with PI. 1 x 10^4 cells were seeded in six-well plates overnight followed by treatment of IgG1 Fc, WT-RAGE V-Fc and RAGE V13-Fc. The cells were collected at 96 hours after the treatment. The cells were processed according to the manufacturer's protocol. Attune NxT Flow Cytometer was used for quantification. All flow cytometry data were analysed by using FlowJo 10.4 software.

2.5.4 Adhesion assay

96-well plates were first pre-coated with 1 in 10 Matrigel Matrix at 37℃ for 2 hours (356234; Corning). 5 x 10^4 MDA-MB-231 cells were resuspended in 100 µl serum-free DMEM containing IgG1 Fc, WT-RAGE V-Fc or RAGE V13-Fc. The treated cells were then seeded into the pre-coated plate and incubated at 37℃ and 5% CO_2 for 2 hours. After washing with PBS, the adhered cells were stained with the crystal violet solution. The images were taken using Celigo Image Cytometer (Nexcelom). The adhered cells in the 90% of central well area was quantified.

2.5.5 Migration assay

For each well, 5 x 10^4 TNBC cells were resuspended in 100 µl serum-free DMEM and placed in 8.0 µm Pore Polycarbonate Membrane Inserts (3422; Corning). The cells in the top chamber were treated with different concentrations of IgG1 Fc, WT-RAGE V-Fc or RAGE V13-Fc ten minutes before filling the bottom chamber with 750 µl DMEM supplemented with 10% FBS and penicillin-streptomycin. Subsequently, the plates were incubated at 37℃ and 5% CO_2 for 24 hours. The inserts were stained using the crystal violet solution for 20 minutes and washed with distilled water. Cotton swabs were used to remove the non-migrated cells in the inserts. After drying the inserts, images were

taken and analysed using Celigo Image Cytometer (Nexcelom). The migrated cells in the 20% of central well area was quantified.

2.5.6 Invasion assay

8.0 µm Pore Polycarbonate Membrane Insert (3422; Corning) was coated with 20 µl of 1 in 10 Matrigel Matrix (356234; Corning) and incubated at 37℃ for 2 hours. 5 x 10^4 cells were suspended in 100 µl serum-free DMEM containing IgG1 Fc, WT-RAGE V-Fc or RAGE V13-Fc and placed in the coated inserts. The bottom chambers were then filled with 750 µl DMEM supplemented with 10% FBS and penicillin-streptomycin. The plates were then incubated at 37℃ and 5% CO_2 for 24 h. Next, the inserts were stained using the crystal violet solution for 20 minutes and washed with distilled water. Cotton swabs were used to remove the non-migrated cells in the inserts. After drying the inserts, images were taken and analysed using Celigo Image Cytometer (Nexcelom). The migrated cells in the 15% of central well area was quantified.

2.5.7 Wound healing assay

MDA-MB-231 was seeded in 48-well plates at a density of 2.5 x 10^5 cells per well. Scratching was performed with a sterile 200µl pipette tip after one-cell-thick monolayers were formed. PBS was then used to wash off the cell debris caused by the disruption. Next, cells were treated with different concentrations of IgG1 Fc, WT-RAGE V-Fc or RAGE V13-Fc prepared in DEME supplemented with 0.5% FBS. Live time imaging was carried out for 24 hours by using a Nikon Ti-E microscope. The scratch area was measured using ImageJ.

2.6 Primary cell growth and mobility

2.6.1 B cell proliferation assay

Mouse B cells were isolated from C57BL/6 mouse spleens using EasySep™ mouse B cell isolation kits. Human B cells (70033) were purchased from StemCell. 1 x 10^5 human or mouse cells/well were seeded in 96-well plates. The seeded cells were treated with

IgG1 Fc, WT-TACI-Fc, atacicept or BS7-10-Fc. Cell Counting Kit 8 (WST-8 / CCK8) (ab228554; Abcam) was used for measuring relative cell growth after the treatment. Each sample was treated with 10 µl of CCK8 reagent for 4 hours at 37℃ before measuring OD460 using a plate reader (BMG Labtech POLARstar Omega).

2.6.2 NK cells and CD8+ T cell migration assay

Human Peripheral Blood NK Cells (70036) and Human Peripheral Blood CD8+ T Cells (200-0164) were purchased from StemCell. The NK cells and T cells were expanded for 72 hours before the experiment. Human T or NK cells (5 x 10^5 cells/ml) were resuspended in serum-free RPMI 1640 media and then seeded in 6.5 mm Transwell® with 5.0 µm pore polycarbonate membrane inserts (3421; Corning). The seeded cells were subsequently treated with different concentrations of IgG1 Fc, WT-RAGE V-Fc or RAGE V13-Fc. RPMI 1640 supplemented with 10% FBS was used as a chemoattractant and placed in the bottom chamber 10 minutes after the drug treatment. After 4-hour incubation at 37℃ in a 5% CO2 atmosphere, the transwell inserts were removed. The NK or T cells that migrated to the bottom chamber were quantified using Celigo. The migrated cells in the 20% of central well area was quantified.

2.6.3 Assessing the purity of B, NK and T cells using flow cytometry

The purity of primary cells purchased from StemCell or isolated from mouse spleens were assessed using flow cytometry. Human B cells, murine B cells, human NK and human CD8+ T cells were washed and resuspended in PBS supplemented with 2% FBS and blockers (Mouse BD Fc Block™, 553142 or Human BD Fc Block™, 564220). The cells were then stained with antibodies against different surface markers including FITC anti-mouse CD3 Antibody (100203), APC anti-mouse CD19 Antibody(152409), FITC anti-mouse CD45 Antibody (157213), FITC anti-human CD19 Antibody (302205), APC anti-human CD3 Antibody (317317), APC anti-human CD45 (982304), FITC anti-human CD56 (NCAM) Antibody(362545) and FITC anti-human CD8 (980908). These antibodies

were purchased from BioLegend. Flow cytometry was carried out on the Attune NxT Flow Cytometer. All flow cytometry data were analysed by using FlowJo 10.4 software.

2.7 Animal study

2.7.1 Animal welfare

All animal experiments were supervised by a project license holder Yanyan Jiang (PP4558762) and carried out by a personal license holder Yizhou Wang (PIL A,B &C license holder: I67159927) according to the Animals Scientific Procedures Act of 1986 (UK). Female NOD-scid gamma mice (5-8 weeks) and C57BL/6 mice (6-8 weeks) were purchased from Charles River. The purchased mice were acclimated for 96 hours before any experiments. Mice were housed in individually ventilated cages (maximum six mice per cage) in a sterile animal facility with a 12-hour light and 12-hour dark cycle and a climate control system that maintains at 22℃ and 50% humidity. Certified rodent diet, filtered water and sterilised bedding sets were provided for mice at all times. The daily health check and twice-a-week weight measurement were carried out at all time. Mice with more than 10% body weight loss in between two weight measurements were euthanised via cervical dislocation or pentobarbital overdose.

2.7.2 Tumour induction, treatment and measurement

Ten million of Su-DHL-6 or two million of MDA-MB-231 cells were resuspended in media containing 50% DEME and 50% Matrigel (356234; Corning) and subcutaneously injected in the right flank of NOD-scid gamma mice. 0.2 million of EO771 cells were resuspended in 50% DEME and 50% Matrigel (356234; Corning) and subcutaneously injected in the right flank of C57BL/6 mice. The intraperitoneally injected drugs, including WT-TACI-Fc, atacicept, BS7-10-Fc, BS7-10-Fc (68-110 a.a.), WT-RAGE V-Fc and RAGE V13-Fc were manufactured by Chempartner. The purity of each recombinant protein was higher than 95%. Endotoxin levels of all recombinant proteins were lower than 3 EU/mg. Body weight

and tumour volume were measured every 48 h. The tumour volume was estimated by using the formula $1/2 * l * w * h$.

2.7.3 Hematoxylin and eosin staining

Tissues were fixed in 10% neutral buffered formalin overnight, Stored in 70% ethanol, processed in a STP120 tissue processor and embedded in paraffin blocks. Next, 4 µm tissue slices were prepared using a microtome. After warming the slides at 50℃ for 10 minutes, the slides were rehydrated in 100% Citroclear (2x), 100% ethanol (2x), 70% ethanol and 50% ethanol for 3 minutes each. For haematoxylin and eosin staining, tissues were stained with Harris's haematoxylin for 5 minutes. The slides were dipped in Scott's tap water, 0.5% lithium carbonate, 50% ethanol, 70% ethanol and 90% ethanol before being stained with alcoholic eosin for 3 minutes. After the tissue was dehydrated with 90% and 100% ethanol, the slides were placed in xylene I and xylene II and mounted with coverslips. Images were taken using ScanScope. ImageScope was used for analysis.

2.7.4 Conjugation of BS7-10-Fc with Alexa Fluor® 488

Alexa Fluor® 488 Conjugation Kit (Fast) - Lightning-Link® (ab236553) was used to conjugate BS7-10-Fc with Alexa Fluor® 488. The procedures followed the manufacturer's protocol. 5 mg/kg of BS7-10-Fc Alexa Fluor® 488 was injected intraperitoneally. Mouse blood was collected through cardiac puncture at 3, 24, 48 and 72 hours post-injection. Serum was separated in blood collection tubes by centrifugation at 3000 g for 15 minutes. Serum fluorescence was measured using a plate reader BMG Labtech POLARstar Omega at excitation 495 nm and emission 519 nm.

2.7.5 ELISA to measure mouse serum BAFF level

To measure mouse serum BAFF level, ELISA was performed on mouse serum isolated through cardiac puncture of Su-DHL-6 bearing NSG mice 24 hours after IgG1 Fc, WT-RAGE V-Fc or RAGE V13-Fc treatment. Serum was isolated in blood collection tubes by

centrifugation at 3000 g for 15 minutes. 1 in 20 diluted serum samples were used for ELISA assay. A mouse BAFF ELISA kit (ELM-BAFF-1; RayBiotech) was used for quantification of murine serum BAFF level. All steps were carried out according to the manufacturer's protocol. OD 450 nm was measured by using a plate reader BMG Labtech POLARstar Omega.

2.8 Immunoprecipitation-Mass Spectrometry (IP-MS)

2.8.1 Immunoprecipitation

Immunoprecipitation for mass spectrometry was performed using Pierce™ MS-Compatible Magnetic IP Kit, protein A/G (15312627; Thermo Scientific). The methods were followed in accordance with the manufacturer's protocol. All reagents were provided by the kit. Briefly, 5 µg of IgG1 Fc, 5 µg of WT-RAGE V-Fc or 5 µg of RAGE V13-Fc were incubated with either 500 µl of 4 mg/ml of MDA-MB-231 cell lysate or 500 µl of 1 in 100 diluted normal human serum (S1-100ML; Merck) overnight at 4℃ to precipitate potential interactors. Each reaction was supplemented with protease and phosphatase inhibitors. The reaction mixtures were then incubated with pre-washed protein A/G beads for 1 hour at room temperature. The coated beads were then washed five times with washing buffers to remove unbound components. 5% beads were used for western blot analysis, where bead pellets were incubated in Bolt™ LDS Sample Buffer (B0007; Invitrogen) supplemented with Bolt™ sample reducing agent (B0009; Invitrogen) at 95℃ for 5 minutes. The samples were subsequently centrifuged at 10,000 g for 10 minutes. The supernatant was used for western blot analysis. 95% of beads were subject to on-bead trypsin digestion for mass spectrometry analysis.

2.8.2 Mass spectrometry identification of potential interactors in MDA-MB-231 cell lysate and human serum

All MS experiments were carried out by Iolanda Vendrell. The immunoprecipitated proteins were subjected to the on-bead digestion. All Samples were prepared (IV) using

the soluble smart trypsin following the “MS PRO0015: On bead digest using Smart trypsin (60109-101-MB, Thermo Scientific)” protocol. Briefly, pre-washed beads were resuspended in trypsin smart buffer and incubated with 3.5 µl of trypsin for 1 hour 50 minutes at 70℃. Digestion was stopped with 0.1% Trifluoroacetic Acid (TFA). Samples were then desalted using sola HRP cartridges. Subsequently, the eluted peptides were dried down and resuspended in solvent A containing 2% acetonitrile and 0.1% TFA. A one-hour gradient was employed using a Fusion Lumos system coupled with an Ultimate 3000 UHPLC. EasySpray column was used as a trap column. The instrument settings for the two MS analysis are summarised below:

MS (MDA-MB-231 cell lysate-dervied samples): 120K resolution, m/z 400-1500, AGC 4e5, s-lens RF30

MS (Human serum-derived samples): Ion trap with rapid scan mode, Quad isolation 1.6, 40% AGC, maximum injection time 25 msec,

MS data analysis was performed by using Label free quantiation, maxquant (v. 1.6.14.0). Maxquant is a software that includes a data search engine (Andromeda). The output of the data search was used to generate quantitative proteomics outputs (labelled or label free). For the MS data analysis, I used the Label free quant approach. Data was searched using human UniProt/SwissProt. 2-sample student t test was used for statistical analysis between different treatment groups.

2.9 RNA sequencing and functional analysis

2.9.1 RNA sequencing

5 x 10^5 of MDA-MB-231 cells were seeded in 9 mm Petri dishes overnight before being treated with 40 µg/ml of IgG1 Fc, 40 µg/ml of WT-RAGE V-Fc or 40 µg/ml of RAGE V13-Fc for 24h. The cell pellets were shipped to SourceBioscience, where the cDNA preparation and RNA sequencing were carried out. Qiagen RNeasy Mini Kit was used to

isolate RNA from the cell pellets. polyA selection and stranded cDNA library were carried out using NEBNext® Ultra™ II Directional RNA Library Prep Kit for Illumina and NEBNext® Poly(A) mRNA Magnetic Isolation Module. 150 bp pair-end sequencing was performed on the NovaSeq 6000 S4 Lane 150 PE Read mode at Genomics Core Facility, Source BioScience (Nottingham, UK). 30 million read pairs minimum were obtained per sample (9 Gb per sample).

2.9.2 Bioinformatic analysis for RNA sequencing results

2.9.2.1 Adapter trimming

For RNA sequencing, demultiplexed raw FASTQ files were adapter-trimmed using bbduk (bbmap Version 38.94).

2.9.2.2 Quantification of gene expression

Gene expression was quantified using the tool Salmon. Relative transcript abundance was determined by performing a quasi-alignment to trimmed FASTQ files using Salmon (v1.6.0) to count and generate transcripts per million (TPM) which is required for downstream comparative analyses.

2.9.2.3 Differential Gene Expression Analysis

To quantify differences between conditions and measure statistical significance, the DeSeq2 package (v1.28.1) was used to estimate the dispersion and logarithmic fold change between comparative groups for each gene. The Wald test was used for significance testing with the Benjamini-Hochberg approach for data correction. Genes with fold-change > 2 and Benjamini-Hochberg p values < 0.05 were considered to be significantly differentially expressed.

2.9.2.4 Gene set enrichment analysis (GSEA)

Differential gene expression analysis results, including the log2(fold-change) and Benjamini-Hochberg p values for each gene were used to carry out pre-ranked GSEA

analysis (GSEA v4.2.3). Gene sets database (h.all.v2022.1.Hs.symbols.gmt Hallmarks) was used for analysis to provide more insights into the anti-tumour functions of RAGE V13-Fc. Three comparisons were carried out (IgG1 Fc vs WT-RGAE V-Fc; Fc vs RAGE V13-Fc and WT-RAGE V-Fc vs RAGE V13-Fc). FDRq ≤ 0.05 was considered to be statistically significant.

2.10 *In silico* structural analysis

2.10.1 Alpha-fold 2 structural prediction

The structure of RAGE V13 was predicted by alpha-fold2 as monomers by ChemPartner. WT-RAGE V-Fc and RAGE V13-Fc were predicted as dimer formats. All models were predicted by Alphafold v2.3.1. The Aphafold2 predicted structures were unrelaxed models which underwent an Amber relaxation procedure. The predicted LDDT (pLDDT) scores were used for model ranking. The model with the highest confidence was used for this study.

2.10.2 Computational structural simulation

Interactions between the TACI ectodomain and its ligands (APRIL and BAFF) was computationally simulated and analysed using a range of prediction software. Due to the structural complexity of the TACI, the modelling was only successfully performed for truncated versions of the TACI ectodomains, including TACI CRD1 (35-67 a.a.) and TACI CRD2 (68-106 a.a.) and TACI CRD1 + CRD2 (35–106 a.a.). The amino acid sequences used for the modelling are summarised in **Table A5**. The structural analysis only encompassed three out of ten mutations identified in BS7-10. The modelling of receptor-ligand interactions was carried out using multiple software including Prime from Schrödinger Suites 2021-2, Alphafold2 v2.3.1, RoseTTAFold, trRosetta and RosettaRemodel. The amino acid sequences and structural information from Protein Data bank ID 1XU1 were used as a basis for modelling. The changes in amino acid distance, specific interactions and surface complementarity caused by point mutations,

including H56R, R60H, I92V, was calculated by Protein Interaction Analysis module from Bioluminate, Schrödinger. The changes in affinity and stability caused by the three mutations were calculated by using Residue Scanning Calculation Module from Bioluminate, Schrödinger.

2.11 Immunofluorescence

MDA-MB-231 cells were fixed with 4% PFA for 20 minutes at room temperature. Permeabilisation was performed by incubating cells with 0.5% triton X-114 for 20 minutes at room temperature. Then, the cells were blocked with PBS supplemented with 1% BSA, and 2% FBS for 1 hour at room temperature. 50 µg/ml of IgG1 Fc, WT-RAGE V-Fc or RAGE V13-Fc were used as primary antibodies and incubated with MDA-MB-231 cells in PBS overnight at 4℃. The cells were subsequently stained with 1: 200 goat anti-human IgG Fc (FITC) antibody (ab98594; Abcam) for 1 hour in the dark at room temperature. The nucleus was stained with Hoescht (5 ug/ml) for 15 minutes in the dark at room temperature. Zeiss LSM 710 Confocal Microscope was used to take images. FIJI (Image J) was used for image analysis (National Institutes of Health).

2.12 Reciprocal immunoprecipitation

Regular reciprocal immunoprecipitation was performed by using Pierce™ MS-Compatible Magnetic IP Kit, protein A/G (15312627; Thermo Scientific). The methods were followed in accordance with the manufacturer's protocol. All reagents were provided by the kit. Briefly, 5 µg of IgG1 Fc, 5 µg of WT-RAGE V-Fc or 5 µg of RAGE V13-Fc were incubated with 5 µg of recombinant human His-tagged GRP78/HSPA5 protein (NBC1-18378; Novus Biologicals) or recombinant human HMMR protein (ab125997; Abcam) in 500 µl of lysis buffer with rotating overnight at 4℃. The lysis buffer was supplemented with protease and phosphatase inhibitors. The reaction mixtures were then incubated with pre-washed protein A/G beads or Dynabeads™ His-Tag Isolation (10104D; Thermo Scientific) at room temperature for 1 hour. After 5-time

washes with washing buffer, the magnetic beads were subject to on-bead digestion where bead pellets were incubated in Bolt™ LDS Sample Buffer (B0007; Invitrogen) supplemented with Bolt™ sample reducing agent (B0009; Invitrogen) at 95℃ for 5 minutes. The samples were centrifuged at 10,000 g for 10 minutes. The supernatant was used for western blot analysis.

2.13 Surface Plasmon Resonance (SPR)

Biacore T200 (Sir William Dunn School of Pathology) was used for SPR analysis. WT-TACI-Fc, atacicept and BS7-10-Fc were immobilised to a density of 500 RU by anti-human IgG1 Fc antibody, which was captured by amine coupling to the surface of a CM5 chip. Experiments were performed at room temperature using a flow rate of 70 µl/min and PBS as a running buffer. Different concentrations of human APRIL and BAFF were injected over all flow cells. BIAevaluation Software was used for data correction (double referencing).

2.14 Flow cytometry

MDA-MB-231 cells were washed and resuspended in PBS supplemented with 2% FBS and blockers (Human BD Fc Block™, 564220). The cells were then incubated with 40 µg/ml of IgG1 Fc, WT-RAGE V-Fc or RAGE V13-Fc for 30 minutes. Subsequently, the cells were washed and stained with Goat Anti-Human IgG Fc (FITC) antibody (ab98594; Abcam). Flow cytometry was carried out on the Attune NxT Flow Cytometer. All flow cytometry data were analysed by using FlowJo 10.4 software. The geometric mean of fluorescence was used to indicate the intensity of fluorescence.

2.15 Statistics

Statistical analysis was carried out using GraphPad Prism 8.4.3 (GraphPad Software Inc., La Jolla, California). Two sample student's t-test was performed to compare

differences between two independent groups. One-way analysis of variance (ANOVA) was used to compare more than two groups.

Chapter 3: Engineering a high affinity TACI decoy receptor for DLBCL and evaluating its therapeutic potential

3.1 Introduction

Overexpression of APRIL and BAFF play critical roles in DLBCL disease progression and drug resistance (Kuo et al., 2008; Moreaux et al., 2004). In particular, the TACI receptor has a high binding affinity to both APRIL and BAFF, making it an ideal template for developing high affinity APRIL and BAFF antagonists. Using the wild-type ectodomain of TACI as a decoy receptor to sequester APRIL and BAFF has been previous reported (Dillon et al., 2010; Kaegi et al., 2020; Rossi et al., 2009). However, the wild-type ectodomain of TACI did not demonstrate appreciable clinical efficacy due to its identical ligand binding affinity as cellular TACI (Dillon et al., 2010; Kaegi et al., 2020; Rossi et al., 2009). To overcome this issue, I engineered a high affinity TACI variant by using a yeast surface display platform. The TACI variant identified with the highest ligand binding affinity (BS7-10) demonstrated an 8-fold increase in binding affinity to APRIL and BAFF compared to commercially available WT-TACI decoy receptors. Furthermore, BS7-10 could also have a newly acquired high affinity binding site based on SPR analysis. A higher level of BAFF sequestration was observed in the BS7-10-treated sample

compared to WT-TACI-treated samples in the B cell proliferation assay. However, in a DLBCL mouse model, no significant improvement was detected between the BS7-10-Fc-treated group and the WT-TACI-FC-treated group. Taken together, BS7-10 had an enhanced APRIL and BAFF binding affinity but failed to demonstrate a significantly higher clinical efficacy than WT-TACI-Fc in the DCBCL mouse model. Extreme variations of tumour growth in the mouse model may account for the less-than-expected outcomes observed.

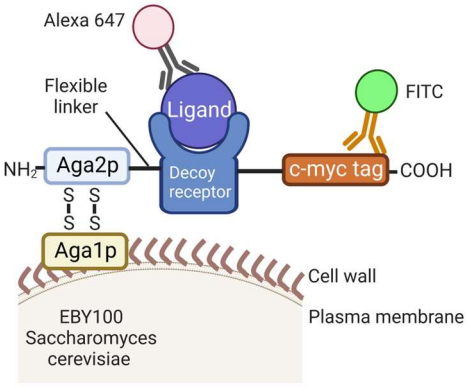
3.2 Results

3.2.1 Principle of yeast surface display technology

Yeast surface display is a versatile platform for high throughput screening of affinity reagents, such as antibodies and natural receptors, from a complex molecular library (**Figure 3.1A & B**) (Uchanski et al., 2019). This study relies on the commonly used yeast display strain *Saccharomyces cerevisiae* EBY100 (ATCC® MYA-4941™) which has a genomic insertion of alpha-agglutin 1 (aga1). Aga1 is a cell wall anchoring protein, and its transcription is regulated by galactose-inducible promoter 1 (GAL1). TACI receptor ectodomain coding sequence was cloned in the pctCon2 plasmid as a fusion protein with Alpha-Agglutin 2 (Aga2). The GAL1 promoter was used to drive the expression of the Aga2 fusion protein. Upon galactose-induced protein expression, the Aga2 fusion protein traffics to the cell surface through the yeast secretory pathway and initiates spontaneous anchorage to the yeast cell wall where two disulfide bonds connecting Aga1 and Aga2 are formed (**Figure 3.1A**). For flow cytometry analysis, anti-myc antibodies were used to determine that decoy receptors were successfully expressed and displayed on the yeast surface. Antibodies against the ligands were used to assess binding between yeast-displayed receptors and ligands. The fusion protein expression level and ligand-receptor binding signals can then be quantified by using flow cytometry.

For library generation, mutant DNA sequences of receptor ectodomain were produced through error-prone PCR using a wild-type receptor ectodomain coding sequence as a template. Ultra-high efficiency transformation enabled the efficient delivery of mutated PCR products and linearised plasmids to yeast cells where plasmids were assembled by yeast-driven homologous recombination (**Figure 3.1B**). The recovered transformants were considered to be the unsorted yeast library. By using a cell sorter, high affinity clones enriched after each sorting round were collected and analysed. The variant with the highest ligand binding affinity was produced as a fusion protein with human IgG1 Fc for *in vitro* and *in vivo* testing.

(A)



(B)

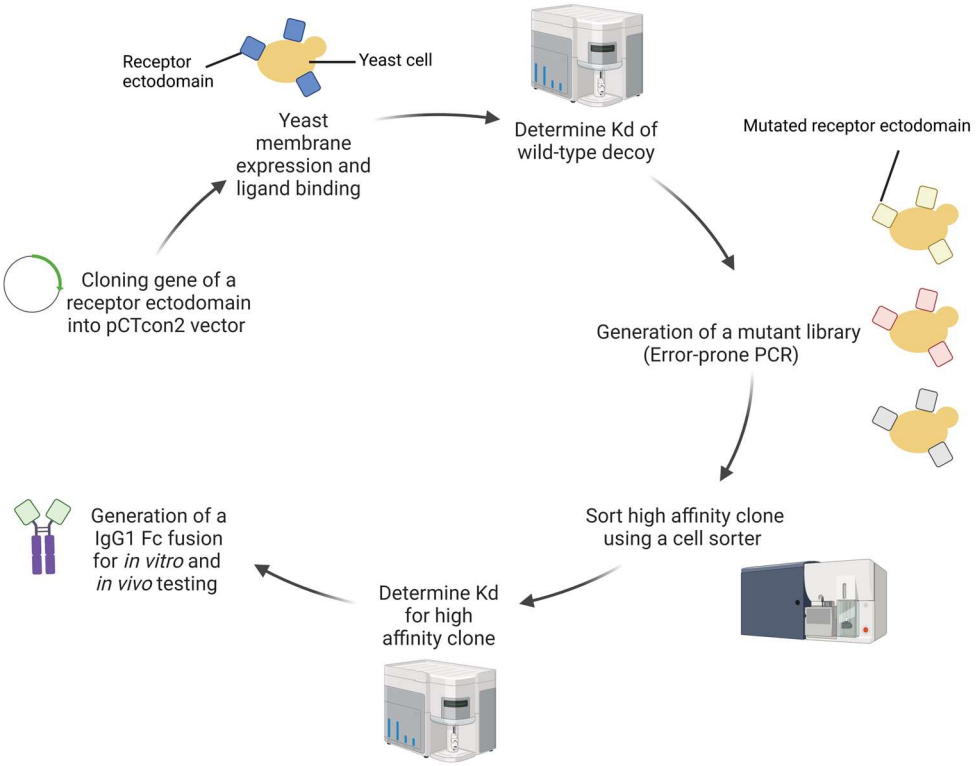


Figure 3.1. Diagrammatic representation of direct evolution of receptor ectodomains using yeast surface display. (A) Principle of yeast surface display. Saccharomyces cerevisiae EBY100 is a yeast display strain that has a genomic insertion of aga1p. The gene encoding receptor ectodomain was encoded in the pCTcon2 plasmids between aga2p and a c-myc. Both Aga2p-receptor ectodomain fusion protein and Aga1 expression were controlled by Gal1 inducible promoters. Upon galactose induction, the Aga1 was expressed on the yeast cell wall. The receptor ectodomain was anchored on the yeast cell wall through sponetaneous formation of two disulphide bonds between Aga1 and Aga2. Antibody conjugated with FITC against c-myc tag was used to indicate the expression of receptor domain. After incubating the galactose-induced yeast cells with the target ligands, an antibody conjugated with Alexa 647 was used to assess if there were ligand-receptor binding events. The binding affinity and fusion protein expression can then be quantified by using flow cytometry. **(B)** Affinity maturation workflow. The gene encoding the soluble decoy receptor was cloned into the yeast display plasmid. After confirming the wild-type decoy receptor expression, ligand-receptor interactions were examined through binding assays where the binding affinity (KD) was determined. Mutant decoy receptor sequences were generated using error-prone PCR. A yeast library was then created where each yeast cell displayed a soluble receptor variant. High affinity clones were isolated using a cell sorter and sequenced. The soluble receptor varaint with the highest ligand binding affinity was produced as a fusion protein with human IgG1 Fc fragment for downstream analysis.

3.2.2 Interaction between yeast-displayed TACI and two TACI ligands, APRIL and BAFF

To determine the binding affinity between yeast-displayed WT-TACI and its ligands, I expressed the TACI ectodomain as a fusion protein with Aga2p on the yeast cell surface. Over 30% of the transformed yeast poplulation displayed the TACI ectodomain on their cell surface (**Figure 3.2A & C**). To determine ligand binding affinity, the yeast cells were treated with various concentrations of APRIL and BAFF.

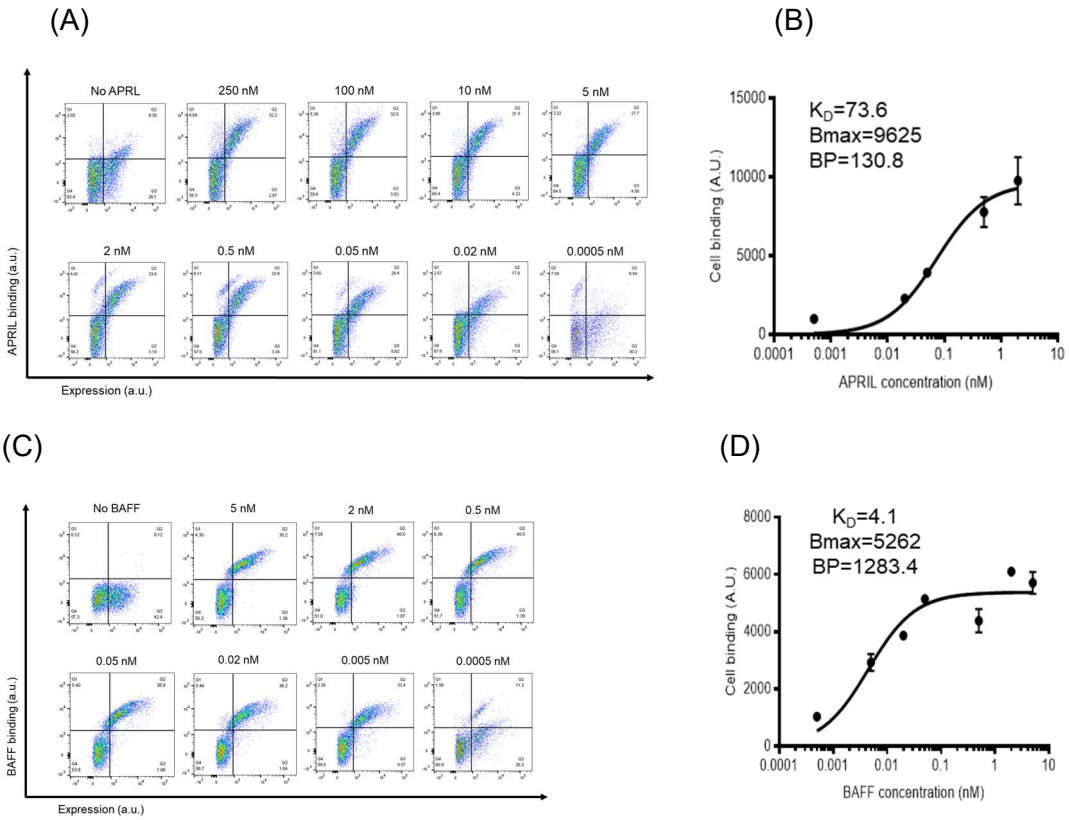


Figure 3.2. Interaction between yeast-displayed WT-TACI and its ligands, APRIL and BAFF. Yeast-displayed WT-TACI was incubated with different concentrations of APRIL or BAFF. Antibodies conjugated with different fluorochrome were used to quantify the binding signal and protein expression level. **(A & C)** Flow cytometry dot plots showing binding of yeast-displayed WT-TACI to APRIL and BAFF, receptively. **(B & D)** Four-parameter sigmoidal curves fit by binding titrations (N=2). Error bars represent standard deviation of the mean. KD: binding affinity. B_{max}: maximum binding capacity. BP: binding potential (BP= B_{max} /KD).

A dose-dependent binding signal was observed for both APRIL and BAFF binding assays. Based on the binding curve, the KD of APRIL-TACI and BAFF-TACI was determined to be around 73.6 pM and 4.1 pM, respectively (**Figure 3.2B & D**). This finding indicated that yeast surface display is a feasible platform for screening high affinity TACI variants.

3.2.3 Mutant library generation (Yeast-displayed TACI)

The mutant sequences of TACI ectodomain were created by using error-prone PCR. Mutagenic nucleotide analogues, including 8-oxo-2'-deoxyguanosine-5'-Triphosphate (8-oxo-dGTP) and 2'-Deoxy-P-nucleoside-5'-Triphosphate (2'-dPTP) were used to

randomly integrate mutations into the TACI ectodomain DNA sequences during PCR amplification. The average amino acid mutation rate adjusted to 10% to avoid significant protein structure disruptions at a high mutation rate and low variant diversity at a low mutation rate. The mutant PCR products were co-transformed with linearised yeast display plasmids (pctCon2) through ultra-high efficiency electroporation. Plasmids were assembled through yeast-driven homologous recombination. The resulting yeast mutant library size was estimated to be around $2x10^8$ transformants. Around 14% of the population showed detectable binding signals when treated with either 2 nM APRIL or 2 nM BAFF. This suggests that a reasonable proportion of TACI mutants were functional and able to interact with APRIL and BAFF.

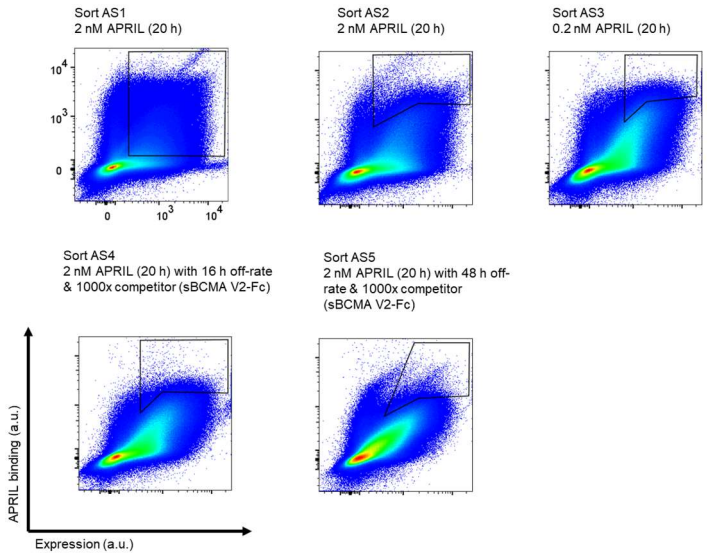
3.2.4 Sort progression (APRIL- and BAFF-directed sorting)

Two separate sorting experiments were performed in parallel to screen for variants that have a high binding affinity specifically to either APRIL or BAFF. For each sorting experiment, progressive rounds of sorts were carried out to enrich for high affinity TACI variants. For each round of sorting, around $2x10^8$ cells were processed and sorted. Finally, a TACI variant that had an improvement in both APRIL and BAFF binding was identified in both sorting experiments.

For APRIL-directed sorting (AS), five rounds of sorts were carried out (AS1-5). The first three rounds were equilibrium binding sorts (**Figure 3.3A**). At a given APRIL concentration, high affinity variants were more likely to interact with APRIL than wild-type TACI and other low affinity varaints after the binding reaction reached equilibrium. AS1 aims to collect all variants that show detectable binding signals when treated with 2 nM APRIL regardless of binding affinity. The concentration of APRIL was then reduced successively from 2 nM to 0.2 nM in the following two sort rounds in order to increase selective stringency. Approximately 2% of the population with the highest binding signal was collected from each sort round. The sort gates were created based on the estimated

ratio of the number of cell-bound APRIL to the number of receptors expressed on cell surface. Kinetic off-rate sorts were used for AS4-5 to screen for variants that have a slower disassociation rate. This approach requires an incubation of yeasts with APRIL followed by a wash with an excessive number of competitors to remove the weakly bound APRIL, thereby leaving only the high affinity variants bound to APRIL. The competitor I used here was sBCMA V2-Fc, an affinity-enhanced version of soluble BCMA developed by our group that binds both APRIL and BAFF at a subnanomolar affinity (Miao et al., 2022). The washing time was increased from 16 hours for AS4 to 48 hours for AS5, allowing the TACI variants with fast off-rate to be removed from samples and the ones with slow off-rate to be collected.

(A)



(B)

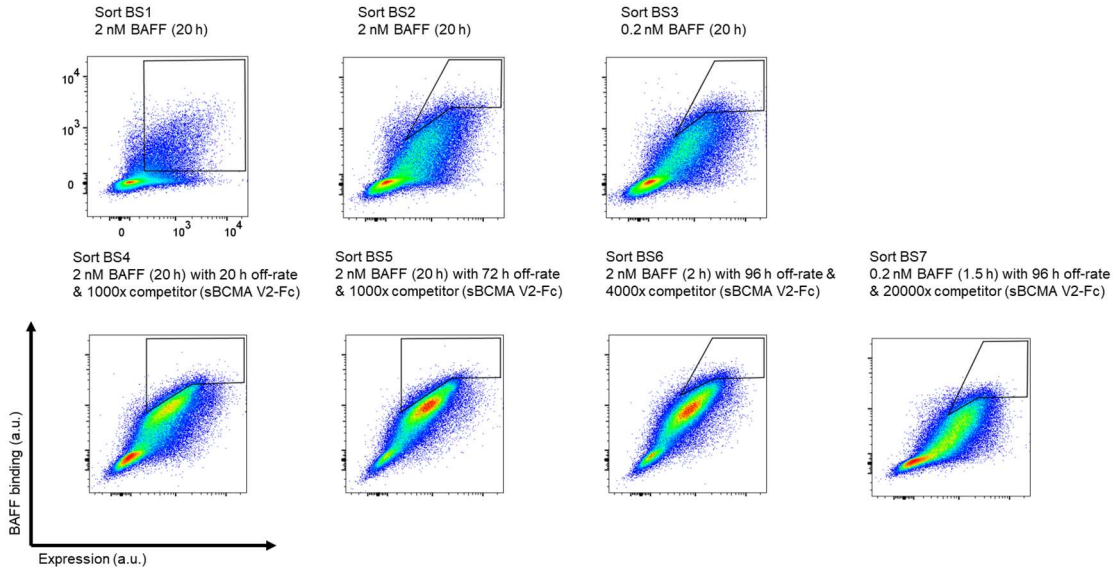


Figure 3.3. Flow cytometry dot plots representing the sorting strategies used for screening high affinity APRIL and BAFF binders from yeast-displayed TACI mutant library. (A) Flow cytometry dot plots showing APRIL-directed sorting. **(B)** Flow cytometry dot plots showing and BAFF-directed sorting. 2.5 x 10^6 dots are shown in each APRIL sort plots and 1 x 10^5 dots are shown in each BAFF sort plot. The equilibrium bining sorts and kinetic off-rate sorts were performed for both APRIL-directed and BAFF-directed sorts. The yeast mutant libraries were incubated with different concentrations of APRIL or BAFF for 1.5-20 hours. The gated populations were collected and amplified in yeast culture either for the next round of cell sorting or receptor variant sequence analysis.

For BAFF-directed sorting (BS), seven rounds of FACS sorts were conducted (BS1-7) (**Figure 3.3B)**. Similar to APRIL sorts, equilibrium binding sorts were performed prior to kinetic off-rate sorts. Briefly, BAFF concentrations were reduced from 2 nM (BS1) to 0.2 nM (BS2-3) to enrich high affinity variants. Regarding kinetic off-rate sorts, several parameters were adjusted to gradually increase selective stringency. The yeasts-ligand incubation time was reduced from 20 hours (BS4) to 1.5 hours (BS7). Also, the competitive wash time increased from 24 hours (BS4) to 96 hours (BS7). Moreover, the ratio of estimated bound BAFF to the number of competitors increased from 1/1000 (BS4) to 1/20000 (BS7). A majority of the yeast-displayed TACI variants from the last rounds of BAFF sorts demonstrated significant binding signal after the off-rate wash, suggesting an enriched population of high affinity TACI variants.

3.2.5 Sequence analysis of variants identified in AS5 and BS7

To monitor the mutant diversity in the two most affinity-enhanced TACI mutant libraries (AS5 & BS7), twenty clones were randomly selected and sequenced from each library (**Table 3.1A & B**). Mutations that occurred in over 25% of the sequenced variants were considered to be high-frequency mutations. For AS5, high-frequency mutations included E18G, E19G, H56R, I92V and E125G. For BS7, high-frequency mutations were comprised of E18G, F21L, H56R, S58N and I92V. The shared high-frequency mutations identified in both AS5 and BS7 libraries included E18G, H56R and I92V suggesting their involvement in both APRIL and BAFF binding.

Table 3.1. Sequencing results of randomly isolated clones from AS5 and BS7. Sequencing results show the mutations identified in the 20 clones isolated from AS5 **(A)** and BS7 **(B).** The first row shows the amino acid positions. The second row indicates the WT-RAGE V sequence. High-frequency mutations are highlighted in yellow, green or pink. The mutations highlighted in pink were identified in both AS5 and BS7 libraries. The grey areas highlighted in BS7 are truncated regions.

(A) AS5

(B) BS7

Amino acid		1	4	7	8	13	16	17	18	19	20	21	27	29	30	31	34	35	37	38	41	43	47	48	49	50	51	52	53	54	56	58	60	62	63	65	66	67	69	70	72	77	81	84	91	92	106	109	113	114	117	121	124	125	126	127	128	130	131	132	134	136	137	138	141	142	143	146	148
WT-TACI		M	L	S	R	S	D	Q	E	E	R	F	T	V	A	M	C	P	E	Q	D	L	C	M	S	C	K	T	I	C	H	S	R	C	A	F	C	R	L	S	R	K	H	R	S	I	N	R	N	L	E	Q	G	E	V	E	N	S	D	N	G	Y	Q	G	H	R	G	A	P
Clone #	AS5-1									G																R					R														V							G																					
Clone #	AS5-2	A					G		G	G						R					N	P	R		F	Y	E		T	S			Y		S					C									R		G	S																		
Clone #	AS5-3									G																R					R														V							G																		
Clone #	AS5-4	V					G		G	G									K							R							H			S																																							
Clone #	AS5-5	V		G		N			G										G			P							T															G		P		S																														
Clone #	AS5-6							R	G											R						R	R									S	Y							G					P								A							R			S												
Clone #	AS5-7									G																					R					V										V							G														D												
Clone #	AS5-8									G																					R					V										V							G																								
Clone #	AS5-9										H			T	T					R						R	R			R			R		S	R		P	G		E							R									D								D												
Clone #	AS5-10									G																					R					V										V							G																								
Clone #	AS5-11				G		G		G			L	A																		R		H														V								G								R												
Clone #	AS5-12									G																					R					V										V							G																								
Clone #	AS5-13									G																					R					V										V							G																								
Clone #	AS5-14		P			G		R	G			S						S	G																			G													K																												
Clone #	AS5-15		P							G		L		A															A							T																																												
Clone #	AS5-16										H			T	T					R						R	R			R			R		S	R		P	G		E							R									D								D												
Clone #	AS5-17									G																					R					V										V							G																								
Clone #	AS5-18									G																					R					V										V							G																								
Clone #	AS5-19									G																					R					V										V							G																								
Clone #	AS5-20	V	P							G														V								G											P							G			S	P				H																		
Clone #	AS5-21				G					G		L	A																		R		H			V										V																														
Clone #	AS5-22									G										R						R	R										Y								G					P								A							R			S												

Amino acid		1	3	6	7	8	9	13	14	15	16	17	18	19	21	27	30	31	33	51	52	53	54	55	56	58	60	61	65	67	69	73	77	91	92	102	103	109	110	113	114	123	124	127	128	133	136	137	138	139	141	142	147	148	151	154	156	157	160	162	163
WT-TACI		M	G	R	S	R	R	S	R	V	D	Q	E	E	F	T	A	M	S	K	T	I	C	N	H	S	R	J	F	R	L	K	S	I	Y	F	R	S	N	L	S	G	E	N	S	Y	Q	G	L	H	R	S	P	P	K	S	A	V	L	V
Clone #	BS7-1	T			G										L										R			A																																					
Clone #	BS7-2	V	D				Q		H					G			T	T	P				Y	S						S	G	H								N	G	P															N									
Clone #	BS7-3		D										G		L						A	V						E			V	H	V										G					Y				L				P		
Clone #	BS7-4					G	Q			A				G	S										N								E			S																		L			E						
Clone #	BS7-5		D										G		L						A	V						E			V	H	V										G					Y				L				P		
Clone #	BS7-6	V		W				G						G						E				S	R	N								V												E													A
Clone #	BS7-7																																																P										A		
Clone #	BS7-8	V		W				G						G						E				S	R	N								V												E													A
Clone #	BS7-9				G								G			A																	E																							E						
Clone #	BS7-10					G					G		G		L	A									R		H							V										G				R													
Clone #	BS7-11				G										L										N									V																													
Clone #	BS7-12		D										G		L						A	V						E			V	H	V										G					Y				L				P		
Clone #	BS7-13	V					G								S			T											E	P							G		S							S														
Clone #	BS7-14	V			G										S										N								V			G	G			G					R		R	G	G	S		E		V					
Clone #	BS7-15																																	P																								A					
Clone #	BS7-16																																	P																								A					
Clone #	BS7-17					G					G		G		L	A									R		H							V										G				R													
Clone #	BS7-18	V		W				G						G						E				S	R	N								V												E													A
Clone #	BS7-19																																	P																								A					
Clone #	BS7-20				G								G			A												E																													E						

Interestingly, there was a specific variant sequence detected in both AS5 and BS7 libraries which is shared by three clones including AS5-11, BS7-10 and BS7-17. I hypothesised that these enriched variant sequences in the two libraries presented enhanced binding affinity to both APRIL and BAFF. In this study, the unique variant sequence was named BS7-10 for simplicity. In addition, multiple truncated sequences were detected in BS7. Overall, BS7-10 seems to be the most promising high affinity candidate.

3.2.6 Determining binding affinity of yeast-displayed TACI variants

Having identified several potential high affinity TACI variants, the next step was to determine the binding affinity of those variants to APRIL and BAFF. Several representative mutants were tested (**Figure 3.4A & B**). All variants had certain degrees of improvement in either APRIL or BAFF binding. AS5-22 had the highest APRIL binding affinity of 21.4 pM while its APRIL binding potential was lower than BS7-10. Among all variants, BS7-10 had the highest BAFF binding affinity of 1.8 pM and the highest binding potential to both APRIL and BAFF.

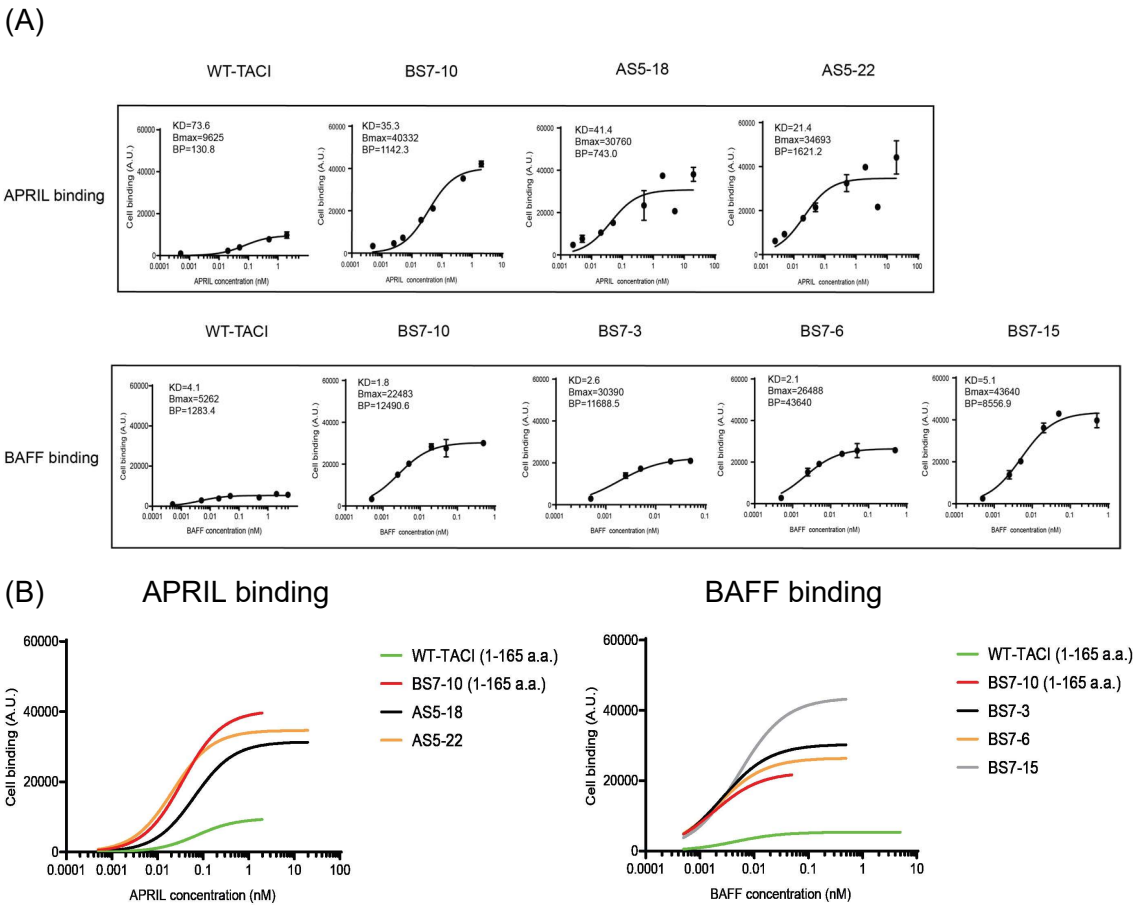


Figure 3.4. Determination of binding affinity of yeast-displayed variants to APRIL or BAFF. (A) Flow cytometry-based binding curve showing the binding of yeast-displayed TACI varaints to APRIL and BAFF (N=2). The binding signal was quantified by using flow cytometry. **(B)** Summary of the binding assays. Four-parameter sigmoidal curves were determined by binding titrations. Error bars represent standard deviation of the mean. Calculated KD, B_{max} and BP are indicated on each plot. A.U., arbitrary units.

Compared to WT-TACI, BS7-10 had around a 2-fold increase in both APRIL and BAFF binding and approximately a 4-fold increase in B_{max}. Given the dominant feature of BS7-10 in both APRIL and BAFF sorted libraries, BS7-10 was considered to be the best variant and used for further investigation.

3.2.7 Artificial TACI mutants have no major improvement in APRIL or BAFF binding.

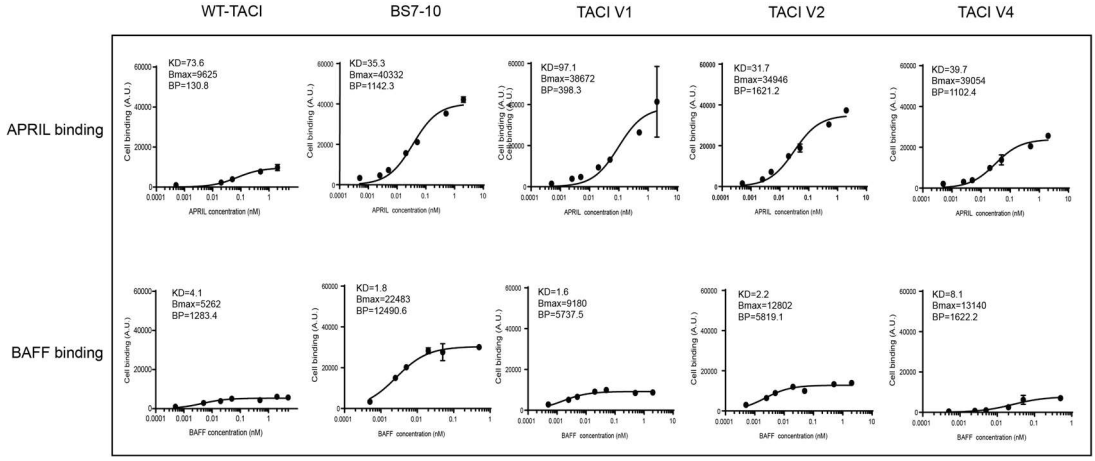
Based on sequence analysis, three artificial TACI mutants were created (TACI V1, V2, and V4, **Figure 3.5A**). Each mutant contained three high-frequency mutations (E18G, H56R and I92V) and additional mutations that were found with a relatively lower frequency. Compared to WT-TACI, all three artificial mutants showed an increase in

binding affinity to APRIL and BAFF (**Figure 3.5B**). Compared to BS7-10, TACI V1 exhibited a higher binding affinity to BAFF but a lower binding affinity to APRIL.

(A)

Amino acid		8	16	18	19	21	27	56	58	60	92	125	127	137
WT-TACI		R	D	E	E	F	T	H	S	R	I	E	E	Q
Clone #	TACI V1			G	G	L		R			V	G		
Clone #	TACI V2			G	G	L		R	N		V		G	
Clone #	TACI V4	G	G	G		L	A	R	N	H	V		G	R

(B)



(C)

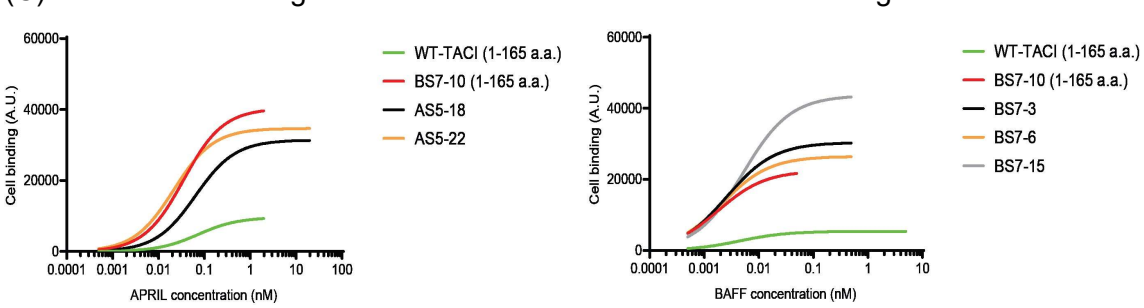


Figure 3.5. Determination of binding affinity of yeast-displayed artificial TACI mutants to APRIL and BAFF. (A) Amino acid mutations in the artificial TACI mutants. The high-frequency mutations identified in the AS5 and BF7 libraries are highlighted in pink. The moderate frequency mutations are shown in yellow and green. The low-frequency mutations are indicated in white. **(B)** Flow cytometry-based binding curve showing the binding of yeast-displayed artificial TACI mutants to either APRIL or BAFF (N=2). **(C)** Summary of the binding assays. Four-parameter sigmoidal curves were determined by binding titrations. Error bars represent standard deviation of the mean. Calculated KD, B_{max} and BP are indicated on each plot. A.U., arbitrary units.

Opposite to TACI V1, TACI V3 had an improvement in APRIL binding but a weaker BAFF binding. TACI V2 was similar to BS7-10 in terms of binding affinity to both APRIL and BAFF while the B_{max} of BS7-10 to both APRIL and BAFF was higher than TACI V2.

Overall, the three artificial mutants failed to show a major improvement in APRIL and BAFF binding compared to BS7-10 (**Figure 3.5C**).

3.2.8 Exploring the high affinity basis of BS7-10 through mutagenesis (reverse mutations and truncations)

To understand the high affinity basis of BS7-10, I created several reverse mutants and truncated versions of BS7-10. Ten mutations were identified in BS7-10 with the majority scattered around CRD1. Each reverse mutant of BS7-10 contained a reverse mutation, leaving the rest nine mutations unchanged (**Figure 3.6A**). N-terminal and C-terminal truncated versions of TACI ectodomains were created to study the role of CRD1 and CRD2 in ligand binding.

WT-TACI, BS7-10 and the ten reverse mutants were examined for their ability to interact with either 50 pM APRIL or 5 pM BAFF (**Figure 3.6B**). WT-TACI showed a significantly lower APRIL and BAFF binding signal than BS7-10 and all reverse mutants. The ten reverse mutants showed lower APRIL and BAFF binding signals than BS7-10, suggesting that all mutations played a role in the enhanced binding signals. V92I as the only mutation located inside of the known binding interface caused the most significant reduction in APRIL binding signal. The average APRIL and BAFF binding signal of the reverse mutant (I92V) was also the lowest, suggesting that I92V could be a major contributor for the enhanced ligand binding.

(A)

Amino acid		8	16	18	21	27	56	60	92	127	137
WT-TACI		R	D	E	F	T	H	R	I	E	Q
Clone #	BS7-10	G	G	G	L	A	R	H	V	G	R
Clone #	BS7-10 G8R		G	G	L	A	R	H	V	G	R
Clone #	BS7-10 G16D	G		G	L	A	R	H	V	G	R
Clone #	BS7-10 G18E	G	G		L	A	R	H	V	G	R
Clone #	BS7-10 L21F	G	G	G		A	R	H	V	G	R
Clone #	BS7-10 A27T	G	G	G	L		R	H	V	G	R
Clone #	BS7-10 R56H	G	G	G	L	A		H	V	G	R
Clone #	BS7-10 H60R	G	G	G	L	A	R		V	G	R
Clone #	BS7-10 V92I	G	G	G	L	A	R	H		G	R
Clone #	BS7-10 G127E	G	G	G	L	A	R	H	V		R
Clone #	BS7-10 R137Q	G	G	G	L	A	R	H	V	G	

(B) Cell binding to 50 pM APRIL Cell binding to 5 pM BAFF

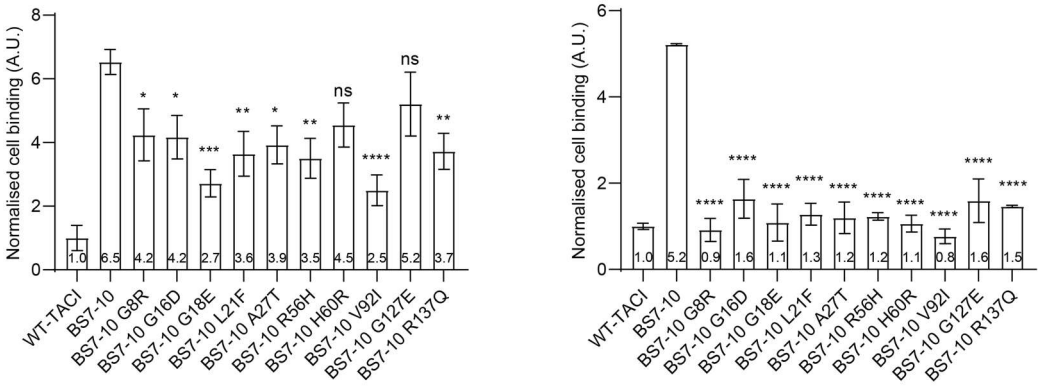
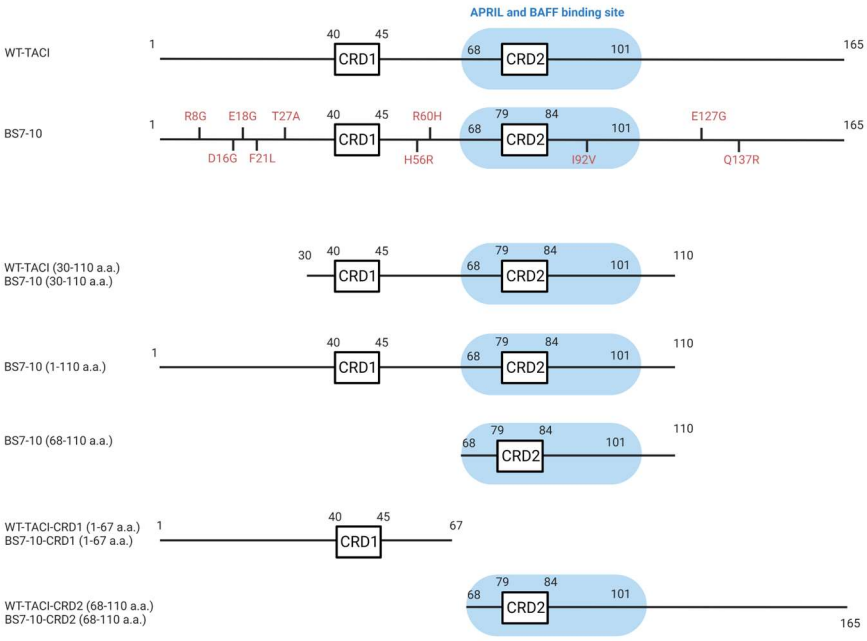


Figure 3.6. Binding of yeast-displayed BS7-10 reverse mutants to APRIL and BAFF. **(A)** Amino acid mutations in the ten BS7-10 reverse mutants. Blank denotes wild-type TACI sequences. **(B)** Relative binding signals of the ten yeast-displayed BS7-10 reverse mutants to 50 pM APRIL and 5 pM BAFF (n ≥2). All data were normalised against the binding signal of yeast-displayed WT-TACI. Error bars represent standard deviation of the mean. One-way ANOVA was performed to compare between treatment groups. The asterisks on top of the bars indicate the significance when comparing different mutants with BS7-10. The average is shown at the bottom of each bar. P<0.05, **P<0.01, ***P<0.001, ****P<0.0001 or not statistically significant (ns).

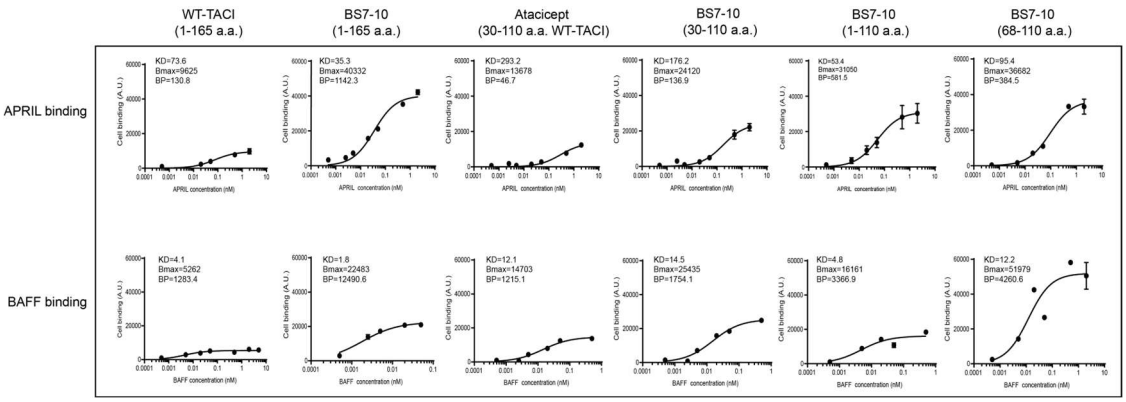
Given that several truncated TACI variants were detected in BS7 library, it was assumed that truncation could improve ligand binding. Here, I created three truncated versions of WT-TACI including WT-TACI (30-110 a.a.), WT-TACI (1-67 a.a. CRD1) and WT-TACI (68-110 a.a. CRD2), and five truncated versions of BS7-10 including BS7-10 (30-110 a.a.), BS7-10 (1-110 a.a.), BS7-10 (68-110 a.a.), BS7-10 (1-67 a.a. CRD1) and BS7-10 (68-110 a.a. CRD2) (**Figure 3.7A**). Compared to all truncated mutants, the full-length BS7-10 (1-165 a.a.) remains to be the best variant which has an around 8-fold higher

binding affinity to both APRIL and BAFF compared to atacicept, a trucated TACI decoy receptor, also known as WT-TACI (30-110 a.a.) (**Figure 3.7B & C**). Full length WT-TACI showed a higher binding affinity than atacicept. All truncations seemed to have minor effects on APRIL and BAFF binding for both WT-TACI and BS7-10. The truncated variant BS7-10 (68-110 a.a.) was the shortest version of BS7-10 which showed a comparable binding capacity to WT-TACI (30-110 a.a.) and only around 3-fold lower binding affinity to APRIL and BAFF than full-length WT-TACI. Overall, the designed truncations were not shown to enhance ligand binding of BS7-10. Interestingly, ligand binding was also not severely weakened by the designed truncations.

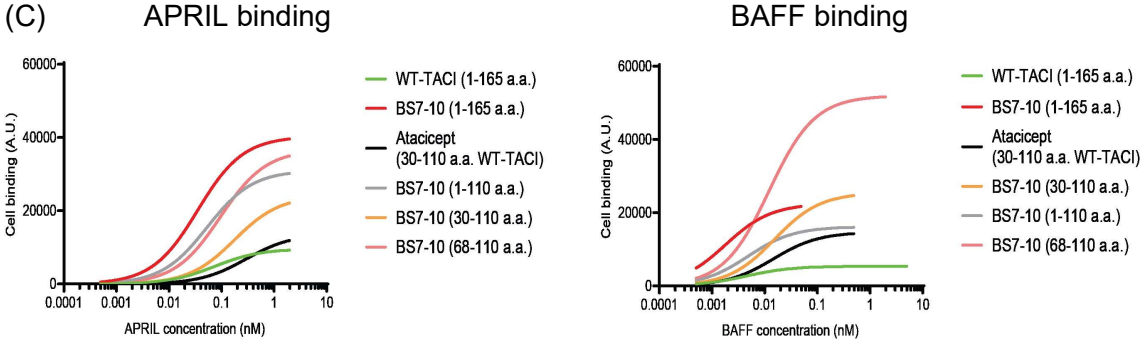
(A)


APRIL and BAFF binding site
WT-TACI
BS7-10
R8G
E18G
T27A
D16G
F21L
R60H
H56R
I92V
E127G
Q137R
CRD1
CRD2
WT-TACI (30-110 a.a.)
BS7-10 (30-110 a.a.)
BS7-10 (1-110 a.a.)
BS7-10 (68-110 a.a.)
WT-TACI-CRD1 (1-67 a.a.)
BS7-10-CRD1 (1-67 a.a.)
WT-TACI-CRD2 (68-110 a.a.)
BS7-10-CRD2 (68-110 a.a.)

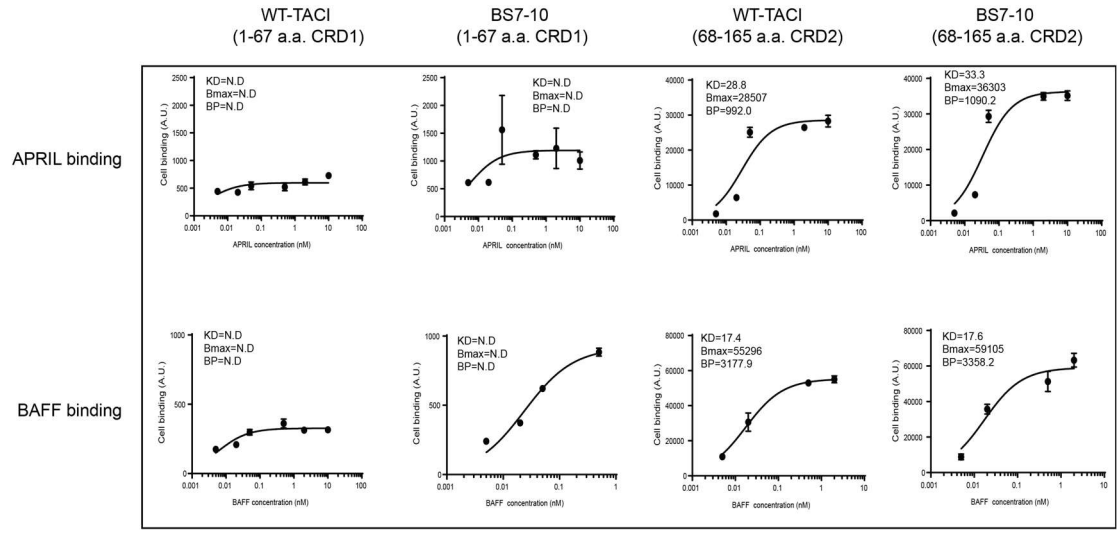
(B)


WT-TACI (1-165 a.a.)
BS7-10 (1-165 a.a.)
Atacicept (30-110 a.a. WT-TACI)
BS7-10 (30-110 a.a.)
BS7-10 (1-110 a.a.)
BS7-10 (68-110 a.a.)
APRIL binding
BAFF binding
Cell binding (A.U.)
APRIL concentration (nM)
BAFF concentration (nM)

(C)


APRIL binding
BAFF binding
Cell binding (A.U.)
APRIL concentration (nM)
BAFF concentration (nM)
WT-TACI (1-165 a.a.)
BS7-10 (1-165 a.a.)
Atacicept (30-110 a.a. WT-TACI)
BS7-10 (30-110 a.a.)
BS7-10 (1-110 a.a.)
BS7-10 (68-110 a.a.)

(D)



(E)

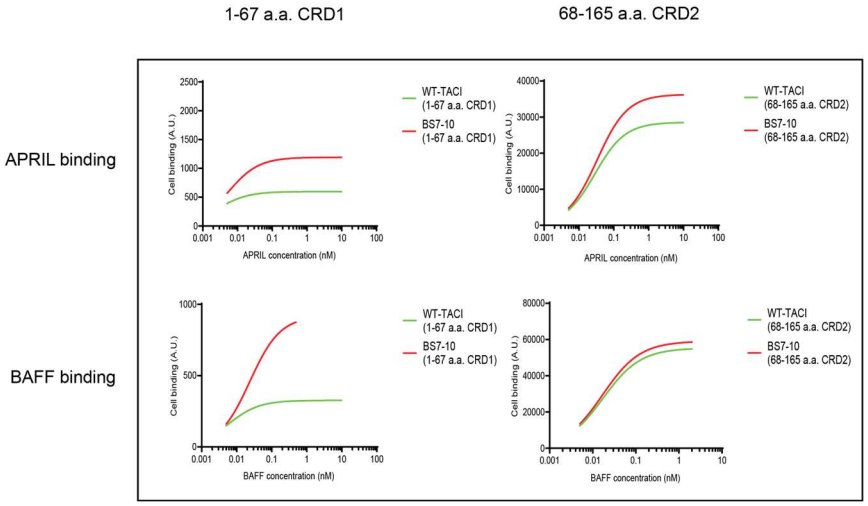


Figure 3.7. Determination of binding affinity of yeast-displayed truncated WT-TACI and BS7-10 to APRIL or BAFF. The yeast cells were incubated with different concentrations of APRIL or BAFF. The binding signal was quantified by using flow cytometry. **(A)** Diagrammatic representation showing the mutations in BS7-10 and artificial truncated versions of WT-TACI and BS7-10. In total, ten mutations were found in BS7-10 which are highlighted in red. **(B)** Comparison of the truncated TACI receptors to WT-TACI and BS7-10 in terms of their ability to interact with APRIL and BAFF (N=2). **(C)** Summary of the binding assays of truncated TACI variants. **(D)** Comparison of WT-TACI CRD1 and CRD2 to BS7-10 CRD1 and CRD2 in terms of their ability to interact with APRIL and BAFF (N=2). **(E)** Summary of the binding assays of TACI CRDs. Four-parameter sigmoidal curves were determined by binding titrations. Error bars represent standard deviation of the mean. Calculated KD, B_{max} and BP are indicated on each plot. A.U., arbitrary units.

Due to multiple mutations scattering around CRD1, I next investigated the effects of the mutations on the ligand binding of CRD1 and CRD2 individually (**Figure 3.7D & E**). BS7-10 (1-67 a.a. CRD1) showed a higher B_{max} than WT-TACI (1-67 a.a. CRD1) while the binding affinity was not accurately determined due to the low binding signal intensity. Similar to the CRD1 domain, BS7-10 (68-110 a.a. CRD2) demonstrated a higher B_{max} to both APRIL and BAFF compared to WT-TACI (68-110 a.a. CRD2) but their share similar ligand binding affinity. This suggests that the mutations in BS7-10 could potentially improve the ligand binding of both CRD1 and CRD2.

3.2.9 Computational structural simulation of TACI-derived sequences in complex with their ligands

To investigate the structural basis of the enhanced ligand binding affinity of BS7-10, I carried out structural simulations using computational modelling. Protein structures predicted by Alphafold2 were used as backbones for mapping mutations in the BS7-10. Due to the structural complexity of TACI ectodomain, I was only able to successfully predict and simulate the APRIL-TACI and BAFF-TACI interactions using truncated TACI structures including TACI CRD1 (35-67 a.a.) and TACI CRD2 (68-106 a.a.) and TACI CRD1 + CRD2 (35–106 a.a.). The computationally resolved structure only contains three out of ten mutations including H56R, R60H and I92V.

Comparing the predicted complex of WT-TACI/APRIL with BS7-10/APRIL, mutation R60H could create a new hydrogen bonding with Asp15 on APRIL and thereby increase the surface complementarity (**Table 3.2**). Comparing the predicted complex of WT-TACI/BAFF with BS7-10/BAFF, mutation H56R gave rise to an increase in overall complementarity with BAFF. Counter-intuitively, mutation I92V on BS7-10 did neither promote APRIL nor BAFF binding in the simulation.

Table 3.2. Comparison of intermolecular interactions between WT-TACI and BS7-10. All models were predicted by Alphafold v2.3.1. Surface complementarity and molecular distance were calculated by using the protein interaction analysis module from Bioluminate, Schrödinger. Given that the TACI structure is highly flexible and only partially resolved, the three predicted models including TACI CRD1 (35-67 a.a.), TACI CRD2 (68-106 a.a.) and TACI CRD1 + CRD2 (35–106 a.a.) were used for structural simulation. T: TACI. A: APRIL. B: BAFF. HB: Hydrogen bonding.

Model*	Residues of TACI	Residues of APRIL or BAFF	Distance (Å)	Specific Interactions	Surface Complementarity	Interaction enhancement
TACI CRD1 + CRD2 (35–106 a.a.); Role of I92V in APRIL and BAFF binding						
WT-TACI_APRIL	T:Ile 92	A:Phe 62	2.8		0.92	**No**
BS7-10_APRIL	T:Val 92	A:Phe 62	2.9		0.92	
WT-TACI_BAFF	T:Ile 92	B:Tyr 65	2.8		0.9	**No**
BS7-10_BAFF	T:Val 92	B:Tyr 65	3		0.88	
TACI CRD1 alone (35-67 a.a.); Role of R60H and H56R in APRIL and BAFF binding						
WT-TACI_CRD1_APRIL	T:Arg 60	A:Asp 18	2.2	1x HB to A:Asp 18	0.66	**Yes**
	T:Arg 60	A:Asp 16	2.3		0.63	
	T:His 56	A:Thr 61	2.5		0.62	
	T:His 56	A:Val 60	2.4		0.75	
	T:His 56	A:Phe 62	4		0.74	
BS7-10_CRD1_APRIL	T:His 60	A:Asp 18	2.2	1x HB to A:Asp 18	0.69	
	T:His 60	A:Asp 16	2.7		0.61	
	T:His 60	A:Asp 15	2.1	1x HB to A:Asp 15	0.68	
	T:Arg 56	A:Thr 61	2.6		0.72	
	T:Arg 56	A:Phe 62	2.2		0.69	
	T:Arg 56	A:Arg117	2.2		0.7	
WT-TACI_CRD1_BAFF	T:Arg 60	B:Glu 125	2.4	2x HB to B:Glu 125	0.88	**Yes**
	T:His 56	B:Thr 64	2.8		0.67	
	T:His 56	B:Asp 62	3.5		0	
	T:His 56	B:Lys 63	2.5		0.86	
BS7-10_CRD1_BAFF	T:His 60	B:Glu 125	2.5		0.86	
	T:Arg 56	B:Thr 64	2.4		0.87	
	T:Arg 56	B:Arg 124	3.3		0.73	
	T:Arg 56	B:Tyr 65	2.4		0.83	
	T:Arg 56	B:Ala 66	3.9		0.72	
TACI CRD2 alone (68-106 a.a.); Role of I92V in APRIL and BAFF binding						
WT-TACI_CRD2_APRIL	T:Ile 92	A:Phe 62	2.8		0.92	**No**
BS7-10_CRD2_APRIL	T:Val 92	A:Phe 62	2.9		0.92	
WT-TACI_CRD2_BAFF	T:Ile 25	B:Tyr 65	2.8		0.9	**No**
BS7-10_CRD2_BAFF	T:Val 25	B:Tyr 65	3		0.89	

To further study the impact of these mutations on the thermodynamics of BS7-10 and APRIL/BAFF complexes, the estimated changes in binding affinity and complex stability for individual mutations and grouped mutations were summarised in **Table 3.2**. A more negative value implies a higher binding affinity or higher complex stability. H56R and R60H were likely to promote APRIL and BAFF binding affinity and complex stability, while I92V might have no or minor unfavourable effects on ligand binding. H56R seemed to be more important for APRIL binding than BAFF binding. In contrast, R60H might

contribute more to the enhanced BAFF binding. Overall, H56R and R60H as mutations outside of the known ligand binding pocket potentially increased complex stability while I92V did not seem to affect the binding at all.

Table 3.3 Computionally estimated variations of affinity and stability (in kcal/mol) for individual mutations in BS7-10. This was performed by using the residue scanning calculations module from Bioluminate. d Affinity: Change in binding affinity. A negative value denotes an increase in binding affinity. d Stability (solvated) (kcal/mol): Change in the stability. It is calculated using the prime energy function with an implicit solvent term. Stability is defined as the difference in free energy between the folded state and the unfolded state. A negative value of the change indicates an increase in complex stability.

TACI Residue	Original	Mutated	d Affinity	d Stability (solvated) (kcal/mol)
WT-TACI_CRD1 vs BS7-10_CRD1 (35-67 a.a.)_APRIL				
56	His	Arg	-15.88	-16.24
60	Arg	His	0.82	4.41
56 60	His Arg	Arg His	-10.31	-9.89
WT-TACI_CRD1 vs BS7-10_CRD1 (35-67 a.a.)_BAFF				
56	His	Arg	-12.7	-13.69
60	Arg	His	9.4	8.82
56 60	His Arg	Arg His	-6	-7.8
WT-TACI_CRD2 vs BS7-10_(68-106 a.a.)_APRIL				
92	Ile	Val	1.95	6.25
WT-TACI_CRD2 vs BS7-10_(68-106 a.a.)_BAFF				
92	Ile	Val	2.33	7.05

3.2.10 Reformatting TACI-10 into Fc fusions

The clinical efficacy of a therapeutic is affected by many factors, including pharmacokinetics. One of the most important pharmacokinetic parameters is the half-life, the time required for the body to clear half the starting dose of a particular substance (Toutain & Bousquet-Melou, 2004). Proteins with a molecular weight lower than 60 kDa usually have a short half-life and rapid renal clearance (Deen et al., 2001). The molecular weight of many receptor ectodomains including TACI, is smaller than 60 kDa, suggesting a fast clearance. Therefore, frequent or large doses are required to achieve desired efficacy. As protein-based therapeutics, invasive routes like intravenous or subcutaneous administrations are required to maximise the body intake which limits the

frequency of dosing. To increase the therapeutic half-life, enlarging the protein-based biologics above the kidney cut-off is a feasible solution (Deen et al., 2001). Creating IgG Fc fusion protein is an ideal approach for increasing TACI molecular weight. IgG Fc has a molecular weight of around 20 kDa and is expressed as homodimers which could easily increase the decoy receptor size above 60 kDa.

Another advantage of creating an IgG Fc fusion protein is the facilitation of target clearance by immune cells. Antibody-dependent cellular phagocytosis (ADCP) is a process by which interactions between Fcγ receptors on macrophages and the IgG Fc domain of antibody-opsonised entity trigger phagocytosis (Kamen et al., 2019). There are four classes of IgG (IgG1, IgG2, IgG3, IgG4), each having different binding affinity to Fcγ receptors and thereby resulting in different levels of ADCP (Yu et al., 2020). If ordered from strong to weak, IgG1 shows the highest ADCP capacity followed by IgG3, IgG2, and IgG4 (Yu et al., 2020). Since I aim to neutralise serum APRIL and BAFF, a crystallisable IgG1 Fc domain was used as a fusion partner of the TACI ectodomain and its variants.

IgG1 Fc, WT-TACI-Fc, atacicept, BS7-10-Fc (2-165 a.a.) and BS7-10-Fc (68-110 a.a.) were produced and secreted by HEK293F cells through transient transfection of corresponding expression plasmids. Protein purification was carried out by protein A affinity chromatography followed by size exclusion chromatography. Analytical size exclusion chromatography was used to assess the protein purity (**Figure 3.8A**). Single sharp peaks indicate the collected proteins with high purity.

(A) (B)

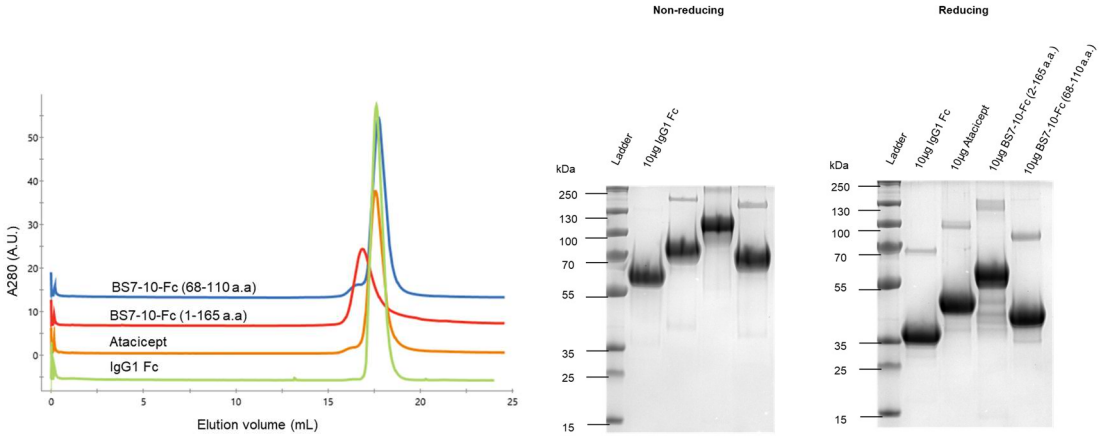


Figure 3.8. Analytical size exclusion chromatography (Superose 6 Increase 10/300 GL) and SDS-PAGE results of recombinant IgG1 Fc fusion proteins. (A) Analytical size exclusion chromatography (Superose 6 Increase 10/300 GL) results. **(B)** SDS-PAGE results. IgG1 Fc, atacicept, BS7-10-Fc (2-165 a.a.) and BS7-10-Fc (68-110 a.a.) were analysed. WT-TACI-Fc was not shown due to low yield.

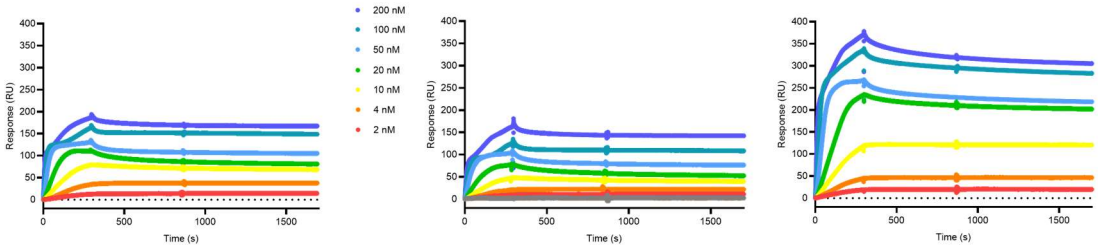
SDS-PAGE was conducted under non-reducing and reducing conditions to examine whether the protein homodimers were properly formed (**Figure 3.8B**). The yields for IgG1 Fc, WT-TACI-Fc, Atacicept, BS7-10-Fc (2-165 a.a.) and BS7-10-Fc (68-110 a.a.) were around 200 mg/L, 4 mg/L, 18 mg/L , 9 mg/L, 130 mg/L, respectively. All recombinant proteins were successfully produced with a high purity.

3.2.11 SPR analysis of APRIL and BAFF concentration-dependent binding of BS7-10, WT-TACI, Atacicept

The binding kinetics of WT-TACI-Fc, atacicept and BS7-10-Fc (2-165 a.a.) were investigated by surface plasmon resonance. The Kon and Koff were calculated for each binding curve in order to determine the KD. Given the caveat of significant variations across different binding curves, an estimated binding affinity range was proposed. The binding affinity range of APRIL to WT-TACI-Fc, atacicept and BS7-10-Fc (2-165 a.a.) was estimated to be 2.62 nM-203.58 nM, 45 nM-855.15 nM and 0.18 nM-58 nM, respectively. The binding affinity range of BAFF to WT-TACI-Fc, atacicept and BS7-10-Fc (2-165 a.a.) was estimated to be 40.84 nM-96.17 nM, 55.06 nM-121.78 nM and 29.73 nM-65.76 nM, respectively.

APRIL binding

(A) WT-TACI-Fc (B) Atacicept (C) BS7-10-Fc



BAFF binding

(D) WT-TACI-Fc (E) Atacicept (F) BS7-10-Fc

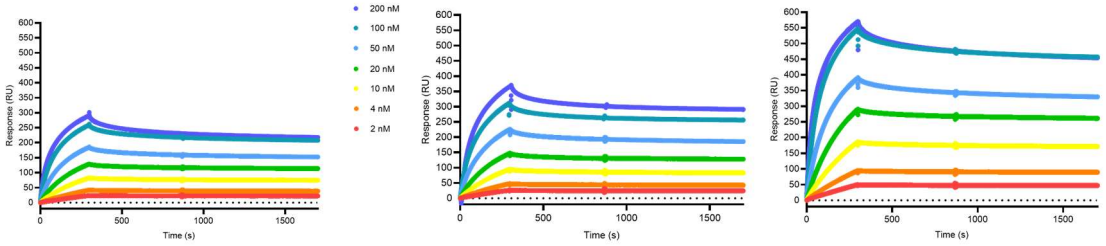


Figure 3.9. Biacore surface plasmon resonance (SPR) analysis of WT-TACI-Fc, atacicept and BS7-10-Fc. Sensogram plots produced indicate the real-time analysis of association and disassociation between CM5-chip immobilised BS7-10-Fc, WT-TACI-Fc and atacicept and analytes including APRIL **(A-C)** and BAFF **(D-E)**. All Fc fusion proteins were immobilised to a density of 500 RU by anti-human IgG1 Fc antibody on a CM5 chip. Different concentrations (2 nM – 200nM) of APRIL and BAFF were prepared in 10 mM HEPES, pH 7.4 and were injected separately for SPR analysis. BIAevaluation Software was used for data correction (double referencing).

Interestingly, the maximum response unit for all binding curves of BS7-10-Fc was two times higher than WT-TACI-Fc and atacicept for both APRIL and BAFF binding. This suggested that more ligands were captured by BS7-10-Fc when treated with the same concentrations of ligands. Overall, the binding affinity of BS7-10-Fc to APRIL and BAFF was similar to WT-TACI-Fc and atacicept, while BS7-10-Fc showed 2-fold increase in maximum binding capacity.

3.2.12 Effects of BS7-10 on Human Su-DHL-6 cell growth.

To investigate the effects of BS7-10-Fc on human Su-DHL-6 proliferation, I carried out CCK8 proliferation assays to measure the relative growth after the TACI decoy receptor treatment. MDA-MB-231, a breast cancer cell line was used as a negative control since it does not express TACI. Western blot results indicated a significantly higher expression level of TACI and BCMA in Su-DHL-6 compared to MDA-MB-231 (**Figure 3.10A**). A similar level of BAFF-R, APRIL and BAFF expression was detected in both cell lines.

(A)

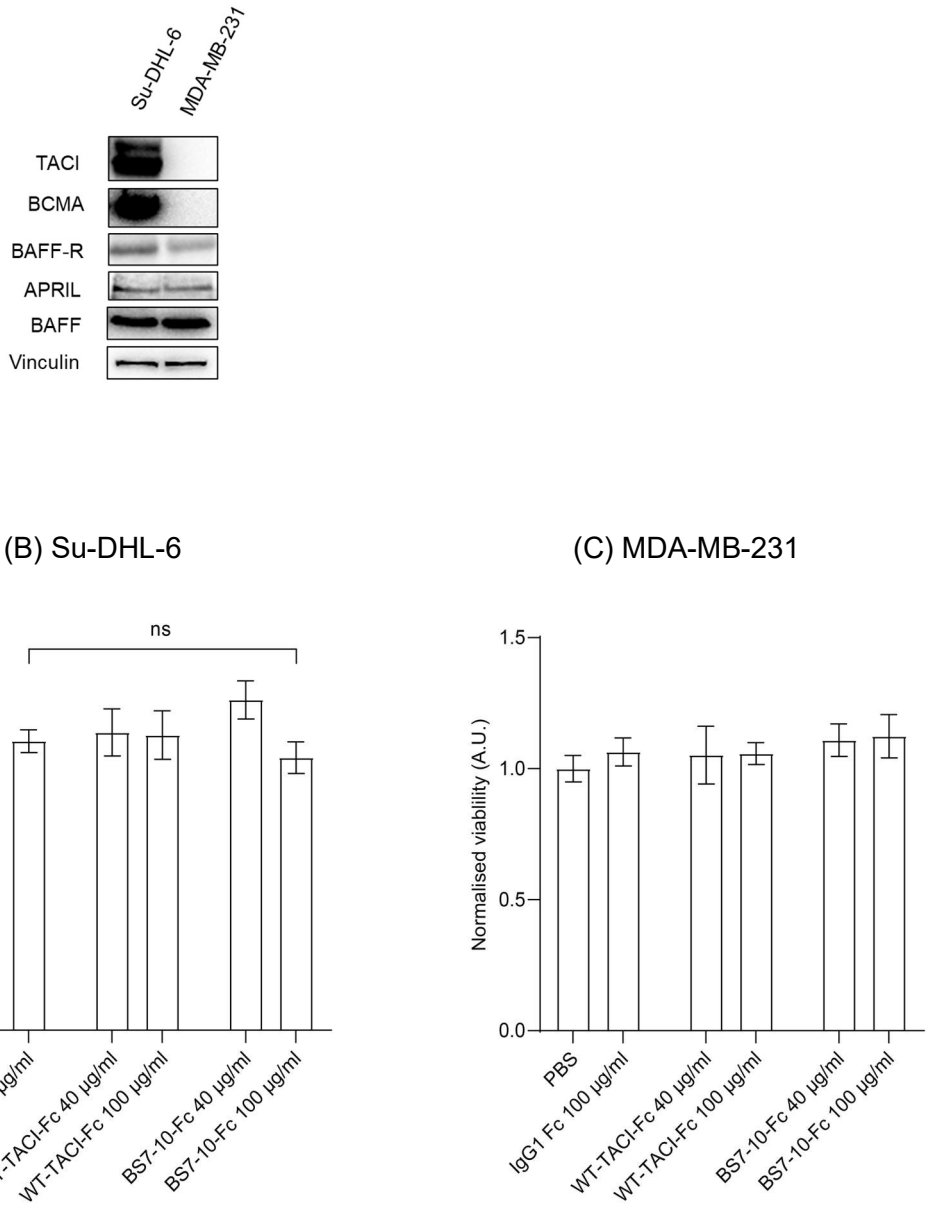


Figure 3.10. CCK-8 proliferation assay showing no inhibitory effects of BS7-10-Fc on MDA-MB-231 and Su-DHL-6 proliferation *in vitro*. One thousand cells of MDA-MB-231 or 10,000 cells of Su-DHL-6 were seeded in 96-well plates overnight followed by treatment with PBS, IgG1 Fc, WT-TACI-Fc or BS7-10-Fc. CCK8 proliferation assays were conducted at 72 hours post-treatment. **(A)** Western blot results showing TACI, BCMA, BAFF-R, APRIL and BAFF expression in Su-DHL-6 and MDA-MB-231. **(B)** Effects of WT-TACI-Fc and BS7-10-Fc on Su-DHL-6 proliferation (N=4). **(C)** Effects of WT-TACI-Fc and BS7-10-Fc on MDA-MB-231 proliferation (N=4). All data were normalised against PBS-treated samples. Error bars represent standard deviation of the mean. One-way ANOVA was performed to compare between treatment groups. Not statistically significant (ns).

WT-TACI-Fc and BS7-10-Fc were used to sequester APRIL and BAFF in SU-DHL-6 and

MDA-MB-231 cell culture. CCK8 proliferation assay demonstrated that 100 µg/ml of WT-

TACI-Fc and BS7-10-Fc failed to suppress SU-DHL-6 and MDA-MB-231 cell growth appreciably (**3.10B & C**). MDA-MB-231, as a negative control, could not repsond to the treatment. Unexpectedly, sequestration of APRIL and BAFF also had little impact on Su-DHL-6 growth in *in vitro* settings.

3.2.13 Mouse and Human B cell proliferation assay.

Another approach to test the efficacy of WT-TACI-Fc and BS7-10-Fc was by using B cell proliferation assays. Human BAFF is known to promote both human and mouse B cell proliferation in the presence of anti IgM-antibodies. In this study, 100 ng/ml of BAFF was able to promote both human and mouse B cell growth (**Figure 3.11A & B**).

(A) Mouse B cell proliferation

(B) Human B cell proliferation

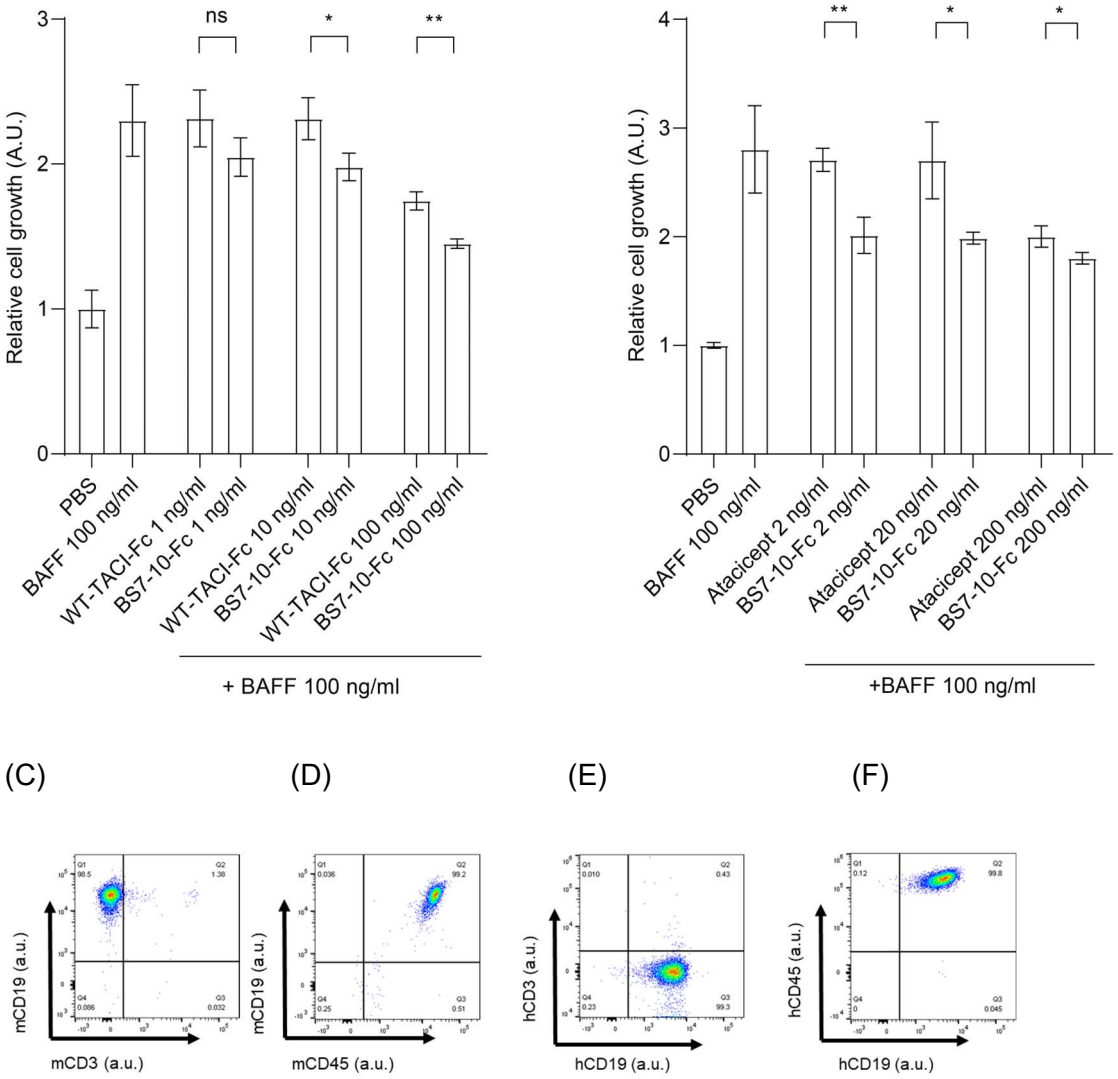


Figure 3.11. CCK-8 proliferation assay showing the inhibitory effects of BS7-10-Fc on mouse B cell and human B cell proliferation. (A) Effects of WT-TACI-Fc and BS7-10-Fc on mouse B cell proliferation (N=4). **(B)** Effects of WT-TACI-Fc and BS7-10-Fc on human B cell proliferation (N=4). Representative flow cytometry plots indicate the purity of mouse B cells **(C & D)** and human B cells **(E & F)** used in the experiments. The B cells were grown in RPMI supplemented with anti-human or anti-mouse IgM antibodies and 10% FBS. Mouse B cell medium requires an additional 0.1% 2-Mercaptoethanol for cell survival. All data were normalised against PBS-treated samples. Error bars represent standard deviation of the mean. One-way ANOVA was performed to compare between treatment groups. *P<0.05, **P<0.01 or not statistically significant (ns).

For mouse B cell proliferation assay, BS7-10-Fc treatment showed a more significant B cell growth inhibition than WT-TACI-Fc (**Figure 3.11A**). Likewise, for the human B cell proliferation assay, BS7-10-Fc showed a more substantial growth inhibition on B cells

than atacicept (**Figure 3.11B**). Accordingly, BS7-10 was able to sequester both mouse and human BAFF and demonstrated greater efficacy than WT-TACI-Fc and atacicept.

3.2.14 Evaluating the therapeutic potential of BS7-10 in DLBCL lymphoma mouse models.

To gain an insight into the pharmacokinetic properties of BS7-10-Fc in mice, I measured the murine serum BS7-10-Fc level after a single dose intraperitoneal injection of 5 mg/kg BS7-10-Fc conjugated with a fluorochrome Alexa 488. The blood was drawn at 3, 24 ,48 and 72 hours post-injection. Serum BS7-10-Fc level was quantified by using a plate reader. The majority BS7-10-Fc was cleared from serum 48 hours after the injection (**Figure 3.12A**). The half-life of BS7-10 was estimated to be around 24 hours. Accordingly, the drug injection was suggested to be performed every 48 hours.

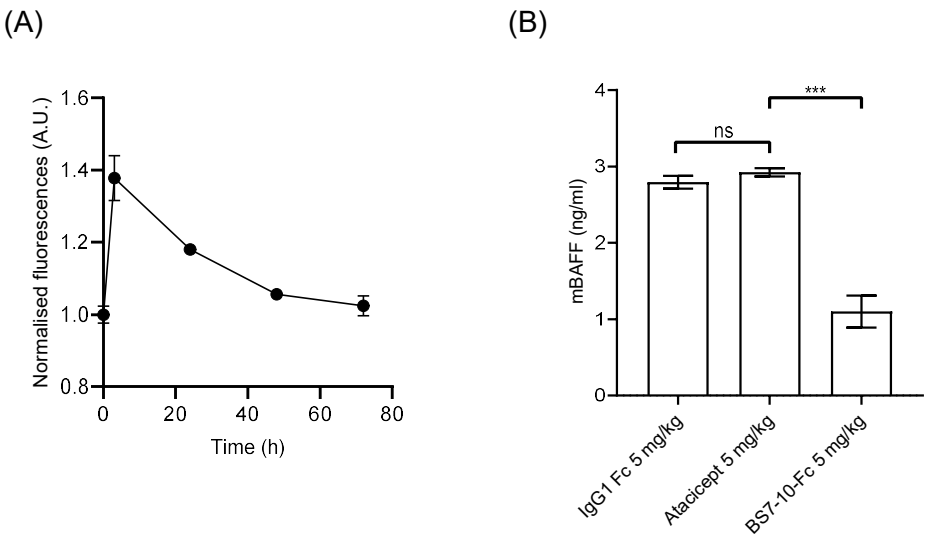


Figure 3.12. Pharmacokinetic study of BS7-10-Fc in NSG mice. **(A)** Serum clearance kinetics of BS7-10-Fc labelled with Alexa Fluor® 488 in NSG mice (N=2). The serum fluorescence was measured using a plate reader at 3 h, 24 ,48 and 72 hours after intraperitoneal injection of 5 mg/kg of BS7-10-Fc Alexa Fluor® 488. **(B)** Serum level of murine BAFF 24 hours after a single-dose injection of 5 mg/ml of IgG1 Fc, WT-TACI-Fc and BS7-10-Fc (N=3). Error bars represent standard deviation of the mean. One-way ANOVA was performed to compare between treatment groups. *P<0.05, ***P<0.001 or not statistically significant (ns).

To initially assess the *in vivo* efficacy of BS7-10-Fc, I measured mouse serum BAFF level 24 hours after a single dose injection of 5 mg/kg of IgG1 Fc, atacicept and BS7-10-Fc (**Figure 3.12B**). A similar serum level of BAFF was detected in IgG1 Fc- and atacicept-treated mice. However, BS7-10-Fc-treated mice had a much lower serum BAFF level than IgG1 Fc- and atacicept-treated mice. Overall, 5 mg/kg of BS7-10-Fc was able to maintain mouse serum BAFF at a relatively low level 24 hours post-injection.

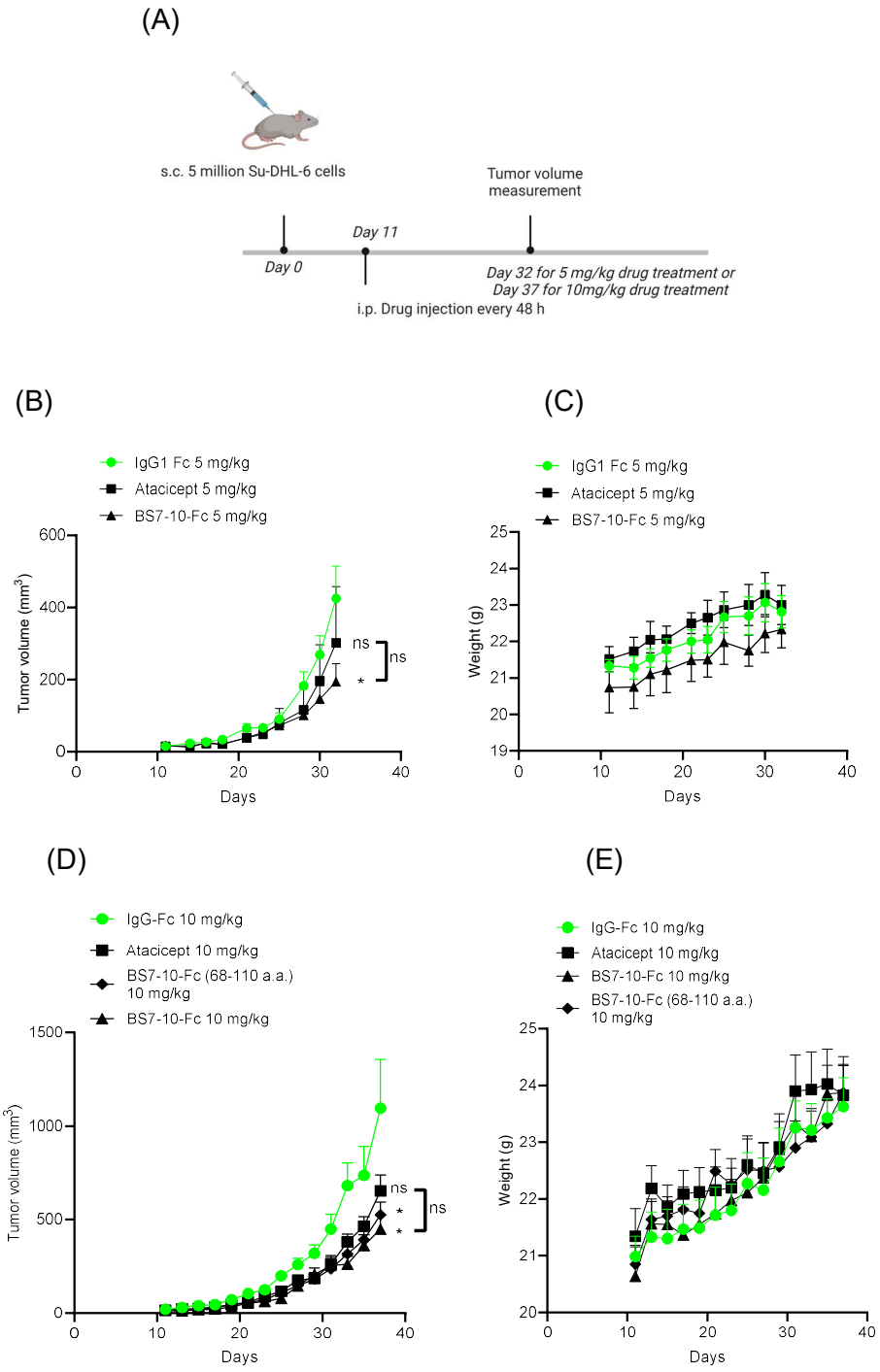


Figure 3.13. Evaluating the anti-tumour activity of WT-TACI-Fc, BS7-10-Fc (68-110 a.a.) and BS7-10-Fc in Su-DHL-6 bearing NSG mice. (A) Diagrammatic representation of the mouse experiment procedures. Five million of Su-DHL-6 cells were injected subcutaneously into the right flank of NSG mice. The Su-DHL-6 bearing NSG mice were treated with 5 mg/kg (**B**, N=6) or 10 mg/kg (**D**, N≥8) of IgG1 Fc, WT-TACI-Fc, BS7-10-Fc or BS7-10-Fc (68-110 a.a.) every 48 hours from day 11 and ending at the humane endpoint. Subcutaneous tumour volume change **(B & D)** and mouse body weight change **(C-E)** were recorded every 48 hours. Error bars represent standard error of the mean. One-way ANOVA was performed to compare tumour size after the last drug injection between treatment groups. *P<0.05 or not statistically significant (ns).

The *in vivo* anti-tumour efficacy of BS7-10-Fc was evaluated in Su-DHL-6-bearing NSG mice. Su-DHL-6 was subcutaneously implanted into the right flank of NSG mice. The treatment started on day 11 after the tumour induction when tumour size reached 50 mm^3. Two separate experiments with different drug dosages were performed. For the low-dose group (5 mg/kg), BS7-10-Fc showed significant inhibition on tumour growth, while no differences in tumour volume between atacicept-treated and IgG1 Fc-treated groups were detected (**Figure 3.13B**). A similar pattern was observed for the high-dose group (10 mg/kg) (**Figure 3.13D**). In addition, 10 mg/kg of BS7-10-Fc (68-110 a.a.)-treated group demonstrated a significantly lower tumour volume than the control group. Overall, there were no statistically significant differences between BS7-10-Fc-treated and atacicept-treated groups, suggesting that BS7-10-Fc could not demonstrate a clinical superiority over atacicept in the Su-DHL-6 animal model.

3.3 Discussion

Given that APRIL and BAFF are potential therapeutic targets for DLBCL, I engineered a high affinity TACI decoy receptor variant , namely BS7-10 which has eight times higher binding affinity to both APRIL and BAFF than commercially available WT-TACI decoy receptor, atacicept. BS7-10 harvests ten mutations. I92V was the only mutation identified in the known ligand binding pocket. Reverse mutagenesis results indicated that I92V contributes most to the high affinity binding to APRIL and BAFF. However, computational structural simulation suggested that I92V has no major contribution to the enhanced ligand binding. Instead, H56R and R60H could enhance ligand binding affinity by increasing surface complementarity and stability of the ligand-receptor complexes.

The inconsistency between the structural simulation results and the experimental data on the reverse mutants raised a question of whether I92V contributed to the enhanced ligand binding affinity. Based on the crystal structure of mouse APRIL bound to human TACI, amino acid residue I92 along with several hydrophobic side chains in human TACI

forms a hydrophobic binding cavity in TACI which interacts with 166F in mouse APRIL (**Figure 3.14A & B**). A study has demonstrated that TACI residues F78, D80, L82 and P97 are essential for APRIL binding, and D80, L82, R84 and I87 are important for BAFF binding (Bossen & Schneider, 2006). I92 was not on the list suggesting a non-critical role of I92 in APRIL or BAFF binding. Also, a shotgun alanine scanning mutagenesis indicated that I92A mutation did not have a detrimental effect on ligand binding which similarly suggested a low involvement of I92 in ligand binding (**Figure 3.15**) (Hymowitz et al., 2005). This coincides with computational structural modelling results where I92V did not improve surface complementarity or stability of ligand-receptor complexes. Conversely, reverse mutagenesis results demonstrated a relatively more important role of I92V in enhanced ligand binding compared to other mutations. It is plausible that I92V mutation might indirectly improve ligand binding by modifying the binding interface. Here, I propose a potential mechanism of I92V in promoting ligand-receptor interactions. In brief, conversion of I92 into V92 resulted in a loss of a methyl group which could potentially enlarge the hydrophobic cavity and allow APRIL residue 166F to be further embedded into the hydrophobic cavity, thereby enhancing the binding affinity (**Figure 3.14A & B**).

(A)

```
Page 1 APRIL [Mus musculus]

                    1                                                   50
APRIL [Homo sapiens] MPASSPFLLAPKGPPGNMGGPVREPALSVALWLSWGAALGAVACAMALLT
APRIL [Mus musculus] ---------MPASSPGHMGGSVREPALSVALWLSWGAVLGAVTCAVALLI

.....................................................................................

                    51                                                  100
APRIL [Homo sapiens] QQTELQSLRREVSRLQGTGGPSQNGEGYPWQSLPEQSSDALEAWENGERS
APRIL [Mus musculus] QQTELQSLRREVSRLQRSGGPSQKQGERPWQSLWEQSPDVLEAWKDGAKS

.....................................................................................

                    101                                                 150
APRIL [Homo sapiens] RKRRAVLTQKQKKQHSVLHLVPINATSKDDSDVTEVMWQPALRRGRGLQA
APRIL [Mus musculus] RRRRAVLTQKHKKKHSVLHLVPVNITSK-DSDVTEVMWQPVLRRGRGLEA

.....................................................................................

                    151                                                 200
APRIL [Homo sapiens] QGYGVRIQDAGVYLLYSQVLFQDVTFTMGQVVSREGQGRQETLFRCIRSM
APRIL [Mus musculus] QGDIVRVWDIGIYLLYSQVLFHDVTFTMGQVVSREGQGRRETLFRCIRSM

.....................................................................................

                    201                                                 250
APRIL [Homo sapiens] PSHPDRAYNSCYSAGVFHLHQGDILSVIIPRARAKLNLSPHGTFLGFVKL
APRIL [Mus musculus] PSDPDRAYNSCYSAGVFHLHQGDITTVKIPRANAKLSLSPHGTFLGFVKL

.....................................................................................
```

(B)

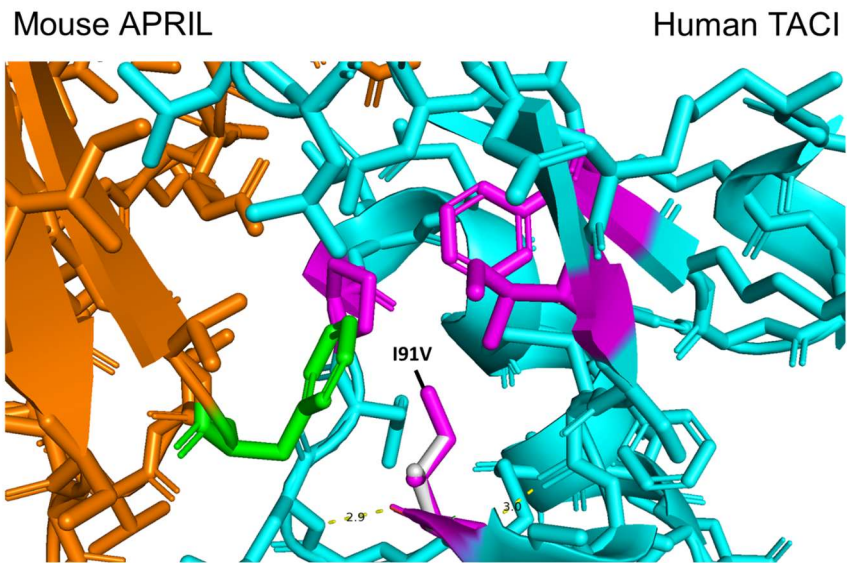


Figure 3.14. Mutation I92V in BS7-10 could potentially enhance mouse APRIL binding by promoting hydrophobic interactions. (A) Amino acid sequence alignment of human APRIL with Mouse APRIL. Human APRIL and mouse APRIL share 78% sequence similarity. **(B)** The crystal structure of mouse APRIL bound to human TACI (PDB 1X1U). Mouse APRIL is highlighted in orange. Human TACI is highlighted in cyan. The mouse APRIL Phe residue (green) interacts with a hydrophobic cavity (purple) in human TACI. The I92V mutation in BS7-10 results in a loss of methyl group which could increase the accessibility of Phe to the hydrophobic cavity, thereby increasing the binding affinity.

Ligand-receptor interactions rely on three major factors including surface complementarity, thermodynamics and related physiochemical characteristics (Nolan et

al., 2009). Surface complementarity is centrally involved in ligand binding which encompasses hydrogen bonding, ionic, Van der Waals, CH- π, Cation- π and covalent interactions (Nolan et al., 2009). Among them, non-covalent forces are primarily responsible for binding reactions. Given their weak nature, multiple non-covalent interactions are usually required for the formation of stable ligand-receptor complex. Thermodynamic characteristics plays a direct role in ligand-receptor interaction which are comprised of binding free energy (ΔG), binding enthalpy (ΔH) and binding entropy (ΔS) (Nolan et al., 2009). Binding free energy describes the difference in stability between unbound receptor-ligand and receptor-ligand complex (Hata et al., 2021). Binding enthalpy (ΔH) represents the energy changes in a ligand-receptor binding process where various non-covalent interactions are disrupted and subsequently formed (Nolan et al., 2009). Binding entropy (ΔS) describes the energy change in conformational freedom and solvation during ligand-receptor binding (Singh & Warshel, 2010). Physiochemical characteristics of ligands and receptors could also have an impact on complex formation, such as Stericity, electrostatics, and lipophilicity (Nolan et al., 2009).

Computational method was used to investigate the impact of three out of ten mutations (H56R, R60H and I92V) in BS7-10 on surface complementarity and thermodynamics of ligand-receptor complexes. Compared to the binding of WT-TACI to APRIL and BAFF, improvement in surface complementarity and thermodynamics was detected in both BS7-10-APRIL and BS7-10-BAFF complexes where H56R and R60H are the major contributors. As residues located outside of the known binding interface, H56 and R60 have not been shown to interact with either APRIL or BAFF (Hymowitz et al., 2005). This highlights the advantage of yeast surface display technology that allows the mutant library to be screened in a non-biased manner. Certain mutations could create previously non-existed interactions that enhance the overall ligand-receptor binding affinity.

Other than I92V, H56R and R60H mutations, the rest of the mutations are primarily scattered around CRD1. A previous study indicated that TACI CRD1 is at least 100 times weaker than CRD2 in terms of APRIL and BAFF binding affinity (Hymowitz et al., 2005). Given the CRD1 structure remains unsolved, structural analysis of that region cannot be conducted. However, according to SPR analysis, BS7-10-Fc always binds twice amounts of APRIL or BAFF than WT-TACI-Fc and atacicept at a given ligand concentration (**Figure 3.9**). This suggests a two-binding-site model where CRD1 in BS7-10 is a highly functional binding site unlike the CRD1 in WT-TACI that exhibits extremely weak ligand binding affinity. The two-binding-site model can also be supported by the fact that BS7-10 CRD1 had higher ligand binding signals than WT- TACI CRD1 (**Figure 3.7C**). Another supportive evidence is that the maxmimum binding capacity of BS7-10 to both APRIL and BAFF was eight times higher than atacicept (**Figure 3.7B**).

Both WT-TACI-Fc and BS7-10-Fc treatment failed to suppress Su-DHL-6 proliferation even though they express BCMA, TACI, BAFF-R, APRIL and BAFF (**Figure 3.10**). This is consistent with a previous study where the sBCMA mutant alone has little impact on *in vitro* Su-DHL-6 cell growth (Miao et al., 2022). This may lie on the fact that cell media contains factors that can compensate for the loss of BAFF and APRIL, thereby sustaining cell growth. It was shown that persistent BAFF treatment for a long period of time is required to sensitise Su-DHL-6 before the proliferation assay (Miao et al., 2022). However, an attempt to sensitise Su-DHL-6 with excessive BAFF for three months did not result in sensitisation (data not shown). Fortunately, there was another approach to test *in vitro* efficacy of BS7-10-Fc, namely the B cell proliferation assay. BAFF is known to be important for B cell survival and costimulates B cell proliferation with IgM-antigen complexes (Abu-Rish et al., 2013). Both human and mouse primary B cell proliferation assays pointed out that BS7-10-Fc is better at sequestering BAFF than WT-TACI-Fc and

atacicept (**Figure 3.11**). This finding coincides with BS7-10 having an enhanced binding affinity to BAFF and possessing two functional binding sites.

In terms of the animal experiments, BS7-10-Fc and BS7-10-Fc (68 -110 a.a.) demonstrated significant tumour suppression in Su-DHL-6-bearing mice (**Figure 3.13**). However, both did not show superior anti-tumour efficacy compared to atacicept. The inconsistency between the *in vitro* and *in vivo* data could attribute to multiple factors. The serum BAFF level in mice 24 hours after BS7-10-Fc treatment was around 1 ng/ml which was lower than the atacicept-treated group but could still be sufficient to promote Su-DHL-6 cell growth (**Figure 3.12**). Also, a shorter *in vivo* half-life could have a major impact on drug efficacy. Although a single time point serum BAFF measurement demonstrated the superiority of BS7-10-Fc over atacicept, the duration of BS7-10-Fc's inhibitory effect may not be long-lasting. Therefore, multiple time point measurements of serum APRIL and BAFF levels in mice after the drug treatment would be recommended for future study.

BS7-10-Fc (68 -110 a.a.) as the CRD2-binding-site-only decoy receptor demonstrated tremendous potential to become a better clinical therapeutic than atacicept. Although BS7-10-Fc (68 -110 a.a.) has a lower binding affinity to APRIL and BAFF than full-length BS7-10, atacicept does not outcompete BS7-10-Fc (68 -110 a.a.) where BS7-10-Fc (68 -110 a.a.) still has a similar BAFF binding affinity and a 3-fold higher APRIL binding. Among all TACI variants created, the binding potential of BS7-10-Fc (68 -110 a.a.) is only second to full-length BS7-10. Furthermore, more repeats included in the mouse study might be able to demonstrate that BS7-10-Fc (68 -110 a.a.) has a significantly higher efficacy than atacicept. Additionally, the yield of BS7-10-Fc (68 -110 a.a.) is around eight times higher than atacicept and 14 times higher than full-length BS7-10. This could reduce the production cost significantly and benefit more patients.

Overall, BS7-10-Fc is more effective in sequestering BAFF compared to atacicept. The difficulty of achieveing better clinical efficacy may lie on the fact that WT-TACI has an excellent binding affinity to APRIL and BAFF where disassociation rarely occurs after ligand binding. Direct evolution is able to enhance ligand-receptor binding affinity from micromolar to picomolar range, a 10^6-fold enhancement, but unlikely to obtain a similar magnitude enhancement for a wild-type receptor that has a picomolar binding affinity to its ligands (Miao et al., 2021). The strength of protein-protein interaction has its upper limit, which cannot easily be surpassed.

Chapter 4. Engineering and characterising high affinity variants of the RAGE receptor.

4.1 From TACI to RAGE

The development of BS7-10-Fc served as a solid foundation for engineering other receptor ectodomains. APRIL-directed and BAFF-directed screening eventually led to the discovery of the same variant BS7-10. This suggests that the affinity maturation process directed towards a single ligand could provide variants with enhanced binding affinity to multiple ligands. This concept could be applied to other receptors, particularly muti-ligand receptors such as RAGE. Improving the binding affinity of RAGE to one of its ligands may also lead to enhanced binding affinity to multiple RAGE ligands.

4.2 Introduction

RAGE ligands have been implicated in promoting TNBC growth and metastasis as well as playing a role in chronic inflammation. Targeting RAGE ligands with RAGE decoy receptors is an attractive strategy for suppressing not only RAGE receptor signalling pathways but also other receptor signalling pathways cross-activated by RAGE ligands in both tumour and stroma cells. The RAGE V domain, an immunoglobulin-like domain, is responsible for binding to most RAGE ligands, making it an ideal target for engineering. Given that wild-type RAGE has a generally low binding affinity to its ligands, I aimed to engineer a high affinity RAGE V decoy receptor using yeast surface display. Unlike the screening process for TACI variants, it is not practical to carry out dozens of screenings in parallel with all RAGE ligands. The screening process needs to be focused and simplified. In this case, a single ligand was carefully selected and used as a selective pressure.

RAGE V domain is known to interact with a range of molecules such as AGE, HMGB1, S100 proteins, and C3a. There were several factors to consider when selecting a RAGE ligand for screening high affinity variants. First, the ligand needs to be easily produced and purified in large quantities, considering that the screening process requires at least 20 mM of ligand. Second, there needs to be an available antibody against the ligand,

which is a prerequisite for performing yeast surface display. Third, the anti-ligand antibody cannot block the ligand binding site or interact non-specifically with yeast cell surface components to generate false negative or false positive signals. Fourth, the ligand needs to play a role in promoting cancer growth or metastasis. Taking these factors into consideration, C3a was thought to be the best candidate to direct RAGE affinity maturation. The C-terminal end of C3a was shown to be responsible for C3aR binding (Gao et al., 2020). A previous study indicated that RAGE has a higher binding affinity to C3a than C3a-desArg, suggesting that C3a C-terminus could be important for RAGE binding (Ruan et al., 2010). Moreover, an anti-C3a antibody that targets C3a N-terminus is commercially available. In addition, C3a-C3aR axis has been shown to promote breast cancer lung metastasis by regulating cancer-associated fibroblasts (Shu et al., 2020). Therefore, C3a was used as a selective pressure for high affinity RAGE V screening processes. In this chapter, C3a-directed screening revealed the most enriched variant RAGE V13 which showed similar binding affinity but a higher maximum binding capacity to multiple RAGE ligands compared to WT-RAGE V. Alphafold2-predicted WT-RAGE V-Fc structure was more distorted than RAGE V13-Fc, suggesting that mutations in RAGE V13 might contribute to structural stability. Overall, RAGE V13-Fc was shown to be superior than WT-RAGE V-Fc in terms of ligand binding.

4.3 Results

4.3.1 Interaction between yeast-displayed RAGE V and C3a

Similar to the TACI ectodomain, the RAGE V domain was fused with Aga2p and displayed on the yeast cell surface. The principle of yeast surface display has previously been mentioned in section 3.2.1. I first determined the binding affinity of yeast-displayed RAGE V to C3a. The yeast cells were treated with different concentrations of C3a followed by staining with anti-myc and anti-C3a antibodies. Flow cytometry was used to quantify the binding signals.

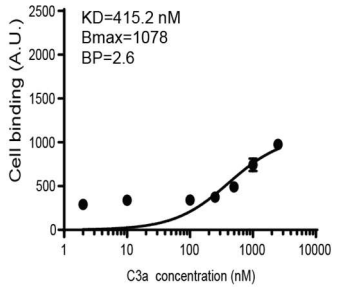


Figure 4.1. Interaction between yeast-displayed WT-RAGE V and C3a. Yeast-displayed WT-RAGE V was treated with different concentrations of C3a overnight. Antibodies conjugated with different fluorochromes were used to quantify the binding signals and protein expression level. Four-parameter sigmoidal curves were determined by binding titrations (N=2). Error bars represent standard deviation of the mean. KD: binding affinity. B_{max}: maximum binding capacity. BP: Binding potential (BP= B_{max} /KD).

A dose-dependent increase in C3a binding to RAGE was observed in binding assays (**Figure. 4.1**). Based on the binding curve, the binding affinity and maximum binding capacity of yeast-displayed RAGE V to C3a were determined to be around 415.2 nM and 1078 nM, respectively (**Figure. 4.1**). This suggests that yeast-displayed RAGE V could directly interact with C3a. Accordingly, directed evolution of RAGE V domain could then be performed by using yeast surface display.

4.3.2 Mutant library generation (Yeast-displayed RAGE V)

Similar to TACI mutant library generation (Section 3.2.3), RAGE V mutant sequences were created through error-prone PCR with an average mutation rate of 10%. A yeast library was then generated by co-transformation of the amplified mutant RAGE V sequences and cut pctCon2 plasmid into competent EBY100 yeast cells where plasmid assembly is mediated by homologous recombination. The yeast library size was estimated to be around $1.4x10^8$ transformants. Unlike the TACI library, the majority of RAGE V mutants lost the ability to interact C3a with only 1% of the population showing detectable binding signals (**Figure 4.2**). Taken together, the unsorted library included at least 1 million mutants able to interact with C3a.

4.3.3 Sort progression (C3a-directed sorting)

The yeast-displayed RAGE V mutant library was sorted by using recombinant C3a as a selective pressure. Five rounds of equilibrium binding sorts were carried out. The high affinity variants were enriched by increasing the selective stringency progressively such as by reducing C3a concentration gradually and the ligand incubation time (**Figure 4.2**). RAGE V domain variants that non-specifically bind to the anti-C3a antibody were detected after C3a sort round 2 (CS2) which caused a strong false-positive signal (data not shown). To remove the clones that generate false-positive signals, another set of reagents, including recombinant C3a-HIS-GST and anti-His antibody conjugated with a fluorochrome were used for CS3-5. Overall, after using the new set of ligands and antibodies, a true C3a-binding population emerged over the sort progression suggesting a successful enrichment of high affinity C3a binders.

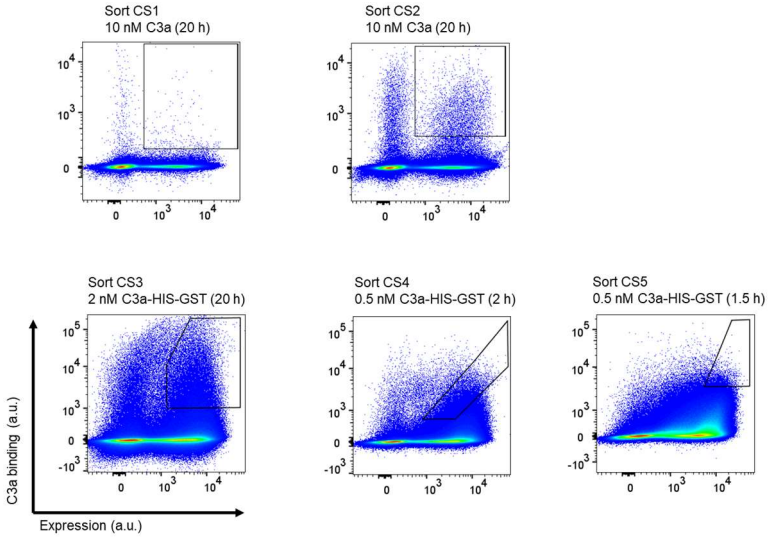


Figure 4.2. Flow cytometry dot plots representing the sorting strategies used for screening high affinity C3a binders from yeast-displayed RAGE V mutant library. Flow cytometry dot plots (1 x 10^5 dots shown in each plot) represent the sorting strategies used for screening high affinity C3a binders. Five rounds of equilibrium binding sorts were performed. The yeast mutant libraries were incubated with different concentrations of C3a for 1.5-20 h. The gated populations were collected and amplified in yeast culture either for the following round of sorting or the RAGE V variant sequence analysis. For CS1-2, recombinant C3a without tags was used. To avoid a false positive signal caused by direct interaction between the C3a antibody and certain RAGE V mutants, recombinant C3a-HIS-GST and anti-His antibody were used for CS3-5 to enrich high affinity C3a binders.

4.3.4 Sequence analysis of RAGE V variants identified in the CS5 library

To identify RAGE V varaint sequences enriched in the CS5 library, twenty clones were isolated and sequenced. According to the sequencing results, 75% of the population share an identical amino acid sequence which contained six mutations, including T5A, K22R, K30R, E37K, Q78R and K85E (**Table 4.1**). Five out of the six mutations (i.e. except for K85E) were also found in 25% of the population. This suggests that the K85E mutation could be relatively less involved in ligand binding.

Table 4.1. Sequencing results of 20 clones from the CS5 library. The first row shows the amino acid positions. The second row indicates the WT-RAGE V amino acid sequence. High-frequency mutations are highlighted in orange.

Amino acid		2	3	5	8	10	12	14	16	21	22	25	26	28	30	32	33	37	39	40	42	46	47	51	59	78	81	83	85
wt-RAGE-V		Q	N	T	I	E	L	L	C	K	K	Q	R	E	K	N	T	E	W	K	L	G	G	D	N	Q	N	N	K
Clone #	S5.1-1			A							R				R			K								R			E
Clone #	S5.1-2			A							R				R			K								R			E
Clone #	S5.1-3	R		A		G		P	R	R				K		S				E	P		G						
Clone #	S5.1-4			A							R				R			K								R			E
Clone #	S5.1-5			A							R				R			K								R			E
Clone #	S5.1-6			A							R				R			K								R			E
Clone #	S5.1-7		S		V	A	P	P	R		R			G	R		A		R			R		G	S				
Clone #	S5.1-8			A							R				R			K								R			E
Clone #	S5.1-9			A							R				R			K								R			E
Clone #	S5.1-10			A							R				R			K								R			E
Clone #	S5.1-11			A							R				R			K								R			E
Clone #	S5.1-12			A							R				R			K								R			E
Clone #	S5.1-13			I	V					R	R	R						K										D	
Clone #	S5.1-14			A							R				R			K								R			E
Clone #	S5.1-15			A							R				R			K								R			E
Clone #	S5.1-16			A							R				R			K								R			E
Clone #	S5.1-17			A							R				R			K								R			E
Clone #	S5.1-18									R			Q													R	S		
Clone #	S5.1-19			A							R				R			K								R			E
Clone #	S5.1-20			A							R				R			K								R			E

Given that glycosylation is an essential characteristic of protein folding, transport, localisation and activity, losing wild-type glycosylation pattern could result in the exposure of neo-antigen, which is undesirable for receptor-based drugs when used in clinical settings (Pon et al., 2020). Maintaining a wild-type glycosylation pattern in the RAGE receptor is therefore optimal. The mutation T5A disrupted a glycosylation site (N-X-S/T) in the RAGE V domain, resulting in de-glycosylation (Osawa et al., 2007). Overall, K85E and T5A mutations were considered to be undesired mutations and therefore removed from the mutant sequence to form the artificial mutant RAGE V13 (**Figure 4.3A**). According to the RAGE crystal structure, all remaining mutated residues were surface-exposed and could potentially interact with C3a (**Figure 4.3B & C**). Additionally, the isoelectric points (pI) were much higher in RAGE V13 (pI = 11.2) compared to WT-RAGE V (pI = 10.1) (Prot pi | Protein Tool).

(A)

Amino acid	5	22	30	37	78	85
WT-RAGE-V	T	K	K	E	Q	K
CS5-75% of clones	A	R	R	K	R	E
RAGE V13		R	R	K	R	

(B) WT-RAGE V (pI=10.099) (C) RAGE V13 (pI=11.173)

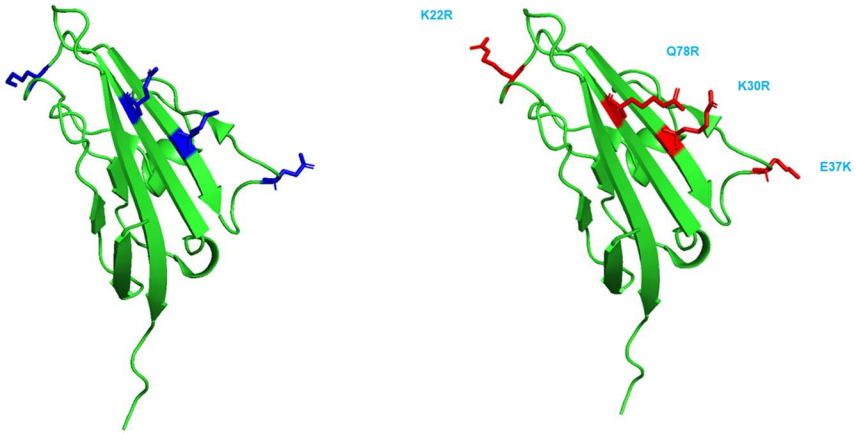


Figure 4.3. Sequence and structural characteristics of RAGE V13, an artificial mutant designed based on CS5 library sequencing results. (A) Amino acid mutations enriched in the CS5 library. Blank denotes WT-RAGE V sequences. T5A and K85E identified in the CS5 library were not included in RAGE V13. The mutation T5A could result in undesired de-glycosylation at 3N. K85E is the least frequent mutation compared to the other five high-frequency mutations found in the CS5 library. **(B)** Crystal structure of WT-RAGE V (PDB: 4LP4). Mutation positions in the RAGE V13 are highlighted in blue. **(C)** Putative structure of RAGE V13 was created by replacing the amino acid residues in WT-RAGE V (PDB: 4LP4) with mutations in RAGE V13. The mutated residues are highlighted in red. pI: isoelectric point.

To determine the binding affinity of WT-RAGE V and RAGE V13 to different RAGE ligands, multiple binding assays were carried out. Yeasts that displayed WT-RAGE V and RAGE V13 were treated with different concentrations of C3a, C3a desArg, S100A4 or HMGB1 overnight to reach binding equilibrium. Flow cytometry was used to quantify the binding signal after antibody staining. Yeast-displayed RAGE V13 had around 3-fold lower binding affinity and 3-fold higher maximum binding capacity to C3a compared to yeast-displayed WT-RAGE (**Figure 4.4A & B**). Both WT-RAGE V and RAGE V13 had weak binding affinity to C3a desArg where KD and B_{max} could not be accurately

determined. Similar to C3a binding, yeast-displayed RAGE V13 had a lower binding affinity but a higher B_{max} to S100A4 and HMGB1 compared to yeast-displayed WT-RAGE V. Overall, yeast-displayed RAGE V13 had a higher maximum binding capacity and a lower binding affinity to multiple RAGE ligands.

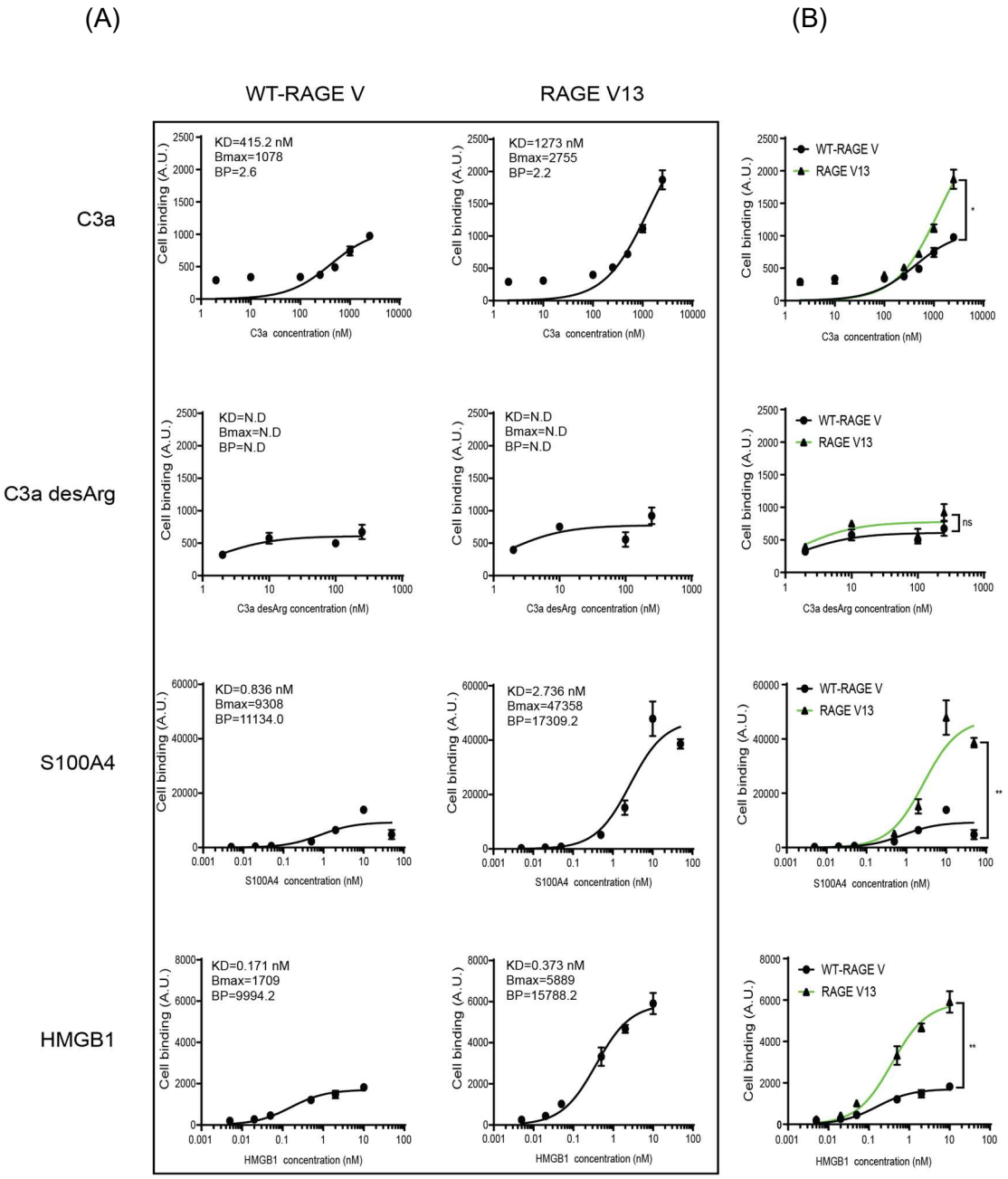
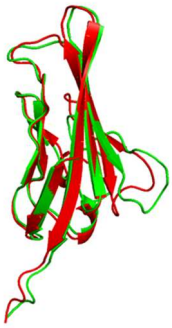


Figure 4.4. Four-parameter sigmoidal curves showing the interaction between several RAGE ligands and yeast-displayed WT-RAGE V and RAGE V13. The yeast cells that displayed WT-RAGE V or RAGE V13 were incubated with different concentrations of C3a, C3a desArg, S100A4 or HMGB1 before antibody staining. The binding signal was quantified by using flow cytometry. **(A)** Binding of yeast-displayed WT-RAGE V and RAGE V13 to the four RAGE ligands (N=2). Calculated KD, B_{max} and BP are indicated on each plot. A.U., arbitrary units. **(B)** Summary of the binding assays. Four-parameter sigmoidal curves were determined by binding titrations. Error bars represent standard deviation of the mean. Error bars represent standard deviation of the mean. A two-tailed t-test t-test was performed to compare between treatment groups. *P<0.05, **P<0.01 or not statistically significant (ns).

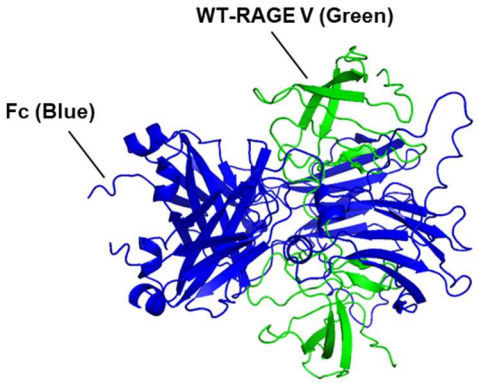
4.3.5 Reformatting WT-RAGE V and RAGE V13 into Fc fusions

Extracellular RAGE structure had previously been determined using X-ray crystallography at a resolution of 3.80 Å. Alpha-fold 2 was used to predict the structure of RAGE V13, WT-RAGE V-Fc and RAGE V13-Fc. The most confident predicted structures are shown in **Figure 4.5**. The predicted RAGE V13 structure was similar to WT-RAGE V, suggesting that mutations did not cause dramatic structural disruptions (**Figure 4.5A**). In terms of Fc fusion proteins, IgG1 Fc as a fusion domain had almost no impact on RAGE V13 structural integrity (**Figure 4.5C**). Unlike RAGE V13-Fc, the WT-RAGE V-Fc showed apparent structural alterations in the WT-RAGE V domain, possibly caused by intramolecular interaction between the WT-RAGE V and the IgG1 Fc domain (**Figure 4.5B**). This suggests that RAGE V13 could be structurally more stable than WT-RAGE V.

(A) WT-RAGE V (Green; 4lp5) vs RAGE V13 (Red; AF2)



(B) WT-RAGE V-Fc dimer



(C) RAGE V13-Fc dimer

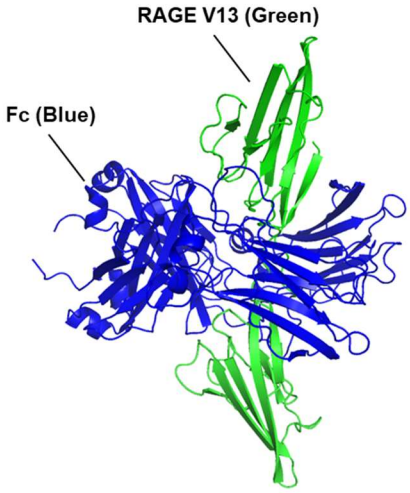


Figure 4.5. Alpha-fold 2 predicted ribbon structures of RAGE V13, WT-RAGE V-Fc and RAGE V13-Fc. (A) Predicted RAGE V13 structure (red) compared with WT-RAGE V crystal structure (PDB: 4LP4, green). **(B)** WT-RAGE V-Fc and **(C)** RAGE V13-Fc were predicted as dimer formats. The predicted structures shown here are the most confident models.

IgG1 Fc, WT-RAGE V-Fc and RAGE V13-Fc were recombinantly produced in HEK293F. Protein A chromatography was performed to isolate recombinant proteins from conditioned media which was followed by size exclusion chromatography to further purify recombinant proteins. Analytical size exclusion chromatography was conducted to assess the purity of the collected proteins (**Figure 4.6A**). Non-reducing and reducing SDS-PAGE results confirmed the dimerisation of the Fc fragments (**Figure 4.6B**).

(A) (B)

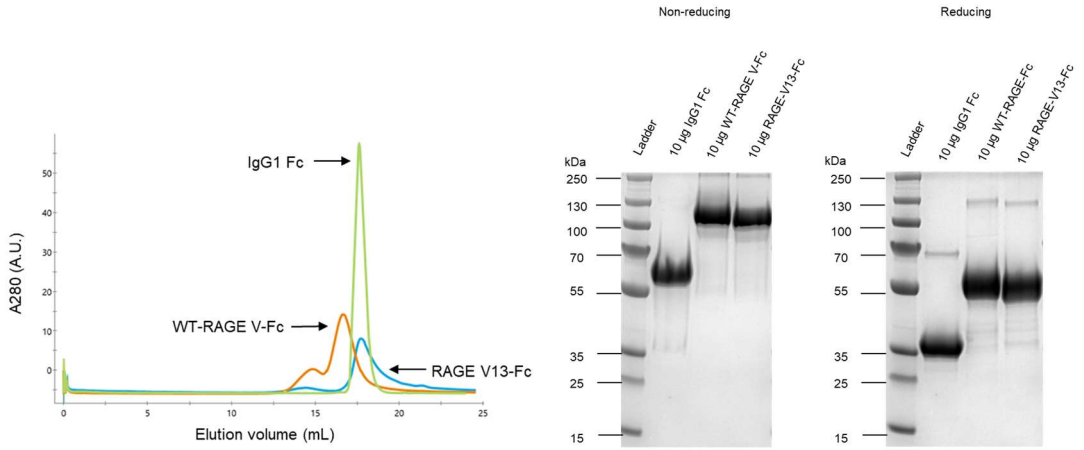


Figure 4.6. Analytical size exclusion chromatography and SDS-PAGE results. (A) Analytical size exclusion chromatography (Superose 6 Increase 10/300 GL). Each peak represents a recombinant protein. **(B)** SDS-PAGE results of recombinant IgG1 Fc, WT-RAGE V-Fc and RAGE V13-Fc used in *in vitro* and *in vivo* studies.

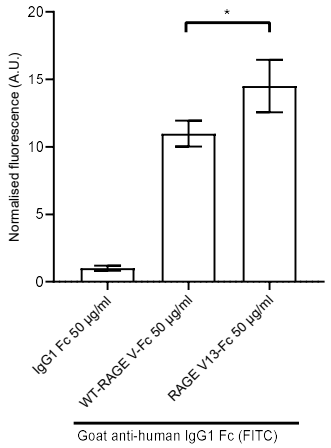
Both WT-RAGE V-Fc and RAGE V13-Fc were well expressed and secreted by HEK293F. The yields for IgG1 Fc, WT-RAGE V-Fc and RAGE V13-Fc were around 200 mg/L, 90 mg/L and 90 mg/L, respectively.

4.3.6 Assessing binding of WT-RAGE V-Fc and RAGE V13-Fc to MDA-MB-231 cellular components.

The ability of WT-RAGE V-Fc and RAGE V13-Fc to interact directly with MDA-MB-231 cellular components was investigated. MDA-MB-231 cells were incubated with either WT-RAGE V-Fc or RAGE V13-Fc, followed by treatment with an anti-human Fc antibody conjugated with a fluorochrome. The binding was quantified and visualised by using flow cytometry and confocal microscopy, respectively. Both WT-RAGE V-Fc and RAGE V13-Fc were shown to interact with certain MDA-MB-231 cell surface components (**Figure 4.7A**). Notably, RAGE V13-Fc-treated samples demonstrated a stronger binding signal than WT-RAGE V-Fc-treated samples. The confocal microscopic images also confirmed

the binding of WT-RAGE V-Fc and RAGE V13-Fc to MDA-MB-231 cellular components (**Figure 4.7B**).

(A)



(B) IgG1 Fc WT-RAGE V-Fc RAGE V13-Fc

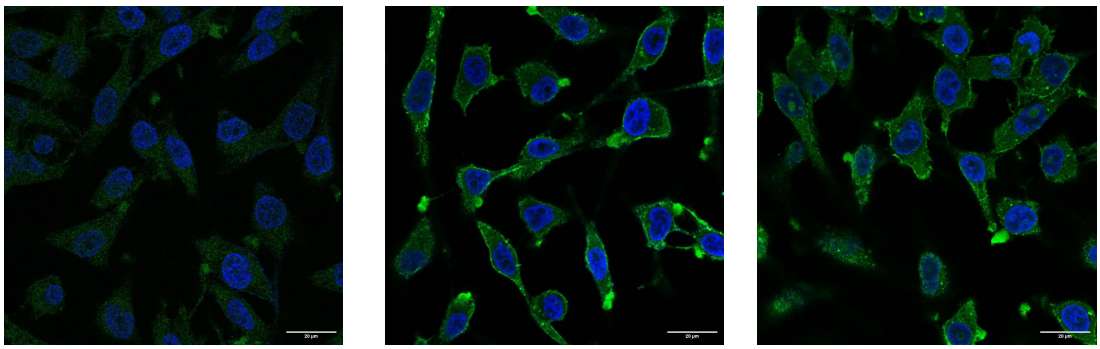


Figure 4.7. Binding of WT-RAGE V-Fc and RAGE V13-Fc to MDA-MB-231 cellular components. **(A)** Flow cytometry results show the binding of WT-RAGE V-Fc and RAGE V13-Fc to MDA-MB-231 cell surface components (N=3). The MDA-MB-231 cells were incubated with IgG1 Fc, WT-RAGE V-Fc or RAGE V13-Fc, followed by incubation with fluorescently tagged anti-human Fc domain antibodies. Flow cytometry was used to quantify the fluorescent signal. All data were normalised against PBS-treated samples. Error bars represent standard deviation of the mean. *P<0.05; ****P<0.0001; **(B)** Confocal microscopy images showing cells labelled with IgG1 Fc, WT-RAGE V-Fc or RAGE V13-Fc. The fixed MDA-MB-231 cells were incubated with both WT-RAGE V-Fc and RAGE V13-Fc for 30 minutes, followed by incubation with fluorescently tagged anti-human Fc domain antibody. The images were taken using confocal microscopy. Scale bar: 20 µm.

4.4 Discussion

To block RAGE ligands-induced signalling pathways, I engineered a high binding capacity RAGE V decoy receptor, namely RAGE V13 that can interact with more RAGE ligands than WT-RAGE V at a given ligand concentration. During FACS sorting, false positive RAGE V variants that interact directly with anti-C3a antibodies were enriched after CS2. To tackle this issue, I used another set of ligands and antibodies, including a recombinant His-tagged C3a and an anti-His antibody which do not interact with RAGE V variants non-specifically. This issue has not been documented previously. In theory, both ligands and antibodies exert equivalent selective pressures during the screening process. In addition, yeast surface display procedures are not capable of discriminating ligand binders from antibody binders. Positive binding signals are a result of cells coated with antibodies conjugated with fluorochrome. Whether ligands are involved in the "coating" process is not a prerequisite for generating the positive binding signals. Therefore, yeast-displayed RAGE V variants that can directly interact with the antibody could also be enriched during the screening process. As a multi-ligand receptor with a promiscuous ligand specificity, it is plausible that mutations in RAGE V could not only change ligand binding affinity but also result in a shift in ligand diversity and specificity.

RAGE V13 contains four mutations including K22R, K30R, E37K, Q78R (**Figure 4.3A**). Both mutations (K22R, K30R) were conversion of Lys-to-Arg. This specific type of mutation usually promotes conformational stability via the extra side chain (Austerberry et al., 2019). Furthermore, the four mutations resulted in a higher positive charge. The pI value was 10.1 for WT-RAGE V and 11.2 for RAGE V13 (**Figure 4.3B & C**). It is known that the majority of RAGE ligands are negatively charged (Fritz, 2011). RAGE V13 is highly positively charged which could promote charge-charge interaction and enhance ligand-receptor interactions.

The binding affinity of RAGE V13 and WT-RAGE V to the four ligands was similar (**Figure 4.4A & B**). However, RAGE V13 has a higher B_{max} to C3a, S100A4 and HMGB1 than WT-RAGE V-Fc, suggesting that RAGE V13 was able to capture more ligands than WT-RAGE V at a given ligand concentration. A plausible explanation for the enhanced B_{max} is that there were more correctly folded RAGE V13 than WT-RAGE V on the yeast surface. The mutations in RAGE V13 contributed to higher conformation stability. According to the Alpha-fold 2 prediction, WT-RAGE V was structurally distorted when being produced as a fusion protein with human IgG1 Fc fragment, while the RAGE V13-Fc maintained its structural integrity (**Figure 4.5B & C**). This also supported the assumption that RAGE V13 is structurally more stable than WT-RAGE V. Therefore, mutations identified in RAGE V13 were likely to elevate protein stability rather than binding affinity and, as a result, increased maximum binding signals to multiple ligands.

In this chapter, an engineered RAGE V decoy receptor, RAGE V13, with the enhanced maximum binding capacity to multiple ligands was developed. The basis of the enhanced ligand binding is hypothesized to result from enhanced structural stability. An in-depth analysis of ligand-receptor interactions is recommended to better understand the roles of these mutations in ligand binding. The initial binding experiment has indicated that both WT-RAGE V-Fc and RAGE V13-Fc can interact with MDA-MB-231 cellular components. The therapeutic potential of WT-RAGE V-Fc and RAGE V13-Fc will be discussed in the following chapters.

Chapter 5: Evaluating the therapeutic potential of RAGE V13-Fc.

5.1 Introduction

Using the affinity maturation process detailed in Chapter 4, I developed a RAGE V variant known as RAGE V13 which had a higher protein stability and enhanced maximum binding capacity to multiple RAGE ligands compared to WT-RAGE V. Our subsequent investigation aimed to determine if RAGE decoy receptors exhibit anti-tumour activity against TNBC. To achieve this, WT-RAGE V and RAGE V13 were reformatted into Fc fusion proteins for *in vitro* and *in vivo* testing.

This chapter focuses on the examination of the anti-tumour activity of WT-RAGE V-Fc and RAGE V13-Fc against TNBC. The CCK8 proliferation assay indicated that RAGE V13-Fc delayed MD-MBA-231 cell growth by around 40% compared to the control, while WT-RAGE V-Fc demonstrated limited or no anti-proliferative effects. Interestingly, RAGE V13-Fc did not suppress clonogenicity or induce apoptosis in the MDA-MB-231 cells. I also investigated the impact of the RAGE decoy receptor treatment on cell migration and found that RAGE V13-Fc was more potent than WT-RAGE V-Fc in suppressing TNBC cell migration and invasion. The wound healing assay further confirmed the role of RAGE V13-Fc in suppressing tumour cell migration. Notably, both WT-RAGE V-Fc and RAGE V13-Fc triggered a strong inhibitory effect on NK cell mobility. In terms of animal study, RAGE V13-Fc demonstrated significant anti-tumour activity in both immunocompetent and immune-suppressive TNBC mouse models, whereas WT-RAGE V-Fc treatment did not appear to exhibit significant anti-tumour activity.

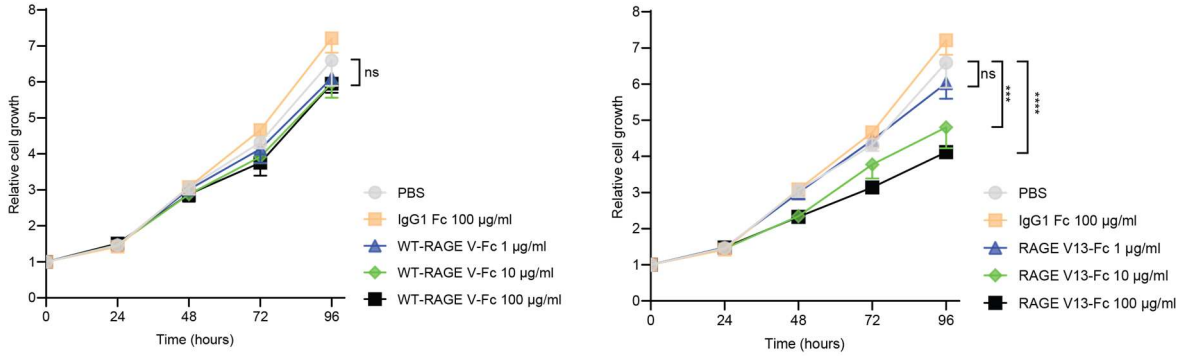
5.2 Results

5.2.1 Inhibitory effects of RAGE V13-Fc on MDA-MB-231 in vitro cell growth

To assess the *in vitro* anti-tumour activity of WT-RAGE V-Fc and RAGE V13-Fc, CCK8 proliferation assays were first performed. MDA-MB-231 cells were treated with different concentrations of WT-RAGE V-Fc or RAGE V13-Fc. Relative cell growth was recorded at 24, 48, 72 and 96 hours post-treatment. 100 µg/ml of RAGE V13-Fc suppressed MDA-

MB-231 cell growth by approximately 40% at 96 hours post-treatment, while WT-RAGE V-Fc did not exhibit significant anti-proliferative activity (**Figure 5.1A & B**). Dose-dependent growth inhibition was observed for RAGE V13-Fc-treated MDA-MB-231 cells but not for WT-RAGE V-Fc-treated groups (**Figure 5.1C**). Notably, 40 μg/ml and 100 μg/ml of RAGE V13-Fc caused a similar level of growth inhibition on MDA-MBA-231 cell growth, suggesting that a maximal efficacy of RAGE V13-Fc was reached at a dosage around 40 μg/ml. Overall, RAGE V13-Fc demonstrated a stronger growth-inhibitory activity against MDA-MB-231 than WT-RAGE V-Fc.

(A) WT-RAGE V-Fc (B) RAGE V13-Fc



(C) WT-RAGE V-Fc vs RAGE V13-Fc

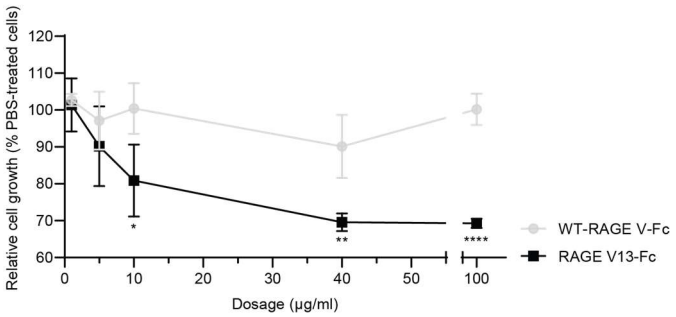


Figure 5.1. CCK-8 proliferation assay showing the inhibitory effects of RAGE V13-Fc on MDA-MB-231 proliferation. One thousand cells of MDA-MB-231 were seeded in 96-well plates overnight and subsequently treated with PBS, IgG1 Fc or different concentrations of WT-RAGE V-Fc or RAGE V13-Fc. Multiple CCK8 proliferation assays were performed at 24, 48, 72 and 96 hours post-treatment. **(A)** Effects of WT-RAGE V-Fc on MDA-MB-231 proliferation (n=4). **(B)** Effects of RAGE V13-Fc on MDA-MB-231 proliferation (n=4). **(C)** Comparison of relative cell growth of WT-RAGE V13-Fc-treated samples with RAGE V13-Fc-treated samples 96 hours post-treatment. All data were normalised against PBS-treated samples. Error bars represent the standard deviation of the mean. One-way ANOVA was performed to compare between treatment groups. *P<0.05, ***P<0.001, ****P<0.0001 or not statistically significant (ns).

The growth-inhibitory property of RAGE V13-Fc was next examined in six breast cancer cell lines, including SUM-159PT, HCC1866, MDA-MB-468, CAL-51, MCF7 and BT-549. The breast cancer cells were treated with 100 µg/ml of WT-RAGE V-Fc or RAGE V13-Fc. Overall, limited or no growth inhibition was detected in the six breast cancer cell lines after the treatment. HCC1886 was the only cell line with a slightly but significantly delayed cell growth after being treated with 100 µg/ml of RAGE V13-Fc treatment

(**Figure 5.2**). This suggests that RAGE V13-Fc might only be able to suppress specific TNBC growth.

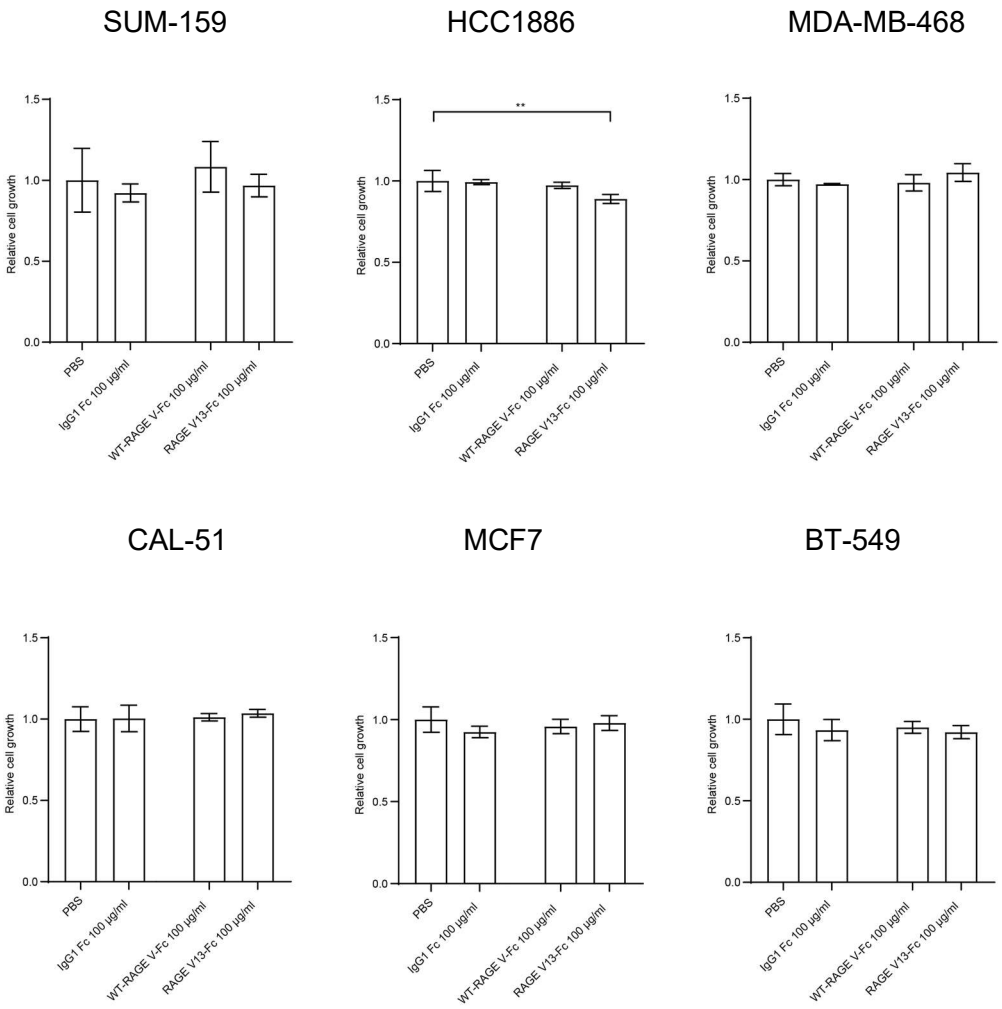


Figure 5.2. CCK-8 proliferation assay demonstrating that WT-RAGE V-Fc and RAGE V13-Fc have limited or no growth inhibition on six breast cancer cell lines, including SUM-159-PT, HCC1866, MDA-MB-468, CAL-51, MCF7 and BT-549. One thousand cells were seeded in 96-well plates overnight and treated with PBS, IgG1 Fc, WT-RAGE V-Fc or RAGE V13-Fc. CCK8 proliferation assays were performed 96 hours after the treatment. All data were normalised against PBS-treated samples. Error bars represent standard deviation of the mean. One-way ANOVA was performed to compare between treatment groups. **P<0.01

A clonogenic assay was carried out to evaluate the anti-tumour effect of WT-RAGE V-Fc and RAGE V13-Fc. After seeding MDA-MB-231 in six-well plates overnight, cells were treated with WT-RAGE V-Fc and RAGE V13-Fc, which were then replenished every 96 hours. Colonies were stained with crystal violet 12 days after the first treatment. The

number of colonies and colony area average were measured using Gel Count (Oxford Optronix). Both WT-RAGE V-Fc and RAGE V13-Fc treatment did not result in a significant decrease in the colony counts (**Figure 5.3A & B**). Interestingly, the average size of the colonies was relatively smaller in RAGE V13-Fc-treated samples than in WT-RAGE V-Fc-treated and IgG1 Fc-treatment samples (**Figure 5.3C**). This suggests that RAGE V13-Fc treatment did not suppress MDA-MB-231 clonogenicity but instead delayed cell growth.

(A) (B) (C)

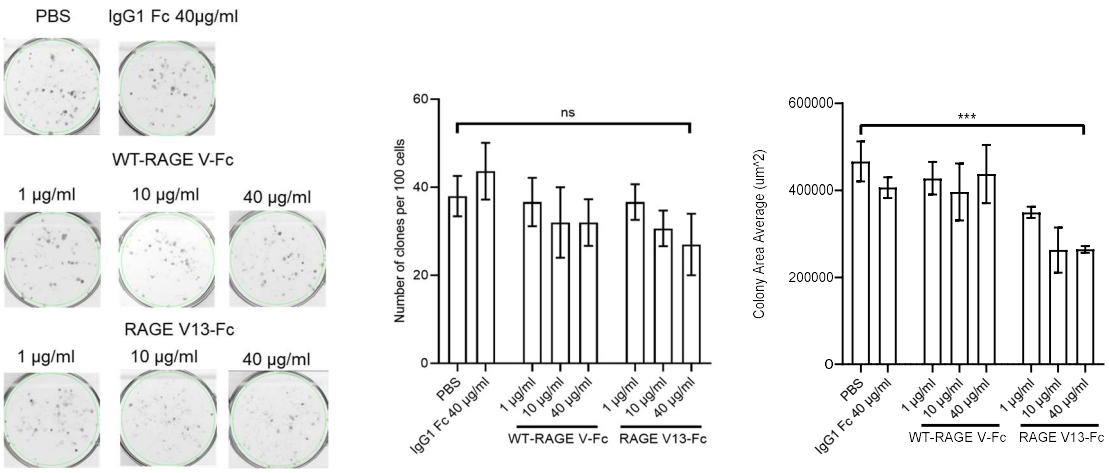
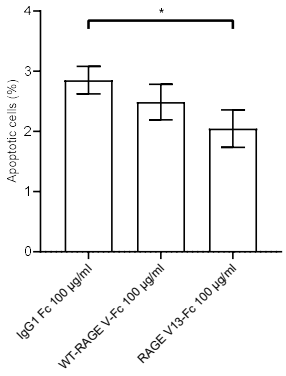


Figure 5.3. Clonogenic assay indicating that RAGE V13-Fc treatment did not suppress clonogenicity but instead delay colony growth. One hundred MDA-MB-231 cells were seeded in 6-well plates 24 hours before the drug treatment. The medium containing IgG1 Fc, WT-RAGE V-Fc or RAGE V13-Fc was replenished every 96 h. The images were taken 12 days after the first drug treatment. Error bars represent standard deviation of the mean. All data were normalised against PBS-treated samples (N=3). ***P<0.001 or not statistically significant (ns).

To investigate whether the RAGE V13-Fc-mediated growth inhibition was a result of apoptosis, Annexin V assays with PI were conducted. After seeding MDA-MB-231 in six-well plates, cells were treated with WT-RAGE V-Fc or RAGE V13-Fc for 96 hours and subsequently collected and used for annexin V assay with PI. All samples contained around 2% – 3% of apoptotic cells (**Figure 5.4**). Despite the small level of apoptosis, RAGE V13-Fc-treated samples had a significantly but slightly lower percentage of

apoptotic cells compared to the control group. This finding indicates that RAGE V13-Fc treatment was unlikely to induce apoptosis.

(A)



(B)

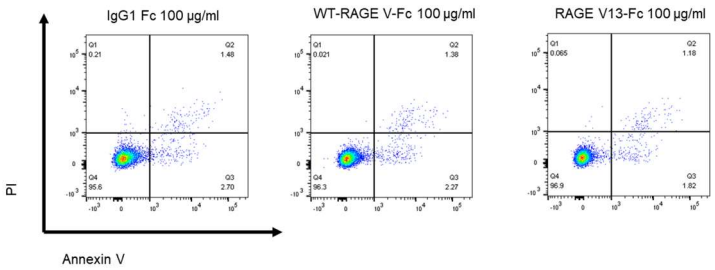


Figure 5.4 Annexin V assay with PI showing no apparent cell apoptosis after WT-RAGE V-Fc and RAGE V13-Fc treatment. 1 x 10^4 cells/ml of MDA-MB-231 were seeded in six-well plates and treated with IgG1 Fc, WT-RAGE V-Fc or RAGE V13-Fc. Annexin V assay with PI was performed at 96 hours post-treatment. All data were normalised against PBS-treated samples (N=3). Error bars represent standard deviation of the mean. *P<0.05.

5.2.2 Inhibitory effects of RAGE V13-Fc on MDA-MB-231 migration and invasion

To investigate the effects of WT-RAGE V-Fc and RAGE V13-Fc on cell adhesion, migration and invasion, transwell migration/invasion assays were performed. MDA-MB-231 cells were pre-treated with WT-RAGE V-Fc and RAGE V13-Fc before being placed in transwell chambers. DMEM medium supplemented with 10% FBS was used as a chemoattractant. Both WT-RAGE V-Fc and RAGE V13-Fc were shown not to interfere with cell adhesion (**Figure 5.5A & B**). Cell migration and invasion were inhibited by both

WT-RAGE V-Fc and RAGE V13-Fc. The inhibitory effect of RAGE V13-Fc on cell migration and invasion was significantly more prominent than WT-RAGE V-Fc. 10 μg/ml of RAGE V13-Fc prevented over 75% of cells from migrating to the back side of the membrane, while 10 μg/ml of WT-RAGE V-Fc had no significant inhibitory effects (**Figure 5.5A & C**). Regarding cell invasion, 10 μg/ml of RAGE V13-Fc inhibited over 90% of cell invasion, whereas 10 μg/ml of WT-RAGE V-Fc suppressed around 25% of cell invasion (**Figure 5.5A & D**).

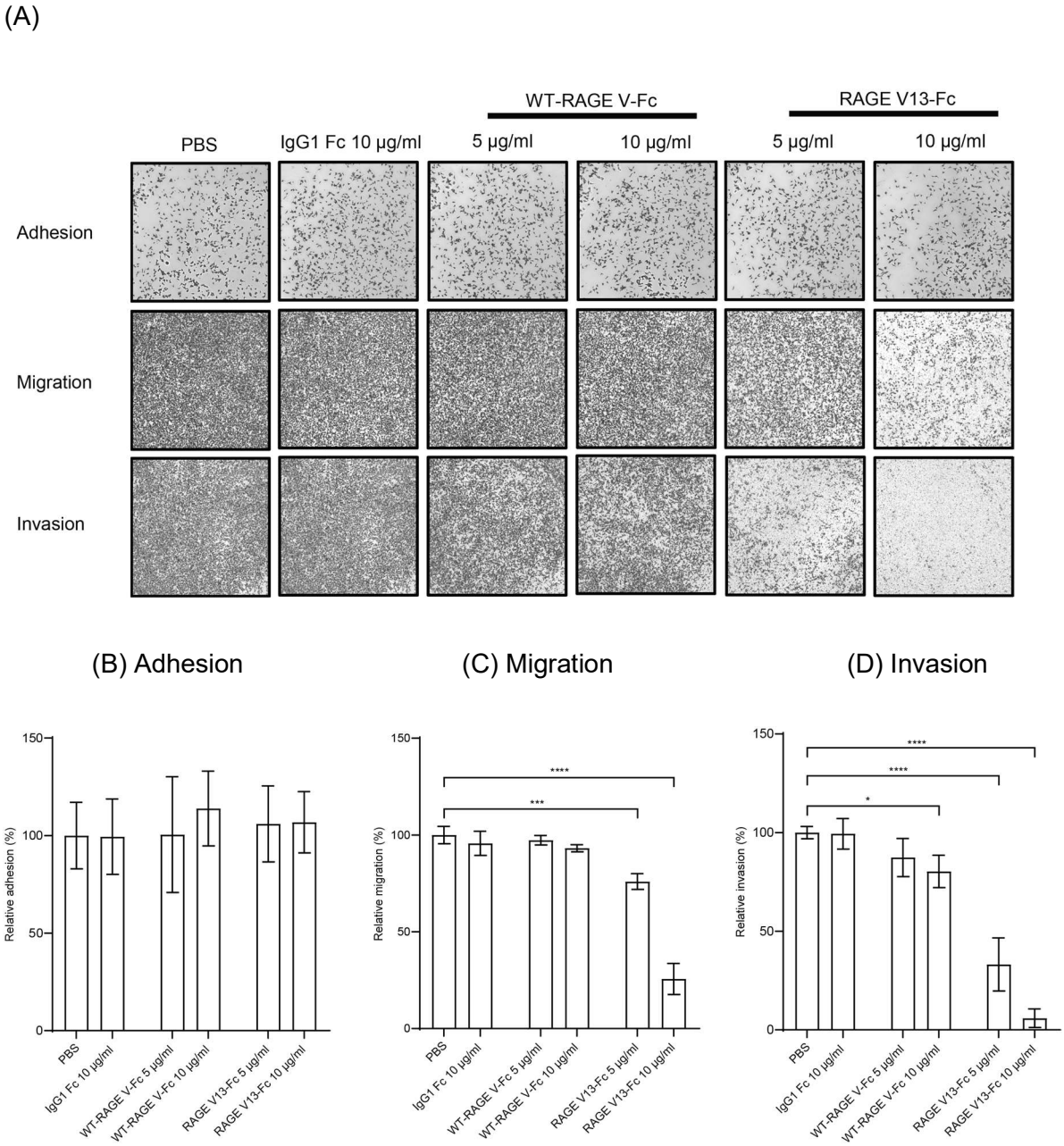


Figure 5.5. Trans-well migration assay showing that RAGE V13-Fc treatment suppresses MDA-MB-231 cell migration and invasion. (A) Representative images of adhered, migrated or invaded cells stained with crystal violet. MDA-MB-231 cells were resuspended in serum-free DMEM, treated with PBS, IgG1 Fc, WT-RAGE V-Fc or RAGE V13-Fc and placed in the top champers. DEME supplemented with 10% FBS was placed in the bottom chamber. After incubation at 37℃ for 24 hours, the cells were stained with crystal violet for visualisation. Adhered **(B)**, migrated **(C)** and invaded **(D)** cells were quantified using Celigo where cells from 90%, 20% and 15% of the central image area were counted. All data were normalised against PBS-treated samples (N≥3). One-way ANOVA was performed to compare between treatment groups. Error bars represent standard deviation of the mean. *P<0.05, ***P<0.001 and ****P<0.0001.

Transwell migration assay was also carried out to investigate the effect of WT-RAGE V-Fc and RAGE V13-Fc on other TNBC cell line migration, including MDA-MB-468 and HCC1886. 100 μg/ml of either WT-RAGE V-Fc or RAGE V13-Fc was shown to prevent migration of over 99% of MDA-MB-231 and HCC1886 cells. Both WT-RAGE V-Fc and RAGE V13-Fc were less effective against MDA-MB-468 which resulted in 85% and 60% migratory inhibition, respectively. WT-RAGE V-Fc seemed to have the ability to suppress cell migration and invastion but have no anti-proliferative effects as previously indicated.

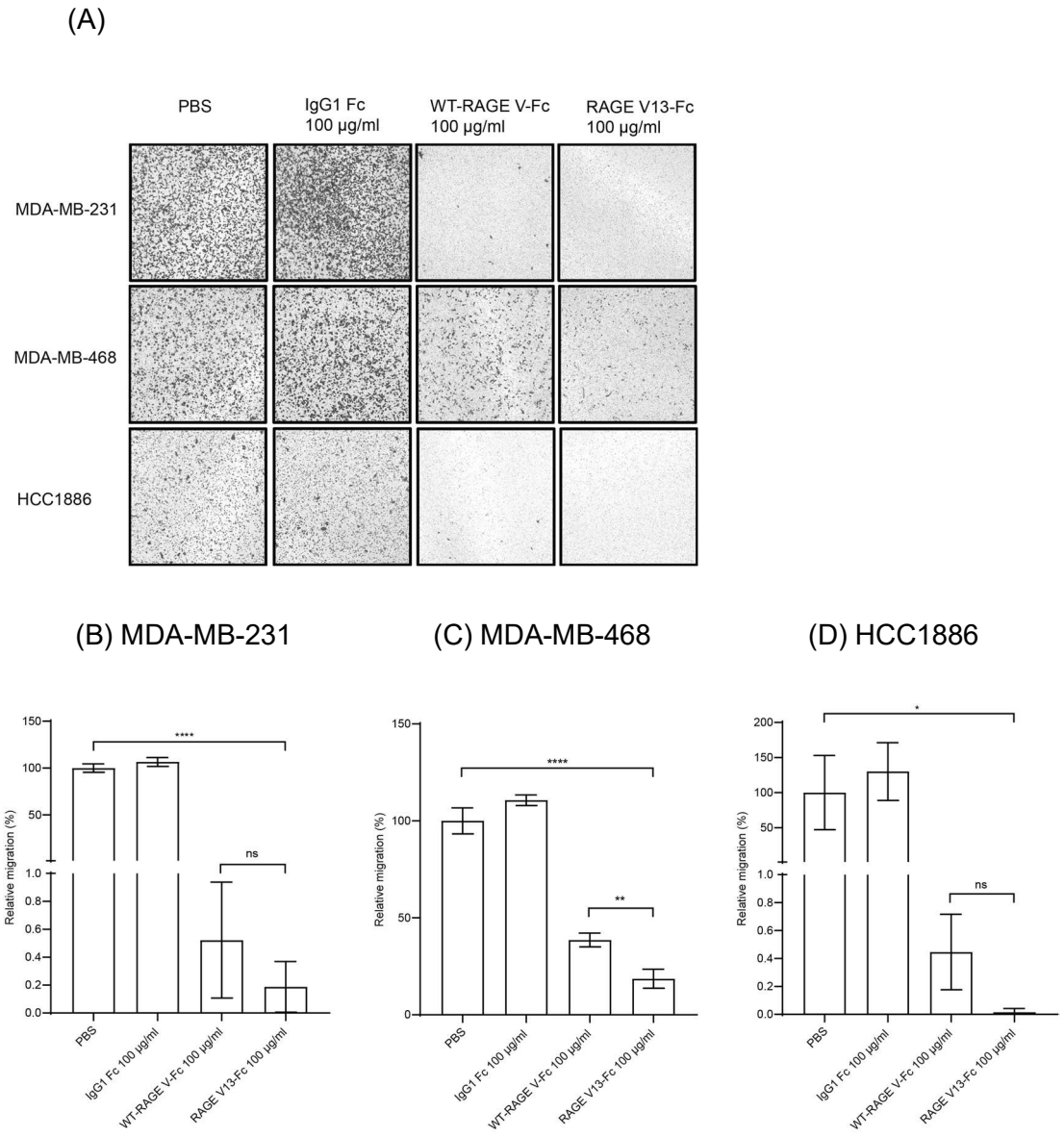


Figure 5.6. Trans-well migration assay demonstrating the WT-RAGE V-induced and RAGE V13-Fc-induced suppressive effects on cell migration in multiple TNBC cell lines including MDA-MB-231, MDA-MB-468 and HCC1886. (A) Representative images of migrated cells stained with crystal violet. TNBC cells were resuspended in serum-free DMEM, treated with PBS, IgG1 Fc, WT-RAGE V-Fc or RAGE V13-Fc and placed in the top champers. DEME supplemented with 10% FBS was placed in the bottom chamber. After incubation at 37℃ for 24 h, cells were stained with crystal violet for visualisation. Adhered **(B)**, migrated **(C)** and invaded **(D)** cells were quantified using Celigo. All data were normalised against PBS-treated samples (N≥3). Error bars represent standard deviation of the mean. One-way ANOVA was performed to compare between treatment groups. *P<0.05, **P<0.01, ****P<0.0001 or not statistically significant (ns).

In addition to the transwell migration assay, wound healing assays were also performed.

MDA-MB-231 monolayers were scratched and treated with either WT-RAGE V-Fc or

RAGE V13-Fc. The live images were taken over a time course of 24 hours after the treatment. MDA-MB-231 treated with RAGE V13-Fc had a significantly larger open wound area at 16 hours and 24 hours post-treatment than those treated with PBS, IgG1-Fc and WT-RAGE V-Fc (**Figure 5.7 A & B**). A lower gap close rate in the RAGE V13-Fc-treated group indicated a role of RAGE V13-Fc in inhibiting cell migration.

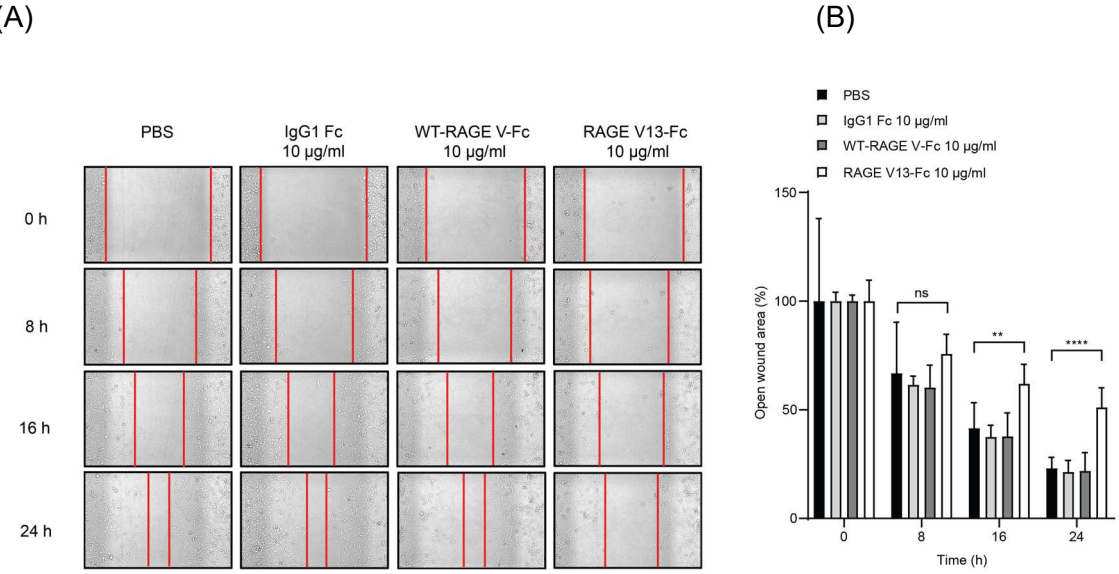


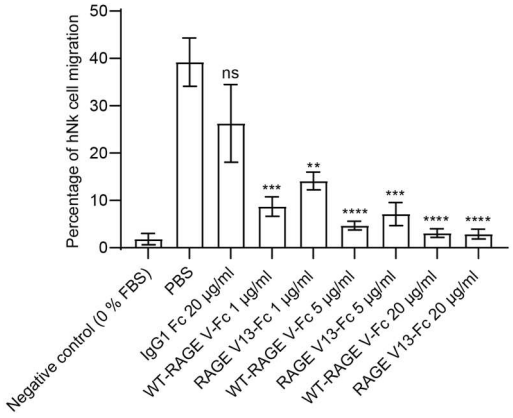
Figure 5.7. Wound healing assay suggesting an inhibitory effect of RAGE V13-Fc on cell migration. 2.5 x 10^5 cells per well were seeded in 24-well plates for 24 hours. Cell medium was changed to serum-free DMEM after scratching the one-cell-thick monolayer with a sterile 200 µl pipette tip. **(A)** Live cell images were taken over 24 hours after PBS, IgG1 Fc, WT-RAGE V-Fc or RAGE V13-Fc treatment. **(B)** Quantification of the open wound area over time. ImageJ was used for quantification. All data were normalised against PBS-treated samples (N=6). Error bars represent standard deviation of the mean. One-way ANOVA was performed to compare between treatment groups. **P<0.01, ****P<0.0001 or not statistically significant (ns).

5.2.3 Inhibitory effects of WT-RAGE V-Fc and RAGE V13-Fc on human NK and T cell mobility

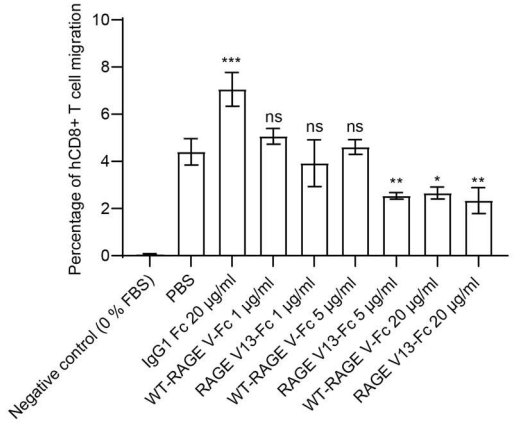
Our next step was to assess the effects of WT-RAGE V-Fc and RAGE V13-Fc on human NK and CD8+ T cell migration using transwell assays. The isolated and expanded human NK cell and CD8+ T cells were treated with different concentrations of WT-RAGE V-Fc and RAGE V13-Fc in the top chambers. The migrated cells in the bottom chamber were counted using Celigo. Both WT-RAGE V-Fc and RAGE V13-Fc demonstrated a strong

inhibitory effect on NK cell migration but a relatively moderate inhibitory effect on CD8+ T cell migration. This suggests a potential immunosuppressive role of WT-RAGE V-Fc and RAGE V13-Fc.

(A) Human NK cell migration assay



(B) Human T cell migration assay



(C) (D) (E) (F)

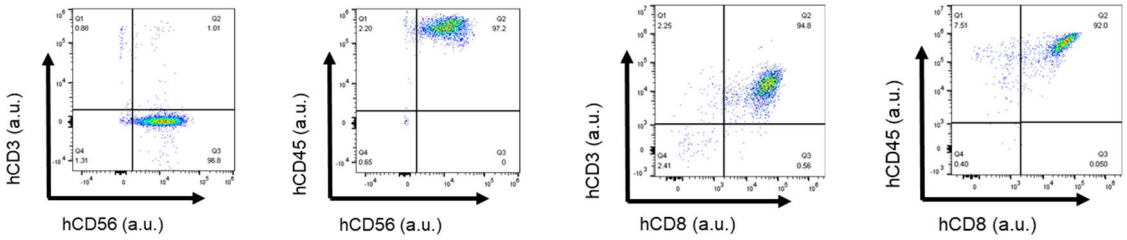
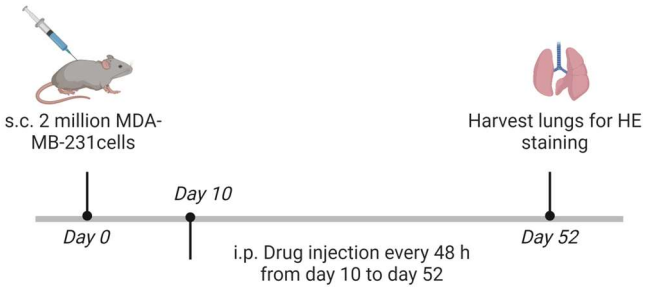


Figure 5.8. RAGE V13-Fc treatment suppresses NK cell and CD8+ T cell migration. Human NK and CD8+ T cells were resuspended in serum-free DMEM medium and treated with PBS, IgG1 Fc, WT-RAGE V-Fc and RAGE V13-Fc. DEME supplemented with 10% FBS was placed in the bottom chamber as a chemoattractant. After incubation at 37℃ for 24 hours, Celigo was used to quantify migrated human NK **(A)** or CD8+ T **(B)** cells in the bottom chamber (N=3). Representative flow cytometry plots demonstrated the purity of NK cells **(C)** and CD8+ T cells **(D)** used in the trans-well assays. All data were normalised against PBS-treated samples. Error bars represent standard deviation of the mean. One-way ANOVA was performed to compare between treatment groups. *P<0.05, ***P<0.001, ****P<0.0001 or not statistically significant (ns).

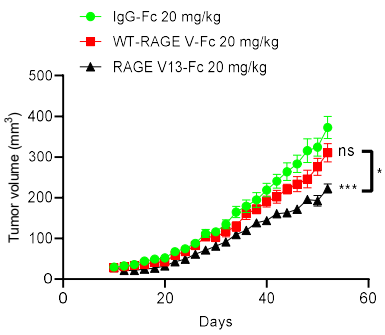
5.2.4 Investigating the impact of WT-RAGE V-Fc and RAGE V13-Fc on MDA-MB-231 xenograft growth and its lung metastasis in NSG mice

The human TNBC cell line MDA-MB-231 has an aggressive phenotype of being able to develop spontaneous metastasis to the lung (Jenkins et al., 2005). I here tested the ability of RAGE V13-Fc to limit tumour growth and lung metastasis in immune-deficient NSG mice (**Figure 5.9A**). Two million MDA-MB-231 cells were subcutaneously injected into the right flank of NSG mice. Drug treatment started when the tumour volume reached 50 mm^3. The mice were dosed every 48 hours via intraperitoneal injection until the humane endpoint. Mice treated with RAGE V13-Fc had a significantly lower tumour burden compared to those treated with WT-RAGE V-Fc or IgG1 Fc (**Figure 5.9B**). WT-RAGE V-Fc treatment did not result in a significant reduction in tumour volume. The mouse weight average for all three experimental groups increased steadily from day 0 to day 48, suggesting that decoy receptors treatment did not cause detrimental toxic effects (**Figure 5.9C**). However, during the last four days of weight measurement (48-52), there was a sudden drop in mouse weight, possibly due to severe lung metastasis. The average weight loss for IgG1-Fc-treated, WT-RAGE-FC-treated and RAGE V13-Fc-treated groups was 2.2 g, 2.0 g and 0.8 g, respectively (**Figure 5.9C**). A relatively lower average weight drop in RAGE V13-Fc-treated group suggests that RAGE V13-Fc treatment inhibited cancer progression. In terms of lung metastasis, mice treated with RAGE V13-Fc had lower tumour burden in the lungs than those treated with IgG1-Fc (**Figure 5.9D & E**). However, there was no significant difference in lung metastasis between WT-RAGE V-Fc, and RAGE V13-Fc treated mice. Overall, RAGE V13-Fc treatment could delay primary tumour growth and suppress spontaneous lung metastasis in MDA-MB-231 bearing NSG mice.

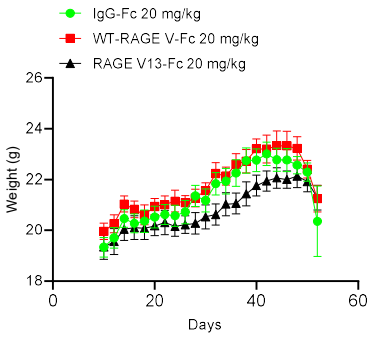
(A)


s.c. 2 million MDA-MB-231cells
Harvest lungs for HE staining
Day 10
Day 0
Day 52
i.p. Drug injection every 48 h from day 10 to day 52

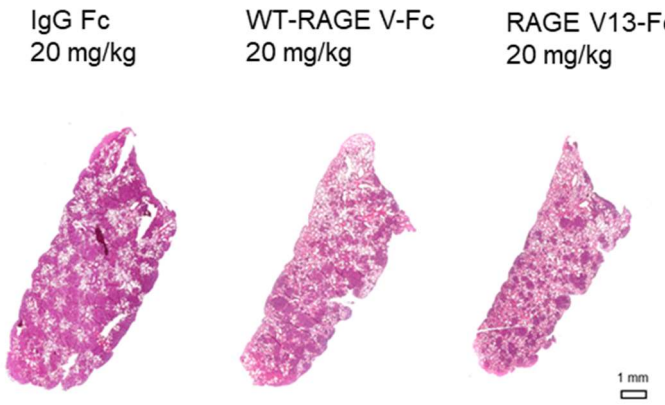
(B)


IgG-Fc 20 mg/kg
WT-RAGE V-Fc 20 mg/kg
RAGE V13-Fc 20 mg/kg
Tumor volume (mm3)
Days
ns
*
***

(C)


IgG-Fc 20 mg/kg
WT-RAGE V-Fc 20 mg/kg
RAGE V13-Fc 20 mg/kg
Weight (g)
Days

(D)


IgG Fc 20 mg/kg
WT-RAGE V-Fc 20 mg/kg
RAGE V13-Fc 20 mg/kg
1 mm

(E)

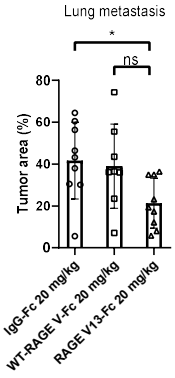
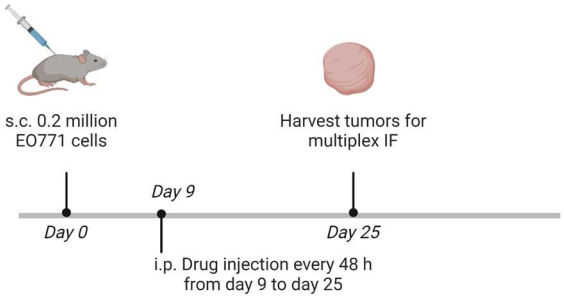

Lung metastasis
*
ns
Tumor area (%)
IgG-Fc 20 mg/kg
WT-RAGE V-Fc 20 mg/kg
RAGE V13-Fc 20 mg/kg

Figure 5.9. Evaluating the anti-tumour activity of WT-RAGE-Fc and RAGE V13-Fc in MDA-MB-231 bearing NSG mice. (A) Schematic representation of the experimental design for tumour induction and drug treatment in NSG mice. **(B)** Subcutaneous volume change of MDA-MB-231 in NSG mice. The mice were treated with 20 mg/kg of IgG1 Fc (N=9), 20 mg/kg of WT-RAGE V-Fc (N=8) or 20 mg/kg of RAGE V13-Fc (N=9) every 48 hours starting from day 10. Error bars represent standard error of the mean. One-way ANOVA was performed to compare tumour size after the last drug injection between treatment groups. **(C)** Mouse body weight change over time. Mouse body weight was measured every 48 hours. **(D)** Hematoxylin and eosin staining showing spontaneous lung metastasis in MDA-MB-231 bearing NSG mice. H & E staining was performed on the mouse's left lung. Scale bar: 1mm. Images were generated with the assistance of Dr Yanyan Jiang. **(E)** Quantification of tumour area in the metastatic lung using ImageScope. Error bars represent standard error of the mean. One-way ANOVA was performed to compare between treatment groups. *P<0.05, ***P<0.001 or not statistically significant (ns).

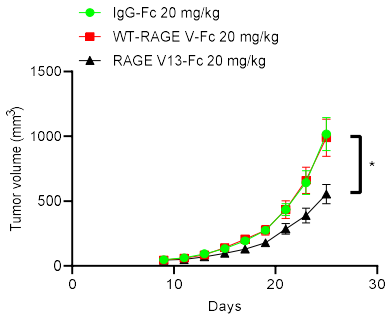
5.2.5 Investigating the impact of WT-RAGE V-Fc and RAGE V13-Fc on EO771 xenograft growth in C57/BL6 mice.

EO771 is a mouse TNBC cell line derived from a spontaneous tumour in C57BL/6 mice (Han et al., 2022). I investigated the anti-tumour effects of WT-RAGE V-Fc and RAGE V13-Fc in immune-competent C57BL/6 mice. C57BL/6 mice were subcutaneously injected with 0.2 million cells and were dosed every 48 hours via intraperitoneal injection (**Figure 5.10A**). RAGE V13-Fc-treated group demonstrated a significantly lower tumour volume compared to IgG1 Fc-treated and WT-RAGE V-Fc-treated groups at day 25 (**Figure 5.10B**). Mouse weight steadily increased for all groups over the course of treatment, suggesting low drug toxicity (**Figure 5.10C**).

(A)



(B)



(C)

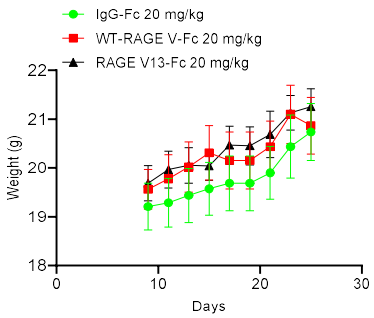


Figure 5.10. Evaluating the anti-tumour activity of WT-RAGE-Fc and RAGE V13-Fc in EO771 bearing C57BL/6 mice. (A) Schematic representation of the experimental design for tumour induction and drug treatment in EO771 mice. **(B)** Subcutaneous tumour volume change of EO771 mice. The mice were treated with 20 mg/kg of IgG1 Fc (N=8), 20 mg/kg of WT-RAGE V-Fc (N=9) or 20 mg/kg of RAGE V13-Fc (N=9) every 48 hours since the average tumour volume reached 50 mm^3. **(C)** Mouse body weights change over time. Mouse body weight was measured every 48 hours. One-way ANOVA was performed to compare between treatment groups. Error bars represent standard error of the mean. *P<0.05

5.3 Discussion

The effects of sequesting RAGE ligands on TNBC has not been well-studied. Its clinical value is even less well-understood. This chapter presents data to indicate that WT-RAGE V-Fc has no or limited anti-tumour activity, which raises the question of whether RAGE ligands are less essential for cancer cell survival than initially thought. However, RAGE V13-Fc significantly suppressed TNBC tumour growth and metastasis both *in vitro* and

in vivo. It was assumed that the differences in maximum binding capacity between WT-RAGE V-Fc and RAGE V13-Fc were the major driver for their different drug actions.

The RAGE V13-Fc was able to induce tumour growth delay. Proliferation assay and apoptosis assay results suggested that RAGE V13-Fc inhibited cell growth without causing direct cell apoptosis (**Figure 5.1 & 5.4**). For the clonogenic assay, a reduced MDA-MB-231 colony area average was observed in RAGE V13-Fc-treated samples, which further suggests a role of RAGE V13-Fc in delaying cell growth (**Figure 5.3**). Among multiple breast cancer cell lines, MDA-MB-231 was the only cell line suppressed by RAGE V13-Fc treatment in terms of cell growth (**Figure 5.2**). This might suggest that RAGE V13-Fc specifically targeted certain pathways only important for MDA-MB-231 growth instead of targeting general cell growth factors or nutrients. In addition, WT-RAGE V-Fc but not RAGE V13-Fc was able to suppress Su-DHL-6 cell growth (**Figure A1**)**.** The role of RAGE in B cell lymphoma remains largely unknown. RAGE receptor was shown to be centrally involved in B cell activation, suggesting a possible growth-stimulating role of RAGE in B cell lymphoma (Avalos et al., 2010; Bangert et al., 2016).

In terms of tumour cell migration and invasion, WT-RAGE V-Fc only demonstrated limited inhibitory effects at a high dosage (**Figure 5.5**). This is consistent with a previous study where RAGE knock-down with shRNAs in breast cancer resulted in lower cell migration and invasion (Kwak et al., 2017). In contrast, RAGE V13-Fc exhibited stronger suppressive activity on TNBC mobility compared to WT-RAGE V-Fc (**Figure 5.5 & 5.7**). WT-RAGE V-Fc-induced and RAGE V13-Fc-induced inhibition of migration was observed in other TNBC cell lines, including HCC1886 and MDA-MB-468 (**Figure 5.6**). RAGE V13-Fc demonstrated a potent efficacy to suppress tumour cell invasion and metastasis while affecting tumour growth in specific tumour types. The superiority of RAGE V13-Fc has also been passed onto the *in vivo* experiments (**Figure 5.9 & 5.10**). In the immunocompromised TNBC mouse model, RAGE V13-Fc not only suppressed

tumour growth but also attenuated lung metastasis (**Figure 5.9D & E**). One of the potential RAGE V13-Fc targets could be glycation end products (AGEs) which have been reported to promote breast cancer metastasis via activating TLR4 and RAGE receptors (Pan et al., 2022).

In addition, the inhibitory effects of WT-RAGE V-Fc and RAGE V13-Fc on cell mobility extended to human NK and CD8+T cells. Unlike responses observed on the TNBC cell line, WT-RAGE V-Fc and RAGE V13-Fc show similar potency in suppression of NK and CD8+ T cell migration (**Figure 5.8A & B**). Of note, the inhibitory effects of both decoy receptors on cell mobility are more prominent on NK cells than CD8+ T cells. The roles of RAGE in immune cell mobilisation have been previously documented. In an AT-3 murine model, RAGE knock-out mice have a significantly lower level of tumour infiltrating leukocytes (Kwak et al., 2017). RAGE was also shown to be involved in leukocyte recruitment by directly interacting with β2-integrin Mac-1 (Chavakis et al., 2003). Moreover, blockade of the RAGE-S100A8/S100A9 axis with FPS-ZM1 suppresses NK cell functions (Narumi et al., 2015). These results might explain WT-RAGE V-Fc-induced and RAGE V13-Fc-induced suppression of NK cell mobility. However, the role of RAGE in CD8+ T cells remains poorly understood. Intriguingly, RAGE-S100A8/S100A9 axis also promotes tumour-promoting immune cell migration such as myeloid-derived suppressor cells (MDSCs) (K. Li et al., 2021). RAGE ligands seem to be important for the mobility of both tumour-promoting and tumour-suppressive immune cells. Taken together, the RAGE decoy receptor might act as an anti-inflammatory molecule that non-discriminately normalises the tumour microenvironment. Further study will be required to determine the action of RAGE receptor in immune responses using an inflammatory pathogenesis model. This also highlights the potential applications of RAGE decoy receptors in other clinical settings, such as diabetes (Schmidt & Stern, 2000).

This chapter presents my studies on the anti-tumour activity of RAGE V13-Fc compared to WT-RAGE V-Fc. As demonstrated in Chapter 4, RAGE V13 has an enhanced ligand binding capacity, and I found that this translated into superior anti-tumour activity for RAGE V13-Fc compared to WT-RAGE V-Fc. Specifically, I observed significant suppression of TNBC growth and metastasis following RAGE V13-Fc treatment. Interestingly, I also found that both WT-RAGE V-Fc and RAGE V13-Fc treatment suppressed NK cells and CD8+ T cell mobility. The underlying mechanisms of these drug actions will be the focus of investigation in the next chapter.

Chapter 6. Understanding the mechanistic basis of WT-RAGE V-Fc and RAGE-V13-Fc using Mass spectrometry and RNA sequencing

6.1 Introduction

Having demonstrated that RAGE V13-Fc has a superior anti-tumour activity than WT-RAGE V-Fc in TNBC, the next step was to investigate the underlying differences between WT-RAGE V-Fc and RAGE V13-Fc. Given that not all RAGE ligands have been revealed, I first performed immunoprecipitation coupled with mass spectrometry (IP-MS) to identify the potential interactors of WT-RAGE V-Fc and RAGE V13-Fc in MDA-MB-231 cell lysates. Due to the nature of RAGE as a nucleic acid receptor and the presence of nucleic acids in the tumour lysate, the majority of interactors for both WT-RAGE V-Fc and RAGE V13-Fc were identified as DNA or RNA-associated proteins (Sirois et al., 2013). Studying the interaction between DNA or RNA-protein complexes and RAGE decoy receptors is out of the scope of this study, which has been summarised elsewhere (Ruan et al., 2010). I sought to identify the direct extracellular interactors of WT-RAGE V-Fc and RAGE V13-Fc that could play a role in promoting TNBC growth and metastasis systemically *in vivo*. Therefore, I performed another IP-MS experiment to identify potential interactors in 1 in 100 diluted normal human serum. This approach led to the discovery of HSPA5 (heat shock protein family A (Hsp70) member 5), also known as GRP78 (78-kDa glucose-regulated protein) and Bip (Binding immunoglobulin protein). I detected direct binding of WT-RAGE V-Fc and RAGE V13-Fc to GRP78 in this study. Moreover, yeast-displayed RAGE V13 exhibited a higher B_{max} to GPR78 than WT-RAGE V. Recombinant GRP78 could potentially rescue the RAGE V13-induced growth arrest in MDA-MB-231 cells. Given that the role of tumour-secreted GRP78 in TNBC remains poorly understood, further experiments need to be performed to rigorously examine the role of GRP78 in the anti-tumour activity of RAGE V13-Fc.

In addition to IP-MS, bulk RNA sequencing was carried out to study the transcriptomic changes in MDA-MB-231 following the treatment with 40 μg/ml of WT-RAGE V-Fc and 40 μg/ml of RAGE V13-Fc. No significant differences were observed in the transcriptomic

profile between IgG1 of Fc-treated and WT-RAGE V-Fc-treated samples. This might explains the little anti-tumour activity induced by 40 μg/ml of WT-RAGE V-Fc treatment. However, RAGE V13-Fc treatment resulted in a significant shift in gene expression, with the downregulation of CXCL3 being the most pronounced change. According to GSEA analysis, multiple pro-tumourigenic enriched hallmarks were suppressed in RAGE V13-Fc-treated samples, including the c-Myc pathway. Western blot and ELISA results confirmed the downregulation of CXCL3 and p-IRF3 in RAGE V13-Fc-treated samples. Moreover, siCXCL3 treatment delayed MDA-MB-231 cell growth, providing further evidence of the role of CXCL3 in TNBC proliferation.

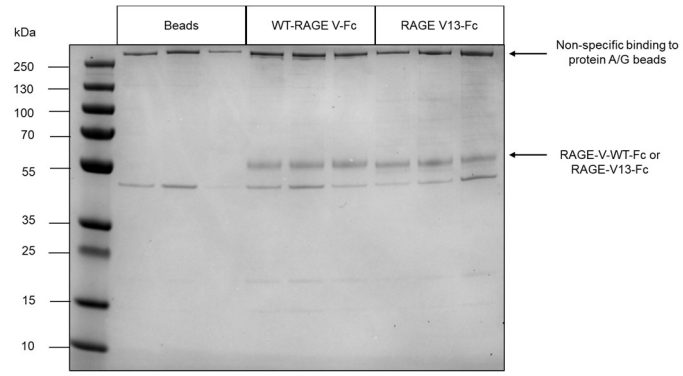
6.2 Results

6.2.1 Immunoprecipitation and mass spectrometry (IP-MS) revealed potential interactors of WT-RAGE V-Fc and RAGE V13-Fc in MDA-MB-231 cell lysate

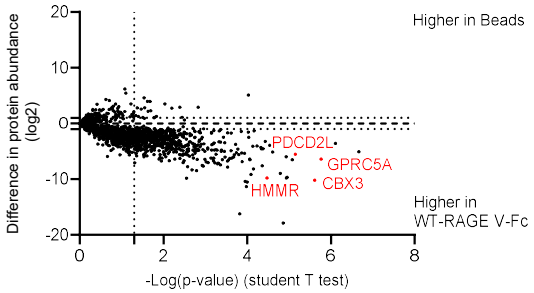
To identify the potential interactors of WT-RAGE V-Fc and RAGE V13-Fc, IP-MS was first carried out to pull down proteins or protein complexes from MDA-MB-231 cell lysates for MS analysis. The SDS-PAGE results represented all the immunoprecipitated proteins or protein complexes in the samples (**Figure 6.1A**). There were no visible bands that could represent the potential interactors of WT-RAGE V-Fc and RAGE V13-Fc. This suggests that the interactors were either not enriched in the samples or were a diverse group of proteins, with each present in a low quantity. For MS results, many potential interactors were enriched in both WT-RAGE V-Fc-treated and RAGE V13-Fc-treated samples. Compared to WT-RAGE V-Fc, RAGE V13-Fc had less number of peptides identified from IP-MS (**Figure 6.1D**). In total, there were 417 WT-RAGE V-Fc-specific, 84 RAGE V13-specific interactors and 327 shared interactors (**Figure 6.1E**). The difference in DNA and RNA binding between WT-RAGE V-Fc and RAGE V13-Fc might be a possible explanation of the drastic change in ligand diversity (**Figure 6.1F**). Overrepresentation analysis demonstrated that most of the interactors identified in both

WT-RAGE V-Fc and RAGE V13-Fc samples were categorised as DNA binding and RNA binding proteins (**Figure 6.1F**). The RAGE receptor is also known to be a nucleic acid receptor that directly interacts with DNA and RNA (Sirois et al., 2013). This might suggest that many of the identified interactors were pulled down as DNA- or RNA-protein complexes by WT-RAGE V-Fc and RAGE V13-Fc. However, I was more interested in the extracellular proteins identified in the MS results. For example, HMMR, CBX3, GRPC5A and PDCD2L were identified as potential interactors for WT-RAGE V-Fc (**Figure 6.1B**). Peg10 and HMMR were identified as potential interactors for RAGE V13-Fc (**Figure 6.1C**).

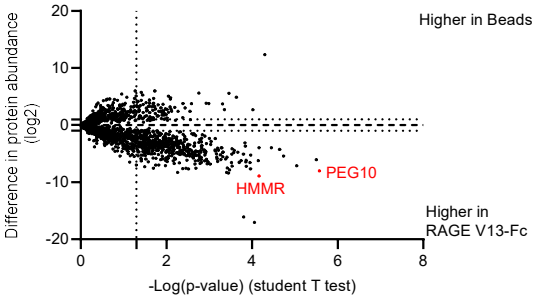
(A)



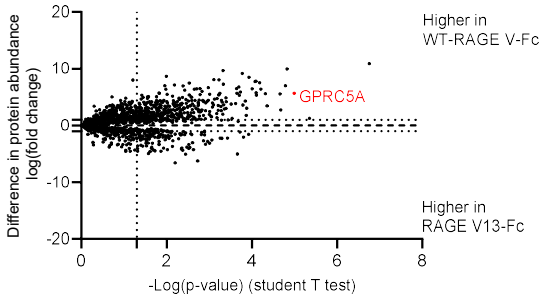
(B) WT-RAGE V-Fc vs Beads



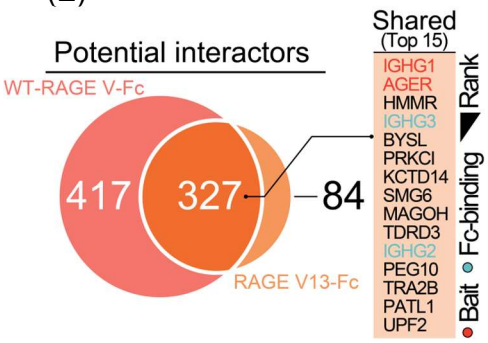
(C) RAGE V13-Fc vs Beads



(D) RAGE V13-Fc vs WT-RAGE V-Fc



(E)



(F)

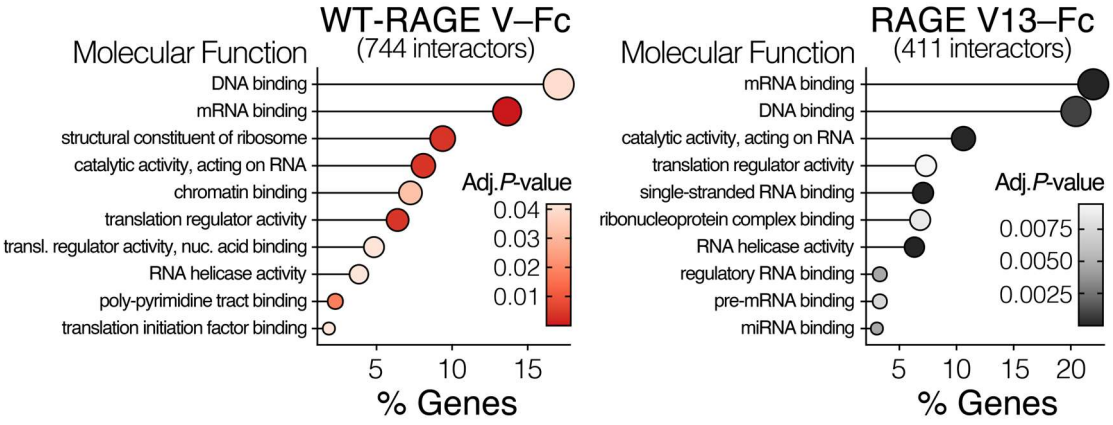


Figure 6.1. Immunoprecipitation and mass spectrometry revealed potential interactors of WT-RAGE V-Fc and RAGE V13-Fc in MDA-MB-231 cell lysate. (A) SDS-PAGE results showing the proteins precipitated by WT-RAGE V-Fc and RAGE V13-Fc. The highlighted bands are either input proteins or proteins that interact with the magnetic beads. **(B-D)** Volcano plot analysis of potential interactors identified in the IP samples by MS. The potential interactors of beads (negative control), WT-RAGE V-Fc and RAGE V13-Fc in MDA-MB-231 cell lysate were interchangeably compared. The negative and positive value of the difference in protein abundance indicates different treatment types. The enriched extracellular interactors are highlighted in red in each plot. 2-sample student test was used for comparing across treatment groups. Fold-change > 2 and q-value ≤ 0.05 were ranked as significant. **(E)** Venn diagram indicating the number of WT-RAGE V-Fc-specific, RAGE V13-Fc-specific and shared interactors. The list on the right denotes the Top 15 shared enriched proteins in the samples. Fc-binding proteins and baits (IGHG1 & AGER) were excluded as potential interactors. **(F)** Overrepresentation analysis plots. Molecular function GO annotations were used for enriched functions among the lists of AGER interactors. Figures (E & F) were generated with assistance of Mr Bruno Beernaert Dominguez.

HMMR (Hyaluronan Mediated Motility Receptor) was the top1 potential interactor shared by both WT-RAGE V-Fc and RAGE V13-Fc. GPRC5A (G Protein-Coupled Receptor Class C Group 5 Member A) and PDCD2L (Programmed Cell Death 2 Like) were WT-RAGE V-Fc-specific. A significantly higher level of mammalian retrovirus-like protein PEG10 was identified in the RAGE V13-Fc-treated samples.

To investigate whether HMMR was involved in direct interaction with WT-RAGE V-Fc and RAGE V13-Fc, I performed reciprocal immunoprecipitations but no direct interaction was detected. Recombinant HMMR-HIS was incubated with IgG1 Fc, WT-RAGE V-Fc and RAGE V13-Fc. The reaction mixture was treated with either anti-His or anti-Fc magnetic beads. Based on western blot analysis, the two reciprocal immunoprecipitation results were not consistent. The intensity of HMMR protein bands highlighted by the red rectangle was similar across all samples (**Figure 6.2A**). Unexpectedly, more RAGE V13-Fc was precipitated by HMMR than IgG1 Fc and WT-RAGE V-Fc (**Figure 6.2B**). This could be a false positive result due to the low purity of recombinant HMMR where the contaminates interacts with WT-RAGE V-Fc and RAGE V13-Fc. Several contaminates were detected in the western blot results (**Figure 6.2A**). This suggests that HMMR is not a direct interactor of WT-RAGE V-Fc and RAGE V13-Fc.

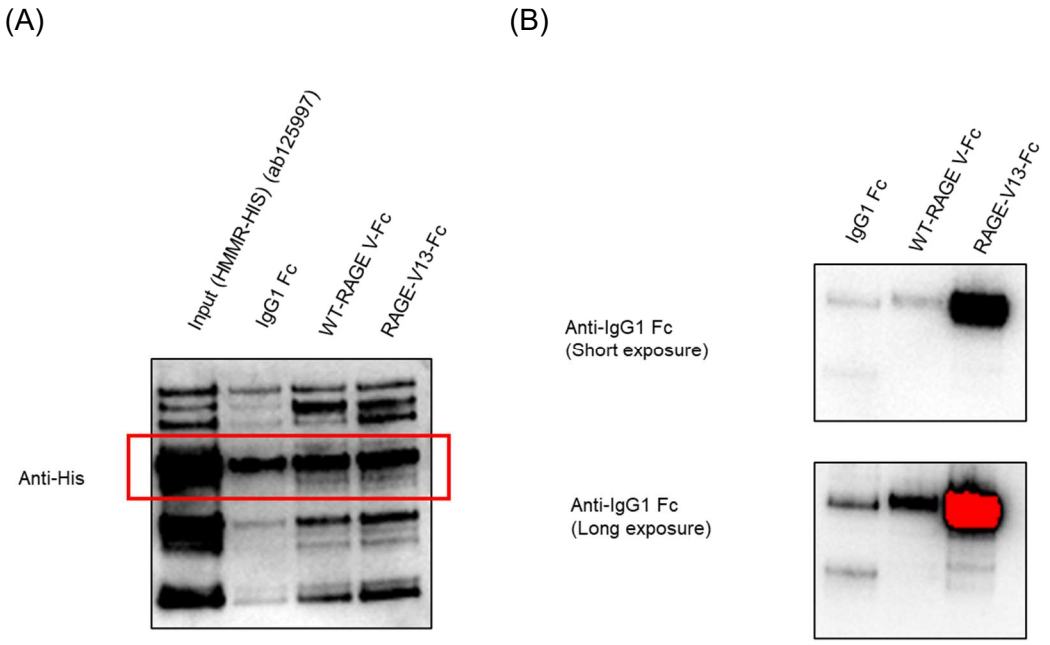


Figure 6.2. Reciprocal immunoprecipitation indicates that HMMR is not likely to be a direct interactor of WT-RAGE V-Fc and RAGE V13-Fc. (A) Western blot results showing detection of HMMR in all samples including the negative control. Protein A beads coated with WT-RAGE V-Fc and RAGE V13-Fc were incubated with recombinant HMMR-HIS. Red rectangles highlight the HMMR-HIS protein band. **(B)** Western blot results showing the detection of IgG1 Fc, WT-RAGE V-Fc or RAGE V13-Fc. Anti-His beads coated with HMMR-HIS were incubated with WT-RAGE V-Fc and RAGE V13-Fc. Short exposure (Top) and long (bottom) exposure images were shown to highlight differences.

6.2.2 Immunoprecipitation and mass spectrometry revealed potential interactors of WT-RAGE V-Fc and RAGE V13-Fc in MDA-MB-231 human serum

To identify systemic interactors of WT-RAGE V-Fc and RAGE V13-Fc, I next performed another IP-MS experiment to determine potential interactors of WT-RAGE V-Fc and RAGE V13-Fc from human serum samples. Due to the presence of large quantities of IgG heavy and light chain in human serum, protein A magnetic beads were preferably bound to serum IgG rather than Fc-tagged WT-RAGE V and RAGE V13 (**Figure 6.3A**). To increase the presence of WT-RAGE V-Fc and RAGE V13-Fc on protein A beads, human serum was diluted 1 in 100. The MS results revealed that the diversity of potential interactors for both WT-RAGE V-Fc and RAGE V13-Fc was lower in human serum than in MDA-MB-231 cell lysate (**Figure 6.3B & C**). The RAGE V13-Fc-specific interactor

identified in human serum was HSPA5 (heat shock protein family A (Hsp70) member 5), also known as GRP78 (78-kDa glucose-regulated protein), Bip (Binding immunoglobulin protein) (**Figure 6.3C & D**).

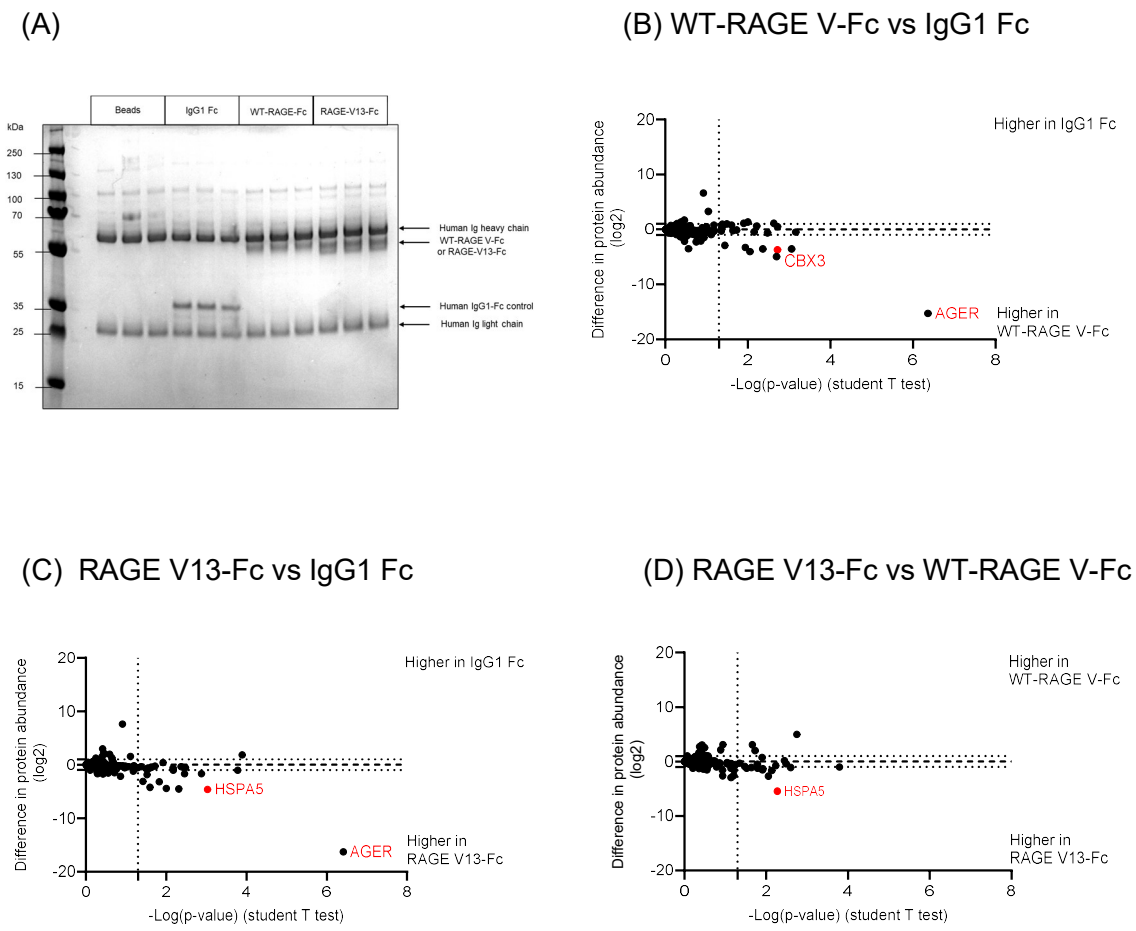
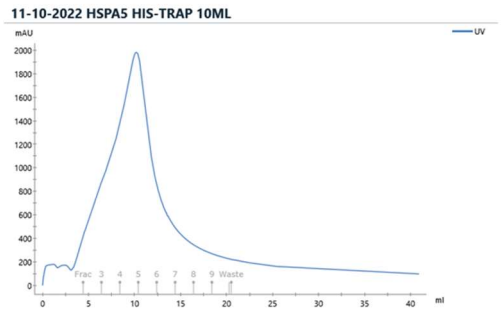


Figure 6.3. Immunoprecipitation and mass spectrometry revealed potential interactors of WT-RAGE V-Fc and RAGE V13-Fc in 1/100 diluted human serum. (A) SDS-PAGE showing the proteins in the pull-down samples of WT-RAGE V-Fc and RAGE V13-Fc. The highlighted bands are IgG1 Fc, WT-RAGE V-Fc, RAGE V13-Fc or molecules that interact with the magnetic beads or IgG1 Fc. Human immunoglobulin heavy chain and light chain were the major contaminants in the sample. **(B)** Volcano plot analysis of potential interactors identified in the IP samples. Potential interactors of IgG1 Fc (negative control), WT-RAGE V-Fc and RAGE V13-Fc were interchangeably compared. The negative and positive value of the difference in protein abundance indicates different treatment types. The enriched extracellular interactors are highlighted in red in each plot. 2-sample student test was used for comparing across treatment groups. Fold-change > 2 and q-value ≤ 0.05 were ranked as significant.

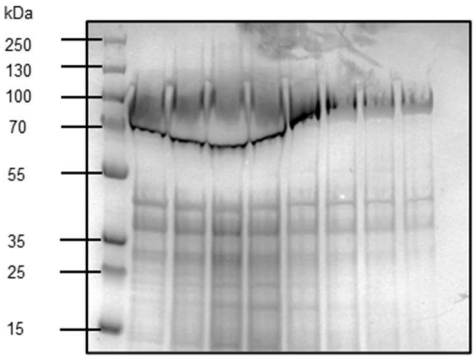
HSPA5/GRP78 was one of the most promising potential interactors of RAGE V13-Fc identified in human serum. Recombinant GRP78/HSPA5 was produced for further

analysis. Briefly, the GRP78 coding sequence with an N-terminal his-tag was transformed into *E. coli* BL21 for protein production. For affinity chromatography, all eluted fractions of GRP78-His were collected (**Figure 6.4A & B**). Size exclusion chromatography was then performed to further separate GRP78 from contaminants where thirteen fractions were collected and concentrated to 30 mg/ml (**Figure 6.4C, D & E**). The total yield was estimated to be around 45 mg per litre.

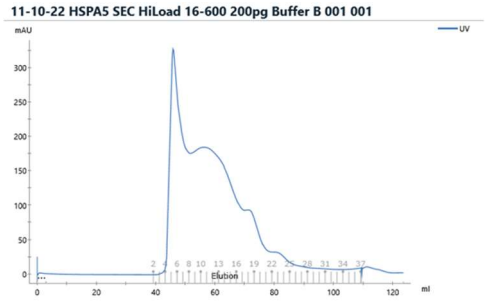
(A)



(B) His Trap FF Crude histidine-tagged protein purification columns (All collected)



(C)



(D) Hload 16/600 Superdex 200 pg SEC (Fraction 6-18 were collected) (E)

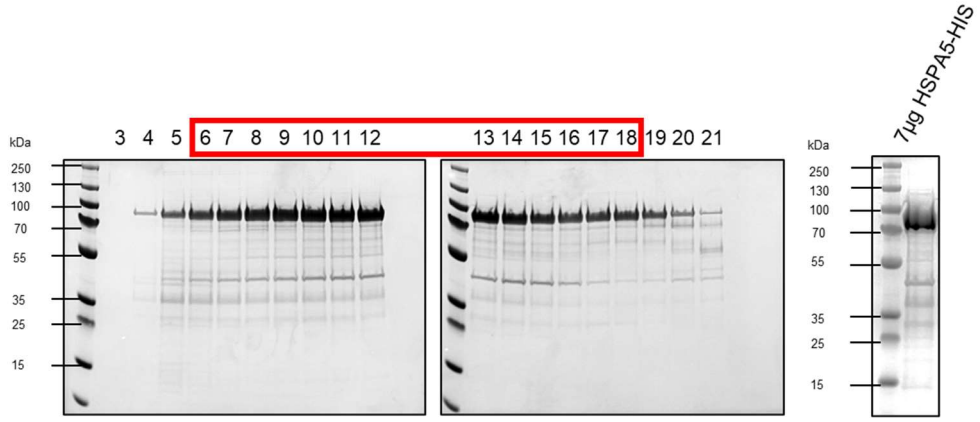


Figure 6.4 SDS-PAGE analysis showing the purification process of recombinant HSPA5-His/GRP78-His using Ni-NTA agarose affinity chromatography and SEC. Recombinant GRP78 was produced in *E.coli* BL21. The cell lysate was subject to affinity chromatography followed by SEC. **(A & B)** His Trap FF Crude histidine-tagged protein purification and its SDS-PAGE analysis. All eluted fractions were collected. **(C & D)** Hload 16/600 Superdex 200 pg SEC and its SDS-PAGE analysis. Fractions 6-18, which are highlighted in a rectangle, were collected. **(E)** SDS-PAGE results show the pooled purified recombinant HSPA5/GRP78.

To validate whether GRP78 is a direct interactor of WT-RAGE V-Fc and RAGE V13-Fc, reciprocal immunoprecipitation was performed. Recombinant GRP78-HIS was incubated with IgG1 Fc, WT-RAGE V-Fc and RAGE V13-Fc. The reaction mixture was subjected

to immunoprecipitation by using either anti-His or anti-Fc magnetic beads. A consistently positive result was obtained. IgG1Fc did not interact with GRP78 while both WT-RAGE V-Fc and RAGE V13-Fc were able to directly interact with GRP78 (**Figure 6.5A & B**). This finding suggests that GRP78 could be a novel interactor of the RAGE receptor. Also, according to the protein band intensity, RAGE V13-Fc bound more GRP78 than WT-RAGE V-Fc at a given GRP78 concentration.

(A) (B)

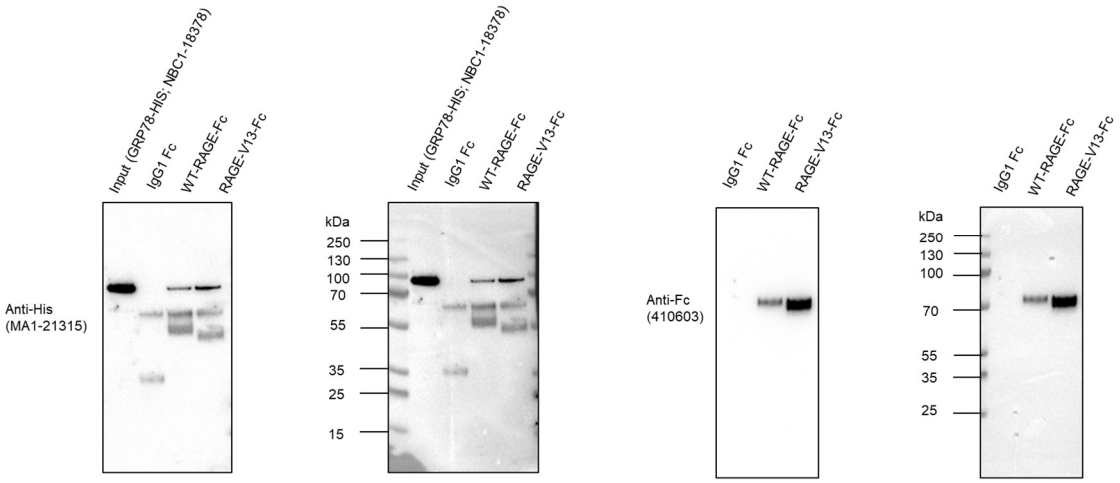


Figure 6.5. Reciprocal Immunoprecipitation showing that GRP78 could be a direct interactor of WT-RAGE V-Fc and RAGE V13-Fc. (A) Western blot results showing the detection of GRP78. Protein A beads coated with WT-RAGE V-Fc and RAGE V13-Fc precipitated GRP78-HIS (Left: No ladder, Right: Image overlay) **(B)** Western blot results showing the detection of IgG1 Fc, WT-RAGE V-Fc or RAGE V13-Fc. Anti-His beads coated with GRP78-HIS precipitated WT-RAGE V-Fc and RAGE V13-Fc. (Left: No ladder, Right: Image overlay).

The next step was to determine the binding affinity of WT-RAGE V and RAGE V13 to GRP78. Yeast cells that displayed WT-RAGE V and RAGE V13 were incubated with different concentrations of recombinant GRP78 (**Figure 6.6A & B**). The binding signal was quantified using flow cytometry. Compared to WT-RAGE, RAGE V13 had a 3-fold higher B_{max} than WT-RAGE V. The binding affinity of WT-RAGE V-Fc was not accurately determined due to low binding signals. Overall, yeast-displayed RAGE V13 demonstrated an ability to bind with more GRP78 than yeast-displayed WT-RAGE V at a given GRP78 concentration.

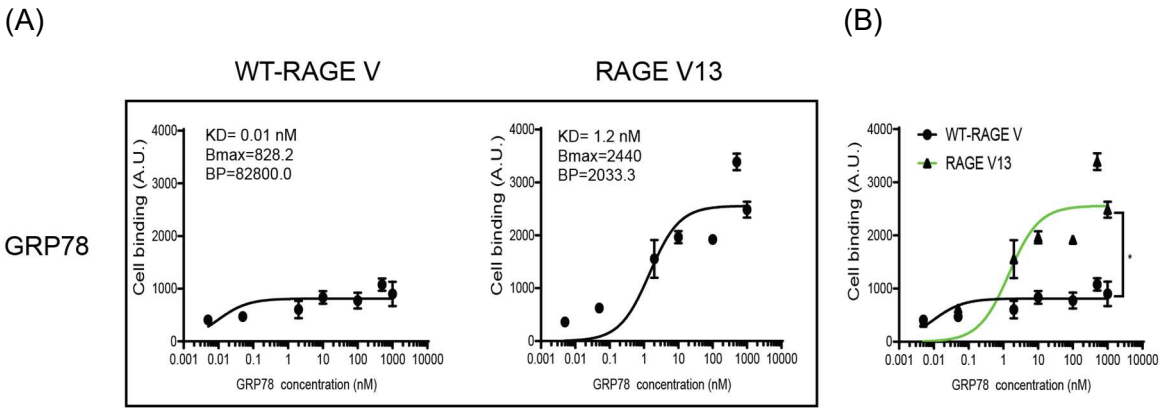


Figure 6.6. RAGE V13 exhibits higher B_{max} than WT-RAGE V to GRP78. The yeast cells that displayed WT-RAGE V or RAGE V13 were incubated with various concentrations of GRP78. The binding signal was quantified by using flow cytometry (N≥2). **(A)** Four-parameter sigmoidal curves showing the binding of yeast-displayed WT-RAGE and RAGE V13 to GRP78. **(B)** Summary of the binding assay. Four-parameter sigmoidal curves were fit by binding titrations. Error bars represent standard deviation of the mean. Calculated KD, B_{max} and BP are indicated on each plot. A.U., arbitrary units.

To test the ability of RAGE V13-Fc to sequester GRP78-His and rescue RAGE V13-Fc-induced growth inhibition in the MDA-MB-231 cell line, I performed a CCK8 proliferation assay. MDA-MB-231 cells were treated with RAGE V13-Fc, GRP78 or a combination treatment of RAGE V13-Fc and GRP78. GRP78 alone did not promote MDA-MB-231 cell growth, while GRP78 did demonstrate the ability to rescue RAGE V13-Fc-induced growth inhibition (**Figure 6.7**).

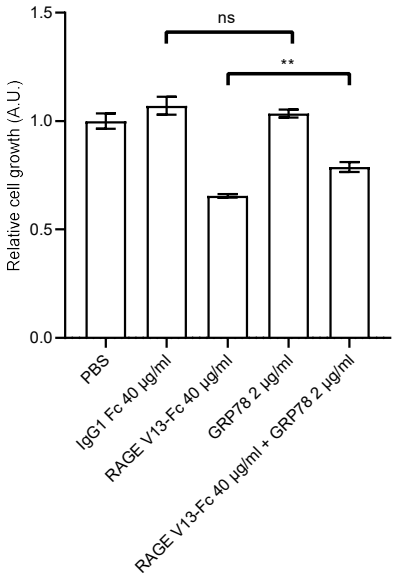


Figure 6.7. CCK8 proliferation assay showing that GRP78 could somewhat rescue RAGE V13-Fc-induced growth inhibition on MDA-MB-231. One thousand cells of MDA-MB-231 were seeded in 96-well plates overnight. MDA-MB-231 cells were treated with PBS, IgG1 Fc, RAGE V13-Fc, GRP78 or a combination treatment of RAGE V13-Fc and GRP78. CCK8 proliferation assays were performed 96 hours after the treatment (n=4). All data were normalised against PBS-treated samples. Error bars represent standard deviation of the mean. One-way ANOVA was performed to compare between treatment groups. **P<0.01 or not statistically significant (ns).

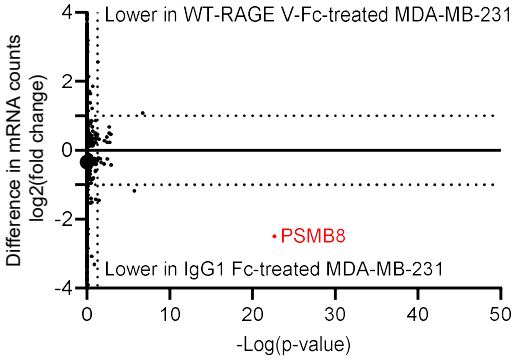
6.2.3 RNA Sequencing

To further understand the underlying anti-tumour mechanism of the RAGE V13-Fc, RNA sequencing was performed for MDA-MB-231 cells treated with IgG1 Fc, WT-RAGE V-Fc or RAGE V13-Fc for 24 hours. Clustering of RNA sequencing results suggested a distinct gene expression pattern of RAGE V13-Fc-treated samples relative to IgG1-Fc-treated or WT-RAGE V-Fc-treated samples (**Figure A2**). There were small differences between WT-RAGE V-Fc-treated and IgG1 Fc-treated samples (**Figure 6.8A**). This indicates that 40 µg/ml of WT-RAGE V-Fc did not have a major impact on MDA-MB-231 transcriptomics which might explain its limited anti-tumour activity. PSMB8 (Proteasome subunit beta type-8) was shown to be the only highly upregulated gene after WT-RAGE V-Fc treatment. In contrast, many alterations in gene expression were observed for RAGE V13-Fc-treated samples compared to the control group (**Figure 6.8B**). CXCL3 (C-X-C Motif Chemokine Ligand 3) was the most significantly downregulated gene in RAGE

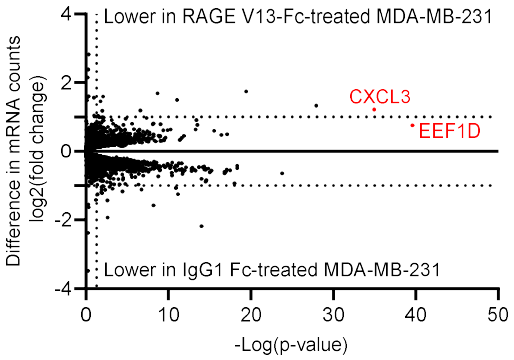
V13-Fc treated samples. Several genes, such as CYP3A5, CXCL1 and CXCL8 were also shown to be transcriptionally suppressed by RAGEV13-Fc treatment. All significantly differentially expressed genes are summarised in Appendix (**Table A1, A2 & A3**). The transcriptomic differences between WT-RAGE V Fc-treated and RAGE V13 Fc-treated samples are similar to those comparing IgG1 Fc-treated samples with RAGE V13 Fc-treated samples (**Figure 6.8C**).

According to GSEA analysis, none of the hallmark gene sets was significantly altered by WT-RAGE V-Fc treatment relative to the control (**Figure 6.8D**). Compared to WT-RAGE V-Fc-treated and IgG1 Fc-treated groups, several hallmark gene sets were significantly downregulated in RAGE V13-Fc-treated samples, including MYC target V1, MYC target V2, E2F targets, Unfolded protein response and Epithelial-mesenchymal transition pathway genes (**Figure 6.8D & E**). There were few significantly elevated gene sets other than PI3K AKT mTOR signalling after RAGE V13-Fc treatment. This suggests that RAGE V13-Fc results in the suppression of multiple tumour-promoting signalling pathways.

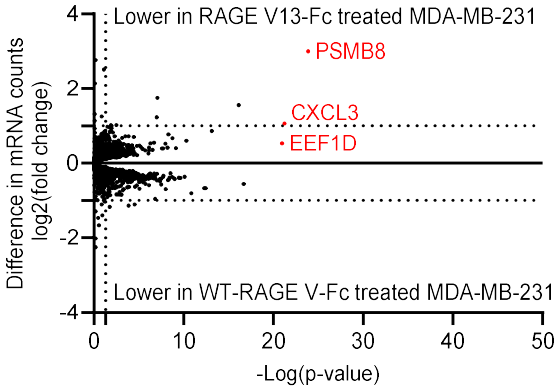
(A) WT-RAGE V-Fc vs IgG1 Fc



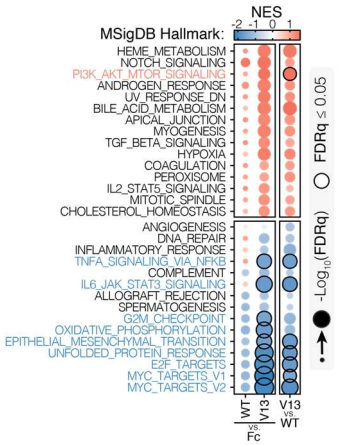
(B) RAGE V13-Fc vs IgG1 Fc



(C) WT-RAGE V-Fc vs RAGE V13-Fc

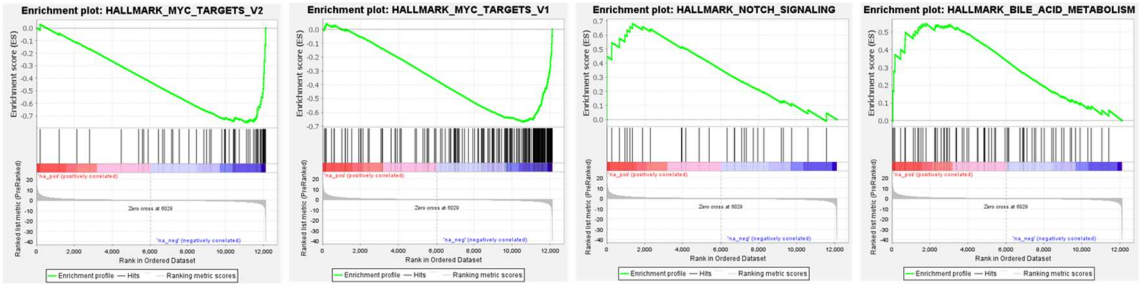


(D)



(E)

RAGE V13-Fc vs IgG1 Fc



RAGE V13-Fc vs WT-RAGE-Fc

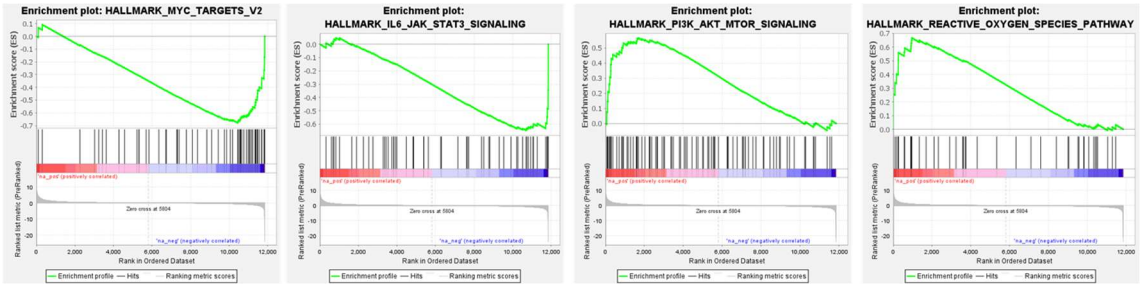


Figure 6.8. RNA sequencing results showing that RAGE V13-Fc treatment suppressed multiple pro-tumorigenic pathways in MDA-MB-231. MDA-MB-231 cells were treated with 40 µg/ml of IgG1 Fc, WT-RAGE V-Fc or RAGE V13-Fc for 24 hours. Total RNA was then extracted and converted to cDNA for RNA sequencing. **(A-C)** Volcano plots analysis of global changes in relative mRNA abundance. All treatment groups were Interchangeably compared. The negative and positive value of the difference in protein abundance indicates different treatment types. Several affected genes are highlighted in red in each plot. Wald test was used for comparing across treatment groups. Fold-change > 2 and q-value ≤ 0.05 were ranked as significant. **(D)** GSEA enrichment analysis indicates the enriched hallmarks in RAGE V13-Fc-treated samples compared to WT-RAGE V-Fc-treated and IgG1 Fc-treated samples. The MSigDB hallmarks shown here are the top 15 most positively enriched and the top 15 most negatively enriched hallmarks. The bubble size maps to the FDRq. The bubbles with a dark outline are enriched at a FDR <= 0.05. Colour maps to NES. **(E)** Enrichment plots for the top 2 upregulated and top 2 downregulated data sets enriched in GSEA hallmark analysis, showing the profile of the running ES Score and positions of gene set members. Figure (D) was generated with assistance of Mr Bruno Beernaert Dominguez.

RT-PCR was performed to verify RNA sequencing results. Total RNA was isolated and converted into a cDNA library for RT-PCR analysis. CXCL3 was shown to be the most significantly downregulated gene after RAGE V13-Fc treatment (**Figure 6.9**). Several genes were also downregulated in RAGE V13-Fc-treated samples including CYP3A5, PEG10, LCN2 (Lipocalin-2), IL8 (Interleukin 8), CXCL1 (chemokine (C-X-C motif) ligand 1), SAA2 (Serum Amyloid A2), LY6E. Notably, some of the affected genes were immune-related molecules such as LCN2, IL8, CXCL1 and SAA2.

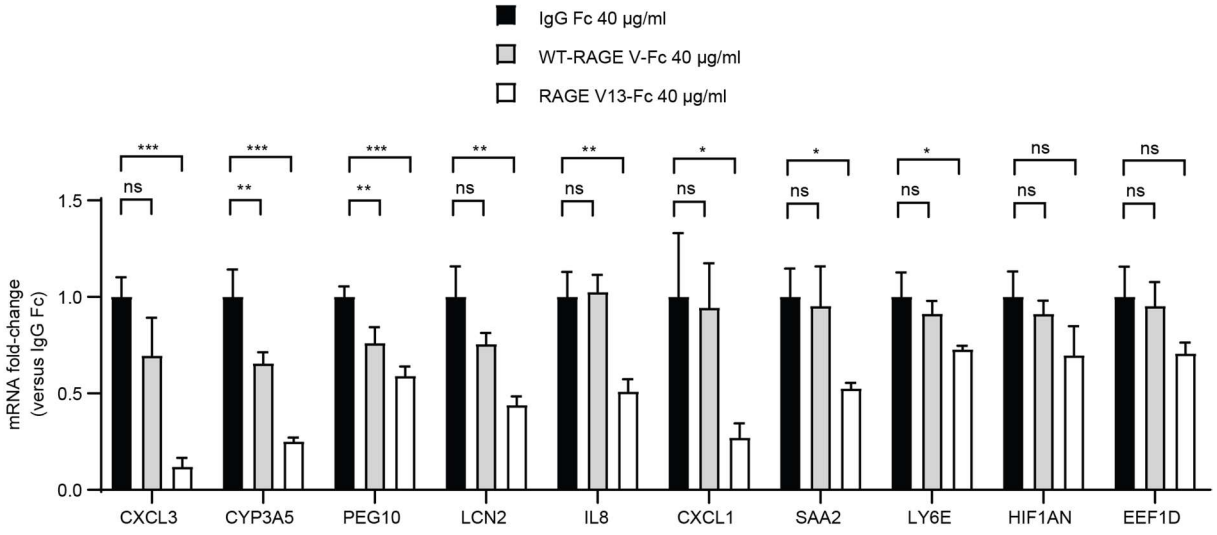


Figure 6.9. RT-PCR showing the relative mRNA fold-change of WT-RAGE V-Fc-treated and RAGE V13-Fc-treated MDA-MB-231 cells compared to IgG1 Fc-treated samples. MDA-MB-231 cells were treated with 40 µg/ml of IgG1, WT-RAGE V-Fc and RAGE V13-Fc for 24 hours before preparing RNA samples for RT-PCR. All data were normalised against IgG1 Fc-treated samples (N=3). Error bars represent standard deviation of the mean. One-way ANOVA was performed to compare between treatment groups. *P<0.05, **P<0.01 ***P<0.001 or not statistically significant (ns).

The next step was to validate the RNA sequencing results on the protein level. I studied the changes in CXCL3 protein level in both MDA-MB-231 cell lysate and cell culture supernatant after WT-RAGE V-Fc or RAGE V13-Fc treatment. CXCL3 protein level was unchanged in WT-RAGE V Fc-treated MDA-MB-231 cells but was significantly downregulated in RAGE V13-Fc-treated MDA-MB-231 cells (**Figure 6.10A**). RAGE V13-Fc treatment also caused a dose-dependent change in CXCL3 level in the MDA-MB-231 cells (**Figure 6.10B**). In the cell culture supernatant, low CXCL3 levels were found in RAGE V13-Fc-treated samples as well as a decrease in CXCL3 level in WT-RAGE V-Fc-treated samples (**Figure 6.10C & D**).

I undertook search for receptors that could be cross activated by RAGE ligands. Toll-like receptor 4 (TLR4) shared many common ligands with RAGE receptors such as HMGB1, S100 proteins, and Heat shock proteins (Jang et al., 2020). Moreover, TLR4, unlike RAGE, can result in IRF3 phosphorylation which regulates cytokine and chemokine production, including CXCL3 (Korostynski et al., 2021; Sakaguchi et al., 2011). It was therefore assumed that RAGE V13-Fc sequestered certain RAGE ligands that could activate TLR4 and promote CXCL3 production via IRF3. p-IRF3 was detected in untreated MDA-MB-231 (**Figure 6.10A & B**). In contrast, both WT-RAGE V-Fc and RAGE V13-Fc decreased p-IRF3, with RAGE V13-Fc being a more potent suppressor. RAGE V13-Fc treatment also resulted in a dose-dependent inhibitory effect on p-IRF3 levels (**Figure 6.10B**). Counter-intuitively, TBK1 (TANK-binding kinase 1), an IRF3 activator, was not affected by WT-RAGE V-Fc or RAGE V13-Fc treatment. Overall,

RAGE V13 seems to function as a TLR4 inhibitor that suppresses CXCL3 production through downregulating IRF3 activation.

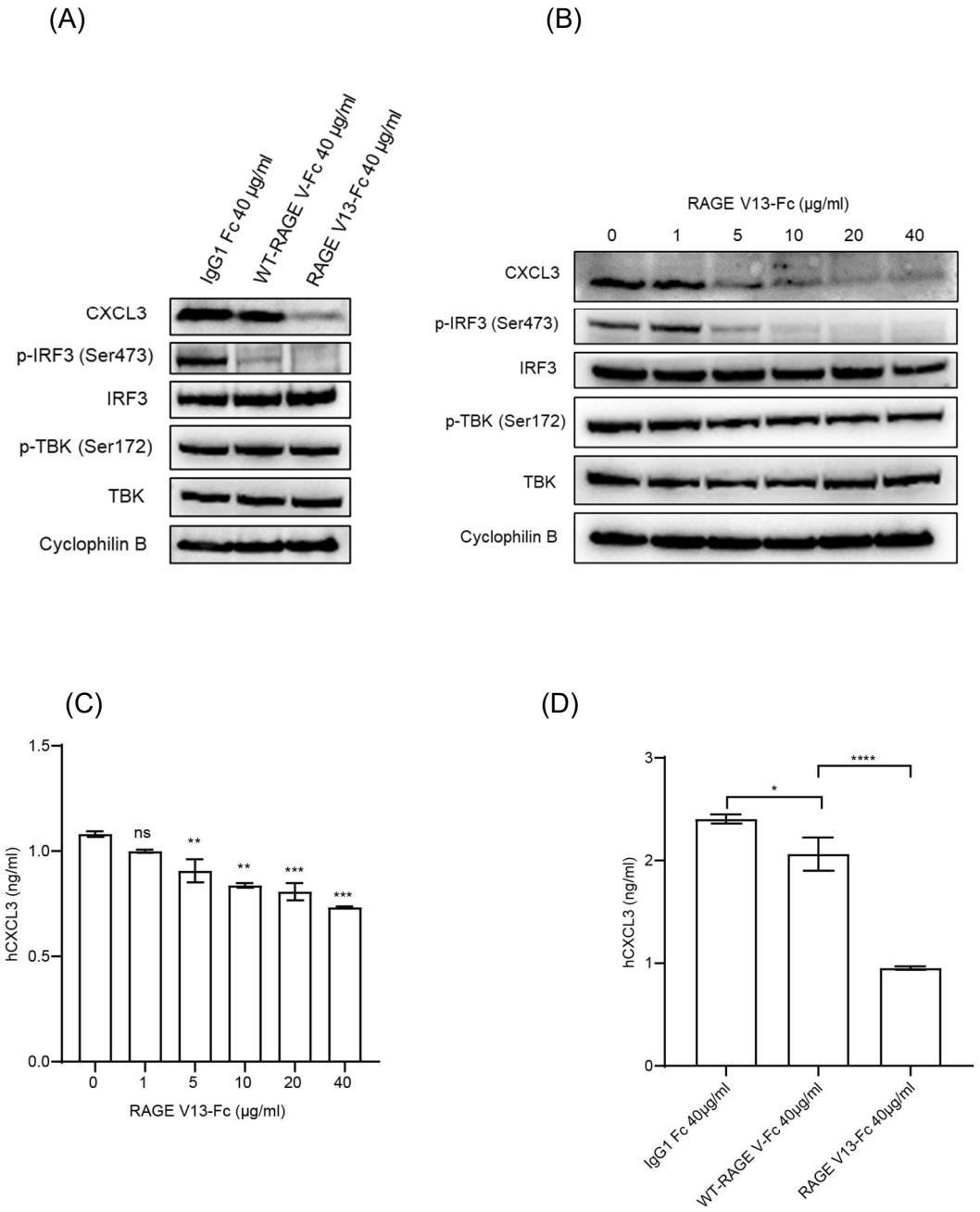


Figure 6.10. The effects of WT-RAGE V-Fc and RAGE V13-Fc on CXCL3 expression in MDA-MB-231. MDA-MB-231 cells were treated with 40 µg/ml of IgG1, WT-RAGE V-Fc or RAGE V13-Fc for 24 or 72 hours before cell lysate preparation or supernatant collection. **(A)** Western blot results showing that WT-RAGE V-Fc and RAGE V13-Fc suppress CXCL3 expression and IRF3 activation in MDA-MB-231 cells 24 hours post-treatment (N=3). **(B)** Western blot results demonstrating a RAGE V13-Fc-induced dose-dependent inhibition of CXCL3 and p-IRF3 in MDA-MB-231 cells 24 hours post-treatment (N=3). **(C)** CXCL3 ELISA showing the CXCL3 level in MDA-MB-231 cell culture supernatant 24 hours after being treated with different concentrations of RAGE V13-Fc

(N=2). **(D)** CXCL3 ELISA showing the CXCL3 level in MDA-MB-231 cell culture supernatant 72 hours after WT-RAGE V-Fc and RAGE V13-Fc treatment (N=3). All data were compared against IgG1 Fc-treated or untreated samples. One-way ANOVA was performed to compare between treatment groups. Error bars represent standard deviation of the mean. *P<0.05, **P<0.01 ***P<0.001, ****P<0.0001 or not statistically significant (ns).

To investigate whether CXCL3 downregulation is associated with RAGE V13-Fc-induced suppression of MDA-MB-231 cell growth and migration, I suppressed CXCL3 expression by siRNA. CCK8 proliferation assays demonstrated that CXCL3 knockdown delayed tumour cell growth by approximately 30% (**Figure 6.11A & B**). In contrast, the transwell migration assay indicated that siCXCL3-treatment had no inhibitory effects on MDA-MB-231 cell migration (**Figure 6.11C & D**). These findings suggest that CXCL3 might play a role in promoting MDA-MB-231 cell growth but does not contribute to MDA-MB-231 cell migration.

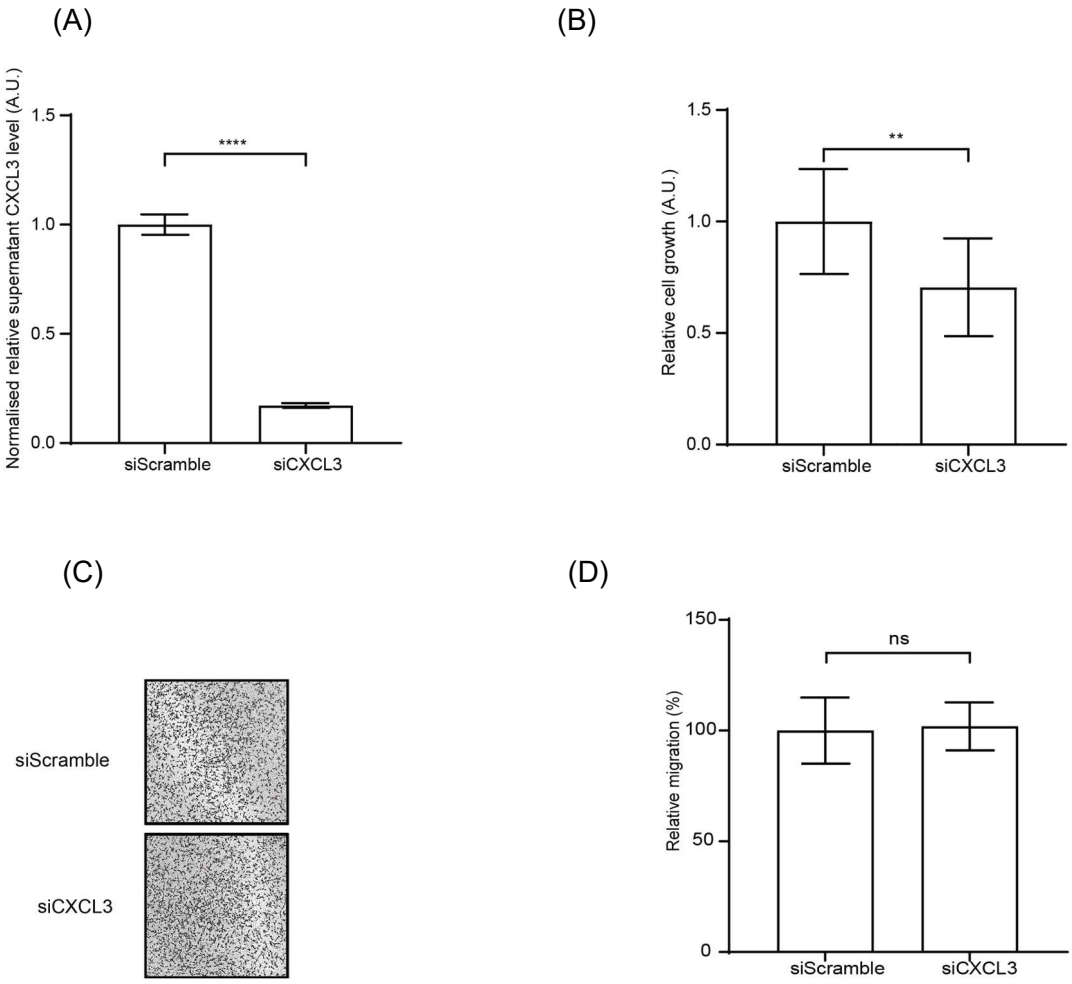


Figure 6.11. Knock-down of CXCL3 by siRNA inhibits MDA-MB-231 cell growth. One thousand MDA-MB-231 cells were plated in 96-well plates on the day before transfection. The transfected cells were incubated for 96 hours before measuring cell growth and 24 hours before transwell migration assay. **(A)** ELISA showing the normalised relative cell culture supernatant CXCL3 level (N=8). The relative CXCL3 level in siCXCL3-treated samples was calculated based on its relative cell growth and normalised against Siscramble-treated samples. **(B)** CCK8 proliferation assay showing the growth suppression caused by CXCL3 knockdown in MDA-MB-231 (N=12). **(C)** Representative images of migrated cells stained with crystal violet. The transfected MDA-MB-231 cells resuspended in serum-free medium were placed in the transwell inserts. DEME supplemented with 10% FBS was placed in the bottom chamber. After incubation at 37℃ for 24 hours, cells were stained with crystal violet for visualisation. **(D)** Relative percentage of the migrated cell (N=6). The migrated cells were quantified using Celigo. Two-sample student t-test was performed to compare between treatment groups. Error bars represent standard deviation of the mean. **P<0.01, ****P<0.0001 or not statistically significant (ns).

The effects of WT-RAGE V-Fc and RAGE V13-Fc treatment on protein expression in MDA-MB-231 were further investigated. MDA-MB-231 cells were treated with IgG1, WT-RAGE V-Fc or RAGE V13-Fc for 24 hours before the cell lysate preparation. Both RAGE

and TLR4 were detected in MDA-MB-231 cell lysate (**Figure 6.12**). Both WT-RAGE V-Fc and RAGE V13-Fc treatment did not result in the downregulation of C3, IGSF9B and EEF1D as indicated by RNA sequencing and RT-PCR results (**Data not shown**). Since both RAGE and TLR4 signalling could potentially be affected by WT-RAGE V-Fc and RAGE V13-Fc treatment, the downstream signalling pathways were investigated. Interestingly, NF-κB was activated by both WT-RAGE V-Fc and RAGE V13-Fc treatment, and RAGE V13-Fc alone seemed to suppress Akt1 activation (**Figure 6.12**). STAT3 signalling was not affected by either WT-RAGE V-Fc or RAGE V13-Fc treatment. Overall, Akt1 downregulation could be one of the underlying anti-tumour mechanisms of RAGE V13-Fc.

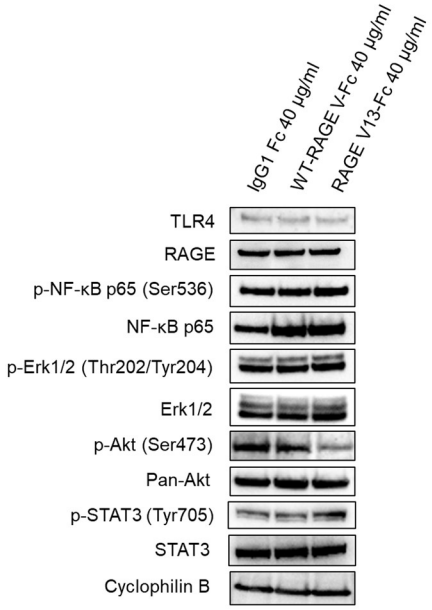


Figure 6.12. Western blot results showing the effects of WT-RAGE V-Fc and RAGE V13-Fc on protein expression in MDA-MB-231. MDA-MB-231 cells were treated with 40 µg/ml of IgG1, WT-RAGE V-Fc or RAGE V13-Fc for 24 hours before cell lysate preparation for western blot analysis.

6.3 Discussion

This chapter investigated the underlying anti-tumour mechanism of RAGE V13-Fc. I first focused on identifying potential interactors of WT-RAGE V-Fc and RAGE V13-Fc in both

MDA-MB-231 cell lysate samples and human serum samples. The majority of potential interactors of WT-RAGE V-Fc and RAGE V13-Fc identified in MDA-MB-231 cell lysate were DNA-binding or RNA-binding proteins due to their ability to directly interact with nucleic acids. Among them, there were over 400 WT-RAGE V-Fc-specific interactors and around 80 RAGE V13-Fc-specific interactors. The differences in ligand diversity may result from multiple factors. First, the mutations in RAGE V13-Fc might result in a drastic change in a dramatic change in its ability to bind certain types of ligands. Second, according to the MS results, unlike WT-RAGE V-Fc which preferentially interacted with DNA-binding proteins, RAGE V13-Fc precipitated more RNA-binding proteins which could be a result of their differences in DNA and RNA binding affinity (**Figure 6.1F**).

For the IP-MS (MDA-MB-231 cell lysate) results, HMMR was shown to be the top shared potential interactor of both WT-RAGE V-Fc and RAGE V13-Fc in MDA-MB-231 cell lysates (**Figure 6.1E**). However, reciprocal immunoprecipitation results demonstrated that HMMR might not be a direct interactor of WT-RAGE V-Fc or RAGE V13-Fc. HMMR can exist in both the cytosol and cell membrane, where it plays completely different roles. Intracellular HMMR was shown to regulate cell division by interacting with BRCA1 (Mateo et al., 2022). As a membrane protein, HMMR could interact with S100 proteins which are also RAGE ligands (Mateo et al., 2022). There are several possible explainations why HMMR was detected in the IP-MS experiment but not in the reciprocal IP experiement. WT-RAGE V-Fc and RAGE V13-Fc might be pulled down by HMMR via S100-RAGE complexes. It is also possible that RAGE interacts with the intracellular domain of HMMR, given that recombinant HMMR used for IP does not contain the intracellular moiety. Therefore, the ectodomain of HMMR is not likely to be a direct interactor of WT-RAGE V-Fc and RAGE V13-Fc.

GPRC5A and PDCD2L are two WT-RAGE V-Fc-specific potential interactors identified in the MDA-MB-231 cell lysate (**Figure 6.1B**). GPRC5A in breast cancer acts as a tumour

suppressor which inhibits EGFR signalling pathways (Yang et al., 2016). As an orphan receptor, there are currently no known ligands for GPRC5A (Richter et al., 2020). The role of PDCD2L in cancers remains unclear. Further studies will be required to determine the role of RAGE and its interaction with GPRC5A and PDCD2L.

PEG10 was shown to be a RAGE V13-Fc-specific potential interactor in MDA-MB-231 cell lysate (**Figure 6.1C**). As an RNA-binding protein, PEG10 protein specifically packages the PEG10 transcripts into a virus-like structure which could transfect other cells to promote PEG10 production (Segel et al., 2021). PEG10 has been demonstrated to be overexpressed in breast cancer and promote cell proliferation, migration and invasion (X. Li et al., 2016). Due to the ability of PEG10 to bind RNA, it is problematic to verify the interaction through IP. NMR crystallography would be recommended in future studies to understand the interplay between PEG10 and RAGE V13-Fc. Additionally, assuming PEG10 is not a direct interactor of RAGE V13-Fc, the enrichment of PEG10 in RAGE V13-Fc samples rather than WT-RAGE V-Fc samples could possibly be explained by RAGE V13-Fc being a more potent RNA binder than WT-RAGE V-Fc.

The second IP-MS experiment focused on identifying potential interactors of WT-RAGE V-Fc and RAGE V13-Fc in the human serum. There were significantly fewer potential interactors identified in the human serum than in the MDA-MB-231 cell lysate. This could be partially explained by the absence of nucleic acids in human serum. Also, the human serum was diluted 1 in 100, suggesting that only the interactors with high abundance or high binding affinity can be detected. The majority of the identified interactors were false positive signals caused by direct interactions between IgG1 Fc-binding protein A magnetic beads and components of human immunoglobulin heavy chains and light chains in human serum. In this case, all human immunoglobulin-associated proteins were excluded.

Chromobox protein homolog 3 (CBX3) is the only WT-RAGE V-Fc-specific potential interactor identified in both IP-MS (MDA-MB-231 cell lysate) and IP-MS (Human serum) analysis. CBX3, which belongs to the heterochromatin protein 1 family, plays a role in regulating gene expression by interacting with dimethylated and trimethylated histone 3Lys9 (H3K9) (Huang et al., 2017; Xu et al., 2022). Intracellularly, CBX3 is a histone binding protein that regulates gene expression (Cheutin et al., 2003). CBX3 was shown to be overexpressed in breast cancer and promotes tumour development (Liang et al., 2017). The function of extracellular CBX3 remains poorly understood. Since WT-RAGE V-Fc did not demonstrate sufficient anti-tumour activity, whether CBX3 is a direct interactor of WT-RAGE V-Fc was not further investigated.

HSPA5, also known as GRP78, was identified as a RAGE V13-Fc-specific interactor and the only direct interactor confirmed by reciprocal IP. GRP78 is a member of the heat shock protein 70 (Hsp70) subfamily which also includes Hsp72 (HSPA1A) and heat shock cognate 70 (Hsc70/HSPA8) (Evans et al., 2010). A previous study suggested that extracellular HSP70 proteins are RAGE ligands but which members of Hsp70 proteins involved in RAGE binding were not identified (Ruan et al., 2010). Taken together, our findings might suggest that GRP78 is a novel ligand of WT-RAGE V-Fc. GRP78 has three functionally different forms, including intracellular, membrane-bound and secreted GRP78. Intracellular GRP78 is commonly considered to be a master regulator of the unfolded protein response (UPR) in normal tissues (Gifford et al., 2016). Intracellular GRP78 mediates pro-survival autophagy and promotes drug resistance in breast cancer (Cook & Clarke, 2015). Membrane-bound GRP78 has been demonstrated to promote breast cancer proliferation and migration through activation of STAT3 pathways (Yao et al., 2015). Tumour-secreted GRP78 promotes resistance to bortezomib, an antiangiogenic drug, through triggering pro-survival signals (Kern et al., 2009). Secreted GRP78 could also play a role in differentiating bone marrow-derived mesenchymal stem

cells (BMSCs) into CAFs as well as polarising tumour-associated macrophages (La et al., 2018; Peng et al., 2013). Given that GRP78 has multiple tumour-promoting mechanisms, it is plasuible to assume that RAGE V13-Fc might have the ability to sequester tumour-secreted GRP78 and membrane-bound GPR78. Additionally, based on IP-MS (human serum) and binding assay results, RAGE V13-Fc seemed to have a higher binding capacity at a given ligand concentration, which might imply the superiority of RAGE V13-Fc over WT-RAGE V13-Fc in suppressing MDA-MB-231 growth.

RNA sequencing results revealed that RAGE V13-Fc treatment resulted in more significant transcriptomic changes than WT-RAGE V-Fc treatment compared to the control group. The majority of the changes were associated with the downregulation of gene expression. This inhibition of gene expression has also been reflected in GSEA results, where multiple enriched pro-tumorigenic hallmarks were downregulated in RAGE V13-Fc-treated samples. Among all RNA-seq data, CXCL3 was the most significantly downregulated gene. Western blot results suggested a lower p-IRF3 level in MDA-MB-231 after RAGE V13-Fc treatment.There is no previous study that has implicated CXCL3 and p-IRF3 as part of the RAGE downstream signalling pathway. However, TLR4, which shared multiple ligands with RAGE, has previously been shown to promote CXCL3 production through IRF3 activation (Suh et al., 2009). Therefore, I propose that dose-dependent inhibition of IRF3 activation and CXCL3 expression by RAGE V13-Fc treatment in MDA-MB-231 is the result of TLR4 signalling suppression. RT-PCR results indicated that CXCL1 and IL8 were similarly downregulated in RAGE V13-Fc-treated mice. This is consistent with a previous finding that CXCL1, CXCL3, and CXCL8 are co-regulated in breast cancer (Bieche et al., 2007). With p-IRF3 downregulation in the RAGE V13-Fc-treated MDA-MB-231 cells, the p-TBK1 level was unchanged. This lack of change in p-TBK-1 levels could be explained by the fact that IRF3 can be alternatively activated by another kinase, IKKepsilon (Fitzgerald et al., 2003).

Taking together, I propose that CXCL3 downregulation is not a result of direct inhibition of RAGE signalling but a suppression of TLR4 signalling.

The inhibitory effects of RAGE V13-Fc on MDA-MB-231 cell growth and migration is most probably a consequence of CXCL3 and IRF3 downregulation. I have shown that knockdown of CXCL3 in MDA-MB-231 can delay tumour cell growth. Similarly, several studies have demonstrated that CXCL3 could promote hepatocellular carcinoma, cervical cancer and prostate cancer growth by activating ERK1/2 (DiNatale et al., 2022; Qi et al., 2020; Xin et al., 2018). CXCL3 might play a similar growth-promoting role in TNBC. However, p-ERK1/2 downregulation was not detected in the RAGE V13-Fc-treated MDA-MB-231 cells (**Figure 6.12**). Moreover, CXCL3 was reported to be overexpressed in 1881 tumour tissues and shown to promote metastatic processes (See et al., 2014). CXCR2, a CXCL3 receptor, was also shown to be overexpressed in breast cancer tissues and involved in promoting invasion and metastasis (Nannuru et al., 2011). In contrast, in my study, I found that CXCL3 knockdown did not affect MDA-MB-231 cell migration. This suggests that the RAGE V13-Fc-triggered inhibitory effects on tumour cell invasion and metastasis might not be a result of CXCL3 downregulation but instead a result of sequestration of other chemoattractants produced by MDA-MB-231 such as AGEs.

p-IRF3 has recently been found to form a complex with Yes-associated protein (YAP) and TEAD4, which could result in nuclear retention and activation of YAP and thereby promote expression of YAP-TEAD4-regulated genes (Jiao et al., 2018). TEAD4 was shown to interact with the enhancer sequence of TRAM2 (Translocation Associated Membrane Protein 2), an important modulator of cell growth and metastasis (W. Li et al., 2016). In addition, IRF3 knock-down was shown to be able to suppress gastric cancer proliferation (Jiao et al., 2018). Overall, p-IRF3 downregulation could result in suppressed cell growth and cell mobility.

The RAGE V13-Fc treatment was also shown to modestly downregulate p-Akt1 in MDA-MB-231 and upregulate p-NF-κB levels (**Figure 6.12 & 6.15**). p-Akt1 downregulation could be a result of TLR4 suppression caused by RAGE V13-Fc treatment. it was shown that TLR4 could promote breast cancer cell migration through Akt/GSK3β/β-Catenin pathway (Li et al., 2017). This may also explain the RAGE V13-Fc-induced inhibtiory effects on TNBC migration and invasion. The upregulation of p-NF-κB caused by WT-RAGE V-Fc and RAGE V13-Fc treatment is consistent with a previous study where soluble RAGE can promote IFN-γ production through activating NF-κB in macrophages (Zhang et al., 2019).

In this chapter, several potential interactors of WT-RAGE V-Fc and RAGE V13-Fc were identified based on the IP-MS data. Among them, secreted GRP78 is of most interest because of its role in oncogenesis. RNA sequencing data revealed CXCL3 as the most downregulated gene in MDA-MB-231 after RAGE V13-Fc treatment. The RAGE V13-Fc triggered CXCL3 and p-IRF3 downregulation might be responsible for the inhibited cell growth and metastasis. To connect the IP-MS and RNA-seq data, TLR4 may serve as a possible link between CXCL3 and GRP78. However, the complexity of RAGE receptor-ligand interactions, including non-protein ligands, presents a challenge in fully understanding the anti-tumour mechanism of RAGE V13-Fc. Further investigations are necessary to provide a comprehensive analysis of the therapeutic potential of RAGE V13-Fc.

Chapter 7. General discussion and conclusion

7.1 Summary of BS7-10-Fc and its prospects

Our study found that the engineered TACI decoy, BS7-10 had an approximately 8-fold increase in binding affinity to both APRIL and BAFF compared to atacicept (**Figure 7.1**). In addition to improved binding affinity, BS7-10 also demonstrated an enhanced B_{max} to APRIL and BAFF compared to atacicept. Based on SPR results, I propose a two-binding-site model in BS7-10 where both CRD1 and CRD2 exhibit high affinity binding to both APRIL and BAFF. In addition, mutations near CRD1 in BS7-10 might contribute to the enhanced ligand binding affinity of CRD1, which in turn led to the increased B_{max}. In the B cell proliferation assay, BS7-10-Fc was found to be more effective than both WT-TACI-Fc and atacicept in sequestering BAFF. However, in the DLBCL mouse model, BS7-10-Fc did not significantly outperform atacicept in suppressing tumour growth. Although BS7-10-Fc had only modest activity against DLBCL, my findings unambiguously demonstrate its superiority in APRIL and BAFF binding over atacicept and WT-TACI-Fc.

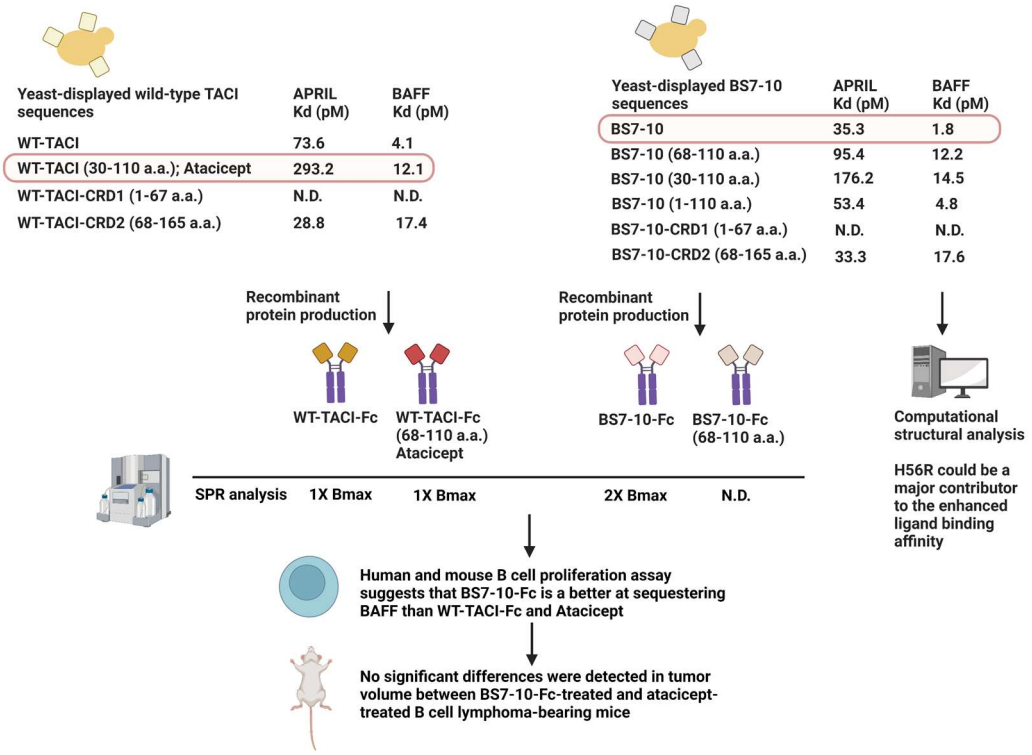


Figure 7.1. Diagrammatic summary of the TACI project from engineering high affinity TACI variants to *in vitro* and *in vivo* efficacy testing. BS7-10-Fc is a TACI decoy variant with modest superiority over atacicept. I suggested that BS7-10-Fc has the potential to be used for sequestration of APRIL and BAFF in DLBCL.

The disappointing *in vivo* results also raise the question of whether sequestering APRIL and BAFF are sufficient to adequately suppress DLBCL growth. The pro-tumorigenic mechanism of APRIL and BAFF in B cell lymphoma remains poorly understood. A previous study indicates that the role of APRIL in multiple myeloma is involved in protein translation machinery (Miao et al., 2022). Also, it was shown that glucose and RNA metabolism are upregulated in B cells treated with excessive BAFF (Yang et al., 2014). Sequestering APRIL and BAFF in B cell lymphoma seem to act in cytostatic manner by reducing cellular metabolism and delaying tumour growth. In comparison, BAFF-based CAR-T therapy, despite its potential side effects, such as causing cytokine storms, could still be a more effective treatment for B cell lymphoma patients because of its direct tumour-killing capability. For patients who are not suitable for CAR-T therapy, BS7-10-Fc treatment could be a promising approach for delaying DLBCL growth.

Regardless of having anti-tumour activity, BS7-10-Fc still possesses enormous therapeutic potential in other diseases such as systemic lupus erythematosus (SLE) (Vincent et al., 2014). As a chronic autoimmune disorder, SLE is characterised by the overexpression of autoantibodies and systemic accumulation of immune complexes, which could result in widespread organ damage (Merrill et al., 2018). The treatment approaches for SLE patients are severity-dependent. For individuals with mild to moderate SLE, immunosuppressive agents and anti-malarial drugs are sufficient to ease the symptoms (Durcan et al., 2019). However, there are almost no effective therapeutics against severe SLE other than glucocorticosteroids which only serve to slow down SLE progression (Durcan et al., 2019). Given that B cell-secreted autoantibodies are the main source of symptoms in SLE, suppressing B cell activity by sequestering APRIL and BAFF could theoretically reduce autoantibody production and alleviate tissue damage.

Telitacicept is a WT-TACI decoy which is currently undergoing a clinical Phase III trial for the treatment of SLE (Fan et al., 2022). Compared to atacicept, Telitacicept can be produced at higher levels in Chinese hamster ovary (CHO) cells by removing a proprotein convertase cleavage site (Fan et al., 2022). Both BS7-10-Fc and BS7-10-Fc (68-110 a.a.) demonstrated higher binding affinity than atacicept, and BS7-10-Fc (68-110 a.a.) has a yield of 130 mg/L compared to atacicept 18 mg/L. Therefore, if TACI inhibitors ultimately get approved for the treatment of SLE, BS7-10-Fc and BS7-10-Fc (70-110 a.a.) would prove more cost-effective and potentially more efficacious for the treatment of SLE.

7.2 Summary of RAGE V13-Fc and its prospects

RAGE V13 is an engineered high affinity RAGE V domain variant that has an enhanced B_{max} to multiple RAGE ligands compared to wild-type RAGE V. I have demonstrated that RAGE V13-Fc has more potent anti-tumour activity than WT-RAGE V-Fc both *in vitro* and *in vivo* (**Figure 7.2**). Briefly, RAGE V13-Fc had an enhanced ability to suppress TNBC cell proliferation, migration and invasion. Also, both WT-RAGE V-Fc and RAGE V13-Fc inhibited NK cell and CD8+ T cell migration. In TNBC mouse models, RAGE V13-Fc suppressed tumour growth and lung metastasis. In terms of the underlying anti-tumour mechanism, RAGE V13-Fc treatment inhibits CXCL3 and IRF3 phosphorylation in MDA-MB-231 cells. Given that IRF3 and CXCL3 have not been implicated in the downstream signaling of RAGE, we propose that RAGE V13-Fc sequesters certain ligands that could pleiotropically interact with multiple receptors. The secreted GRP78, identified as a novel potential interactor for both WT-RAGE V-Fc and RAGE V13-Fc based on MS and reciprocal IP results, could be the RAGE target ligand responsible for promoting TNBC growth. Such a hypothesis is based on the fact that GRP78 is a member of HSP70 family which can activate multiple receptors including RAGE and TLR4 (Somensi et al., 2017). Also, TLR4 but not RAGE have the ability to activate IRF3 and

promote CXCL3 expression (Suh et al., 2009). Therefore, RAGE V13-Fc might target GRP78, which could lead to TLR4 suppression followed by phospho-IRF3 and CXCL3 downregulation. I have also found that CXCL3 knock-down in MDA-MB-231 cells suppresses MDA-MB-231 cell growth. However, the RAGE V13-Fc-induced inhibition on cell mobility remains largely unknown. Taken together, the anti-tumour mechanism of RAGE V13-Fc is complex given the nature of RAGE being a multiligand receptor.

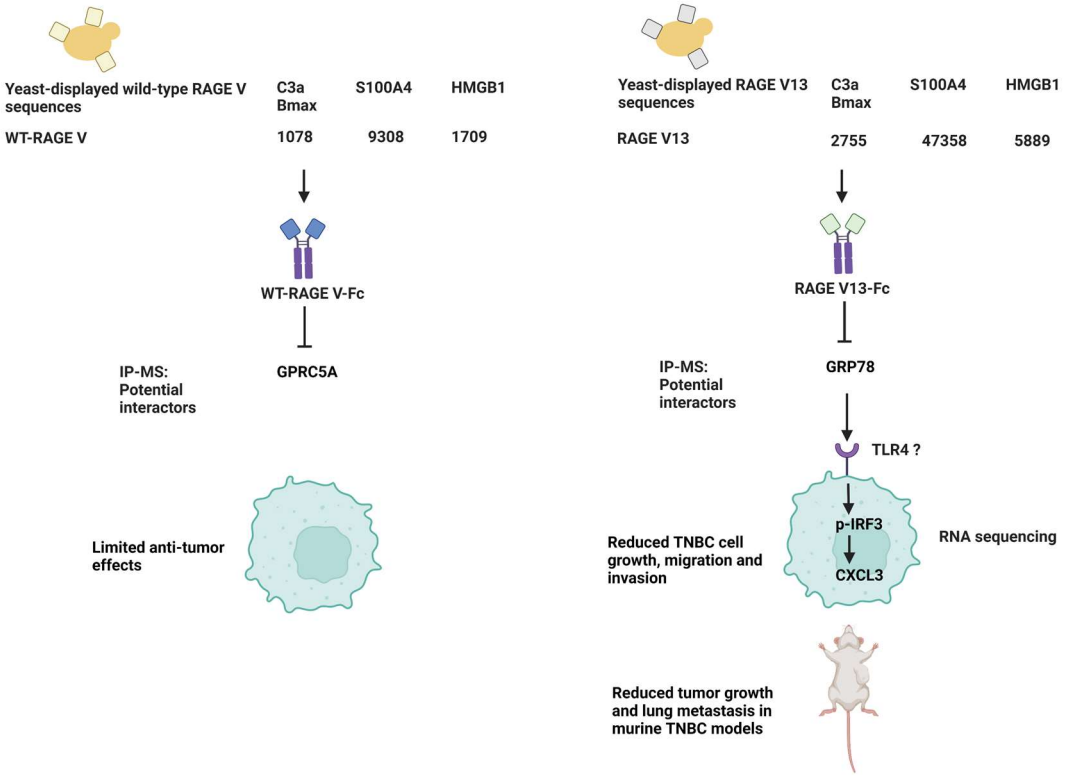


Figure 7.2. Diagrammatic summary of RAGE project from engineering the high affinity RAGE V variants, to *in vitro* and *in vivo* efficacy testing and to investigating underlying anti-tumor mechanism. RAGE V13-Fc had an enhanced B_{max} to multiple ligands and showed superior anti-tumor activity over WT-RAGE V-Fc. However, the underlying anti-tumor mechanism remains poorly understood and needs to be further investigated.

Given that RAGE has been implicated in diabetes, RAGE V13-Fc might be able to provide dual benefits for TNBC patients with diabetes. RAGE signalling has been reported to increase the risk of breast cancer in diabetic patients (Garcia-Jimenez et al., 2016). There are three critical factors in diabetic patients associated with higher cancer

risks which includes hyperinsulinemia, hyperglycemia and inflammation (Gallagher & LeRoith, 2015; Giovannucci et al., 2010). As a result of insulin resistance in type II diabetes patients, hyperinsulinemia has been linked with cancers (Perseghin et al., 2012). Higher insulin level could promote cancer growth by increasing expression of insulin like growth factor-1 (IGF-1) in breast cancer (Gallagher & LeRoith, 2010). Around 20% -40% of TNBCs are IGF-1 receptor positive, and this phenotype is associated with poor patient survival (Farabaugh et al., 2015). Hypoglycemia could not only establish a high carbohydrate environment to meet the demands of increased metabolic process in cancers but also elevate the production of AGEs, a RAGE ligand involved in promoting oncogenesis (Duan et al., 2014; K. J. Lee et al., 2018). Inflammation is a well-documented trait in both cancer and diabetes (Chhipa et al., 2019). Diabetic conditions could result in elevated production of proinflammatory RAGE ligands including S100 and HMGB1 which also play a role in promoting TNBC growth (Nogueira-Machado et al., 2011). For example, TLR4-HMGB1 signaling was shown to cause neuroinflammation and neuropathic pain in diabetic patients, and RAGE-HMGB1 promote breast cancer invasion and drug resistance (Amornsupak et al., 2022; Chhipa et al., 2019).

Cancer patients with diabetes have been shown to be more likely to have diabetic complications than normal diabetic patients and tends to have worse overall survival than cancer patients without diabetes (Farabaugh et al., 2015; Vissers et al., 2015; Worndl et al., 2018). A potential underlying mechanism behind the exacerbation of cancer progression and diabetic complications in diabetic breast cancer patients could be the mutually augmented RAGE and TLR4 signaling. Inflammation in both cancer and diabetic conditions results in the release of numerous RAGE ligands which could promote progression of both diseases. Therefore, RAGE V13-Fc has the potential to be a therapeutic for the treatment of diabetic TNBC patients.

Currently, no monoclonal antibodies with a similarly promiscuous target specificity as RAGE V13-Fc have been proposed for therapeutic usage. A monoclonal antibody with such degree of target specificity would never be considered as a treatment approach for cancer because of unpredictable outcomes and increased off-target effects. With the unique properties of the engineered multiligand decoy receptors including enhanced ligand binding ability, inherent specificity and immunotolerance, RAGE V13-Fc demonstrated the capacity of suppressing tumor growth and metastasis without causing detectable side-effects in animal models. As the first of its kind, this study also elaborated the feasibility of using engineered pattern recognition receptor for the treatment of TNBC.

7.3 What factors determine the success of affinity maturation?

Engineering both BS7-10 and RAGE V13 involved the usage of yeast surface display technology. Library generation relies heavily on error-prone PCR to generate mutant decoy receptor sequences. Choosing a correctly tailored, engineerable decoy receptor sequence template is essential for creating a high quality mutant library. Empirically, I summarise several factors that need to be considered when designing the template decoy receptor sequences.

1. A shorter decoy receptor sequence is desired. Since the mutation rate was controlled to be around 10%, a longer sequence means a larger number of mutations. This could increase the chance of introducing a pre-mature stop codon and reduce the number of functional variants in the library. The size of decoy receptor variants developed by our lab group ranges from 40 – 100 amino acid residues (such as AXL, BCMA, PD-1, RAGE, TACI).
2. Tryptophan is not a desired amino acid in the decoy receptor sequence. UGG is the only codon encoding tryptophan which could be easily converted into a stop codon like UAG and UGA with a single point mutation. Premature stop codons are more likely to be generated at tryptophan residues than other amino acid

residues. The RAGE V domain contains 3 tryptophan amino acid residues which result in a relatively lower number of functional RAGE V variants. Removing the tryptophan containing sequences that are unnecessary for ligand binding would be the best solution. Alternatively, engineering tRNA or using small molecules that promote translational readthrough could be a plausible solution if the ligand binding domain has a large number of tryptophan (Lueck et al., 2019).

3. Receptors composed of immunoglobulin (Ig)-like domains are advantageous. Both Axl and RAGE receptor contains Ig-like domains which can be easily produced as IgG1 Fc fusion proteins without the need to tailor the ectodomain. In addition, the Fc fragment could enhance the ligand binding affinity of Ig-like domains. For example, the fusion of IgG1 Fc with affinity-enhanced Axl variant increases the ligand binding affinity by 100-fold (Kariolis et al., 2014).
4. Receptors with less structural flexibility could be more tolerant to high mutation burdens. For example, a rigid receptor that has intricate intramolecular interactions is more likely to maintain the structural integrity after a point mutation compared to a flexible receptor stabilised by less intramolecular interactions. Theoretically, creating a mutant library with lower mutation rate for the flexible structures would provide more functional mutants.
5. Receptors with a high level of post-translational modifications such as glycosylation are not desired. First, post-translational modifications (PTM) usually prevent certain self-antigens from being exposed in the environment. Mutations at the modification sites could increase the immunogenicity of decoy receptor. Second, changes in amino acid sequences are less likely to enhance ligand binding affinity if PTM is directly involved in ligand binding. It has been shown that receptor glycosylation could be directly involved in ligand binding (Margraf-Schonfeld et al., 2011).

6. The mutant library of multi-ligand receptors is likely to contain variants that could generate false positive signals by interacting directly with anti-ligand antibodies. Multi-ligand receptors such as the RAGE receptor has a fairly “forgiving” and “promiscuous” specificity. The variants of these receptors could inherit the multi-ligand features and potentially interact with a novel group of epitopes. For the binding assay, ligands and anti-ligand antibodies are both selective pressures. Variants that gain the ability to interact with the antibody would give rise to false-positive signals and become the dominant population in the sorting library. In this case, false positive signals are more likely to be generated in a mutant library of multi-ligand receptors. To tackle this issue, a counter-selective approach could be applied to minimise the false-positive population by filtering out the antibody binders. Alternatively, a new set of ligands with specific tags and antibodies can be used to avoid the false positive population.

7.4 Yeast surface display is a better approach than phage display for engineering high affinity decoy receptors

Currently, the most extensively used approaches for protein affinity maturation are phage display and yeast display. There are several reasons why yeast surface display instead of phage display was used for decoy receptor affinity maturation in this study. First, yeast surface display is a more controllable process where the desired population with certain binding affinities can be accurately collected during FACS screening while phage display screening is subject to simple washing steps (Boder et al., 2012). Second, unlike phage, yeast cells use eukaryotic translational machinery to display target proteins which reduces chances of protein misfolding and employs proper post-translational modifications. This is particularly important for this study given that the wild-type receptors including RAGE and TACI have a human origin. Third, the binding affinity of yeast-displayed decoy receptor can easily be determined by using flow cytometry.

7.5 Limitations of yeast-surface display-based affinity maturation process

Yeast surface display technology has its limitations. First, there are 20^{50} difference protein sequence combinations for a protein comprised of 50 amino acids. The yeast library size ranges from 10^7 to 10^{10} variants which only accounts for a trivial fraction of all possible variants (Benatuil et al., 2010). Second, many of variants cannot be properly expressed by yeast cells which further limits the size of functional library. As a translational-based affinity maturation process, codon usage, mRNA secondary structure and PTM could have a negative impact on production of decoy receptor variants (Brule & Grayhack, 2017; Hall et al., 1982). The fused genetic material (aga2) might not only reduce translational efficacy but also distort decoy receptor structure. Third, yeast cell wall is negatively charged which could increase the risk of non-specific interaction between yeast cell wall and target ligand (Kregiel et al., 2012). Fourth, each yeast cell displays around 1×10^4 to 1×10^5 decoy receptors which could promote multivalent ligand binding. It was shown that RAGE ligands tend to oligomerise (Sitkiewicz et al., 2013). This suggests that the FACS sorting process might enrich variants with high ligand avidity instead of affinity (Sheehan & Marasco, 2015). Avidity is a measurement of accumulated strength of multivalent interactions (Gaspar & De Gaspari, 2021). Fifth, sequencing results of twenty clones picked from the last round of sorting library are not a comprehensive and informative representation of the population. Combining yeast display with next generation sequencing could provide more insight into the enriched high affinity mutations at a population level and avoid omitting affinity-enhancing mutations in the library (Nannini et al., 2021).

7.6 Golden Gate cloning coupled with error-prone PCR to create DNA sequence with regional mutations.

Randomly introducing mutations into the decoy receptor sequences may not be suitable for all receptors. For the RAGE project, a vast majority (> 95 %) of the unsorted yeast-displayed RAGE V variants were not functional which indicates that certain mutations in RAGE could have a detrimental effect on the ligand binding. Avoiding mutating these critical sites could be important for generating variants with an improved ligand binding affinity. For the DNA sequencing data of the TACI project, there were almost no mutations around CRD2. Computational structural analysis also indicated an almost saturated surface complementarity in CRD2-APRIL and CRD2-BAFF complexes, suggesting that an improvement on the ligand binding cannot be made by introducing mutations in the CRD2. To this end, I conceptualised a new approach to create a mutant library of decoy receptor variants with mutations only in specifically designed regions with high potential of developing affinity-enhancing mutations (**Figure 7.3**). This approach aims to create tailored decoy receptor mutant libraries by using computational analysis, Golden gate cloning and error-prone PCR.

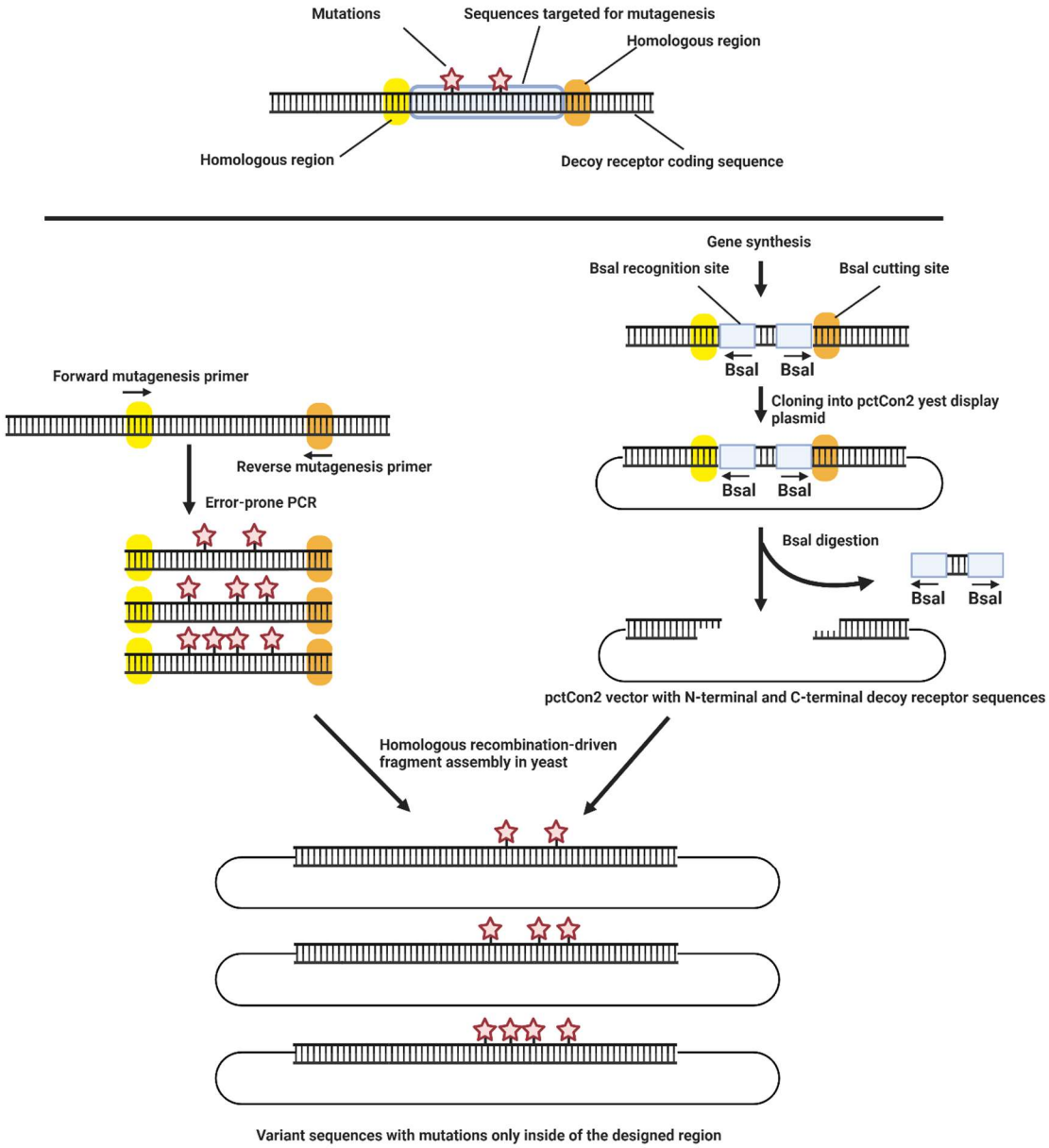


Figure 7.3. Concept of partial coding sequence mutagenesis by combining golden gate cloning with error-prone PCR. The partial receptor coding sequence of interest is amplified and mutagenized by using Error-prone PCR. The plasmid is designed to contain a decoy receptor coding sequence that has an insertion of two opposite BsaI recognition sites in place of the region of interest. BsaI digestion create overhangs homologous to the mutagenised PCR products. Seamless assembly of mutagenized sequences can then be performed by yeast-driven homologous recombination.

With the advancement of computational biology and artificial intelligence, the structural prediction of protein-protein interactions becomes more accessible and reliable. The first step of the conceptualised approach is to obtain the structural information through computational methods which could identify the binding interface with high surface

complementarity. The region with high surface complementarity would not be mutagenised. Second, golden-gate cloning coupled with error-prone PCR could create partially mutated decoy receptor sequences (**Figure 7.3**). Golden-gate cloning allows seamless ligation of multiple DNA fragments by using type IIS restriction enzymes which recognise specific sequences and directionally cleave random sequences next to the recognition sites (**Figure 7.3**) (Marillonnet & Grutzner, 2020). BsaI, the most commonly used type IIS restriction enzyme, is located inside of the decoy receptor coding sequence that has been cloned into the pctCon2 plasmids (**Figure 7.3**). Upon enzymatic digestion, the BsaI recognition site would be removed and leave two sticky ends on the pctCon2 vector. The sticky ends are part of decoy receptor coding sequences and homologous to the N-terminal and C-terminal regions of error-prone PCR products. Yeast-driven homologous recombination allows assembly of the specially designed vectors with mutagenized partial decoy receptor coding sequences. The same downstream procedures would be followed as indicated in section 3.2.1.

In this study, I used yeast display-based affinity maturation processes for engineering high affinity TACI and RAGE ectodomains for treatment of cancers. Our results showed that BS7-10-Fc demonstrated an enhanced ligand binding affinity and similar efficacy in DLBCL animal model compared to atacicept. Furthermore, RAGE V13-Fc was the first affinity-enhanced pattern recognition receptor developed so far which demonstrated a superior anti-tumor activity against TNBC than its wild-type counterpart. Both decoy receptor variants were functional and effectively sequestered their corresponding ligands. As protein-based biologics, these decoy receptors have the potential to be used in different disease models to benefit patients. In addition, a more rational and efficient approach to engineering receptor-based therapeutics could be achieved in the future by combining computational analysis, golden gate cloning and yeast surface display.

References

Abramson, J. S., Palomba, M. L., Gordon, L. I., Lunning, M. A., Wang, M., Arnason, J., Mehta, A., Purev, E., Maloney, D. G., Andreadis, C., Sehgal, A., Solomon, S. R., Ghosh, N., Albertson, T. M., Garcia, J., Kostic, A., Mallaney, M., Ogasawara, K., Newhall, K., . . . Siddiqi, T. (2020). Lisocabtagene maraleucel for patients with relapsed or refractory large B-cell lymphomas (TRANSCEND NHL 001): a multicentre seamless design study. *Lancet*, *396*(10254), 839-852. https://doi.org/10.1016/S0140-6736(20)31366-0

Abu-Rish, E. Y., Amrani, Y., & Browning, M. J. (2013). Toll-like receptor 9 activation induces expression of membrane-bound B-cell activating factor (BAFF) on human B cells and leads to increased proliferation in response to both soluble and membrane-bound BAFF. *Rheumatology (Oxford)*, *52*(7), 1190-1201. https://doi.org/10.1093/rheumatology/ket006

Akirav, E. M., Preston-Hurlburt, P., Garyu, J., Henegariu, O., Clynes, R., Schmidt, A. M., & Herold, K. C. (2012). RAGE expression in human T cells: a link between environmental factors and adaptive immune responses. *PLoS One*, *7*(4), e34698. https://doi.org/10.1371/journal.pone.0034698

Amornsupak, K., Thongchot, S., Thinyakul, C., Box, C., Hedayat, S., Thuwajit, P., Eccles, S. A., & Thuwajit, C. (2022). HMGB1 mediates invasion and PD-L1 expression through RAGE-PI3K/AKT signaling pathway in MDA-MB-231 breast cancer cells. *BMC Cancer*, *22*(1), 578. https://doi.org/10.1186/s12885-022-09675-1

Austerberry, J. I., Thistlethwaite, A., Fisher, K., Golovanov, A. P., Pluen, A., Esfandiary, R., van der Walle, C. F., Warwicker, J., Derrick, J. P., & Curtis, R. (2019). Arginine to Lysine Mutations Increase the Aggregation Stability of a Single-Chain Variable Fragment through Unfolded-State Interactions. *Biochemistry*, *58*(32), 3413-3421. https://doi.org/10.1021/acs.biochem.9b00367

Avalos, A. M., Kiefer, K., Tian, J., Christensen, S., Shlomchik, M., Coyle, A. J., & Marshak-Rothstein, A. (2010). RAGE-independent autoreactive B cell activation in response to chromatin and HMGB1/DNA immune complexes. *Autoimmunity*, *43*(1), 103-110. https://doi.org/10.3109/08916930903384591

Bangert, A., Andrassy, M., Muller, A. M., Bockstahler, M., Fischer, A., Volz, C. H., Leib, C., Goser, S., Korkmaz-Icoz, S., Zittrich, S., Jungmann, A., Lasitschka, F., Pfitzer, G., Muller, O. J., Katus, H. A., & Kaya, Z. (2016). Critical role of RAGE and HMGB1 in inflammatory heart disease. *Proc Natl Acad Sci U S A*, *113*(2), E155-164. https://doi.org/10.1073/pnas.1522288113

Bardia, A., Mayer, I. A., Diamond, J. R., Moroose, R. L., Isakoff, S. J., Starodub, A. N., Shah, N. C., O'Shaughnessy, J., Kalinsky, K., Guarino, M., Abramson, V., Juric, D., Tolaney, S. M., Berlin, J., Messersmith, W. A., Ocean, A. J., Wegener, W. A., Maliakal, P., Sharkey, R. M., . . . Vahdat, L. T. (2017). Efficacy and Safety of Anti-Trop-2 Antibody Drug Conjugate Sacituzumab Govitecan (IMMU-132) in Heavily Pretreated Patients With Metastatic Triple-Negative Breast Cancer. *J Clin Oncol*, *35*(19), 2141-2148. https://doi.org/10.1200/JCO.2016.70.8297

Belnoue, E., Pihlgren, M., McGaha, T. L., Tougne, C., Rochat, A. F., Bossen, C., Schneider, P., Huard, B., Lambert, P. H., & Siegrist, C. A. (2008). APRIL is critical for plasmablast survival in the bone marrow and poorly expressed by early-life bone marrow stromal cells. *Blood*, *111*(5), 2755-2764. https://doi.org/10.1182/blood-2007-09-110858

Benatuil, L., Perez, J. M., Belk, J., & Hsieh, C. M. (2010). An improved yeast transformation method for the generation of very large human antibody libraries. *Protein Eng Des Sel*, *23*(4), 155-159. https://doi.org/10.1093/protein/gzq002

Bertucci, F., Ng, C. K. Y., Patsouris, A., Droin, N., Piscuoglio, S., Carbuccia, N., Soria, J. C., Dien, A. T., Adnani, Y., Kamal, M., Garnier, S., Meurice, G., Jimenez, M., Dogan, S., Verret, B., Chaffanet, M., Bachelot, T., Campone, M., Lefeuvre, C., . . . Andre, F. (2019). Genomic characterization of metastatic breast cancers. *Nature*, *569*(7757), 560-564. https://doi.org/10.1038/s41586-019-1056-z

Bianchini, G., Balko, J. M., Mayer, I. A., Sanders, M. E., & Gianni, L. (2016). Triple-negative breast cancer: challenges and opportunities of a heterogeneous disease. *Nat Rev Clin Oncol*, *13*(11), 674-690. https://doi.org/10.1038/nrclinonc.2016.66

Bianchini, G., De Angelis, C., Licata, L., & Gianni, L. (2022). Treatment landscape of triple-negative breast cancer - expanded options, evolving needs. *Nat Rev Clin Oncol*, *19*(2), 91-113. https://doi.org/10.1038/s41571-021-00565-2

Bieche, I., Chavey, C., Andrieu, C., Busson, M., Vacher, S., Le Corre, L., Guinebretiere, J. M., Burlinchon, S., Lidereau, R., & Lazennec, G. (2007). CXC chemokines located in the 4q21 region are up-regulated in breast cancer. *Endocr Relat Cancer*, *14*(4), 1039-1052. https://doi.org/10.1677/erc.1.01301

Boder, E. T., Raeeszadeh-Sarmazdeh, M., & Price, J. V. (2012). Engineering antibodies by yeast display. *Arch Biochem Biophys*, *526*(2), 99-106. https://doi.org/10.1016/j.abb.2012.03.009

Bossen, C., & Schneider, P. (2006). BAFF, APRIL and their receptors: structure, function and signaling. *Semin Immunol*, *18*(5), 263-275. https://doi.org/10.1016/j.smim.2006.04.006

Brule, C. E., & Grayhack, E. J. (2017). Synonymous Codons: Choose Wisely for Expression. *Trends Genet*, *33*(4), 283-297. https://doi.org/10.1016/j.tig.2017.02.001

Bryant, H. E., Schultz, N., Thomas, H. D., Parker, K. M., Flower, D., Lopez, E., Kyle, S., Meuth, M., Curtin, N. J., & Helleday, T. (2005). Specific killing of BRCA2-deficient tumours with inhibitors of poly(ADP-ribose) polymerase. *Nature*, *434*(7035), 913-917. https://doi.org/10.1038/nature03443

Cachero, T. G., Schwartz, I. M., Qian, F., Day, E. S., Bossen, C., Ingold, K., Tardivel, A., Krushinskie, D., Eldredge, J., Silvian, L., Lugovskoy, A., Farrington, G. K., Strauch, K., Schneider, P., & Whitty, A. (2006). Formation of virus-like clusters is an intrinsic property of the tumor necrosis factor family member BAFF (B cell activating factor). *Biochemistry*, *45*(7), 2006-2013. https://doi.org/10.1021/bi051685o

Cai, Z., Liu, N., Wang, C., Qin, B., Zhou, Y., Xiao, M., Chang, L., Yan, L. J., & Zhao, B. (2016). Role of RAGE in Alzheimer's Disease. *Cell Mol Neurobiol*, *36*(4), 483-495. https://doi.org/10.1007/s10571-015-0233-3

Castelli, M. S., McGonigle, P., & Hornby, P. J. (2019). The pharmacology and therapeutic applications of monoclonal antibodies. *Pharmacol Res Perspect*, *7*(6), e00535. https://doi.org/10.1002/prp2.535

Chavakis, T., Bierhaus, A., Al-Fakhri, N., Schneider, D., Witte, S., Linn, T., Nagashima, M., Morser, J., Arnold, B., Preissner, K. T., & Nawroth, P. P. (2003). The pattern recognition receptor (RAGE) is a counterreceptor for leukocyte integrins: a novel pathway for inflammatory cell recruitment. *J Exp Med*, *198*(10), 1507-1515. https://doi.org/10.1084/jem.20030800

Cheutin, T., McNairn, A. J., Jenuwein, T., Gilbert, D. M., Singh, P. B., & Misteli, T. (2003). Maintenance of stable heterochromatin domains by dynamic HP1 binding. *Science*, *299*(5607), 721-725. https://doi.org/10.1126/science.1078572

Chhipa, A. S., Borse, S. P., Baksi, R., Lalotra, S., & Nivsarkar, M. (2019). Targeting receptors of advanced glycation end products (RAGE): Preventing diabetes induced cancer and diabetic complications. *Pathol Res Pract*, *215*(11), 152643. https://doi.org/10.1016/j.prp.2019.152643

Clarke, J. M., & Hurwitz, H. I. (2013). Understanding and targeting resistance to anti-angiogenic therapies. *J Gastrointest Oncol*, *4*(3), 253-263. https://doi.org/10.3978/j.issn.2078-6891.2013.036

Coiffier, B., Thieblemont, C., Van Den Neste, E., Lepeu, G., Plantier, I., Castaigne, S., Lefort, S., Marit, G., Macro, M., Sebban, C., Belhadj, K., Bordessoule, D., Ferme, C., & Tilly, H. (2010). Long-term outcome of patients in the LNH-98.5 trial, the first randomized study comparing rituximab-CHOP to standard CHOP chemotherapy in DLBCL patients: a study by the Groupe d'Etudes des Lymphomes de l'Adulte. *Blood*, *116*(12), 2040-2045. https://doi.org/10.1182/blood-2010-03-276246

Cook, K. L., & Clarke, R. (2015). Role of GRP78 in promoting therapeutic-resistant breast cancer. *Future Med Chem*, *7*(12), 1529-1534. https://doi.org/10.4155/FMC.15.80

Cortes, J., Cescon, D. W., Rugo, H. S., Nowecki, Z., Im, S. A., Yusof, M. M., Gallardo, C., Lipatov, O., Barrios, C. H., Holgado, E., Iwata, H., Masuda, N., Otero, M. T., Gokmen, E., Loi, S., Guo, Z., Zhao, J., Aktan, G., Karantza, V., . . . Investigators, K.-. (2020). Pembrolizumab plus chemotherapy versus placebo plus chemotherapy for previously untreated locally recurrent inoperable or metastatic triple-negative breast cancer (KEYNOTE-355): a randomised, placebo-controlled, double-blind, phase 3 clinical trial. *Lancet*, *396*(10265), 1817-1828. https://doi.org/10.1016/S0140-6736(20)32531-9

Crump, M., Neelapu, S. S., Farooq, U., Van Den Neste, E., Kuruvilla, J., Westin, J., Link, B. K., Hay, A., Cerhan, J. R., Zhu, L., Boussetta, S., Feng, L., Maurer, M. J., Navale, L., Wiezorek, J., Go, W. Y., & Gisselbrecht, C. (2017). Outcomes in refractory diffuse large B-cell lymphoma: results from the international SCHOLAR-1 study. *Blood*, *130*(16), 1800-1808. https://doi.org/10.1182/blood-2017-03-769620

Czajkowsky, D. M., Hu, J., Shao, Z., & Pleass, R. J. (2012). Fc-fusion proteins: new developments and future perspectives. *EMBO Mol Med*, *4*(10), 1015-1028. https://doi.org/10.1002/emmm.201201379

Dattilo, B. M., Fritz, G., Leclerc, E., Kooi, C. W., Heizmann, C. W., & Chazin, W. J. (2007). The extracellular region of the receptor for advanced glycation end products is composed of two independent structural units. *Biochemistry*, *46*(23), 6957-6970. https://doi.org/10.1021/bi7003735

Day, E. S., Cachero, T. G., Qian, F., Sun, Y., Wen, D., Pelletier, M., Hsu, Y. M., & Whitty, A. (2005). Selectivity of BAFF/BLyS and APRIL for binding to the TNF family receptors BAFFR/BR3 and BCMA. *Biochemistry*, *44*(6), 1919-1931. https://doi.org/10.1021/bi048227k

Deen, W. M., Lazzara, M. J., & Myers, B. D. (2001). Structural determinants of glomerular permeability. *Am J Physiol Renal Physiol*, *281*(4), F579-596. https://doi.org/10.1152/ajprenal.2001.281.4.F579

den Brok, W. D., Schrader, K. A., Sun, S., Tinker, A. V., Zhao, E. Y., Aparicio, S., & Gelmon, K. A. (2017). Homologous Recombination Deficiency in Breast Cancer: A Clinical Review. *JCO Precis Oncol*, *1*, 1-13. https://doi.org/10.1200/PO.16.00031

Dillon, S. R., Harder, B., Lewis, K. B., Moore, M. D., Liu, H., Bukowski, T. R., Hamacher, N. B., Lantry, M. M., Maurer, M., Krejsa, C. M., Ellsworth, J. L., Pederson, S., Elkon, K. B., Wener, M. H., Dall'Era, M., & Gross, J. A. (2010). B-lymphocyte stimulator/a proliferation-inducing ligand heterotrimers are elevated

in the sera of patients with autoimmune disease and are neutralized by atacicept and B-cell maturation antigen-immunoglobulin. *Arthritis Res Ther*, *12*(2), R48. https://doi.org/10.1186/ar2959
DiNatale, A., Castelli, M. S., Nash, B., Meucci, O., & Fatatis, A. (2022). Regulation of Tumor and Metastasis Initiation by Chemokine Receptors. *J Cancer*, *13*(11), 3160-3176. https://doi.org/10.7150/jca.72331
Drago, J. Z., Modi, S., & Chandarlapaty, S. (2021). Unlocking the potential of antibody-drug conjugates for cancer therapy. *Nat Rev Clin Oncol*, *18*(6), 327-344. https://doi.org/10.1038/s41571-021-00470-8
Duan, W., Shen, X., Lei, J., Xu, Q., Yu, Y., Li, R., Wu, E., & Ma, Q. (2014). Hyperglycemia, a neglected factor during cancer progression. *Biomed Res Int*, *2014*, 461917. https://doi.org/10.1155/2014/461917
Durcan, L., O'Dwyer, T., & Petri, M. (2019). Management strategies and future directions for systemic lupus erythematosus in adults. *Lancet*, *393*(10188), 2332-2343. https://doi.org/10.1016/S0140-6736(19)30237-5
Ebos, J. M., Lee, C. R., & Kerbel, R. S. (2009). Tumor and host-mediated pathways of resistance and disease progression in response to antiangiogenic therapy. *Clin Cancer Res*, *15*(16), 5020-5025. https://doi.org/10.1158/1078-0432.CCR-09-0095
El-Far, A. H., Sroga, G., Jaouni, S. K. A., & Mousa, S. A. (2020). Role and Mechanisms of RAGE-Ligand Complexes and RAGE-Inhibitors in Cancer Progression. *Int J Mol Sci*, *21*(10). https://doi.org/10.3390/ijms21103613
Evans, C. G., Chang, L., & Gestwicki, J. E. (2010). Heat shock protein 70 (hsp70) as an emerging drug target. *J Med Chem*, *53*(12), 4585-4602. https://doi.org/10.1021/jm100054f
Fan, Y., Gao, D., & Zhang, Z. (2022). Telitacicept, a novel humanized, recombinant TACI-Fc fusion protein, for the treatment of systemic lupus erythematosus. *Drugs Today (Barc)*, *58*(1), 23-32. https://doi.org/10.1358/dot.2022.58.1.3352743
Farabaugh, S. M., Boone, D. N., & Lee, A. V. (2015). Role of IGF1R in Breast Cancer Subtypes, Stemness, and Lineage Differentiation. *Front Endocrinol (Lausanne)*, *6*, 59. https://doi.org/10.3389/fendo.2015.00059
Farmer, H., McCabe, N., Lord, C. J., Tutt, A. N., Johnson, D. A., Richardson, T. B., Santarosa, M., Dillon, K. J., Hickson, I., Knights, C., Martin, N. M., Jackson, S. P., Smith, G. C., & Ashworth, A. (2005). Targeting the DNA repair defect in BRCA mutant cells as a therapeutic strategy. *Nature*, *434*(7035), 917-921. https://doi.org/10.1038/nature03445
Fishman, S. L., Sonmez, H., Basman, C., Singh, V., & Poretsky, L. (2018). The role of advanced glycation end-products in the development of coronary artery disease in patients with and without diabetes mellitus: a review. *Mol Med*, *24*(1), 59. https://doi.org/10.1186/s10020-018-0060-3
Fitzgerald, K. A., McWhirter, S. M., Faia, K. L., Rowe, D. C., Latz, E., Golenbock, D. T., Coyle, A. J., Liao, S. M., & Maniatis, T. (2003). IKKepsilon and TBK1 are essential components of the IRF3 signaling pathway. *Nat Immunol*, *4*(5), 491-496. https://doi.org/10.1038/ni921
Foulkes, W. D., Smith, I. E., & Reis-Filho, J. S. (2010). Triple-negative breast cancer. *N Engl J Med*, *363*(20), 1938-1948. https://doi.org/10.1056/NEJMra1001389
Fritz, G. (2011). RAGE: a single receptor fits multiple ligands. *Trends Biochem Sci*, *36*(12), 625-632. https://doi.org/10.1016/j.tibs.2011.08.008
Fu, L., Lin-Lee, Y. C., Pham, L. V., Tamayo, A., Yoshimura, L., & Ford, R. J. (2006). Constitutive NF-kappaB and NFAT activation leads to stimulation of the BLyS survival pathway in aggressive B-cell lymphomas. *Blood*, *107*(11), 4540-4548. https://doi.org/10.1182/blood-2005-10-4042

Gallagher, E. J., & LeRoith, D. (2010). The proliferating role of insulin and insulin-like growth factors in cancer. *Trends Endocrinol Metab*, *21*(10), 610-618. https://doi.org/10.1016/j.tem.2010.06.007
Gallagher, E. J., & LeRoith, D. (2015). Obesity and Diabetes: The Increased Risk of Cancer and Cancer-Related Mortality. *Physiol Rev*, *95*(3), 727-748. https://doi.org/10.1152/physrev.00030.2014
Galluzzi, L., Humeau, J., Buque, A., Zitvogel, L., & Kroemer, G. (2020). Immunostimulation with chemotherapy in the era of immune checkpoint inhibitors. *Nat Rev Clin Oncol*, *17*(12), 725-741. https://doi.org/10.1038/s41571-020-0413-z
Gao, S., Cui, Z., & Zhao, M. H. (2020). The Complement C3a and C3a Receptor Pathway in Kidney Diseases. *Front Immunol*, *11*, 1875. https://doi.org/10.3389/fimmu.2020.01875
Garcia-Jimenez, C., Gutierrez-Salmeron, M., Chocarro-Calvo, A., Garcia-Martinez, J. M., Castano, A., & De la Vieja, A. (2016). From obesity to diabetes and cancer: epidemiological links and role of therapies. *Br J Cancer*, *114*(7), 716-722. https://doi.org/10.1038/bjc.2016.37
Gaspar, E. B., & De Gaspari, E. (2021). Avidity assay to test functionality of anti-SARS-Cov-2 antibodies. *Vaccine*, *39*(10), 1473-1475. https://doi.org/10.1016/j.vaccine.2021.02.003
Ghosh, M., Saha, S., Bettke, J., Nagar, R., Parrales, A., Iwakuma, T., van der Velden, A. W. M., & Martinez, L. A. (2021). Mutant p53 suppresses innate immune signaling to promote tumorigenesis. *Cancer Cell*, *39*(4), 494-508 e495. https://doi.org/10.1016/j.ccell.2021.01.003
Gifford, J. B., Huang, W., Zeleniak, A. E., Hindoyan, A., Wu, H., Donahue, T. R., & Hill, R. (2016). Expression of GRP78, Master Regulator of the Unfolded Protein Response, Increases Chemoresistance in Pancreatic Ductal Adenocarcinoma. *Mol Cancer Ther*, *15*(5), 1043-1052. https://doi.org/10.1158/1535-7163.MCT-15-0774
Giovannucci, E., Harlan, D. M., Archer, M. C., Bergenstal, R. M., Gapstur, S. M., Habel, L. A., Pollak, M., Regensteiner, J. G., & Yee, D. (2010). Diabetes and cancer: a consensus report. *Diabetes Care*, *33*(7), 1674-1685. https://doi.org/10.2337/dc10-0666
Gruosso, T., Gigoux, M., Manem, V. S. K., Bertos, N., Zuo, D., Perlitch, I., Saleh, S. M. I., Zhao, H., Souleimanova, M., Johnson, R. M., Monette, A., Ramos, V. M., Hallett, M. T., Stagg, J., Lapointe, R., Omeroglu, A., Meterissian, S., Buisseret, L., Van den Eynden, G., . . . Park, M. (2019). Spatially distinct tumor immune microenvironments stratify triple-negative breast cancers. *J Clin Invest*, *129*(4), 1785-1800. https://doi.org/10.1172/JCI96313
Guedan, S., Ruella, M., & June, C. H. (2019). Emerging Cellular Therapies for Cancer. *Annu Rev Immunol*, *37*, 145-171. https://doi.org/10.1146/annurev-immunol-042718-041407
Hahne, M., Kataoka, T., Schroter, M., Hofmann, K., Irmler, M., Bodmer, J. L., Schneider, P., Bornand, T., Holler, N., French, L. E., Sordat, B., Rimoldi, D., & Tschopp, J. (1998). APRIL, a new ligand of the tumor necrosis factor family, stimulates tumor cell growth. *J Exp Med*, *188*(6), 1185-1190. https://doi.org/10.1084/jem.188.6.1185
Hall, M. N., Gabay, J., Debarbouille, M., & Schwartz, M. (1982). A role for mRNA secondary structure in the control of translation initiation. *Nature*, *295*(5850), 616-618. https://doi.org/10.1038/295616a0
Han, Y., Liu, D., & Li, L. (2020). PD-1/PD-L1 pathway: current researches in cancer. *Am J Cancer Res*, *10*(3), 727-742. https://www.ncbi.nlm.nih.gov/pubmed/32266087

Hanahan, D. (2022). Hallmarks of Cancer: New Dimensions. *Cancer Discov*, *12*(1), 31-46. https://doi.org/10.1158/2159-8290.CD-21-1059
Hanahan, D., & Weinberg, R. A. (2000). The hallmarks of cancer. *Cell*, *100*(1), 57-70. https://doi.org/10.1016/s0092-8674(00)81683-9
Hanahan, D., & Weinberg, R. A. (2011). Hallmarks of cancer: the next generation. *Cell*, *144*(5), 646-674. https://doi.org/10.1016/j.cell.2011.02.013
Hassett, B., Singh, E., Mahgoub, E., O'Brien, J., Vicik, S. M., & Fitzpatrick, B. (2018). Manufacturing history of etanercept (Enbrel((R))): Consistency of product quality through major process revisions. *MAbs*, *10*(1), 159-165. https://doi.org/10.1080/19420862.2017.1388483
Hata, H., Phuoc Tran, D., Marzouk Sobeh, M., & Kitao, A. (2021). Binding free energy of protein/ligand complexes calculated using dissociation Parallel Cascade Selection Molecular Dynamics and Markov state model. *Biophys Physicobiol*, *18*, 305-316. https://doi.org/10.2142/biophysico.bppb-v18.037
He, B., Chadburn, A., Jou, E., Schattner, E. J., Knowles, D. M., & Cerutti, A. (2004). Lymphoma B cells evade apoptosis through the TNF family members BAFF/BLyS and APRIL. *J Immunol*, *172*(5), 3268-3279. https://doi.org/10.4049/jimmunol.172.5.3268
He, M. Y., & Kridel, R. (2021). Treatment resistance in diffuse large B-cell lymphoma. *Leukemia*, *35*(8), 2151-2165. https://doi.org/10.1038/s41375-021-01285-3
Hengeveld, P. J., & Kersten, M. J. (2015). B-cell activating factor in the pathophysiology of multiple myeloma: a target for therapy? *Blood Cancer J*, *5*(2), e282. https://doi.org/10.1038/bcj.2015.3
Hirata, N., Yamada, S., Yanagida, S., Ono, A., Yasuhiko, Y., Nishida, M., & Kanda, Y. (2022). Lysophosphatidic Acid Promotes the Expansion of Cancer Stem Cells via TRPC3 Channels in Triple-Negative Breast Cancer. *Int J Mol Sci*, *23*(4). https://doi.org/10.3390/ijms23041967
Hoffmann, F. S., Kuhn, P. H., Laurent, S. A., Hauck, S. M., Berer, K., Wendlinger, S. A., Krumbholz, M., Khademi, M., Olsson, T., Dreyling, M., Pfister, H. W., Alexander, T., Hiepe, F., Kumpfel, T., Crawford, H. C., Wekerle, H., Hohlfeld, R., Lichtenthaler, S. F., & Meinl, E. (2015). The immunoregulator soluble TACI is released by ADAM10 and reflects B cell activation in autoimmunity. *J Immunol*, *194*(2), 542-552. https://doi.org/10.4049/jimmunol.1402070
Huang, C., Su, T., Xue, Y., Cheng, C., Lay, F. D., McKee, R. A., Li, M., Vashisht, A., Wohlschlegel, J., Novitch, B. G., Plath, K., Kurdistani, S. K., & Carey, M. (2017). Cbx3 maintains lineage specificity during neural differentiation. *Genes Dev*, *31*(3), 241-246. https://doi.org/10.1101/gad.292169.116
Hudson, B. I., & Lippman, M. E. (2018). Targeting RAGE Signaling in Inflammatory Disease. *Annu Rev Med*, *69*, 349-364. https://doi.org/10.1146/annurev-med-041316-085215
Hunter, S. A., & Cochran, J. R. (2016). Cell-Binding Assays for Determining the Affinity of Protein-Protein Interactions: Technologies and Considerations. *Methods Enzymol*, *580*, 21-44. https://doi.org/10.1016/bs.mie.2016.05.002
Hutchinson, K. E., Yost, S. E., Chang, C. W., Johnson, R. M., Carr, A. R., McAdam, P. R., Halligan, D. L., Chang, C. C., Schmolze, D., Liang, J., & Yuan, Y. (2020). Comprehensive Profiling of Poor-Risk Paired Primary and Recurrent Triple-Negative Breast Cancers Reveals Immune Phenotype Shifts. *Clin Cancer Res*, *26*(3), 657-668. https://doi.org/10.1158/1078-0432.CCR-19-1773
Hymowitz, S. G., Patel, D. R., Wallweber, H. J., Runyon, S., Yan, M., Yin, J., Shriver, S. K., Gordon, N. C., Pan, B., Skelton, N. J., Kelley, R. F., & Starovasnik, M. A. (2005). Structures of APRIL-receptor complexes: like BCMA, TACI employs only a single cysteine-rich domain for high affinity ligand binding. *J Biol Chem*, *280*(8), 7218-7227. https://doi.org/10.1074/jbc.M411714200

Jackson, S. P., & Bartek, J. (2009). The DNA-damage response in human biology and disease. *Nature*, *461*(7267), 1071-1078. https://doi.org/10.1038/nature08467
Jang, G. Y., Lee, J. W., Kim, Y. S., Lee, S. E., Han, H. D., Hong, K. J., Kang, T. H., & Park, Y. M. (2020). Interactions between tumor-derived proteins and Toll-like receptors. *Exp Mol Med*, *52*(12), 1926-1935. https://doi.org/10.1038/s12276-020-00540-4
Jenkins, D. E., Hornig, Y. S., Oei, Y., Dusich, J., & Purchio, T. (2005). Bioluminescent human breast cancer cell lines that permit rapid and sensitive in vivo detection of mammary tumors and multiple metastases in immune deficient mice. *Breast Cancer Res*, *7*(4), R444-454. https://doi.org/10.1186/bcr1026
Jiao, S., Guan, J., Chen, M., Wang, W., Li, C., Wang, Y., Cheng, Y., & Zhou, Z. (2018). Targeting IRF3 as a YAP agonist therapy against gastric cancer. *J Exp Med*, *215*(2), 699-718. https://doi.org/10.1084/jem.20171116
Juranek, J. K., Daffu, G. K., Geddis, M. S., Li, H., Rosario, R., Kaplan, B. J., Kelly, L., & Schmidt, A. M. (2016). Soluble RAGE Treatment Delays Progression of Amyotrophic Lateral Sclerosis in SOD1 Mice. *Front Cell Neurosci*, *10*, 117. https://doi.org/10.3389/fncel.2016.00117
Kaegi, C., Steiner, U. C., Wuest, B., Crowley, C., & Boyman, O. (2020). Systematic Review of Safety and Efficacy of Atacicept in Treating Immune-Mediated Disorders. *Front Immunol*, *11*, 433. https://doi.org/10.3389/fimmu.2020.00433
Kamen, L., Myneni, S., Langsdorf, C., Kho, E., Ordonia, B., Thakurta, T., Zheng, K., Song, A., & Chung, S. (2019). A novel method for determining antibody-dependent cellular phagocytosis. *J Immunol Methods*, *468*, 55-60. https://doi.org/10.1016/j.jim.2019.03.001
Kariolis, M. S., Miao, Y. R., Jones, D. S., 2nd, Kapur, S., Mathews, II, Giaccia, A. J., & Cochran, J. R. (2014). An engineered Axl 'decoy receptor' effectively silences the Gas6-Axl signaling axis. *Nat Chem Biol*, *10*(11), 977-983. https://doi.org/10.1038/nchembio.1636
Kay, A. M., Simpson, C. L., & Stewart, J. A., Jr. (2016). The Role of AGE/RAGE Signaling in Diabetes-Mediated Vascular Calcification. *J Diabetes Res*, *2016*, 6809703. https://doi.org/10.1155/2016/6809703
Keren, L., Bosse, M., Marquez, D., Angoshtari, R., Jain, S., Varma, S., Yang, S. R., Kurian, A., Van Valen, D., West, R., Bendall, S. C., & Angelo, M. (2018). A Structured Tumor-Immune Microenvironment in Triple Negative Breast Cancer Revealed by Multiplexed Ion Beam Imaging. *Cell*, *174*(6), 1373-1387 e1319. https://doi.org/10.1016/j.cell.2018.08.039
Kern, J., Untergasser, G., Zenzmaier, C., Sarg, B., Gastl, G., Gunsilius, E., & Steurer, M. (2009). GRP-78 secreted by tumor cells blocks the antiangiogenic activity of bortezomib. *Blood*, *114*(18), 3960-3967. https://doi.org/10.1182/blood-2009-03-209668
Korostynski, M., Hoinkis, D., Piechota, M., Golda, S., Pera, J., Slowik, A., & Dziedzic, T. (2021). Toll-like receptor 4-mediated cytokine synthesis and post-stroke depressive symptoms. *Transl Psychiatry*, *11*(1), 246. https://doi.org/10.1038/s41398-021-01359-x
Kregiel, D., Berlowska, J., & Szubzda, B. (2012). Novel permittivity test for determination of yeast surface charge and flocculation abilities. *J Ind Microbiol Biotechnol*, *39*(12), 1881-1886. https://doi.org/10.1007/s10295-012-1193-y
Kuo, S. H., Yeh, P. Y., Chen, L. T., Wu, M. S., Lin, C. W., Yeh, K. H., Tzeng, Y. S., Chen, J. Y., Hsu, P. N., Lin, J. T., & Cheng, A. L. (2008). Overexpression of B cell-activating factor of TNF family (BAFF) is associated with Helicobacter pylori-independent growth of gastric diffuse large B-cell lymphoma with histologic evidence of MALT lymphoma. *Blood*, *112*(7), 2927-2934. https://doi.org/10.1182/blood-2008-02-137513

Kwak, T., Drews-Elger, K., Ergonul, A., Miller, P. C., Braley, A., Hwang, G. H., Zhao, D., Besser, A., Yamamoto, Y., Yamamoto, H., El-Ashry, D., Slingerland, J. M., Lippman, M. E., & Hudson, B. I. (2017). Targeting of RAGE-ligand signaling impairs breast cancer cell invasion and metastasis. *Oncogene*, *36*(11), 1559-1572. https://doi.org/10.1038/onc.2016.324

La, X., Zhang, L., Li, H., Li, Z., Song, G., Yang, P., & Yang, Y. (2018). Ajuba receptor mediates the internalization of tumor-secreted GRP78 into macrophages through different endocytosis pathways. *Oncotarget*, *9*(21), 15464-15479. https://doi.org/10.18632/oncotarget.24090

Larsen, C. P., Pearson, T. C., Adams, A. B., Tso, P., Shirasugi, N., Strobert, E., Anderson, D., Cowan, S., Price, K., Naemura, J., Emswiler, J., Greene, J., Turk, L. A., Bajorath, J., Townsend, R., Hagerty, D., Linsley, P. S., & Peach, R. J. (2005). Rational development of LEA29Y (belatacept), a high-affinity variant of CTLA4-Ig with potent immunosuppressive properties. *Am J Transplant*, *5*(3), 443-453. https://doi.org/10.1111/j.1600-6143.2005.00749.x

Lee, J. B., Ha, S. J., & Kim, H. R. (2021). Clinical Insights Into Novel Immune Checkpoint Inhibitors. *Front Pharmacol*, *12*, 681320. https://doi.org/10.3389/fphar.2021.681320

Lee, K. J., Yoo, J. W., Kim, Y. K., Choi, J. H., Ha, T. Y., & Gil, M. (2018). Advanced glycation end products promote triple negative breast cancer cells via ERK and NF-kappaB pathway. *Biochem Biophys Res Commun*, *495*(3), 2195-2201. https://doi.org/10.1016/j.bbrc.2017.11.182

Lee, Y. T., Tan, Y. J., & Oon, C. E. (2018). Molecular targeted therapy: Treating cancer with specificity. *Eur J Pharmacol*, *834*, 188-196. https://doi.org/10.1016/j.ejphar.2018.07.034

Lehmann, B. D., Bauer, J. A., Chen, X., Sanders, M. E., Chakravarthy, A. B., Shyr, Y., & Pietenpol, J. A. (2011). Identification of human triple-negative breast cancer subtypes and preclinical models for selection of targeted therapies. *J Clin Invest*, *121*(7), 2750-2767. https://doi.org/10.1172/JCI45014

Lehmann, B. D., Jovanovic, B., Chen, X., Estrada, M. V., Johnson, K. N., Shyr, Y., Moses, H. L., Sanders, M. E., & Pietenpol, J. A. (2016). Refinement of Triple-Negative Breast Cancer Molecular Subtypes: Implications for Neoadjuvant Chemotherapy Selection. *PLoS One*, *11*(6), e0157368. https://doi.org/10.1371/journal.pone.0157368

Li, J., Yin, J., Shen, W., Gao, R., Liu, Y., Chen, Y., Li, X., Liu, C., Xiang, R., & Luo, N. (2017). TLR4 Promotes Breast Cancer Metastasis via Akt/GSK3beta/beta-Catenin Pathway upon LPS Stimulation. *Anat Rec (Hoboken)*, *300*(7), 1219-1229. https://doi.org/10.1002/ar.23590

Li, K., Shi, H., Zhang, B., Ou, X., Ma, Q., Chen, Y., Shu, P., Li, D., & Wang, Y. (2021). Myeloid-derived suppressor cells as immunosuppressive regulators and therapeutic targets in cancer. *Signal Transduct Target Ther*, *6*(1), 362. https://doi.org/10.1038/s41392-021-00670-9

Li, W., Dong, S., Wei, W., Wang, G., Zhang, A., Pu, P., & Jia, Z. (2016). The role of transcriptional coactivator TAZ in gliomas. *Oncotarget*, *7*(50), 82686-82699. https://doi.org/10.18632/oncotarget.12625

Li, X., Xiao, R., Tembo, K., Hao, L., Xiong, M., Pan, S., Yang, X., Yuan, W., Xiong, J., & Zhang, Q. (2016). PEG10 promotes human breast cancer cell proliferation, migration and invasion. *Int J Oncol*, *48*(5), 1933-1942. https://doi.org/10.3892/ijo.2016.3406

Li, Y., Vennapusa, B., Chang, C. W., Tran, D., Nakamura, R., Sumiyoshi, T., Hegde, P., & Molinero, L. (2021). Prevalence Study of PD-L1 SP142 Assay in Metastatic Triple-negative Breast Cancer. *Appl Immunohistochem Mol Morphol*, *29*(4), 258-264. https://doi.org/10.1097/PAI.0000000000000857

Liang, Y. K., Lin, H. Y., Chen, C. F., & Zeng, D. (2017). Prognostic values of distinct CBX family members in breast cancer. *Oncotarget*, *8*(54), 92375-92387. https://doi.org/10.18632/oncotarget.21325
Liu, Z., Li, M., Jiang, Z., & Wang, X. (2018). A Comprehensive Immunologic Portrait of Triple-Negative Breast Cancer. *Transl Oncol*, *11*(2), 311-329. https://doi.org/10.1016/j.tranon.2018.01.011
Logsdon, C. D., Fuentes, M. K., Huang, E. H., & Arumugam, T. (2007). RAGE and RAGE ligands in cancer. *Curr Mol Med*, *7*(8), 777-789. https://doi.org/10.2174/156652407783220697
Lopez-Fraga, M., Fernandez, R., Albar, J. P., & Hahne, M. (2001). Biologically active APRIL is secreted following intracellular processing in the Golgi apparatus by furin convertase. *EMBO Rep*, *2*(10), 945-951. https://doi.org/10.1093/embo-reports/kve198
Lueck, J. D., Yoon, J. S., Perales-Puchalt, A., Mackey, A. L., Infield, D. T., Behlke, M. A., Pope, M. R., Weiner, D. B., Skach, W. R., McCray, P. B., Jr., & Ahern, C. A. (2019). Engineered transfer RNAs for suppression of premature termination codons. *Nat Commun*, *10*(1), 822. https://doi.org/10.1038/s41467-019-08329-4
Lynaugh, H., Li, H., & Gong, B. (2013). Rapid Fc glycosylation analysis of Fc fusions with IdeS and liquid chromatography mass spectrometry. *MAbs*, *5*(5), 641-645. https://doi.org/10.4161/mabs.25302
Magnez, R., Thiroux, B., Taront, S., Segaoula, Z., Quesnel, B., & Thuru, X. (2017). PD-1/PD-L1 binding studies using microscale thermophoresis. *Sci Rep*, *7*(1), 17623. https://doi.org/10.1038/s41598-017-17963-1
Mahtani, R., Kittaneh, M., Kalinsky, K., Mamounas, E., Badve, S., Vogel, C., Lower, E., Schwartzberg, L., Pegram, M., & Breast Cancer Therapy Expert, G. (2021). Advances in Therapeutic Approaches for Triple-Negative Breast Cancer. *Clin Breast Cancer*, *21*(5), 383-390. https://doi.org/10.1016/j.clbc.2020.12.011
Maia, S., Pelletier, M., Ding, J., Hsu, Y. M., Sallan, S. E., Rao, S. P., Nadler, L. M., & Cardoso, A. A. (2011). Aberrant expression of functional BAFF-system receptors by malignant B-cell precursors impacts leukemia cell survival. *PLoS One*, *6*(6), e20787. https://doi.org/10.1371/journal.pone.0020787
Mansour, A. M., Stewart, M. W., Farah, M. E., Mansour, H. A., & Chhablani, J. (2019). Ziv-aflibercept: A cost-effective, off-label, highly potent antagonist of vascular endothelial growth factor. *Acta Ophthalmol*. https://doi.org/10.1111/aos.14328
Margraf-Schonfeld, S., Bohm, C., & Watzl, C. (2011). Glycosylation affects ligand binding and function of the activating natural killer cell receptor 2B4 (CD244) protein. *J Biol Chem*, *286*(27), 24142-24149. https://doi.org/10.1074/jbc.M111.225334
Marillonnet, S., & Grutzner, R. (2020). Synthetic DNA Assembly Using Golden Gate Cloning and the Hierarchical Modular Cloning Pipeline. *Curr Protoc Mol Biol*, *130*(1), e115. https://doi.org/10.1002/cpmb.115
Markham, A. (2020). Luspatercept: First Approval. *Drugs*, *80*(1), 85-90. https://doi.org/10.1007/s40265-019-01251-5
Mateo, F., He, Z., Mei, L., de Garibay, G. R., Herranz, C., Garcia, N., Lorentzian, A., Baiges, A., Blommaert, E., Gomez, A., Mirallas, O., Garrido-Utrilla, A., Palomero, L., Espin, R., Extremera, A. I., Soler-Monso, M. T., Petit, A., Li, R., Brunet, J., . . . Pujana, M. A. (2022). Modification of BRCA1-associated breast cancer risk by HMMR overexpression. *Nat Commun*, *13*(1), 1895. https://doi.org/10.1038/s41467-022-29335-z
Merrill, J. T., Wallace, D. J., Wax, S., Kao, A., Fraser, P. A., Chang, P., Isenberg, D., & Investigators, A. I. (2018). Efficacy and Safety of Atacicept in Patients With Systemic Lupus Erythematosus: Results of a Twenty-Four-Week, Multicenter,

Randomized, Double-Blind, Placebo-Controlled, Parallel-Arm, Phase IIb Study. *Arthritis Rheumatol*, *70*(2), 266-276. https://doi.org/10.1002/art.40360
Miao, Y. R., Thakkar, K., Cenik, C., Jiang, D., Mizuno, K., Jia, C., Li, C. G., Zhao, H., Diep, A., Xu, Y., Zhang, X. E., Yang, T. T. C., Liedtke, M., Abidi, P., Leung, W. S., Koong, A. C., & Giaccia, A. J. (2022). Developing high-affinity decoy receptors to treat multiple myeloma and diffuse large B cell lymphoma. *J Exp Med*, *219*(9). https://doi.org/10.1084/jem.20220214
Miao, Y. R., Thakkar, K. N., Qian, J., Kariolis, M. S., Huang, W., Nandagopal, S., Yang, T. T. C., Diep, A. N., Cherf, G. M., Xu, Y., Moon, E. J., Xiao, Y., Alemany, H., Li, T., Yu, W., Wei, B., Rankin, E. B., & Giaccia, A. J. (2021). Neutralization of PD-L2 is Essential for Overcoming Immune Checkpoint Blockade Resistance in Ovarian Cancer. *Clin Cancer Res*, *27*(15), 4435-4448. https://doi.org/10.1158/1078-0432.CCR-20-0482
Michmerhuizen, A. R., Spratt, D. E., Pierce, L. J., & Speers, C. W. (2020). ARe we there yet? Understanding androgen receptor signaling in breast cancer. *NPJ Breast Cancer*, *6*, 47. https://doi.org/10.1038/s41523-020-00190-9
Moore, P. A., Belvedere, O., Orr, A., Pieri, K., LaFleur, D. W., Feng, P., Soppet, D., Charters, M., Gentz, R., Parmelee, D., Li, Y., Galperina, O., Giri, J., Roschke, V., Nardelli, B., Carrell, J., Sosnovtseva, S., Greenfield, W., Ruben, S. M., . . . Hilbert, D. M. (1999). BLyS: member of the tumor necrosis factor family and B lymphocyte stimulator. *Science*, *285*(5425), 260-263. https://doi.org/10.1126/science.285.5425.260
Moreaux, J., Legouffe, E., Jourdan, E., Quittet, P., Reme, T., Lugagne, C., Moine, P., Rossi, J. F., Klein, B., & Tarte, K. (2004). BAFF and APRIL protect myeloma cells from apoptosis induced by interleukin 6 deprivation and dexamethasone. *Blood*, *103*(8), 3148-3157. https://doi.org/10.1182/blood-2003-06-1984
Mullard, A. (2021). FDA approves 100th monoclonal antibody product. *Nat Rev Drug Discov*, *20*(7), 491-495. https://doi.org/10.1038/d41573-021-00079-7
Nandagopal, S., Li, C. G., Xu, Y., Sodji, Q. H., Graves, E. E., & Giaccia, A. J. (2022). C3aR Signaling Inhibits NK-cell Infiltration into the Tumor Microenvironment in Mouse Models. *Cancer Immunol Res*, *10*(2), 245-258. https://doi.org/10.1158/2326-6066.CIR-21-0435
Nannini, F., Senicar, L., Parekh, F., Kong, K. J., Kinna, A., Bughda, R., Sillibourne, J., Hu, X., Ma, B., Bai, Y., Ferrari, M., Pule, M. A., & Onuoha, S. C. (2021). Combining phage display with SMRTbell next-generation sequencing for the rapid discovery of functional scFv fragments. *MAbs*, *13*(1), 1864084. https://doi.org/10.1080/19420862.2020.1864084
Nannuru, K. C., Sharma, B., Varney, M. L., & Singh, R. K. (2011). Role of chemokine receptor CXCR2 expression in mammary tumor growth, angiogenesis and metastasis. *J Carcinog*, *10*, 40. https://doi.org/10.4103/1477-3163.92308
Narumi, K., Miyakawa, R., Ueda, R., Hashimoto, H., Yamamoto, Y., Yoshida, T., & Aoki, K. (2015). Proinflammatory Proteins S100A8/S100A9 Activate NK Cells via Interaction with RAGE. *J Immunol*, *194*(11), 5539-5548. https://doi.org/10.4049/jimmunol.1402301
Nasser, M. W., Wani, N. A., Ahirwar, D. K., Powell, C. A., Ravi, J., Elbaz, M., Zhao, H., Padilla, L., Zhang, X., Shilo, K., Ostrowski, M., Shapiro, C., Carson, W. E., 3rd, & Ganju, R. K. (2015). RAGE mediates S100A7-induced breast cancer growth and metastasis by modulating the tumor microenvironment. *Cancer Res*, *75*(6), 974-985. https://doi.org/10.1158/0008-5472.CAN-14-2161
Neelapu, S. S., Locke, F. L., Bartlett, N. L., Lekakis, L. J., Miklos, D. B., Jacobson, C. A., Braunschweig, I., Oluwole, O. O., Siddiqi, T., Lin, Y., Timmerman, J. M., Stiff, P. J., Friedberg, J. W., Flinn, I. W., Goy, A., Hill, B. T., Smith, M. R., Deol, A., Farooq, U., . . . Go, W. Y. (2017). Axicabtagene Ciloleucel CAR T-Cell

Therapy in Refractory Large B-Cell Lymphoma. *N Engl J Med*, *377*(26), 2531-2544. https://doi.org/10.1056/NEJMoa1707447
Nogueira-Machado, J. A., Volpe, C. M., Veloso, C. A., & Chaves, M. M. (2011). HMGB1, TLR and RAGE: a functional tripod that leads to diabetic inflammation. *Expert Opin Ther Targets*, *15*(8), 1023-1035. https://doi.org/10.1517/14728222.2011.575360
Nolan, T., Singh, N., & McCurdy, C. R. (2009). Ligand macromolecule interactions: theoretical principles of molecular recognition. *Methods Mol Biol*, *572*, 13-29. https://doi.org/10.1007/978-1-60761-244-5_2
Osawa, M., Yamamoto, Y., Munesue, S., Murakami, N., Sakurai, S., Watanabe, T., Yonekura, H., Uchigata, Y., Iwamoto, Y., & Yamamoto, H. (2007). De-N-glycosylation or G82S mutation of RAGE sensitizes its interaction with advanced glycation endproducts. *Biochim Biophys Acta*, *1770*(10), 1468-1474. https://doi.org/10.1016/j.bbagen.2007.07.003
Palanissami, G., & Paul, S. F. D. (2018). RAGE and Its Ligands: Molecular Interplay Between Glycation, Inflammation, and Hallmarks of Cancer-a Review. *Horm Cancer*, *9*(5), 295-325. https://doi.org/10.1007/s12672-018-0342-9
Pan, S., Guan, Y., Ma, Y., Cui, Q., Tang, Z., Li, J., Zu, C., Zhang, Y., Zhu, L., Jiang, J., & Liu, Z. (2022). Advanced glycation end products correlate with breast cancer metastasis by activating RAGE/TLR4 signaling. *BMJ Open Diabetes Res Care*, *10*(2). https://doi.org/10.1136/bmjdrc-2021-002697
Patel, D. R., Wallweber, H. J., Yin, J., Shriver, S. K., Marsters, S. A., Gordon, N. C., Starovasnik, M. A., & Kelley, R. F. (2004). Engineering an APRIL-specific B cell maturation antigen. *J Biol Chem*, *279*(16), 16727-16735. https://doi.org/10.1074/jbc.M312316200
Peng, Y., Li, Z., & Li, Z. (2013). GRP78 secreted by tumor cells stimulates differentiation of bone marrow mesenchymal stem cells to cancer-associated fibroblasts. *Biochem Biophys Res Commun*, *440*(4), 558-563. https://doi.org/10.1016/j.bbrc.2013.09.108
Perseghin, G., Calori, G., Lattuada, G., Ragogna, F., Dugnani, E., Garancini, M. P., Crosignani, P., Villa, M., Bosi, E., Ruotolo, G., & Piemonti, L. (2012). Insulin resistance/hyperinsulinemia and cancer mortality: the Cremona study at the 15th year of follow-up. *Acta Diabetol*, *49*(6), 421-428. https://doi.org/10.1007/s00592-011-0361-2
Poggio, F., Bruzzone, M., Ceppi, M., Ponde, N. F., La Valle, G., Del Mastro, L., de Azambuja, E., & Lambertini, M. (2018). Platinum-based neoadjuvant chemotherapy in triple-negative breast cancer: a systematic review and meta-analysis. *Ann Oncol*, *29*(7), 1497-1508. https://doi.org/10.1093/annonc/mdy127
Polak, P., Kim, J., Braunstein, L. Z., Karlic, R., Haradhavala, N. J., Tiao, G., Rosebrock, D., Livitz, D., Kubler, K., Mouw, K. W., Kamburov, A., Maruvka, Y. E., Leshchiner, I., Lander, E. S., Golub, T. R., Zick, A., Orthwein, A., Lawrence, M. S., Batra, R. N., . . . Getz, G. (2017). A mutational signature reveals alterations underlying deficient homologous recombination repair in breast cancer. *Nat Genet*, *49*(10), 1476-1486. https://doi.org/10.1038/ng.3934
Pon, R., Marcil, A., Chen, W., Gadoury, C., Williams, D., Chan, K., Zhou, H., Ponce, A., Paquet, E., Gurnani, K., Chattopadhyay, A., & Zou, W. (2020). Masking terminal neo-epitopes of linear peptides through glycosylation favours immune responses towards core epitopes producing parental protein bound antibodies. *Sci Rep*, *10*(1), 18497. https://doi.org/10.1038/s41598-020-75754-7
Pradet-Balade, B., Medema, J. P., Lopez-Fraga, M., Lozano, J. C., Kolfschoten, G. M., Picard, A., Martinez, A. C., Garcia-Sanz, J. A., & Hahne, M. (2002). An endogenous hybrid mRNA encodes TWE-PRIL, a functional cell surface

TWEAK-APRIL fusion protein. *EMBO J*, *21*(21), 5711-5720. https://doi.org/10.1093/emboj/cdf565
Qi, Y. L., Li, Y., Man, X. X., Sui, H. Y., Zhao, X. L., Zhang, P. X., Qu, X. S., Zhang, H., Wang, B. X., Li, J., Qi, S. F., Jia, L. L., Luan, H. Y., Zhang, C. B., & Wang, W. Q. (2020). CXCL3 overexpression promotes the tumorigenic potential of uterine cervical cancer cells via the MAPK/ERK pathway. *J Cell Physiol*, *235*(5), 4756-4765. https://doi.org/10.1002/jcp.29353
Ray, R., Juranek, J. K., & Rai, V. (2016). RAGE axis in neuroinflammation, neurodegeneration and its emerging role in the pathogenesis of amyotrophic lateral sclerosis. *Neurosci Biobehav Rev*, *62*, 48-55. https://doi.org/10.1016/j.neubiorev.2015.12.006
Richter, L., Oberlander, V., & Schmidt, G. (2020). RhoA/C inhibits proliferation by inducing the synthesis of GPRC5A. *Sci Rep*, *10*(1), 12532. https://doi.org/10.1038/s41598-020-69481-2
Roschke, V., Sosnovtseva, S., Ward, C. D., Hong, J. S., Smith, R., Albert, V., Stohl, W., Baker, K. P., Ullrich, S., Nardelli, B., Hilbert, D. M., & Migone, T. S. (2002). BLyS and APRIL form biologically active heterotrimers that are expressed in patients with systemic immune-based rheumatic diseases. *J Immunol*, *169*(8), 4314-4321. https://doi.org/10.4049/jimmunol.169.8.4314
Rossi, J. F., Moreaux, J., Hose, D., Requirand, G., Rose, M., Rouille, V., Nestorov, I., Mordenti, G., Goldschmidt, H., Ythier, A., & Klein, B. (2009). Atacicept in relapsed/refractory multiple myeloma or active Waldenstrom's macroglobulinemia: a phase I study. *Br J Cancer*, *101*(7), 1051-1058. https://doi.org/10.1038/sj.bjc.6605241
Rozenblit, M., Huang, R., Danziger, N., Hegde, P., Alexander, B., Ramkissoon, S., Blenman, K., Ross, J. S., Rimm, D. L., & Pusztai, L. (2020). Comparison of PD-L1 protein expression between primary tumors and metastatic lesions in triple negative breast cancers. *J Immunother Cancer*, *8*(2). https://doi.org/10.1136/jitc-2020-001558
Ruan, B. H., Li, X., Winkler, A. R., Cunningham, K. M., Kuai, J., Greco, R. M., Nocka, K. H., Fitz, L. J., Wright, J. F., Pittman, D. D., Tan, X. Y., Paulsen, J. E., Lin, L. L., & Winkler, D. G. (2010). Complement C3a, CpG oligos, and DNA/C3a complex stimulate IFN-alpha production in a receptor for advanced glycation end product-dependent manner. *J Immunol*, *185*(7), 4213-4222. https://doi.org/10.4049/jimmunol.1000863
Russell, P., Hennessy, B. T., Li, J., Carey, M. S., Bast, R. C., Freeman, T., & Venkitaraman, A. R. (2012). Cyclin G1 regulates the outcome of taxane-induced mitotic checkpoint arrest. *Oncogene*, *31*(19), 2450-2460. https://doi.org/10.1038/onc.2011.431
Ryan, D., Koziol, J., & ElShamy, W. M. (2019). Targeting AXL and RAGE to prevent geminin overexpression-induced triple-negative breast cancer metastasis. *Sci Rep*, *9*(1), 19150. https://doi.org/10.1038/s41598-019-55702-w
Saijo, N. (2010). Progress in cancer chemotherapy with special stress on molecular-targeted therapy. *Jpn J Clin Oncol*, *40*(9), 855-862. https://doi.org/10.1093/jjco/hyq035
Sakaguchi, M., Murata, H., Yamamoto, K., Ono, T., Sakaguchi, Y., Motoyama, A., Hibino, T., Kataoka, K., & Huh, N. H. (2011). TIRAP, an adaptor protein for TLR2/4, transduces a signal from RAGE phosphorylated upon ligand binding. *PLoS One*, *6*(8), e23132. https://doi.org/10.1371/journal.pone.0023132
Sakatani, S., Yamada, K., Homma, C., Munesue, S., Yamamoto, Y., Yamamoto, H., & Hirase, H. (2009). Deletion of RAGE causes hyperactivity and increased sensitivity to auditory stimuli in mice. *PLoS One*, *4*(12), e8309. https://doi.org/10.1371/journal.pone.0008309

Samstein, R. M., Krishna, C., Ma, X., Pei, X., Lee, K. W., Makarov, V., Kuo, F., Chung, J., Srivastava, R. M., Purohit, T. A., Hoen, D. R., Mandal, R., Setton, J., Wu, W., Shah, R., Qeriqi, B., Chang, Q., Kendall, S., Braunstein, L., . . . Riaz, N. (2021). Mutations in BRCA1 and BRCA2 differentially affect the tumor microenvironment and response to checkpoint blockade immunotherapy. *Nat Cancer*, *1*(12), 1188-1203. https://doi.org/10.1038/s43018-020-00139-8

Schmid, P., Adams, S., Rugo, H. S., Schneeweiss, A., Barrios, C. H., Iwata, H., Dieras, V., Hegg, R., Im, S. A., Shaw Wright, G., Henschel, V., Molinero, L., Chui, S. Y., Funke, R., Husain, A., Winer, E. P., Loi, S., Emens, L. A., & Investigators, I. M. T. (2018). Atezolizumab and Nab-Paclitaxel in Advanced Triple-Negative Breast Cancer. *N Engl J Med*, *379*(22), 2108-2121. https://doi.org/10.1056/NEJMoa1809615

Schmidt, A. M., & Stern, D. M. (2000). RAGE: a new target for the prevention and treatment of the vascular and inflammatory complications of diabetes. *Trends Endocrinol Metab*, *11*(9), 368-375. https://doi.org/10.1016/s1043-2760(00)00311-8

Schneider, P., MacKay, F., Steiner, V., Hofmann, K., Bodmer, J. L., Holler, N., Ambrose, C., Lawton, P., Bixler, S., Acha-Orbea, H., Valmori, D., Romero, P., Werner-Favre, C., Zubler, R. H., Browning, J. L., & Tschopp, J. (1999). BAFF, a novel ligand of the tumor necrosis factor family, stimulates B cell growth. *J Exp Med*, *189*(11), 1747-1756. https://doi.org/10.1084/jem.189.11.1747

Schuster, S. J., Bishop, M. R., Tam, C. S., Waller, E. K., Borchmann, P., McGuirk, J. P., Jager, U., Jaglowski, S., Andreadis, C., Westin, J. R., Fleury, I., Bachanova, V., Foley, S. R., Ho, P. J., Mielke, S., Magenau, J. M., Holte, H., Pantano, S., Pacaud, L. B., . . . Investigators, J. (2019). Tisagenlecleucel in Adult Relapsed or Refractory Diffuse Large B-Cell Lymphoma. *N Engl J Med*, *380*(1), 45-56. https://doi.org/10.1056/NEJMoa1804980

Schuster, S. J., Svoboda, J., Chong, E. A., Nasta, S. D., Mato, A. R., Anak, O., Brogdon, J. L., Pruteanu-Malinici, I., Bhoj, V., Landsburg, D., Wasik, M., Levine, B. L., Lacey, S. F., Melenhorst, J. J., Porter, D. L., & June, C. H. (2017). Chimeric Antigen Receptor T Cells in Refractory B-Cell Lymphomas. *N Engl J Med*, *377*(26), 2545-2554. https://doi.org/10.1056/NEJMoa1708566

Schwaller, J., Schneider, P., Mhawech-Fauceglia, P., McKee, T., Myit, S., Matthes, T., Tschopp, J., Donze, O., Le Gal, F. A., & Huard, B. (2007). Neutrophil-derived APRIL concentrated in tumor lesions by proteoglycans correlates with human B-cell lymphoma aggressiveness. *Blood*, *109*(1), 331-338. https://doi.org/10.1182/blood-2006-02-001800

See, A. L., Chong, P. K., Lu, S. Y., & Lim, Y. P. (2014). CXCL3 is a potential target for breast cancer metastasis. *Curr Cancer Drug Targets*, *14*(3), 294-309. https://doi.org/10.2174/1568009614666140305222328

Segel, M., Lash, B., Song, J., Ladha, A., Liu, C. C., Jin, X., Mekhedov, S. L., Macrae, R. K., Koonin, E. V., & Zhang, F. (2021). Mammalian retrovirus-like protein PEG10 packages its own mRNA and can be pseudotyped for mRNA delivery. *Science*, *373*(6557), 882-889. https://doi.org/10.1126/science.abg6155

Seidel, J. A., Otsuka, A., & Kabashima, K. (2018). Anti-PD-1 and Anti-CTLA-4 Therapies in Cancer: Mechanisms of Action, Efficacy, and Limitations. *Front Oncol*, *8*, 86. https://doi.org/10.3389/fonc.2018.00086

Shalabi, H., Kraft, I. L., Wang, H. W., Yuan, C. M., Yates, B., Delbrook, C., Zimbelman, J. D., Giller, R., Stetler-Stevenson, M., Jaffe, E. S., Lee, D. W., Shern, J. F., Fry, T. J., & Shah, N. N. (2018). Sequential loss of tumor surface antigens following chimeric antigen receptor T-cell therapies in diffuse large B-cell lymphoma. *Haematologica*, *103*(5), e215-e218. https://doi.org/10.3324/haematol.2017.183459

Sheehan, J., & Marasco, W. A. (2015). Phage and Yeast Display. *Microbiol Spectr*, *3*(1), AID-0028-2014. https://doi.org/10.1128/microbiolspec.AID-0028-2014
Shu, C., Zha, H., Long, H., Wang, X., Yang, F., Gao, J., Hu, C., Zhou, L., Guo, B., & Zhu, B. (2020). C3a-C3aR signaling promotes breast cancer lung metastasis via modulating carcinoma associated fibroblasts. *J Exp Clin Cancer Res*, *39*(1), 11. https://doi.org/10.1186/s13046-019-1515-2
Shvartsur, A., & Bonavida, B. (2015). Trop2 and its overexpression in cancers: regulation and clinical/therapeutic implications. *Genes Cancer*, *6*(3-4), 84-105. https://doi.org/10.18632/genesandcancer.40
Singh, N., & Warshel, A. (2010). A comprehensive examination of the contributions to the binding entropy of protein-ligand complexes. *Proteins*, *78*(7), 1724-1735. https://doi.org/10.1002/prot.22689
Sirois, C. M., Jin, T., Miller, A. L., Bertheloot, D., Nakamura, H., Horvath, G. L., Mian, A., Jiang, J., Schrum, J., Bossaller, L., Pelka, K., Garbi, N., Brewah, Y., Tian, J., Chang, C., Chowdhury, P. S., Sims, G. P., Kolbeck, R., Coyle, A. J., . . . Latz, E. (2013). RAGE is a nucleic acid receptor that promotes inflammatory responses to DNA. *J Exp Med*, *210*(11), 2447-2463. https://doi.org/10.1084/jem.20120201
Sitkiewicz, E., Tarnowski, K., Poznanski, J., Kulma, M., & Dadlez, M. (2013). Oligomerization interface of RAGE receptor revealed by MS-monitored hydrogen deuterium exchange. *PLoS One*, *8*(10), e76353. https://doi.org/10.1371/journal.pone.0076353
Smulski, C. R., & Eibel, H. (2018). BAFF and BAFF-Receptor in B Cell Selection and Survival. *Front Immunol*, *9*, 2285. https://doi.org/10.3389/fimmu.2018.02285
Somensi, N., Brum, P. O., de Miranda Ramos, V., Gasparotto, J., Zanotto-Filho, A., Rostirolla, D. C., da Silva Morrone, M., Moreira, J. C. F., & Pens Gelain, D. (2017). Extracellular HSP70 Activates ERK1/2, NF-kB and Pro-Inflammatory Gene Transcription Through Binding with RAGE in A549 Human Lung Cancer Cells. *Cell Physiol Biochem*, *42*(6), 2507-2522. https://doi.org/10.1159/000480213
Staaf, J., Glodzik, D., Bosch, A., Vallon-Christersson, J., Reutersward, C., Hakkinen, J., Degasperi, A., Amarante, T. D., Saal, L. H., Hegardt, C., Stobart, H., Ehinger, A., Larsson, C., Ryden, L., Loman, N., Malmberg, M., Kvist, A., Ehrencrona, H., Davies, H. R., . . . Nik-Zainal, S. (2019). Whole-genome sequencing of triple-negative breast cancers in a population-based clinical study. *Nat Med*, *25*(10), 1526-1533. https://doi.org/10.1038/s41591-019-0582-4
Suh, H. S., Zhao, M. L., Choi, N., Belbin, T. J., Brosnan, C. F., & Lee, S. C. (2009). TLR3 and TLR4 are innate antiviral immune receptors in human microglia: role of IRF3 in modulating antiviral and inflammatory response in the CNS. *Virology*, *392*(2), 246-259. https://doi.org/10.1016/j.virol.2009.07.001
Szekely, B., Bossuyt, V., Li, X., Wali, V. B., Patwardhan, G. A., Frederick, C., Silber, A., Park, T., Harigopal, M., Pelekanou, V., Zhang, M., Yan, Q., Rimm, D. L., Bianchini, G., Hatzis, C., & Pusztai, L. (2018). Immunological differences between primary and metastatic breast cancer. *Ann Oncol*, *29*(11), 2232-2239. https://doi.org/10.1093/annonc/mdy399
Taymaz-Nikerel, H., Karabekmez, M. E., Eraslan, S., & Kirdar, B. (2018). Doxorubicin induces an extensive transcriptional and metabolic rewiring in yeast cells. *Sci Rep*, *8*(1), 13672. https://doi.org/10.1038/s41598-018-31939-9
Teissier, T., & Boulanger, E. (2019). The receptor for advanced glycation end-products (RAGE) is an important pattern recognition receptor (PRR) for inflammaging. *Biogerontology*, *20*(3), 279-301. https://doi.org/10.1007/s10522-019-09808-3

Teras, L. R., DeSantis, C. E., Cerhan, J. R., Morton, L. M., Jemal, A., & Flowers, C. R. (2016). 2016 US lymphoid malignancy statistics by World Health Organization subtypes. *CA Cancer J Clin*, *66*(6), 443-459. https://doi.org/10.3322/caac.21357
Toft, D. J., & Cryns, V. L. (2011). Minireview: Basal-like breast cancer: from molecular profiles to targeted therapies. *Mol Endocrinol*, *25*(2), 199-211. https://doi.org/10.1210/me.2010-0164
Tong, Y., Zhong, S., Shan, Z., Yao, W., & Tian, H. (2019). A novel human anti-BAFF neutralizing monoclonal antibody derived from in vitro immunization. *Biomed Pharmacother*, *119*, 109430. https://doi.org/10.1016/j.biopha.2019.109430
Toutain, P. L., & Bousquet-Melou, A. (2004). Plasma terminal half-life. *J Vet Pharmacol Ther*, *27*(6), 427-439. https://doi.org/10.1111/j.1365-2885.2004.00600.x
Tung, N., Garber, J. E., Hacker, M. R., Torous, V., Freeman, G. J., Poles, E., Rodig, S., Alexander, B., Lee, L., Collins, L. C., & Schnitt, S. J. (2016). Prevalence and predictors of androgen receptor and programmed death-ligand 1 in BRCA1-associated and sporadic triple-negative breast cancer. *NPJ Breast Cancer*, *2*, 16002. https://doi.org/10.1038/npjbcancer.2016.2
Uchanski, T., Zogg, T., Yin, J., Yuan, D., Wohlkonig, A., Fischer, B., Rosenbaum, D. M., Kobilka, B. K., Pardon, E., & Steyaert, J. (2019). An improved yeast surface display platform for the screening of nanobody immune libraries. *Sci Rep*, *9*(1), 382. https://doi.org/10.1038/s41598-018-37212-3
Vincent, F. B., Morand, E. F., Schneider, P., & Mackay, F. (2014). The BAFF/APRIL system in SLE pathogenesis. *Nat Rev Rheumatol*, *10*(6), 365-373. https://doi.org/10.1038/nrrheum.2014.33
Vincent, F. B., Saulep-Easton, D., Figgett, W. A., Fairfax, K. A., & Mackay, F. (2013). The BAFF/APRIL system: emerging functions beyond B cell biology and autoimmunity. *Cytokine Growth Factor Rev*, *24*(3), 203-215. https://doi.org/10.1016/j.cytogfr.2013.04.003
Vissers, P. A., Mols, F., Thong, M. S., Pouwer, F., Vreugdenhil, G., & van de Poll-Franse, L. V. (2015). The impact of diabetes on neuropathic symptoms and receipt of chemotherapy among colorectal cancer patients: results from the PROFILES registry. *J Cancer Surviv*, *9*(3), 523-531. https://doi.org/10.1007/s11764-015-0429-z
Voigt, W., Matsui, S., Yin, M. B., Burhans, W. C., Minderman, H., & Rustum, Y. M. (1998). Topoisomerase-I inhibitor SN-38 can induce DNA damage and chromosomal aberrations independent from DNA synthesis. *Anticancer Res*, *18*(5A), 3499-3505. https://www.ncbi.nlm.nih.gov/pubmed/9858931
Vtorushin, S., Dulesova, A., & Krakhmal, N. (2022). Luminal androgen receptor (LAR) subtype of triple-negative breast cancer: molecular, morphological, and clinical features. *J Zhejiang Univ Sci B*, *23*(8), 617-624. https://doi.org/10.1631/jzus.B2200113
Wagner, J., Rapsomaniki, M. A., Chevrier, S., Anzeneder, T., Langwieder, C., Dykgers, A., Rees, M., Ramaswamy, A., Muenst, S., Soysal, S. D., Jacobs, A., Windhager, J., Silina, K., van den Broek, M., Dedes, K. J., Rodriguez Martinez, M., Weber, W. P., & Bodenmiller, B. (2019). A Single-Cell Atlas of the Tumor and Immune Ecosystem of Human Breast Cancer. *Cell*, *177*(5), 1330-1345 e1318. https://doi.org/10.1016/j.cell.2019.03.005
Wang, X. X., Li, Y., Yin, Y., Mo, M., Wang, Q., Gao, W., Wang, L., & Mariuzza, R. A. (2011). Affinity maturation of human CD4 by yeast surface display and crystal structure of a CD4-HLA-DR1 complex. *Proc Natl Acad Sci U S A*, *108*(38), 15960-15965. https://doi.org/10.1073/pnas.1109438108
Wang, Z., Yang, C., Li, L., Jin, X., Zhang, Z., Zheng, H., Pan, J., Shi, L., Jiang, Z., Su, K., Li, B., Shao, X., Qiu, F., Yan, J., & Huang, J. (2020). Tumor-derived HMGB1 induces CD62L(dim) neutrophil polarization and promotes lung metastasis in

triple-negative breast cancer. *Oncogenesis*, *9*(9), 82. https://doi.org/10.1038/s41389-020-00267-x
Wekerle, T., & Grinyo, J. M. (2012). Belatacept: from rational design to clinical application. *Transpl Int*, *25*(2), 139-150. https://doi.org/10.1111/j.1432-2277.2011.01386.x
Winer, E. P., Lipatov, O., Im, S. A., Goncalves, A., Munoz-Couselo, E., Lee, K. S., Schmid, P., Tamura, K., Testa, L., Witzel, I., Ohtani, S., Turner, N., Zambelli, S., Harbeck, N., Andre, F., Dent, R., Zhou, X., Karantza, V., Mejia, J., . . . investigators, K.-. (2021). Pembrolizumab versus investigator-choice chemotherapy for metastatic triple-negative breast cancer (KEYNOTE-119): a randomised, open-label, phase 3 trial. *Lancet Oncol*, *22*(4), 499-511. https://doi.org/10.1016/S1470-2045(20)30754-3
Worndl, E., Fung, K., Fischer, H. D., Austin, P. C., Krzyzanowska, M. K., & Lipscombe, L. L. (2018). Preventable Diabetic Complications After a Cancer Diagnosis in Patients With Diabetes: A Population-Based Cohort Study. *JNCI Cancer Spectr*, *2*(1), pky008. https://doi.org/10.1093/jncics/pky008
Xin, H., Cao, Y., Shao, M. L., Zhang, W., Zhang, C. B., Wang, J. T., Liang, L. C., Shao, W. W., Qi, Y. L., Li, Y., Zhang, Z. Y., Yang, Z., Sun, Y. H., Zhang, P. X., Jia, L. L., & Wang, W. Q. (2018). Chemokine CXCL3 mediates prostate cancer cells proliferation, migration and gene expression changes in an autocrine/paracrine fashion. *Int Urol Nephrol*, *50*(5), 861-868. https://doi.org/10.1007/s11255-018-1818-9
Xu, H., Jiang, C., Chen, D., Wu, Y., Lu, J., Zhong, L., & Yao, F. (2022). Analysis of Pan-Cancer Revealed the Immunological and Prognostic Potential of CBX3 in Human Tumors. *Front Med (Lausanne)*, *9*, 869994. https://doi.org/10.3389/fmed.2022.869994
Yang, L., Ma, T., & Zhang, J. (2016). GPRC5A exerts its tumor-suppressive effects in breast cancer cells by inhibiting EGFR and its downstream pathway. *Oncol Rep*, *36*(5), 2983-2990. https://doi.org/10.3892/or.2016.5062
Yang, S., Li, J. Y., & Xu, W. (2014). Role of BAFF/BAFF-R axis in B-cell non-Hodgkin lymphoma. *Crit Rev Oncol Hematol*, *91*(2), 113-122. https://doi.org/10.1016/j.critrevonc.2014.02.004
Yao, X., Liu, H., Zhang, X., Zhang, L., Li, X., Wang, C., & Sun, S. (2015). Cell Surface GRP78 Accelerated Breast Cancer Cell Proliferation and Migration by Activating STAT3. *PLoS One*, *10*(5), e0125634. https://doi.org/10.1371/journal.pone.0125634
Yin, L., Duan, J. J., Bian, X. W., & Yu, S. C. (2020). Triple-negative breast cancer molecular subtyping and treatment progress. *Breast Cancer Res*, *22*(1), 61. https://doi.org/10.1186/s13058-020-01296-5
Yu, J., Song, Y., & Tian, W. (2020). How to select IgG subclasses in developing anti-tumor therapeutic antibodies. *J Hematol Oncol*, *13*(1), 45. https://doi.org/10.1186/s13045-020-00876-4
Zaheed, M., Wilcken, N., Willson, M. L., O'Connell, D. L., & Goodwin, A. (2019). Sequencing of anthracyclines and taxanes in neoadjuvant and adjuvant therapy for early breast cancer. *Cochrane Database Syst Rev*, *2*(2), CD012873. https://doi.org/10.1002/14651858.CD012873.pub2
Zhang, L., Dutta, S., Xiong, S., Chan, M., Chan, K. K., Fan, T. M., Bailey, K. L., Lindeblad, M., Cooper, L. M., Rong, L., Gugliuzza, A. F., Shukla, D., Procko, E., Rehman, J., & Malik, A. B. (2022). Engineered ACE2 decoy mitigates lung injury and death induced by SARS-CoV-2 variants. *Nat Chem Biol*, *18*(3), 342-351. https://doi.org/10.1038/s41589-021-00965-6
Zhang, X., Cao, X., Dang, M., Wang, H., Chen, B., Du, F., Li, H., Zeng, X., & Guo, C. (2019). Soluble receptor for advanced glycation end-products enhanced the

production of IFN-gamma through the NF-kappaB pathway in macrophages recruited by ischemia/reperfusion. *Int J Mol Med*, *43*(6), 2507-2515. https://doi.org/10.3892/ijmm.2019.4152

Zhou, T., Xu, D., Tang, B., Ren, Y., Han, Y., Liang, G., Wang, J., & Wang, L. (2018). Expression of programmed death ligand-1 and programmed death-1 in samples of invasive ductal carcinoma of the breast and its correlation with prognosis. *Anticancer Drugs*, *29*(9), 904-910. https://doi.org/10.1097/CAD.0000000000000683

Zhu, L., Narloch, J. L., Onkar, S., Joy, M., Broadwater, G., Luedke, C., Hall, A., Kim, R., Pogue-Geile, K., Sammons, S., Nayyar, N., Chukwueke, U., Brastianos, P. K., Anders, C. K., Soloff, A. C., Vignali, D. A. A., Tseng, G. C., Emens, L. A., Lucas, P. C., . . . Lee, A. V. (2019). Metastatic breast cancers have reduced immune cell recruitment but harbor increased macrophages relative to their matched primary tumors. *J Immunother Cancer*, *7*(1), 265. https://doi.org/10.1186/s40425-019-0755-1

Appendix

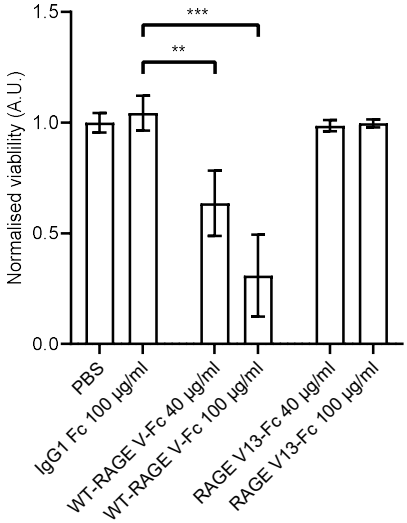


Figure A1. CCK-8 proliferation assay showing the inhibitory effects of WT-RAGE V-Fc on B cell lymphoma cell (Su-DHL-6) growth. Ten thousand of Su-DHL-6 cells were seeded in 96-well plates overnight and were then treated with PBS, IgG1 Fc or different concentrations of WT-RAGE V-Fc or RAGE V13-Fc. CCK8 proliferation assays were performed 96 hours after the treatment (n=4). All data were normalised against PBS-treated samples. One-way ANOVA was performed to compare between treatment groups. Error bars represent standard deviation of the mean. **P<0.01 or ***P<0.001.

A B

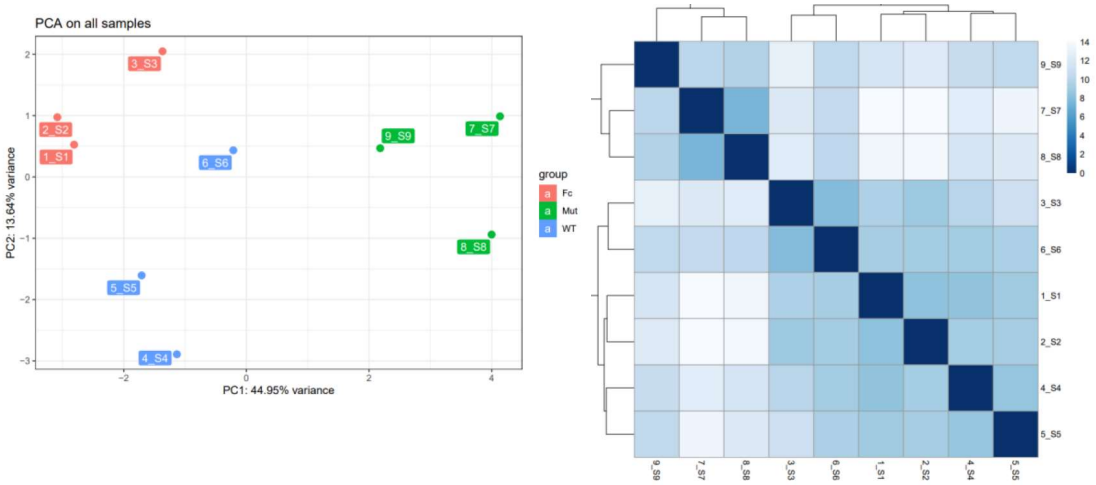


Figure A2. Clustering of RNA sequencing results. (A) PCA plot showing results of all samples in a two-dimensional plane spanned by their first two principal components. Closely related samples are clustered. Fc: IgG1 Fc (1-3). WT: WT-RAGE V-Fc (4-6). Mut: RAGE V13-Fc (7-9). **(B)** Genome-wide gene expression correlation heatmap between all samples. Samples are clustered by the Euclidean distance between rows/columns and single linkage clustering.

Table A1. List of significantly differentially expressed genes (padj < 0.05) between IgG1 Fc and WT-RAGE V-Fc groups (n=23 genes). MDA-MB-231 cells were treated with 40 µg/ml of IgG1 Fc, WT-RAGE V-Fc or RAGE V13-Fc for 24 hours. Total RNA was extracted and converted to cDNA for RNA sequencing. The positive value indicates the downregulation of gene expression in WT-RAGE V-Fc-treated groups. The negative value indicates upregulation of gene expression in WT-RAGE V-Fc-treated groups. Wald test was used for comparing across treatment groups. Fold-change > 2 and q-value ≤ 0.05 were ranked as significant.

Gene	baseMean	log2FoldChange	lfcSE	stat	pvalue	padj	Symbol
ENSG00000159842	82.21	-1.22	0.38	-3.20	1.38E-03	1.10E-02	ABR
ENSG00000125730	953.61	1.33	0.11	11.83	2.84E-32	1.17E-28	C3
ENSG00000138769	46.79	-1.11	0.35	-3.15	1.61E-03	1.24E-02	CDKL2
ENSG00000178662	53.38	-1.43	0.39	-3.71	2.10E-04	2.46E-03	CSRNP3
ENSG00000163734	966.56	1.22	0.09	13.15	1.73E-39	1.07E-35	CXCL3
ENSG00000106258	101.76	1.69	0.25	6.74	1.59E-11	2.11E-09	CYP3A5
ENSG00000205609	69.08	1.60	0.49	3.29	1.02E-03	8.66E-03	EIF3CL
ENSG00000112584	168.09	-10.75	3.91	-2.75	5.94E-03	3.35E-02	FAM120B
ENSG00000137878	85.58	-1.19	0.39	-3.09	1.99E-03	1.46E-02	GCOM1
ENSG00000134864	58.13	-1.04	0.33	-3.15	1.64E-03	1.25E-02	GGACT
ENSG00000220323	213.86	1.74	0.17	10.00	1.55E-23	3.82E-20	H2BC19P
ENSG00000080854	167.64	-1.12	0.32	-3.50	4.71E-04	4.80E-03	IGSF9B
ENSG00000269837	160.62	1.19	0.20	5.90	3.71E-09	2.54E-07	IPO5P1
ENSG00000148346	166.65	1.49	0.20	7.56	4.03E-14	9.01E-12	LCN2
ENSG00000160932	140.47	10.66	3.91	2.73	6.34E-03	3.52E-02	LY6E
ENSG00000108984	93.37	-1.02	0.31	-3.34	8.26E-04	7.42E-03	MAP2K6
ENSG00000101898	106.00	-1.03	0.27	-3.87	1.09E-04	1.42E-03	MCTS2P
ENSG00000275023	871.12	-1.07	0.14	-7.50	6.16E-14	1.27E-11	MLLT6
ENSG00000272410	185.07	-2.19	0.26	-8.48	2.23E-17	9.47E-15	NA
ENSG00000258465	66.91	-1.93	0.52	-3.72	2.01E-04	2.37E-03	NA
ENSG00000283761	127.95	-1.09	0.27	-4.11	4.03E-05	6.36E-04	NA
ENSG00000270558	40.82	1.03	0.37	2.76	5.78E-03	3.28E-02	NA
ENSG00000255346	398.17	-1.12	0.19	-5.96	2.55E-09	1.83E-07	NOX5
ENSG00000196358	53.48	-1.26	0.47	-2.67	7.63E-03	4.03E-02	NTNG2
ENSG00000124208	301.63	-1.57	0.24	-6.56	5.51E-11	6.59E-09	PEDS1-UBE2V1
ENSG00000220848	42.44	1.02	0.39	2.63	8.59E-03	4.43E-02	RPS18P9
ENSG00000151967	54.15	1.18	0.37	3.23	1.23E-03	1.01E-02	SCHIP1
ENSG00000177370	171.45	10.95	3.91	2.80	5.06E-03	2.97E-02	TIMM22
ENSG00000184937	54.64	1.46	0.48	3.04	2.38E-03	1.68E-02	WT1
ENSG00000188707	101.70	-1.17	0.24	-4.84	1.29E-06	3.70E-05	ZBED6CL
ENSG00000164684	304.21	-1.25	0.16	-7.60	3.06E-14	7.10E-12	ZNF704

Table A2. List of significantly differentially expressed genes between IgG1 Fc and RAGE V13-Fc-treated groups (n=31 genes). MDA-MB-231 cells were treated with 40 µg/ml of IgG1 Fc, WT-RAGE V-Fc or RAGE V13-Fc for 24 hours. Total RNA was extracted and converted to cDNA for RNA sequencing. The positive value indicates downregulation of gene expression in RAGE V13-Fc-treated groups. The negative value indicates upregulation of gene expression in RAGE V13-Fc-treated groups. Wald test was used for comparing across treatment groups. Fold-change > 2 and q-value ≤ 0.05 are considered to be significant.

Gene	baseMean	log2FoldChange	lfcSE	stat	pvalue	padj	Symbol
ENSG00000159842	82.21	-1.22	0.38	-3.20	1.38E-03	1.10E-02	ABR
ENSG00000125730	953.61	1.33	0.11	11.83	2.84E-32	1.17E-28	C3
ENSG00000138769	46.79	-1.11	0.35	-3.15	1.61E-03	1.24E-02	CDKL2
ENSG00000178662	53.38	-1.43	0.39	-3.71	2.10E-04	2.46E-03	CSRNP3
ENSG00000163734	966.56	1.22	0.09	13.15	1.73E-39	1.07E-35	CXCL3
ENSG00000106258	101.76	1.69	0.25	6.74	1.59E-11	2.11E-09	CYP3A5
ENSG00000205609	69.08	1.60	0.49	3.29	1.02E-03	8.66E-03	EIF3CL
ENSG00000112584	168.09	-10.75	3.91	-2.75	5.94E-03	3.35E-02	FAM120B
ENSG00000137878	85.58	-1.19	0.39	-3.09	1.99E-03	1.46E-02	GCOM1
ENSG00000134864	58.13	-1.04	0.33	-3.15	1.64E-03	1.25E-02	GGACT
ENSG00000220323	213.86	1.74	0.17	10.00	1.55E-23	3.82E-20	H2BC19P
ENSG00000080854	167.64	-1.12	0.32	-3.50	4.71E-04	4.80E-03	IGSF9B
ENSG00000269837	160.62	1.19	0.20	5.90	3.71E-09	2.54E-07	IPO5P1
ENSG00000148346	166.65	1.49	0.20	7.56	4.03E-14	9.01E-12	LCN2
ENSG00000160932	140.47	10.66	3.91	2.73	6.34E-03	3.52E-02	LY6E
ENSG00000108984	93.37	-1.02	0.31	-3.34	8.26E-04	7.42E-03	MAP2K6
ENSG00000101898	106.00	-1.03	0.27	-3.87	1.09E-04	1.42E-03	MCTS2P
ENSG00000275023	871.12	-1.07	0.14	-7.50	6.16E-14	1.27E-11	MLLT6
ENSG00000272410	185.07	-2.19	0.26	-8.48	2.23E-17	9.47E-15	NA
ENSG00000258465	66.91	-1.93	0.52	-3.72	2.01E-04	2.37E-03	NA
ENSG00000283761	127.95	-1.09	0.27	-4.11	4.03E-05	6.36E-04	NA
ENSG00000270558	40.82	1.03	0.37	2.76	5.78E-03	3.28E-02	NA
ENSG00000255346	398.17	-1.12	0.19	-5.96	2.55E-09	1.83E-07	NOX5
ENSG00000196358	53.48	-1.26	0.47	-2.67	7.63E-03	4.03E-02	NTNG2
ENSG00000124208	301.63	-1.57	0.24	-6.56	5.51E-11	6.59E-09	PEDS1-UBE2V1
ENSG00000220848	42.44	1.02	0.39	2.63	8.59E-03	4.43E-02	RPS18P9
ENSG00000151967	54.15	1.18	0.37	3.23	1.23E-03	1.01E-02	SCHIP1
ENSG00000177370	171.45	10.95	3.91	2.80	5.06E-03	2.97E-02	TIMM22
ENSG00000184937	54.64	1.46	0.48	3.04	2.38E-03	1.68E-02	WT1
ENSG00000188707	101.70	-1.17	0.24	-4.84	1.29E-06	3.70E-05	ZBED6CL
ENSG00000164684	304.21	-1.25	0.16	-7.60	3.06E-14	7.10E-12	ZNF704

Table A3. List of significantly differentially expressed genes between WT-RAGE V-Fc-treated and RAGE V13-Fc-treated groups (n=12 genes). MDA-MB-231 cells were treated with 40 μg/ml of IgG1 Fc, WT-RAGE V-Fc or RAGE V13-Fc for 24 hours. Total RNA was extracted and converted to cDNA for RNA sequencing. The positive value indicates downregulation of gene expression in RAGE V13-Fc-treated groups. The negative value indicates upregulation of gene expression in RAGE V13-Fc-treated groups. Wald test was used for comparing across treatment groups. Fold-change > 2 and q-value ≤ 0.05 were ranked as significant.

Gene	baseMean	log2FoldChange	lfcSE	stat	pvalue	padj	Symbol
ENSG00000125730	999.98	1.02	0.30	3.38	7.21E-04	1.35E-02	C3
ENSG00000163734	957.81	1.06	0.10	10.49	9.68E-26	5.81E-22	CXCL3
ENSG00000106258	111.29	1.75	0.28	6.32	2.64E-10	8.59E-08	CYP3A5
ENSG00000187908	213.56	-1.10	0.21	-5.13	2.86E-07	3.05E-05	DMBT1
ENSG00000111879	89.20	1.03	0.27	3.85	1.17E-04	3.34E-03	FAM184A
ENSG00000220323	227.42	1.55	0.17	9.22	3.09E-20	7.42E-17	H2BC19P
ENSG00000148346	159.87	1.23	0.20	6.28	3.46E-10	1.04E-07	LCN2
ENSG00000270149	57.51	-9.31	1.22	-7.62	2.57E-14	3.08E-11	NA
ENSG00000204264	174.97	3.00	0.27	11.11	1.08E-28	1.30E-24	PSMB8
ENSG00000177370	358.05	11.90	3.91	3.05	2.32E-03	3.02E-02	TIMM22
ENSG00000170006	809.97	-1.17	0.36	-3.27	1.09E-03	1.80E-02	TMEM154
ENSG00000188707	117.91	-1.13	0.24	-4.74	2.11E-06	1.45E-04	ZBED6CL

Table A4. Amino acid sequences of all decoy receptors and recombinant proteins used in this study.

Factor Xa cleavage site: IEGRMD
His-tag-factor Xa site: MNHKVHHHHHHIEGRH
Signal peptide: MGILPSPGMPALLSLVSLLSVLLMGCVAETG

Human IgG1 Fc	PKSCDKTHTCPPCPAPELLGGPSVFLFPPKPKDTLMISRTPEVT CVVVDVSHEDPEVKFNWYVDGVEVHNAKTKPREEQYNSTYRV VSVLTVLHQDWLNGKEYKCKVSNKALPAPIEKTISKAKGQPREP QVYTLPPSRDELTKNQVSLTCLVKGFYPSDIAVEWESNGQPEN NYKTTPPVLDSDGSFFLYSKLTVDKSRWQQGNVFSCSVMHEAL HNHYTQKSLSLSPGK
WT-TACI-Fc (2-165 a.a.)	MSGLGRSRRGGRSRVDQEERFPQGLWTGVAMRSCPEEQYW DPLLGTCMSCKTICNHQSQRTCAAFCRSLSCRKEQGKFYDHLL RDCISCASICGQHPKQCAYFCENKLRSPVNLPPELRRQRSGEV ENNSDNSGRYQGLEHRGSEASPALPGLKLSADQVALVYSIEGR MDPKSCDKTHTCPPCPAPELLGGPSVFLFPPKPKDTLMISRTPE VTCVVVDVSHEDPEVKFNWYVDGVEVHNAKTKPREEQYNSTY RVVSVLTVLHQDWLNGKEYKCKVSNKALPAPIEKTISKAKGQPR EPQVYTLPPSRDELTKNQVSLTCLVKGFYPSDIAVEWESNGQP ENNYKTTPPVLDSDGSFFLYSKLTVDKSRWQQGNVFSCSVMH EALHNHYTQKSLSLSPGK
Atacicept	AMRSCPEEQYWDPLLGTCMSCKTICNHQSQRTCAAFCRSLSC RKEQGKFYDHLLRDCISCASICGQHPKQCAYFCENKLRSEPKS SDKTHTCPPCPAPEAEGAPSVFLFPPKPKDTLMISRTPEVTCVV VDVSHEDPEVKFNWYVDGVEVHNAKTKPREEQYNSTYRVVSV LTVLHQDWLNGKEYKCKVSNKALPSSIEKTISKAKGQPREPQVY TLPPSRDELTKNQVSLTCLVKGFYPSDIAVEWESNGQPENNYK TTPPVLDSDGSFFLYSKLTVDKSRWQQGNVFSCSVMHEALHN HYTQKSLSLSPGK
BS7-10-Fc (2-165 a.a.)	SGLGRSGRGGRSRVGQGERLPQGLWAGVAMRSCPEEQYWD PLLGTCMSCKTICNRQSQHTCAAFCRSLSCRKEQGKFYDHLLR DCISCASVCGQHPKQCAYFCENKLRSPVNLPPELRRQRSGEV GNNSDNSGRYRGLEHRGSEASPALPGLKLSADQVALVYSIEGR MDPKSCDKTHTCPPCPAPELLGGPSVFLFPPKPKDTLMISRTPE VTCVVVDVSHEDPEVKFNWYVDGVEVHNAKTKPREEQYNSTY RVVSVLTVLHQDWLNGKEYKCKVSNKALPAPIEKTISKAKGQPR EPQVYTLPPSRDELTKNQVSLTCLVKGFYPSDIAVEWESNGQP ENNYKTTPPVLDSDGSFFLYSKLTVDKSRWQQGNVFSCSVMH EALHNHYTQKSLSLSPGK
BS7-10-Fc (68-110 a.a.)	SLSCRKEQGKFYDHLLRDCISCASVCGQHPKQCAYFCENKLRS IEGRMDPKSCDKTHTCPPCPAPELLGGPSVFLFPPKPKDTLMIS RTPEVTCVVVDVSHEDPEVKFNWYVDGVEVHNAKTKPREEQY NSTYRVVSVLTVLHQDWLNGKEYKCKVSNKALPAPIEKTISKAK GQPREPQVYTLPPSRDELTKNQVSLTCLVKGFYPSDIAVEWES NGQPENNYKTTPPVLDSDGSFFLYSKLTVDKSRWQQGNVFSC SVMHEALHNHYTQKSLSLSPGK

WT-RAGE V-Fc	AQNITARIGEPLVLKCKGAPKKPPQRLEWKLNTGRTEAWKVLS PQGGGPWDSVARVLPNGSLFLPAVGIQDEGIFRCQAMNRNGK ETKSNYRVRVYQIPGKIEGRMDPKSCDKTHTCPPCPAPELLGG PSVFLFPPKPKDTLMISRTPEVTCVVVDVSHEDPEVKFNWYVD GVEVHNAKTKPREEQYNSTYRVVSVLTVLHQDWLNGKEYKCK VSNKALPAPIEKTISKAKGQPREPQVYTLPPSRDELTKNQVSLT CLVKGFYPSDIAVEWESNGQPENNYKTTPPVLDSDGSFFLYSK LTVDKSRWQQGNVFSCSVMHEALHNHYTQKSLSLSPGK
RAGE V13-Fc	AQNITARIGEPLVLKCKGAPKRPPQRLEWRLNTGRTKAWKVLS PQGGGPWDSVARVLPNGSLFLPAVGIQDEGIFRCRAMNRNGK ETKSNYRVRVYQIPGKIEGRMDPKSCDKTHTCPPCPAPELLGG PSVFLFPPKPKDTLMISRTPEVTCVVVDVSHEDPEVKFNWYVD GVEVHNAKTKPREEQYNSTYRVVSVLTVLHQDWLNGKEYKCK VSNKALPAPIEKTISKAKGQPREPQVYTLPPSRDELTKNQVSLT CLVKGFYPSDIAVEWESNGQPENNYKTTPPVLDSDGSFFLYSK LTVDKSRWQQGNVFSCSVMHEALHNHYTQKSLSLSPGK
HSPA5-His	MNHKVHHHHHHIEGRHEEEDKKEDVGTVVGIDLGTTYSCVGVF KNGRVEIIANDQGNRITPSYVAFTPEGERLIGDAAKNQLTSNPE NTVFDAKRLIGRTWNDPSVQQDIKFLPFKVVEKKTKPYIQVDIG GGQTKTFAPEEISAMVLTKMKETAEAYLGKKVTHAVVTVPAYFN DAQRQATKDAGTIAGLNVMRIINEPTAAAIAYGLDKREGEKNILV FDLGGGTFDVSLLTIDNGVFEVVATNGDTHLGGEDFDQRVMEH FIKLYKKKTGKDVRKDNRAVQKLRREVEKAKRALSSQHQARIEI ESFYEGEDFSETLTRAKFEELNMDLFRSTMKPVQKVLEDSDLK KSDIDEIVLVGGSTRIPKIQQLVKEFFNGKEPSRGINPDEAVAYG AAVQAGVLSGDQDTGDLVLLDVCPLTLGIETVGGVMTKLIPRNT VVPTKKSQIFSTASDNQPTVTIKVYEGERPLTKDNHLLGTFDLTG IPPAPRGVPQIEVTFEIDVNGILRVTAEDKGTGNKNKITITNDQNR LTPEEIERMVNDAEKFAEEDKKLKERIDTRNELESYAYSLKNQIG DKEKLGGKLSSEDKETMEKAVEEKIEWLESHQDADIEDFKAKKK ELEEIVQPIISKLYGSAGPPPTGEEDTAEKDEL

Table A5. Amino acid sequences used for the computational structural simulation of TACI-derived sequences in complex with APRIL or BAFF. Mutations are highlighted in red.

WT-TACI CRD1 + CRD2 (35–106 a.a.);
CPEEQYWDPLLGTCMSCKTICNHQSQRTCAAFCRSLSCRKEQGKFYDHLLRDCIS CASICGQHPKQCAYFCEN
TACI CRD1 + CRD2 (35–106 a.a.);
CPEEQYWDPLLGTCMSCKTICNRQSQHTCAAFCRSLSCRKEQGKFYDHLLRDCIS CASVCGQHPKQCAYFCEN
Mutations: H56R，R60H，I92V
WT-TACI_CRD1 (35-67 a.a.)
CPEEQYWDPLLGTCMSCKTICNHQSQRTCAAFCR
BS7-10_CRD1 (35-67 a.a.)
CPEEQYWDPLLGTCMSCKTICNRQSQHTCAAFCR
Mutations: H56R，R60H
WT-TACI_CRD2 (68-106 a.a.)
SLSCRKEQGKFYDHLLRDCISCASICGQHPKQCAYFCEN
BS7-10_CRD2 (68-106 a.a.)
SLSCRKEQGKFYDHLLRDCISCASVCGQHPKQCAYFCEN
Mutations: I92V